SHOCK COMPRESSION RESPONSE OF ALUMINUM-BASED INTERMETALLIC-FORMING REACTIVE SYSTEMS

A Thesis
Presented to
The Academic Faculty

by

Paul Elliott Specht

In Partial Fulfillment
of the Requirements for the Degree
Doctor of Philosophy in the
School of Material Science and Engineering

Georgia Institute of Technology
May 2013

SHOCK COMPRESSION RESPONSE OF ALUMINUM-BASED INTERMETALLIC-FORMING REACTIVE SYSTEMS

Approved by:

Dr. Naresh N. Thadhani,
Committee Chair
School of Material Science and Engineering
Georgia Institute of Technology

Dr. Naresh N. Thadhani, Advisor
School of Material Science and Engineering
Georgia Institute of Technology

Dr. Mel Baer
Engineering Sciences Center
Sandia National Laboratories

Dr. Arun Gokhale
School of Material Science and Engineering
Georgia Institute of Technology

Dr. David McDowell
School of Material Science and Engineering
Georgia Institute of Technology

Dr. Sathya Hanagud
School of Aerospace Engineering
Georgia Institute of Technology

Date Approved: 22 January 2013

DEDICATION

SCIENCE!

ACKNOWLEDGEMENTS

First and foremost, I want to thank my Advisor, Dr. Naresh N. Thadhani, for all of his help and guidance throughout my graduate career. I also want to thank Dr. Mel Baer for mentoring me during my time at Sandia. I am grateful to Dr. David McDowell and Dr. Arun Gokkale for all their informative conversations and lectures. Additionally, I wish to acknowledge Dr. Sathya Hanagud for on serving my thesis committee. I am also indebted to the CTH development team for all of their assistance in this work: Dr. Steven Attaway, Dr. Robert Schmidt, Dr. Shane Schumacher, Dr. Jim Redmond and Dr. David Crawford. I would also like to thank Sandia National Laboratories for providing me with access to high performance computing resources for much of this work.

I have had the opportunity to work with many talented researchers throughout my career: Dr. Bradley White, Dr. Kit Neel, Dr. D. Anthony Frendenburg, Dr. Chris Wehrenberg, Dr. Greg Kennedy, Dr. Dan Eakins, Dr. Eric Herbold, Brady Aydelotte, Sean Kelly, Mike Tucker, Jenn Breidenich, Ricky Whelchel, Tyler Jackson, and Adam Jakus. Their informative conversations were invaluable.

My family and friends have been a constant source of support for me. To my parents Phil and Sue, thank you for so much. To my sisters Andrea and Gayle, thank you for believing in me. My friends, Sandy Alexander, Clinton Plaza, Laura Levy, Jonathan Sharma, and Eric Hendricks, thanks for filling the scarce free moments with enjoyable memories. Lastly, I am particularly grateful to Caitlin Chapin for always listening. She is a wonderful and beautiful person, who has heard more about shock physics than she ever desired.

Finally, I want to acknowledge the funding provided through MURI grant No.

N00014-07-1-0740, Dr. Cliff Bedford program manager, and involving the University of California at San Diego (Lead), the Johns Hopkins University, and the Georgia Institute of Technology.

TABLE OF CONTENTS

LIST OF TABLES

LIST OF FIGURES

SUMMARY

Heterogeneities at the meso-scale strongly influence the shock compression response of composite materials. These heterogeneities arise from both structural variations and differing physical/mechanical properties between constituents. In mixtures of reactive materials, such as Ni and Al, the meso-scale heterogeneities greatly affect component mixing and activation, which, in turn, can induce a chemical reaction. Cold-rolled multilayered composites of Ni and Al provide a unique system for studying the effects of material heterogeneities on a propagating shock wave, due to their full density, periodic layering, and intimate particle contacts. Computational analysis of the shock compression response of fully dense Ni/Al multilayered composites is performed with real, heterogeneous microstructures, obtained from optical microscopy, using the Eulerian hydrocode CTH. Changes in the orientation, density, structure, and strength of the material interfaces, as well as the strength of the constituents, are used to understand the influence microstructure plays on the multilayered composite response at high strain rates. The results show a marked difference in the dissipation and dispersion of the shock wave as the underlying microstructure varies. These variations can be attributed to the development of two-dimensional effects and the nature of the wave reflections and interactions. Validation of the computational results is then obtained through time-resolved measurements (VISAR, PDV, and PVDF stress gauges) performed during uniaxial strain plate-on-plate impact experiments. The experimental results prove that the computational method accurately represents the multilayered composites, thereby justifying the conclusions and trends extracted from the simulations. The reaction response of cold-rolled multilayer composites is also investigated and characterized using uniaxial stress rod-on-anvil impact experiments

through post-mortem microscopy and x-ray diffraction. This extensive understanding of the shock compression response of the multilayers systems is contrasted with other composites of Ni and Al, including shock consolidated and pressed (porous) powder compacts. A comprehensive design space is then developed to assist in the understanding and design of Ni/Al composites under conditions of high pressure shock compression.

CHAPTER I

INTRODUCTION

1.1 Motivation and Problem Definition

Composite materials are of increasing interest for engineering applications. The extensive heterogeneities in composition and structure of composite materials play a crucial role in their response under extreme conditions. One class of composites that have garnered attention in the shock compression community are termed reactive mixtures. Unlike explosives, which release large amounts of energy through the expansion of a hot gas, reactive mixtures release their chemical energy through highly exothermic reactions. Reactive mixtures can be composed of metal/metal [1, 2, 3, 4, 5, 6], metal/metal oxide [7], and metal/polymer pairs [8] allowing for large variability in density, strength between reactants, and heats of reaction.

Material interfaces play a crucial role in the mechanical response of composite systems under shock compression. The number density, configuration, and strength of these interfaces alter the structure and energy of a propagating shock front. The interfaces can cause multiple wave reflections and interactions, mixing reactant materials and depositing the shock wave energy irreversibly throughout the microstructure. If enough energy is deposited at these reactive material interfaces, ultra-fast chemical reactions can develop. This behavior has been seen in various porous powder compacts of metal/metal reactive mixtures (*e.g.* Ni+Al [1, 2, 9, 10, 11], Sn+S [12, 13], Ti+Si [14, 15, 16], Mo+Si [3, 17, 18], and Nb-Si [16, 17]) through mixing and heat generation as the voids collapse during shock compaction.

Under the right conditions, the reactions can propagate in a self-sustaining manner, completely consuming both constituents. In addition, the reactions can propagate with a characteristic front in what is termed a self-sustaining high-temperature synthesis (SHS) reactions [19]. Reactions of this type have the potential to generate novel or metastable phases possessing interesting or beneficial properties. The formation of metastable phases has already been observed in the Ni/Al system [20], and is of particular importance since the known intermetallics have excellent oxidation, corrosion, creep, and high temperature resistances.

While the potential for these systems to generate new phases exists, most interest in metal/metal reactive composites has come from the defense community. Due to their high density and reactive capabilities, reactive mixtures could enable the generation of structural materials with substantial chemical energy. Materials of this type are often termed multi-functional structural energetic materials (MSEM) and are an active area of research [1, 8]. The use of MSEMs can enable traditionally inert components to contribute to the overall reaction response, leading to the development of safer, more controllable munition systems compared to conventional explosive payloads. This capability can help mitigate collateral damage, which is becoming of increasing importance as conflicts shift to more populated urban areas.

Much of the past work on reactive material systems has focused on the propagation of shock waves through distended powder compacts. In these systems, the collapse of the void space leads to the creation of fresh, nascent surfaces at elevated temperatures along the particle interfaces. The concentration of energy deposition at the material interfaces is critical for reaction initiation. The degree to which this energy is deposited is highly dependent on the underlying microstructure and has been shown to change with particle size [2, 14], particle shape [1, 2, 9], stoichiometry [2], material processing [4], and initial density [21]. While the presence of voids helps in the initiation of reaction, it hinders the development of a strong structural material.

Consequently, there is interest in the development of fully dense reactive material composites with moderate reaction initiation thresholds.

A material configuration that can possibly fill this role is a laminated multilayer composite. Cold-rolled laminated multilayer composites present a unique microstructure vastly different from that of the porous powder compacts previously investigated. They possess continuous and periodic material interfaces with essentially no void space. In addition, multilayer composites are highly reactive under thermal ignition, developing SHS reactions [22]. The application of the highly exothermic reactions in multilayered composites has already gained attention for welding dissimilar materials for electronic components [23] and initiating propellants and pyrotechnics devices [24].

While the full density and reactivity of multilayer composites makes them attractive for MSEMs, it eliminates void space, which is a critical component of reaction initiation in porous powder compacts. This leaves only the coherency of the material interfaces to dissipate the shock wave energy irreversibly into the multilayer composite. The benefit of this dissipation method is that the energy is deposited in the ideal location for the initiation of reaction (*i.e.* the interface between constituents). However, the total amount of energy deposited is significantly less than in a porous powder compact at the same pressure. Material interfaces must then be structured and oriented to maximize energy deposition if reaction is to initiate mechanically. Fortunately, there are a variety of fabrication techniques for the construction of multilayer composites, which allow for variation in the meso-scale microstructure. Such variations in the multilayer composite microstructure have been shown to greatly effect the reaction response under thermal ignition [25, 26], but the potential for microstructural variations to alter the reaction response during mechanical ignition needs further study.

To use laminated multilayer composites for MSEM, a comprehensive study of

their response under dynamic loading must first be undertaken. The material heterogeneities in the multilayer composites create complex loading scenarios that produce deviations from the one-dimensional ideal of the Rankine-Hugoniot jump conditions, strongly influencing the characteristics of a propagating shock energy wave. In addition, the periodicity and large interfacial density generates numerous wave interactions and reflections, dispersing and irreversibly depositing the shock energy. A thorough analysis of such laminar geometries under shock compression can provide a richer understanding of the effect of material interfaces on the shock compression response of composite materials. Through variations in their microstructure, a comprehensive understanding of the wave propagation characteristics of these materials can be obtained. This understanding can then be used to establish guidelines for the fabrication of multilayer composites based on the desired application-based requirements.

1.2 Plan of Work and Research Objectives

The work performed in this study focused on developing a comprehensive understanding of the effects of dissimilar material interfaces on the propagation of a shock wave. To achieve this goal, various composites of Ni and Al, all with vastly different microstructures and interfacial characteristics, are examined under shock compression. Past work on the shock compression of porous powder compacts of Ni and Al utilized computer simulations performed on real, heterogeneous microstructures to investigate the particle level phenomena responsible for the observed response [27]. In much the same fashion, meso-scale simulations are used to understand how various interfacial and material parameters in the multilayer composites affect the shock compression response. The computational results are then validated through the use of uniaxial strain impact experiments.

Cold-rolled Ni/Al multilayered laminated composites present a microstructure ideally suited for such an undertaking. Their long, continuous particle contacts, lack of void space, and periodicity provide a microstructure that lends itself to easy manipulation of the orientation, density, and structure of the material interfaces. Through these microstructural variations, a design space can be developed to understand the effects of various interfacial parameters on the dispersion (*i.e.* the distribution of the wave energy over the microstructure) and dissipation (*i.e.* the deposition of the wave energy irreversibly into the microstructure) of a shock wave. These relationships can then be strengthened through the combined understanding obtained through comparison to past work on porous powder compacts [27], providing a rich description of the effects of material interfaces on shock wave propagation and reaction initiation.

To accomplish these goals, the work presented in this thesis relies heavily on the use of particle-resolved computer simulations, validated through uniaxial strain impact experiments. The analysis focuses on the influence of interfacial orientation, density, structure, and strength, as well as material strength, on the resulting dispersion and dissipative characteristics in cold-rolled Ni/Al multilayer composites. Through these efforts, the following research objectives are addressed.

- Develop a comprehensive design space clearly outlining the relative effects of interfacial and material properties on the resulting dispersion and dissipation of a shock wave in cold-rolled Ni/Al multilayer composites. This is achieved through a detailed computational study on various Ni/Al multilayer microstructures.

- Validate the computational analysis on the cold-rolled Ni/Al multilayer composites with time-resolved uniaxial strain impact experiments. This is accomplished through correlations with the experimentally measured Hugoniot along with the stress and free surface velocity records obtained on the Ni/Al multilayer composites.

- Investigate the reaction response of the cold-rolled Ni/Al multilayered composites under uniaxial stress loading through detailed post-mortem analysis.
- Provide a comparison between the responses of fully dense and porous Ni/Al composites to obtain a deeper understanding of the influence that interfacial properties have on the meso-scale shock compression response in highly heterogeneous systems.

To begin, a brief presentation of some relevant technical background information is provided in Chapter 2. The background section discusses the basic characteristics of a shock wave and theoretical predictions of the equation of state for both solid, distended, and composite materials. In addition, a description of past experimental and computational studies on porous powder and multilayered composites is provided. Chapter 3 presents a detailed characterization of both the cold-rolled and shock compacted Ni/Al composites. The computation results for these composites are then presented in Chapter 4. In this chapter, the effects of interfacial orientation, structure, and strength as well as material strength on the shock compression response of the multilayered composites are thoroughly discussed. These computational results are then validated experimentally in Chapter 5. The Hugoniot for the Ni/Al multilayer composite is determined from uniaxial strain impact experiments. Additionally, comparisons between the experimental records and computational predictions are shown to help further validate the computational analysis. To investigate the reaction response of the multilayered composites, modified rod-on-anvil, uniaxial stress impact experiments were performed, which are discussed in Chapter 6. In Chapter 7, the fully dense and distended composites of Ni and Al are compared to develop a richer understanding of the effects of configurational change on the shock compression response of composite materials. Building on this understanding, the computational analysis is used to formulate a comprehensive design space describing

the dissipative responses of the multilayered composites in Chapter 8. Lastly, the contributions of this research are summarized and possible future extensions of the work are given in Chapter 9.

CHAPTER II

TECHNICAL BACKGROUND AND LITERATURE REVIEW

2.1 Shock Wave Propagation in Materials

2.1.1 Shock Waves and the Solid Hugoniot

Strong, compressive, longitudinal stress waves can be generated in materials through a variety of methods, such as impact by another body, deposition of radiation through a laser, or pressure from the products of a detonating explosive [28]. At large stress amplitudes, the material response becomes nonlinear, and, for a wave to remain stable, the wave speed must increase with increasing stress. This causes the wave front to steepen over time into a shock wave. In an idealized sense, the shock wave is a discontinuous transition from one thermodynamic state to another. In actuality, this transition is not instantaneous, and the shock front does have some thickness. This results from an increase in dissipative effects, such as viscosity, with strain rate [29]. However, this becomes more of an issue at very large strain rates, and, for most purposes, the shock wave can be considered an instantaneous, discontinuous transition [29].

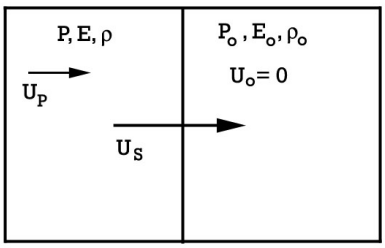

Figure 2.1: Schematic of a shock wave moving to the right in a material at rest.

A schematic of a shock front moving in a material at rest is shown in Figure 2.1. The shock wave is seen to travel at a characteristic speed, U_S, and impart a material or particle velocity, U_P, to the material behind the shock front. The thermodynamic state of the material (*i.e.* pressure, P, internal energy, E, and density, ρ) is also seen to change across the shock front. Equations relating the thermodynamic states across the shock front in fluids were first developed by Rankine [30] and Hugoniot [31] back in the late 1800's. The Rankine-Hugoniot equations represent the conservation of mass, momentum, and energy across the shock front and are given below.

$$\rho_0(U_S - U_0) = \rho(U_S - U_P) \tag{2.1}$$

$$P - P_0 = \rho_0(U_S - U_0)(U_P - U_0) \tag{2.2}$$

$$E - E_0 = \frac{1}{2}(P - P_0)(V_0 - V) \tag{2.3}$$

Here, $V{=}\frac{1}{\rho}$ is the specific volume and U_0 is the initial material velocity, with the subscript 0 signifying the initial state. These equations are often referred to as the "jump condition", since they describe the jump in state across the shock front. Although developed for fluids, the Rankine-Hugoniot equations also hold true for the hydrodynamic component of stress, or pressure, in solids for any wave that is steady in time [32]. Under shock compression, the shear components of stress can be considered small, allowing for the application of the Rankine-Hugoniot equations.

The Rankine-Hugoniot conditions represent a system of three equations with five unknowns (P, E, ρ, U_S, and U_P). However, a simplification of this system of equations can be obtained by noting that most materials exhibit an empirical relation between U_S and U_P. This relationship can be expressed through a polynomial and is often referred to as the equation of state (EOS) of the material.

$$U_s = C_0 + S_1 U_p + S_2 U_p^2 + \cdots \tag{2.4}$$

In Equation 2.4, C_0 is the inert sound speed and S_i are material constants. Most materials can be adequately described with a linear relationship between U_s and U_p [33]. With this empirical EOS known, closure of the Rankine-Hugoniot equations for a material can be obtained through the measurement of a single parameter.

Using the Rankine-Hugoniot equations, a complete representation of the response of a material under shock compression can be presented with a Hugoniot curve, or more simply a Hugoniot. The Hugoniot is a surface in P, E, and V space and defines the locus of equilibrium points achieved during shock compression. The Hugoniot can be expressed with any combination of variables given in Equations 2.1-2.3. Commonly, the Hugoniot is represented in P-V and P-U_P space with the following equations.

$$P = \frac{C_0^2 \left(V_0 - V\right)}{\left[V_0 - S_1 \left(V_0 - V\right)\right]^2} \tag{2.5}$$

$$P = \rho_0 \left(C_0 + S_1 U_p\right) U_p \tag{2.6}$$

A Hugoniot curve in P (or applied stress, σ) vs. V space is shown graphically in Figure 2.2.

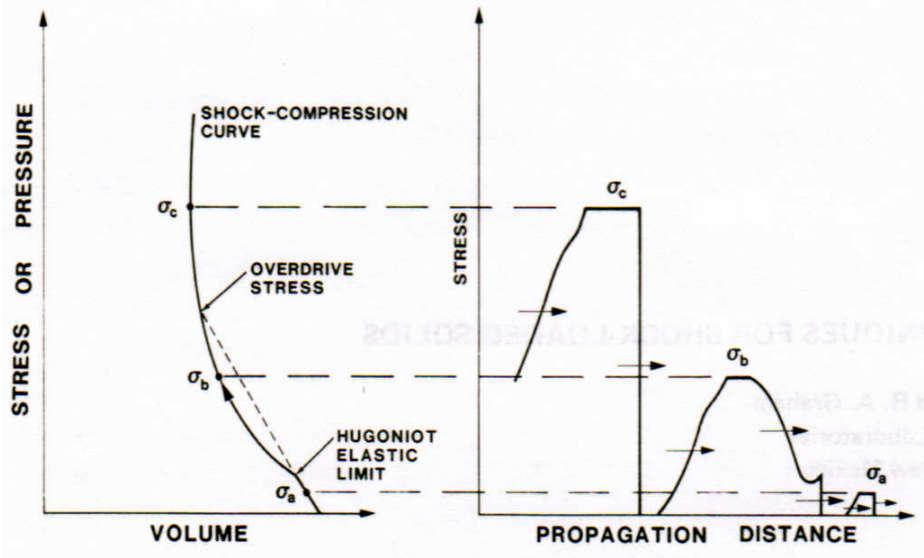

Figure 2.2: Illustration of a Hugoniot curve in P-V space along with shock wave profiles at different locations on the Hugoniot [34].

It is important to note that the Hugoniot curve does not represent the loading

path for a single shock event. Due to the conditions imposed by the Rankine-Hugoniot equations, materials must load along a straight line connecting the initial and final compressed states. This path is referred to as the Rayleigh line, and its slope in P-V space is proportional to the square of the shock speed.

$$-\left(\rho_0 U_s\right)^2 \tag{2.7}$$

Similarly, the slope of the Rayleigh line can be seen to be directly proportional to U_S in P-U_P space through Equation 2.2. This result is not surprising given the assumed discontinuous transition of the shock front. If a material were to load along the Hugoniot, the constraint imposed by Equation 2.7 would mean that the shock speed would change with pressure at the wave front instead of remaining constant. Such a wave would not have a steady, discontinuous front and would not be a shock.

The Hugoniot curve in Figure 2.2 exhibits a linear elastic region at very low pressures, up to its dynamic yield strength, or Hugoniot Elastic Limit (HEL). After that, the Hugoniot follows the quadratic relation expressed by Equation 2.5. The dashed line on the Hugoniot curve represents the Rayleigh line for a loading event at the overdrive stress, which is the stress at which the elastic wave is overtaken by the shock and not detected.

Figure 2.2 also shows wave profiles for various locations along the Hugoniot. Loading in the elastic region is linear and represented by the wave profile at stress σ_a. At stress σ_b, above the HEL but below the overdrive stress, a more complex wave profile develops. At the wave front, there is an initial elastic wave, termed the elastic precursor, followed by some stress relaxation before the material loads up to the peak pressure. This elastic precursor has an amplitude equal to the HEL, but, due to rate effects, the HEL can decrease with increasing propagation distance [35]. When the material is loaded to stress σ_c above the overdrive stress, no elastic precursor is present, and the wave front is essentially a discontinuity. For both applied stresses σ_b

and σ_c, the material unloads first elastically, then plastically, to the ambient conditions.

This release of the material to ambient conditions after the passage of the shock wave occurs along the material isentrope. Since material velocity increases with pressure, release waves are not steady and smear out over time, as seen in Figure 2.2. This means that it is impossible, in most materials, to achieve a release shock [32]. As a result, the Rankine-Hugoniot equations do not hold across a release wave. At moderate pressures the Hugoniot and the isentrope are essentially the same, which can be seen in Figure 2.3 [36]. This means, at moderate pressures, material unloading can be approximated as following the Hugoniot.

The release wave also imparts a velocity on the material, similar to that of a shock wave. This means that the velocity at the free surface of a sample after release is the summation of the particle velocities imparted by the shock and release waves.

$$U_{fs} = U_P + U_R \tag{2.8}$$

It is commonly assumed that the shock and release particle velocities are equal ($\frac{U_P}{U_R} \sim 1$). At moderate pressures, this assumption is perfectly adequate. This enables the determination of the particle velocity in an experiment easily through the measurement of the free surface velocity with an interferometer. Walsh and Christian [37] examined this assumption and developed expressions for the maximum and minimum bounds of this approximation based on the material properties (corrected from [37]).

$$\left(\frac{U_R}{U_P}\right)_{max} = \left[\left(\frac{P+2\beta}{2P}\right) ln\left(\frac{P+\beta}{\beta}\right)\right] \tag{2.9}$$

$$\left(\frac{U_R}{U_P}\right)_{min} = \frac{\int_0^P \left[\left(-\frac{dV}{dP}\right)^{\frac{1}{2}} dP\right]_{Hug}}{[P(V_0 - V)]^{\frac{1}{2}}} \tag{2.10}$$

$$\beta = \frac{C_P}{\alpha V_0} \tag{2.11}$$

In the above equation, α is the linear coefficient of thermal expansion, C_P is the constant pressure specific heat, and the subscript "Hug" implies the integral is taken

along the Hugoniot. Walsh and Christian found that for the materials they investigated (Al, Cu, Zn) this ratio ranged between roughly 0.97 and 1.03 for pressures up to 30 GPa [37].

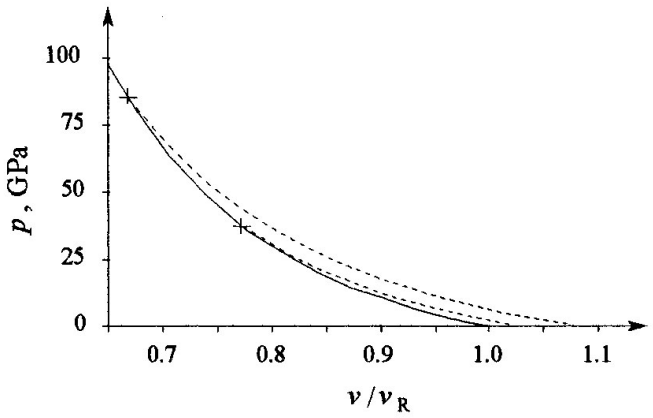

Figure 2.3: Comparison between Hugoniot and isentrope during release from 85 and 38 GPa [36]. At moderate pressures, the isentrope can be approximated with the Hugoniot.

2.1.2 Mie-Grüneisen Equation of State

Often times, it is desirable to describe a material in a state not on the Hugoniot. These states can be described using an alternate EOS that relates the thermodynamic state of the material (P, E, and V) to that of a known reference curve. This is commonly done with the Mie-Grüneisen EOS [38].

$$P - P_R = \frac{\gamma}{V}(E - E_R) \tag{2.12}$$

In the above equation, the subscript R refers to the reference state and the parameter γ, is termed the Grüneisen coefficient [39].

The ability for the Mie-Grüneisen EOS to relate a reference state to the current state is built upon assumptions in the Grüneisen coefficient. The Grüneisen coefficient is commonly expressed by taking Equation 2.12 in differential form.

$$\gamma = V\frac{\partial P}{\partial E}\bigg|_V \tag{2.13}$$

In this form, it becomes clear that the Grüneisen coefficient represents the increase in pressure resulting from an increase in internal energy. This increase of thermal pressure arises from atomic vibrations in the material, making the Grüneisen coefficient a statistical, thermodynamic quantity. An expression for the Grüneisen coefficient can then be derived with quantum statistical mechanics [33], classical mechanics [40], or purely thermodynamic considerations [41]. Commonly, all the atoms are assumed to vibrate at the same frequency (Einstein model) [42]. With this assumption, the Grüneisen coefficient can be expressed solely as a function of volume, $\gamma(V)$, which enables easier comparisons between the reference state, such as the Hugoniot, and the unknown state [38].

The Grüneisen coefficient, $\gamma(V)$, is a hard quantity to accurately determine. However, using Maxwell's relations, the Grüneisen coefficient can be expressed with more familiar thermodynamic quantities [36].

$$\frac{\gamma}{V} = \frac{3\alpha K_T}{C_V} = \frac{3\alpha K_S}{C_P} \tag{2.14}$$

In the above equation, 3α is the volumetric thermal expansion, K_T and K_S are the isothermal and isentropic bulk moduli, and C_V and C_P are the constant volume and pressure specific heats. While there have been more complex forms of $\gamma(V)$ developed by Slater [43] and Dugdale and MacDonald [44] using Debye theory, for many applications the assumption:

$$\frac{\gamma}{V} = \frac{\gamma_0}{V_0} \tag{2.15}$$

is found to be an adequate simplification [45].

2.1.3 McQueen Mixture Theory

There have been many different methods for predicting the Hugoniot response of a homogeneous composite, such as the one developed by Baer *et al.* [46] and later extended by Jordan *et al.* [47]. One of the more prominent mixture routines was

proposed by McQueen *et al.* [45]. McQueen mixture theory is an improvement upon simple averaging techniques, which assume that the mixture volume can be found by adding the volumes of each constituent. For shock loading, this assumption is not particularly accurate since it does not account for the shock heating of each constituent. To account for the volume increases of each constituent as a result of the shock heating, McQueen *et al.* proposed averaging the material along the 0 Kelvin isotherm, or cold compression curve.

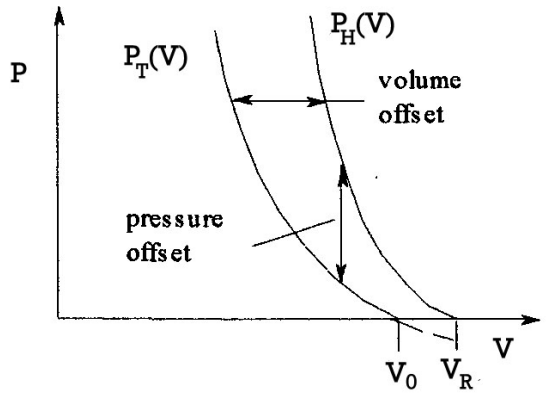

Figure 2.4: Graphical representation of the relationship between the Hugoniot and isotherm [36].

The relationship between the Hugoniot and the isotherm is presented graphically in Figure 2.4. Using the known material Hugoniot and the Mie-Grüneisen EOS (Equation 2.12), an equation for the isotherm can be derived [36].

$$P_H(V) = P_T(V,T) + \frac{\gamma(V)}{V}\left[E_H(V) - E_T(V,T)\right] \tag{2.16}$$

In the above equation, the subscripts H and T refer to states on the Hugoniot and isotherm, respectively. Using the conservation of energy (Equation 2.3), an expression for the energy along the Hugoniot can be obtained [36].

$$E_H(V) = E_R + \frac{1}{2}P_H(V)(V_R - V) \tag{2.17}$$

Here, the subscript R refers to the state at $P = 0$ along the Hugoniot, as seen in

Figure 2.4. An expression for the energy along the isotherm can now be obtained using the first law of thermodynamics and the following relation [36].

$$\left.\frac{\partial S}{\partial V}\right|_T = \frac{\gamma(V)}{V} C_V \tag{2.18}$$

$$E_T(V,T) - E_0 = \int_{V_0}^{V} T\frac{\gamma(V)}{V} C_V(V,T)dV - \int_{V_0}^{V} P_T(V,T)dV \tag{2.19}$$

In the above equation, the subscript 0 refers to states at zero pressure along the isotherm, as seen in Figure 2.4. Equations 2.19 and 2.17 can now be substituted into Equation 2.16 and solved for $P_H(V)$ (corrected from [36]).

$$P_H(V) = \frac{P_T(V,T) + \frac{\gamma(V)}{V}\left[E_R - E_0 - \int_{V_0}^{V} T\frac{\gamma(V)}{V} C_V(V,T)dV + \int_{V_0}^{V} P_T(V,T)dV\right]}{1 - \frac{\gamma(V)}{2V}(V_R - V)} \tag{2.20}$$

Taking the derivative of Equation 2.20 yields a differential equation for $P_T(V,T)$ [36].

$$\begin{aligned}\frac{\partial P_T(V,T)}{\partial V} + \frac{\gamma(V)}{V} P_T(V,T) = \frac{\partial P_H(V)}{\partial V}\left[1 + \frac{\gamma(V)}{2V}(V_R - V)\right] \\ + \frac{\gamma(V)}{2V} P_H(V) + \left(\frac{\gamma(V)}{2V}\right)^2 T C_V(V,T)\end{aligned} \tag{2.21}$$

This is a general expression for an isotherm that can be solved using Equation 2.5 and its derivative with respect to V. These are presented below for completeness and consistency of notation.

$$P_H = \frac{C_0^2 (V_R - V)}{\left[V_R - S_1 (V_R - V)\right]^2} \tag{2.22}$$

$$\frac{\partial P_H(V)}{\partial V} = \frac{-C_0^2(V_R + S_1(V_R - V))}{[V_R - S_1(V_R - V)]^3} \tag{2.23}$$

While Equations 2.20 and 2.21 hold true for any isotherm, simplifications arise for the cold compression curve. At 0 Kelvin, the specific heat term vanishes. An additional simplification can be obtained by assuming $\frac{\gamma}{V}$ is constant (Equation 2.15) [36].

$$P_H(V) = \frac{P_T(V,T) + \frac{\gamma}{V}\left[E_R - E_0 + \int_{V_0}^{V} P_T(V,T)dV\right]}{1 - \frac{\gamma}{2V}(V_R - V)} \tag{2.24}$$

$$\frac{\partial P_{T_0}(V)}{\partial V} + \frac{\gamma_R}{V_R} P_{T_0}(V) = \frac{\partial P_H(V)}{\partial V}\left[1 + \frac{\gamma_R}{2V_R}(V_R - V)\right] + \frac{\gamma_R}{2V_R} P_H(V) \tag{2.25}$$

In these equations, T_0 signifies terms along the 0 Kelvin isotherm. Equation 2.25 can now be solved for $P_{T_0}(V)$ for each material in the mixture. This result can then be combined with the Mie-Grüneisen EOS, assuming $P_0 = E_0 = 0$, to obtain the energy along the cold compression curve[36].

$$E_{T_0}(v) = P_{T_0}\frac{\gamma_R}{V_R} \tag{2.26}$$

This provides a complete description of the cold compression curve in P-V-E space.

With the cold compression curve of each constituent now defined, the cold compression curve of the mixture can be found through mass or volume averaging. While McQueen *et al.* chose to average V(P) and E(P), this averaging can be done regardless of the space.

$$V_K = \sum_i X_i V_i(P) \tag{2.27}$$

$$E_K = \sum_i X_i E_i(P) \tag{2.28}$$

Additionally, McQueen *et al.* assumed C_V and $\frac{V}{\gamma}$ were constant and could be found through simple averaging [45].

$$\left(\frac{V}{\gamma}\right)_K = \sum_i X_i \left(\frac{V}{\gamma}\right)_i \tag{2.29}$$

$$C_{V_K} = \sum_i X_i C_{V_i} \tag{2.30}$$

Here, the subscript K refers to the mixture cold compression curve and X_i represents the mass or volume fraction depending on the averaging method used.

In order to relate the mixture cold compression curve to its Hugoniot via Equation 2.24, the energy of the Hugoniot at zero pressure, E_R, must be determined. Choosing $E_0 = 0$ in Equation 2.24, E_R can be determined relative to that value with the following [36].

$$E_R = \int_{T_0}^{T_R} C_V(V,T)dT \tag{2.31}$$

This leaves only the specific volume at zero Kelvin, V_0, to be found, which can be determined by finding the volume at which $P_T(V_0) = 0$ or substituting V_0 into Equation 2.24 for V [36].

$$\left[1 - \frac{\gamma_R}{V_R}(V_R - V_0)\right] P_H(V_0) = \frac{\gamma_R}{V_R} E_R \tag{2.32}$$

With all the parameters now defined, Equation 2.24 can be solved to determine the mixture Hugoniot.

2.1.4 Dynamic Compaction of Distended Materials

Porous, or distended, materials have a very different response under shock compression than a solid material, due to the presence of void space. Figure 2.5 shows the characteristic responses of a porous and solid material. The P-V response of the porous Hugoniot, shown in Figure 2.5a, is seen to start at a much larger specific volume (*i.e.* lower density), and, then, slowly approach the response of the solid Hugoniot. This behavior is termed the "crush-up" of the porous material, and the pressure at which the material reaches full density is the crush strength. Additionally, at pressures above the "crush strength", the porous Hugoniot begins to deviate from that of the solid Hugoniot, showing an increase in volume at identical pressures. As the material is compacted, void collapse induces plastic flow and particle interactions, which dissipates energy [32]. This heats the material, causing this increase in the volume at higher pressures.

The nature of a particle compact leads to complex wave interactions and loading scenarios during shock compression. These considerations have led to a large amount of computational work to understand the effects of particle morphology on the shock compression response of porous materials, which will be discussed in more detail later. However, this complexity raises a fundamental question of shock stability. If the particulate microstructure leads to changes in the shock wave speed, then the resulting response can not be described by the Rankine-Hugoniot conditions. While,

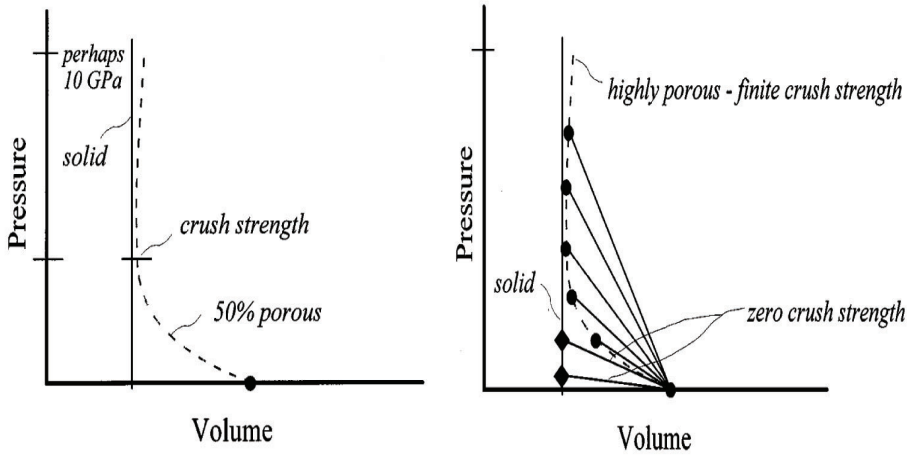

(a) Pressure vs. Volume (b) Pressure vs. Volume

Figure 2.5: Hugoniot relation between porous and solid materials [14].

there is some evidence that the wave speed does change with propagation distance, most studies suggest that porous materials can support a steady shock wave, and confirm the validity of using the Rankine-Hugoniot conditions in their analysis [32].

2.1.4.1 Compaction Models

An analytical description the dynamic compaction of porous systems is commonly done using either the P-α model, developed by Hermann [48], or the the P-λ model, developed by Grady *et al.* [49]. Both models are briefly discussed below.

P-α Model The underlying principle of the P-α compaction model developed by Hermann [48] is that the specific internal energy of the porous material is identical to that of the solid material at any condition. This ignores all surface energies and directly relates the properties of the porous material to those of the solid. Ignoring shear strength, pressure can be expressed as a function of only volume and energy [48].

$$P = f(V, E) \tag{2.33}$$

A porosity term, α, is then introduced,

$$\alpha = \frac{V}{V_S} \tag{2.34}$$

where V and V_S refer to the specific volume of the porous and solid material, respectively. The pressure of the porous material can then be redefined as a function of the V, E and α [48].

$$P = f(\frac{V}{\alpha}, E) \tag{2.35}$$

To complete the description, Hermann [48] assumed that the porosity was only a function of pressure.

$$\alpha = g(P) \tag{2.36}$$

Hermann represented the compaction behavior of the material with two distinct regions. Initially, the porous material compresses elastically to pressure P_e and porosity α_e, as shown in Figure 2.6. Above pressure P_e, the material compresses plastically. Ideally, any unloading from a plastically deformed state is elastic, as shown in Figure 2.6. The material continues to deform plastically, until the crush strength, P_s, is reached. Above this pressure, the material is assumed to be completely dense and described by the solid Hugoniot. This is expressed mathematically as the following for the elastic

$$\begin{array}{ccc} P = 0 & \alpha = \alpha_e & \frac{d\alpha}{dP} = \alpha'_e \\ 0 < P < P_s & \alpha_e > \alpha > 1 & \frac{d\alpha}{dP} < 0 \\ P = P_s & \alpha = 1 & \frac{d\alpha}{dP} = 0 \end{array} \tag{2.37}$$

and plastic regions [48].

$$\begin{array}{ccc} P = P_e & \alpha = \alpha_p & \frac{d\alpha}{dP} = \alpha'_p \\ P_e < P < P_s & \alpha_p > \alpha > 1 & \frac{d\alpha}{dP} < 0 \\ P = P_s & \alpha = 1 & \frac{d\alpha}{dP} = 0 \end{array} \tag{2.38}$$

To describe the behavior of α with pressure, Hermann [48] originally proposed a cubic polynomial. However, Butcher and Karnes [50] found that a quadratic formulation was adequate and leads to the following simplification [48].

$$\frac{\alpha - 1}{\alpha_p - 1} = \left[\frac{(P_s - P)}{(P_s - P_e)}\right]^2 \tag{2.39}$$

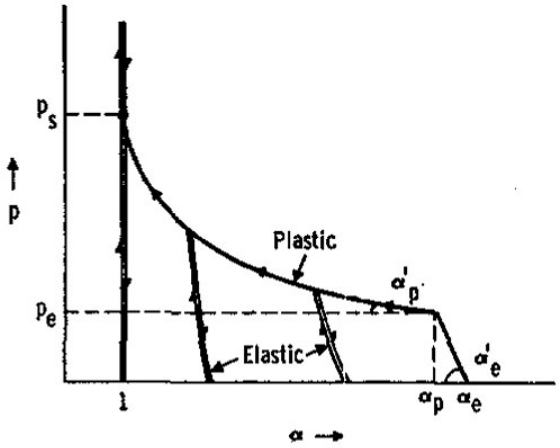

Figure 2.6: Schematic showing the dynamic compaction of ductile powder [48].

It is important to note that the P-α model does not account for rate effects which can be significant [50]. Also, the fits for α are simply empirical. To get a more theoretical basis, Carroll and Holt [51] modified Equation 2.35 after finding that the pressure of the porous material is more closely described with the following.

$$P = \frac{1}{\alpha} f(\frac{V}{\alpha}, E) \tag{2.40}$$

This approximation comes from assuming the pores are traction free and do not experience the same pressure as the matrix material [51].

P-λ Model The P-λ model was developed by Grady *et al.* to provide a simple mixture routine for composites composed of materials with very different compliances [49]. While the P-λ model can be used for a mixture of any number of components, it is often used for porous materials assuming that one component is air or void space.

The model is built on the parameter λ, which describes the relative compaction of the mixture during compression.

Any composite material under slight compression exhibits an unequilibrated elastic response dominated by the stiffer material. At large compressions, the material compacts completely and its response is dominated by the equation of state, yielding a pressure equilibrated response. At intermediate pressures, the material transitions between these two extremes. To describe this transition process, Grady *et al.* assumed the material crushed heterogeneously, as opposed to the homogeneous compaction assumed in the P-α model [48]. This is accomplished through the parameter λ, which describes the fraction of the mixture that has been compacted and represented by the pressure equilibrated equation of state.

For the unequilibrated elastic region, the upper and lower bounds for the response can be determined using the isostrain (Voigt) and isopressure (Reuss) assumptions, respectively. Assuming the strains and pressures of each component are additive [49],

$$d\mu = \sum f_i d\mu_i \tag{2.41}$$

$$dP = \sum f_i dP_i \tag{2.42}$$

the moduli of the mixture based on the isostrain and isopressure assumptions are represented with the following [49].

$$K_\mu = \sum f_i K_i \tag{2.43}$$

$$K_p = \left(\sum \frac{f_i}{K_i} \right)^{-1} \tag{2.44}$$

In these equations, f_i corresponds to the volume fraction of the constituents, μ is the strain, K_P is the isopressure modulus, and K_μ is the isostrain modulus. Grady *et al.* assumed the elastic region is described by the isostrain modulus, K_μ [49], while the high pressure equilibrated region is described by a linear equation of state (Equation

2.4) utilizing the following averaged mixture properties [49].

$$\rho_0 = \sum f_i \rho_i \tag{2.45}$$

$$\rho_0 C_0^2 = \left(\sum \frac{f_i}{\rho_{0_i} C_{0_i}^2} \right)^{-1} \tag{2.46}$$

$$\frac{1}{S_1} = \sum \frac{f_i}{S_{1_i}} \tag{2.47}$$

This enables the P-V response of the mixture to be defined with the parameter λ [49].

$$V_M(P) = \lambda V_h(P) + (1 - \lambda) V_e(P) \tag{2.48}$$

Here, the subscripts M, h, and e refer to the mixture, equilibrated, and unequilibrated regions, respectively.

To solve Equation 2.48, Grady *et al.* assumed the following functional form for λ [49].

$$\lambda = 1 - exp\left[- \left(\frac{P_l}{Y_l} \right)^n \right] \tag{2.49}$$

Here, P_l is a measure of the local stress difference in the mixture and depends on the compliances of each component.

$$P_l = (K_\mu - K_P)\mu \tag{2.50}$$

The parameter Y_l is the local yield strength and is defined with the following relation.

$$Y_l = \sum f_i Y_i \tag{2.51}$$

The parameter n is an empirical measure of the heterogeneity of the compaction process and has no relation to the component properties [49]. Figure 2.7 shows the compaction curve described by the P-λ model. With only one equation, the P-λ model is able to completely describe the compaction event.

2.1.4.2 Equation of State Approximations for Distended Materials

There have been numerous attempts to describe the response of distended materials using their solid Hugoniot [48, 52, 53]. In general two main methods are used to

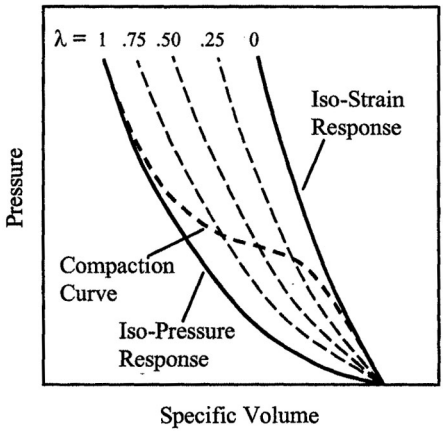

Figure 2.7: Schematic showing the compaction curve predicted by the P-λ model [49].

reference the porous Hugoniot to that of the solid Hugoniot: isochoric (constant volume) and isobaric (constant pressure) shifts. These are shown graphically in Figure 2.8. While the more prominent methods for each are briefly discussed below, a more thorough discussion can be found in the work of Frendenburg [54].

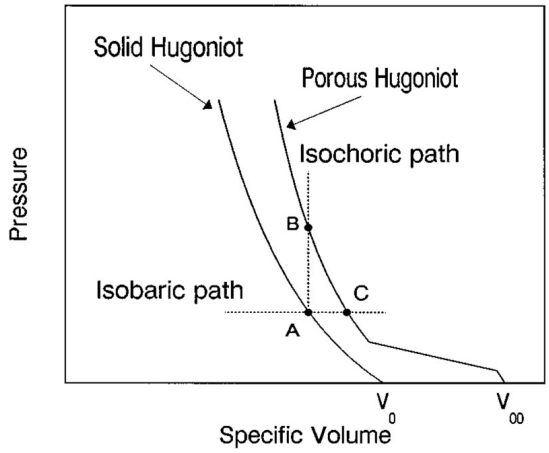

Figure 2.8: Illustration showing the isochoric and isobaric paths used to determine the EOS of a porous material [53].

Isochoric Methods The Mie-Grüneisen EOS (Equation 2.12) can be used to relate the response of a porous material to its solid Hugoniot. The energy of the solid and porous Hugoniots can be expressed using the conservation energy (Equation 2.3)

assuming E_0 and P_0 equal zero.

$$E_{SH} = \frac{1}{2} P_{SH}(V_0 - V) \tag{2.52}$$

$$E_{PH} = \frac{1}{2} P_{PH}(V_{00} - V) \tag{2.53}$$

Here, the subscript SH refers to the solid state with initial specific volume V_0 and the subscript PH refers to the porous state with initial specific volume V_{00}. Plugging equations 2.52 and 2.53 into the Mie-Grüneisen EOS with the solid Hugoniot as the reference state, the porous Hugoniot can be found. Using Equation 2.5, the porous Hugoniot can be represented in P-V space as the following.

$$P_{PH} = \frac{C_0^2(V_0 - V)\left[1 - \frac{\gamma}{2V}(V_0 - V)\right]}{[V_0 - S_1(V_0 - V)]^2\left[1 - \frac{\gamma}{2V}(V_{00} - V)\right]} \tag{2.54}$$

Equation 2.54 describes the EOS behavior of a porous material that exhibits no crush strength. If a material exhibits crush strength, as illustrated in Figure 2.5b, the isochoric shift described by Equation 2.54 can not completely describe the material response. Since the porous material has a larger initial specific volume then the solid material, there are no isochoric paths that can reference the solid response to the material behavior during crush-up. To solve this problem, the Mie-Grüneisen EOS method must be combined with a model describing the material crush up, such as the P-α [48] or the P-λ [49] models, to accurately represent the entire porous Hugoniot.

The Mie-Grüneisen EOS method is best used for moderate levels of porosity. As the porosity increases, the porous Hugoniot deviates more from the solid Hugoniot, making direct correlations less accurate. This is also complicated by the linear relation resulting from assuming a constant Grüneisen coefficient. With the Mie-Grüneisen EOS method, a porosity is eventually reached in which the material response shows an increase in specific volume with increasing pressure. This critical porosity can be represented as the following [55].

$$\frac{V_0}{V_{00}} = \frac{\gamma}{2 + \gamma} \tag{2.55}$$

Since most metals have a $\gamma \sim 2$ [38], this porosity is around 50%. Figure 2.9 shows the predicted Hugoniots for porous copper at varying intial densities. The data for Cu was obtained from Marsh [56] assuming $\gamma = 2$. At 40% TMD (Theoretical Maximum Density)(*i.e.* 60% porosity), the Mie-Grüneisen porous EOS shows a large increases in specific volume with increasing pressure, which is not physically realistic.

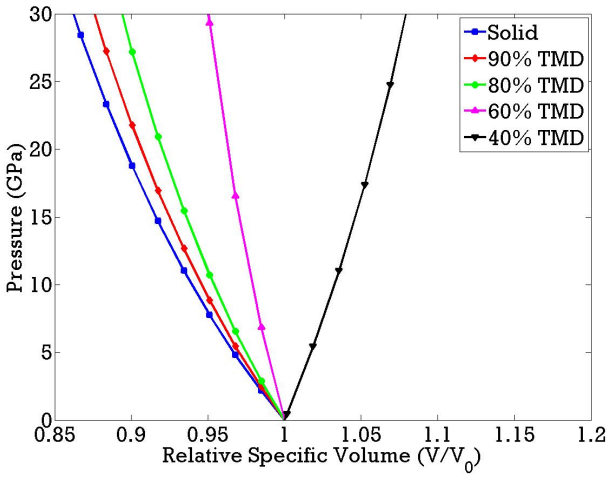

Figure 2.9: Prediction of the porous Hugoniot for Cu using the Mie-Grüneisen isochoric approximation for various initial densities.

Another isobaric approach to describe the Hugoniot behavior of porous materials centers on partitioning into thermal and athermal (isentropic) effects.

$$E = E_C + E_T \tag{2.56}$$

$$P = P_C + P_T \tag{2.57}$$

Here, the subscript C refers to the athermal, or cold compression component, and the subscript T refers to the thermal component. This was first developed by Zel'dovich and Raizer [57] who assumed the total energy could be described as the summation of the elastic, athermal, and the internal, thermal, energies. The elastic energy results from compression of the material lattice during the shock event, which is recovered during release. The internal energy is related to a thermal pressure caused by the

vibrational modes of the atoms [57]. This enables the thermal energy to be described with the Grüneisen coefficient in the following manner [57].

$$E_T = \frac{P_T}{\rho\gamma} \tag{2.58}$$

Using the conservation of energy (Equation 2.3) along with Equations 2.56, 2.57, and 2.58, the porous Hugoniot can be obtained.

$$p = \frac{\frac{2}{\gamma}P_C - 2\rho E_C}{\frac{2}{\gamma} + 1 - \frac{\rho}{\rho_{00}}} \tag{2.59}$$

Simons and Legner [52] used this approach to develop a description of the porous material Hugoniot by assuming that at low and high pressures the athermal and thermal components would dominate, respectively. Based on this assumption, they develop descriptions of the athermal components at low pressures [52].

$$P_C = \frac{\rho - \rho_0}{\rho_0 K} \tag{2.60}$$

$$E_C = \frac{(\rho - \rho_0)^2}{2K\rho_0^3} \tag{2.61}$$

This led to the development of the following EOS [52].

$$\frac{\rho}{\rho_0} = \frac{1 + \left(1 + \frac{\gamma}{2}\right) PK}{1 + \left(\frac{\gamma}{\sum 2}\right) PK} \tag{2.62}$$

Here, K is the initial bulk modulus and $\sum$ is termed the solidity, which is the ratio of the porous density to the initial solid density, $\sum = \frac{\rho_{00}}{\rho_0}$.

Figure 2.10 shows the predicted porous Hugoniot for various initial densities of iron using the Simons-Legner model compared to some experimental results. The Simons-Legner model works moderately well down to porosities of ∼50%. However, the model still assumes no crush strength. In addition, at lower densities, the model suggests an increase in specific volume with increasing pressure, like the Mie-Grüneisen EOS method.

The approach of Simons and Legner [52] was later improved upon by Petrie and Page [58] to remove these problems. Petrie and Page built on the assumption that

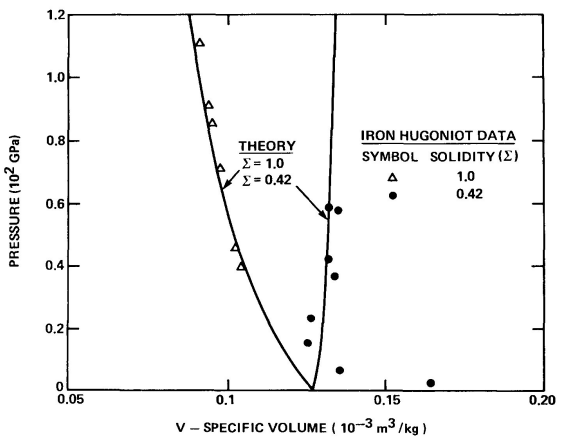

Figure 2.10: Comparison of experimental data to the predicted EOS of porous iron at various initial densities using the Simons-Legner EOS [52].

at low pressures athermal effects would dominate, enabling quasi-static compression data to accurately describe the crush-up behavior of the powder. They utilized the Kawakita equation [59] to describe the material crush-up.

$$\frac{\rho}{\rho_{00}} = \frac{1 + bP_C}{1 + \hat{a}bP_C} \tag{2.63}$$

Here, b refers to the powder stiffness. In the original Kawakita equation [59], a refers to the ratio of the initial powder density to the initial solid material density, $\frac{\rho_{00}}{\rho_{S_0}}$. Petrie and Page [58] modified the parameter in their analysis defining $\hat{a}$ as the ratio between the initial solid material density and the current density, $\hat{\alpha} = \frac{\rho_{S_0}}{\rho}$. With this density ratio, the athermal energy and pressure are defined as the following.

$$E_C = \frac{(\rho_S - \rho_{S_0})^2 K}{2\rho_{S_0}\rho_S^2} \tag{2.64}$$

$$P_C = \frac{1}{\hat{\alpha}} \frac{K(\rho_S - \rho_{S_0})}{\rho_S} \tag{2.65}$$

Equations 2.64 and 2.65 can then be used in Equation 2.59 to develop the porous Hugoniot.

Figure 2.11 shows a comparison of the Petrie-Page and Simons-Legner EOS models for predicting experimental data for porous Cu [58]. The Petrie-Page model is seen

to more closely approximate the crush-up of the material and always define a smaller specific volume with increasing pressures. In this regard, the Petrie-Page model corrects for many of the problems associated with other isochoric approximations.

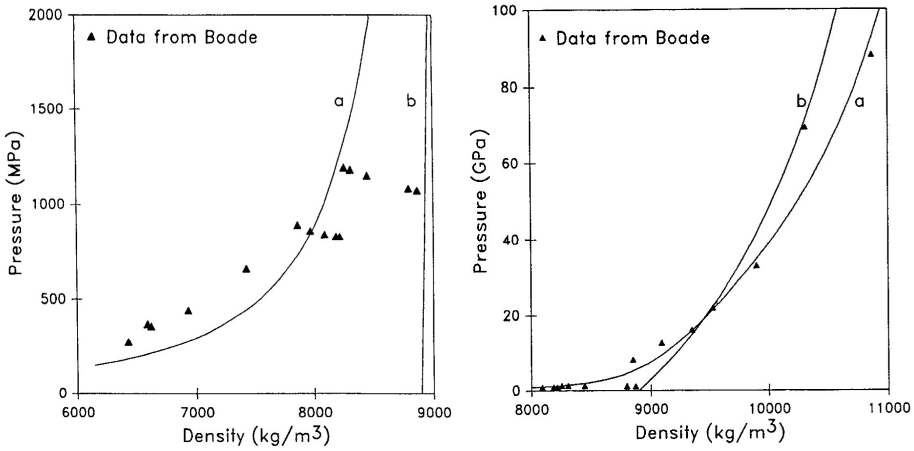

(a) Low Pressure (b) High Pressure

Figure 2.11: Comparison of the Petrie-Page and Simons-Legner EOS models to experimental data on Cu at low pressure (a) and high pressure (b) [58]. The curve marked a corresponds to the Petrie-Page EOS, while the curve marked b corresponds to the Simons-Legner EOS. The Petrie-Page EOS is seen to more accurately represent the porous Cu data.

While these models tend to accurately predict the EOS of distended materials with moderate porosities, the isochoric method has many down sides. As stated previously, many isochoric methods predict increases in volume with increases in pressure at large porosities. They also require the application of two equations to completely describe the porous material behavior. Another significant complication with isochoric methods are their sensitive to uncertainties in γ [60]. This is best visualized in P-E space, as shown in Figure 2.12a. Due to the shallow slope of the porous Hugoniot, slight deviations in γ can lead to large differences when extrapolating from the solid Hugoniot. This is complicated at higher porosities, where the slope of the porous Hugoniot is shallower. However, these complications can be circumvented with an isobaric path.

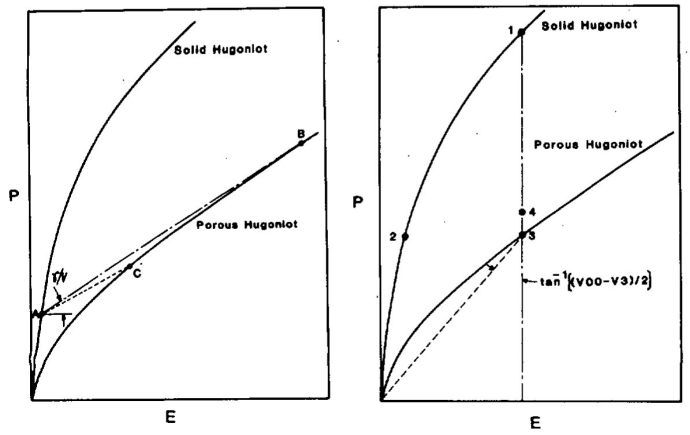

Figure 2.12: The solid and porous Hugoniots in P-E space showing the extrapolation path of the Mie-Grüneisen EOS and the large error resulting from small deviations in γ (states B and C). Using equations 2.66 and the states of equivalent energy (states 1 and 3) and pressure (states 2 and 3) (b), the extrapolated point on the porous Hugoniot is defined by the angle $tan^{-1}[0.5(V_{00} - V_3)]$ from the specified energy line. This method ensures that small deviations in the extrapolated state result in small errors in pressure (states 3 and 4) [60].

Isobaric Methods Oh and Persson used an isobaric approach to develop a single equation to describe the entire porous Hugoniot [60]. Assuming a linear relationship between U_S and U_P, they proposed that the partial derivative of energy with respect to volume along the porous Hugoniot was equal and opposite to the same derivative along the solid Hugoniot.

$$\left(\frac{\partial E_{PH}}{\partial V}\right) \sim -\left(\frac{\partial E_{SH}}{\partial V}\right) \tag{2.66}$$

This provided a simple correlation between the porous and solid Hugoniots through points of identical energy and pressure, which are seen in Figure 2.12b.

$$E_1 = E_3 \tag{2.67}$$

$$P_2 = P_3 \tag{2.68}$$

Using Equation 2.66, the following approximation can be reached [60].

$$V_3 - V_2 \sim V_2 - V_1 \tag{2.69}$$

Geometry can then be used to determine the point on the porous Hugoniot as the following angle in P-E space [60], which is shown in Figure 2.12b.

$$tan^{-1}\left(\frac{E_3}{P_3}\right) = tan^{-1}\left(\frac{0.5P_3(V_{00}-V_3)}{P_3}\right) = tan^{-1}[0.5(V_{00}-V_3)] \tag{2.70}$$

This equations ensures that small deviation in material properties do not cause the large deviations in the extrapolated Hugoniot pressure seen in Figure 2.12a.

The pressures and energies at these states can then be found using the Rankine-Hugoniot equations.

$$P_1 = \frac{C_0^2(V_0-V_1)}{[V_0-S_1(V_0-V_1)]^2} \tag{2.71}$$

$$P_2 = \frac{C_0^2(V_0-V_2)}{[V_0-S_1(V_0-V_2)]^2} \tag{2.72}$$

$$E_1 = \frac{1}{2}P_1(V_0-V_1) \tag{2.73}$$

$$E_2 = \frac{1}{2}P_2(V_0-V_2) \tag{2.74}$$

$$E_3 = \frac{1}{2}P_3(V_{00}-V_3) \tag{2.75}$$

These equations along with Equations 2.67-2.69, represent a system of eight equations with nine unknowns. With the material parameters (C_0 and S_1) and initial volumes (V_0 and V_{00}) known, this set of equations can be solved for the thermodynamic relationship of the porous Hugoniot [60]. Figure 2.13a shows a comparison of experimental data and the Oh-Persson EOS for various initial densities of Cu [60]. Even at low initial densities, the Oh-Persson EOS is seen to match the experimental data quite well. Figure 2.13b shows a comparison of the Oh-Persson EOS and the isochoric Mie-Grüneisen EOS method [60] at low initial densities. The Mie-Grüneisen EOS method is seen to poorly predict the behavior of such highly distended materials when compared to the Oh-Persson method.

In addition to the Oh-Persson EOS [60], another isobaric approach for generating a porous Hugoniot was developed by Wu and Jing [53]. The Wu-Jing model follows

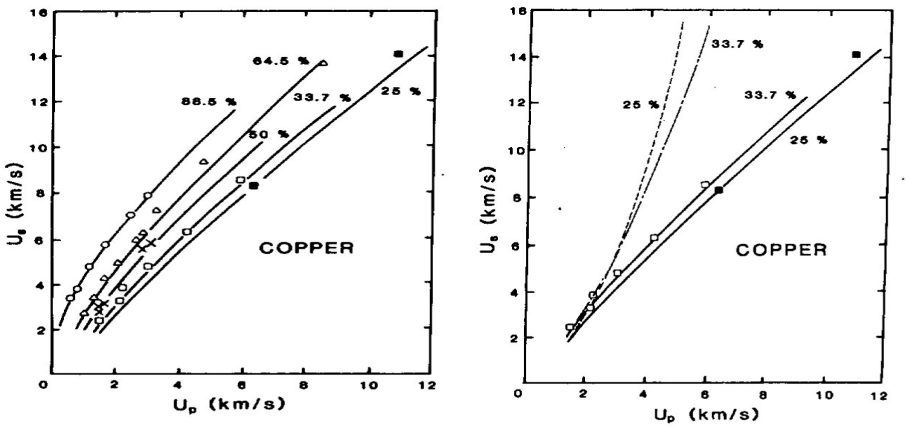

(a) (b)

Figure 2.13: Predicted Hugoniots for various initial densities of Cu powder using the Oh-Persson EOS (solid lines), along with a comparison to the Mie-Grüneisen EOS method (dashed lines) [60].

very closely to that of the Mie-Grüneisen EOS in form, but compares specific volume to specific enthalpy.

$$V - V_C = \frac{R}{P}(H - H_C) \tag{2.76}$$

Here, the subscript C refers to states on the cold-compression curve and R is the Wu-Jing parameter [53]. The Wu-Jing parameter is analogous to the Grüneisen coefficient and the two are related through the following expression [53]:

$$R = \frac{P\gamma}{K_S} = \frac{P\gamma}{\rho C_b^2} \tag{2.77}$$

were C_b is the bulk sound speed.

The EOS developed by Wu and Jing in Equation 2.76 is universal and can be written for both a solid material and its corresponding porous state [53].

$$V_H - V_C = \frac{R}{P}(H - H_C) \tag{2.78}$$

$$V'_H - V'_C = \frac{R}{P}(H' - H'_C) \tag{2.79}$$

In these equations, the subscript H refers to the Hugoniot, and the prime denotes states for the porous material. An expression for the enthalpy along the Hugoniot

and cold-compression curve for the solid material

$$H_C = PV_C + E_C \tag{2.80}$$

$$H = E_0 + \frac{1}{2}P(V_0 + V_H) \tag{2.81}$$

and the porous material can then be found using the Rankine-Hugoniot equations [53].

$$H'_C = PV'_C + E'_C \tag{2.82}$$

$$H' = E_{00} + \frac{1}{2}P_1(V_{00} + V_1) + \frac{1}{2}P(V_1 + V'_H) \tag{2.83}$$

In the porous specific enthalpy equation, the subscripts 00 and 1 refer to the initial porous and fully compacted states, respectively. Combining Equations 2.78-2.83 and assuming $E_0 = E_{00} = 0$ and $E_C = E'_C$, the porous material EOS can be expressed in terms of the solid material response [53].

$$V'_H = \frac{1 - \left(\frac{R}{2}\right)}{\left[1 - \left(\frac{P_1}{P}\right)\right]} V_H + \frac{\left(\frac{R}{2}\right)}{1 - \left(\frac{R}{2}\right)\left[1 - \left(\frac{P_1}{P}\right)\right]} \left((V_1 - V_0) + \frac{P_1}{P}V_{00} + \frac{1 - R}{\left(\frac{R}{2}\right)}(V'_C - V_C) \right) \tag{2.84}$$

In Equation 2.84, P_1 represents the crush strength of the material, meaning the Wu-Jing model does attempt to incorporate the compaction behavior of the material. While the crush strength of a material is not always known, Wu and Jing assumed that the HEL of the material was an adequate approximation [53]. Wu and Jing used the P-α model, assuming $P_1 \sim P_{crit}$, and estimate the value of P_{crit} with the static compaction model for a ductile, porous material developed by Carroll and Holt [61].

$$P_{crit} = \frac{2}{3} Y ln \frac{\alpha_0}{\alpha_0 - 1} \tag{2.85}$$

Here, Y refers to the material yield strength and $\alpha_0 = \frac{V_{00}}{V_0}$. A comparison of the Wu-Jing model to experimental data for Cu is given in Figure 2.14, and shows the Wu-Jing model accurately represent the entire Hugoniot curve, even crush up, with a single equation.

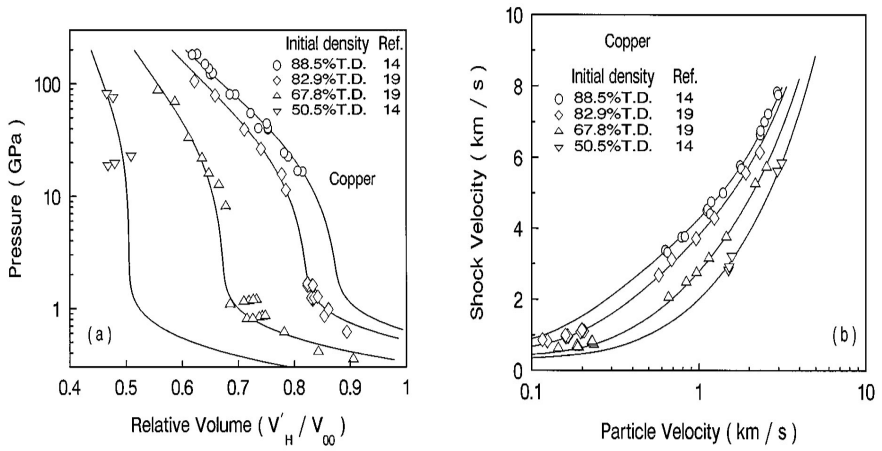

Figure 2.14: Calculated porous Hugoniot for Cu using the Wu-Jing model along with experimental data at various initial densities in P-$\frac{V}{V_0}$ (a) and U_s-U_P (b) space [53].

2.2 Experimental Investigations of the Shock Compression Response of Porous Ni/Al Reactive Mixtures

The dynamic compaction of distended materials has been studied for a variety of applications. Dynamic compaction provides a unique processing method for binding materials with some advantages over more conventional sintering or hot-pressing. During dynamic consolidation, high temperatures are generated exclusively at the material interfaces. This provides adequate mechanical bonding, while leaving the interior of the particles relatively cool and unadulterated [32]. Dynamic compaction has also been used to induce first order transformations in materials. The classic example of this is the formation of diamond during the compaction of porous graphite [62]. Recently, there has been considerable interest in the initiation of chemical reactions in porous reactive powder mixtures through dynamic consolidation. The dynamic consolidation of a powder system is highly complex, due to the differing intrinsic and extrinsic material properties of the constituents and the presence of void space. This creates complex material flows and a discontinuous, dispersed shock front. These complications have made the dynamic response of powder mixtures a rich area of

research. In the following section, a brief review of past shock compression work on porous powders of Ni and Al is presented. For an overview of shock compression of other reactive powders mixtures, the interested reader is directed to the review article by Eakins and Thadhani [63].

2.2.1 Reaction in Porous Ni and Al Powder Compacts

Chemical reactions occurring during the shock consolidation of porous reactive powder mixtures have been observed to progress on two distinct time scales. Thadhani used these characteristic time scales to classify these reaction processes as shock-assisted and shock-induced [64]. Shock-assisted reactions occurs on the time scale of thermal equilibration of the microstructure (10's of μs to 1 ms). In these reactions, the shock compression of the material leads to material mixing, defect generation, and elevated interfacial temperatures, which promotes a solid-state diffusion reaction. Shock-induced reactions occur on the time scale of mechanical equilibration (10's of ns to 1 μs), during the rise of the shock pulse. Unlike the shock-assisted reactions, the ultra-fast shock-induced reactions rely on mechanochemical transport mechanisms, which are not fully understood [64].

To distinguish between these two processes, the time scale of the reaction must be determined. This can only be done with time-resolved diagnostics to identify changes in the high pressure compressibility of the material. While post-shock microstructural analysis can be used to identify if reaction has occurred, it provides no information about the kinetics of the reaction. Microstructural analysis is also complicated by the highly exothermic nature of these reactions. This can melt the product phases, destroying any evidence of the processes leading to reaction initiation. This includes the formation of intermediate or transition states [64]. Even with these limitations, post-mortem microstructural analysis is a useful tool and was used extensively to identify reaction and quantify its extent.

2.2.1.1 Recovery Experiments

The first identification of reaction through the dynamic consolidation of Ni and Al was found by Horie *et al.* [65]. In this work, -325 mesh Al and -200/+325 mesh Ni (30 vol% Al at 60% TMD) was shock compressed with the Sandia recovery fixture [66] shown in Figure 2.15a. In this configuration, a plane wave generator is used to compact the powder inside a Cu capsule [66]. The observed distribution of phase formations, along with the calculated temperature profiles for one of the two experiments, is given in Figure 2.16. The results show the formation of multiple intermetallics of Ni and Al ($AlNi_3$, Al_3Ni_2, Al_3Ni, and AlNi), especially in the regions reaching the highest temperature [65, 67]. Microhardness measurements also found elevated hardnesses in the reaction regions, suggesting the phases rapidly solidified upon release [65]. However, no definitive conclusions could be made about the time scale of the reaction. Horie *et al.* speculated that the consolidation of the powder by the initial shock wave left the material in an activated state, from which solid-state diffusion occurred forming a molten product phase [65]. This enhanced diffusion was aided by the compaction process which causes microfracturing, scuffing, and spallation of the particles. This generated more intimate mixing of the constituents by the shedding of small Ni pieces into an Al melt [67].

Horie *et al.* later extended this work to look at the response of Al particles coated with 80 w% Ni [67]. Microscopy on the compacted composite showed undeformed Al particle cores in a Ni matrix with little evidence of melting. In addition, only minor, localized reactions at the periphery of the capsule, which experience the highest temperatures, were found [67]. These reaction regions, shown in Figure 2.17, exhibited a swirling substructure, believed to be the result of interfacial instability, jetting, or inter-penetration of particles typical of hydrodynamic flows (*i.e.* Kelvin-Helmholtz, Rayleigh-Taylor, Richtmyer-Meshkov instabilities) [67]. The differing reaction response between the mechanically blended Ni/Al and Ni coated powders lies

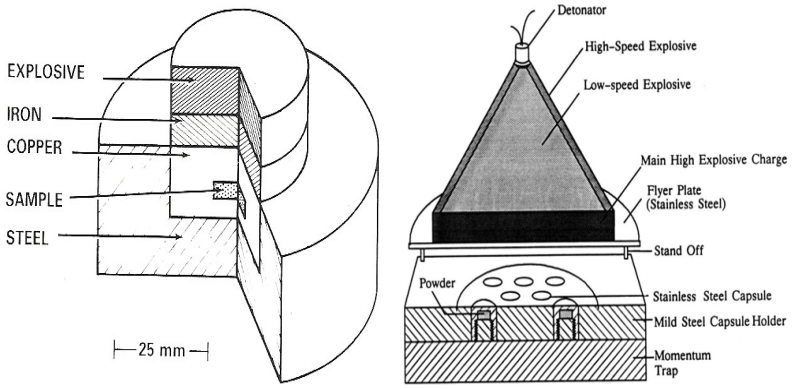

(a) Sandia Recovery Fixture (b) CETR/Sawaoka Fixture

Figure 2.15: Schematic of the Sandia (a) [66] and CETR/ Sawaoka (b) [68] recovery fixtures.

in their compaction characteristics. As voids are collapsed in the mechanically mixed powders, both constituents are present, promoting reaction through the generation of fresh material interfaces between Ni and Al at elevated temperatures. In the Ni coated powders, most interfacial interactions during void collapse involve only Ni. Reaction can only occur through instabilities in the flow that mixes both constituents, such as material jetting or inter-penetration. This leads to significantly lower reaction yields in the Ni coated powders.

The notion of particle "activation" due to shock consolidation through enhanced solid-state diffusion discussed by Horie *et al.* [65] was further characterized by Hammetter *et al.* [69]. Hammetter *et al.* used a differential thermal analyzer (DTA) to investigate changes in the reaction threshold due to shock consolidation for mechanically mixed Ni and Al powders, as well as, Ni coated Al powders. The DTA results showed that the passage of a shock wave could indeed "activate" the powder as hypothesized by Horie *et al.* [65]. This "activation" leads to lower reaction initiation thresholds, as shown in Figure 2.18 [69]. In Figure 2.18, the onset of reaction is seen to occur $\sim 200^0$C lower for the shocked composite (b) than for either the unshocked composite (a) or shocked Ni coated Al particles (c). This lower reaction threshold

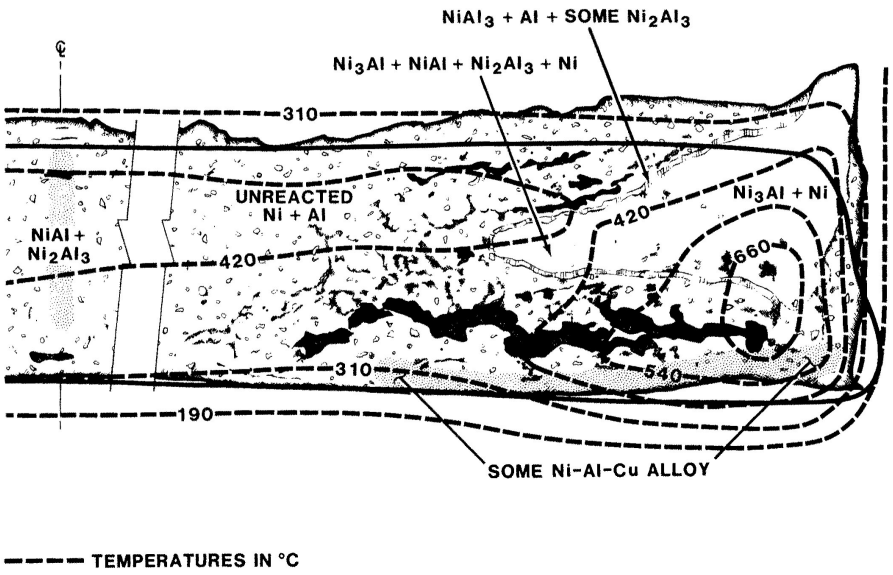

Figure 2.16: Phase formation and calculated temperature profiles for the recovery experiments performed by Horie *et al.* [65].

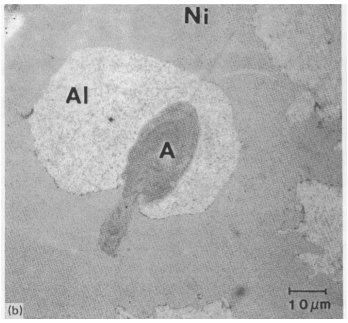

Figure 2.17: Reaction region in the Ni coated Al particles during shock consolidation showing evidence of hydrodynamic flow (A) [67].

was attributed to the elevated levels of material mixing and defect generation caused by the passing shock wave. Additional studies by Hammetter *et al.* found that as the intensity of the compacting shock increases, the observed pre-ignition exotherm also increases [69]. With increasing energy of the shock, material mixing and defect generation also increases, further "activating" the material [69].

Building on the work of Horie *et al.* [65, 67], additional recovery experiments have been performed on the Ni/Al system to investigate the effects of particle size [2, 70], particle shape [2, 9, 70, 71], packing density [2, 71] and stoichiometry [2]. Song and

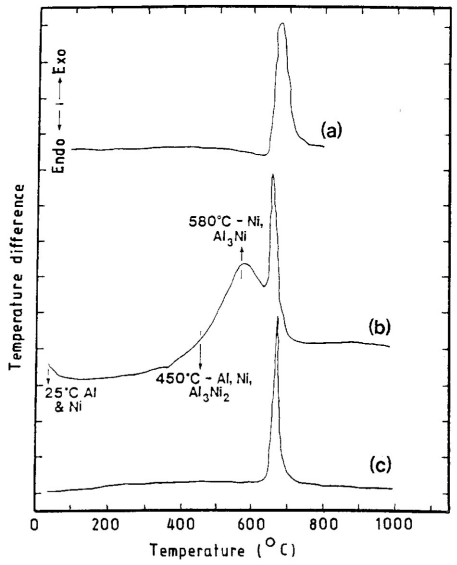

Figure 2.18: DTA traces for the as-mixed (a), shocked Ni-Al composite (b), and shocked Ni coated Al particles (c). The results show a substantial pre-ignition exotherm for the shocked Ni-Al composite (b), but none for the unshocked (a) and shocked Ni coated Al particles (c) [69].

Thadhani [9, 71] investigated the effects of particle morphology and packing density on the reaction response of Ni and Al powders using the CETR/Sawaoka 12-capsule recovery fixture [68], which is shown in Figure 2.15b. Song and Thadhani [9, 71] used -325 mesh powders of spherical Al with either spherical or flake Ni particles mixed to a 3Ni:Al stoichiometry to investigate the effects of powder morphology, packing density, and flier velocity on the reaction response [9, 71]. The results showed that larger impact velocities and decreased packing densities led to an increased rate of reaction in both powder morphologies, due to increased material mixing and energy deposition in the system. Song and Thadhani also found that mixtures with flaky Ni particles exhibited more reaction than corresponding composites with spherical Ni [9, 71]. This increased reaction response was attributed to additional deformation modes and increased mass mixing as the spherical Al particles conformed to the flaky Ni particles [9].

Song and Thadhani also found evidence of a unique reaction path as a result of

shock compression [9]. During thermal ignition, the reaction is diffusion driven and phase formations begin with an Al rich phase and end with the phase closest to the stoichiometry of the mixture (*i.e.* 3Ni+Al $\rightarrow$ Al_3Ni $\rightarrow$ NiAl $\rightarrow$ $AlNi_3$) [9]. During shock consolidation, the reaction initiated with a Ni rich phase and proceeds to a Ni rich AlNi phase, despite the overall stoichiometry corresponding to $AlNi_3$ (*i.e.* 3Ni+Al $\rightarrow$ $AlNi_3$ $\rightarrow$ NiAl+Al_3Ni_2 $\rightarrow$ AlNi) [9]. Since AlNi has the largest heat of reaction of the Ni/Al intermetallics, Song and Thadhani concluded that the thermodynamic properties of the product phase govern the reaction response in the shock consolidated case and not the individual diffusivities of the constituents [9, 71]. This suggests, at higher shock energies, the formation of compounds with larger heats of reaction are favored.

Later, Dunbar *et al.* extended these recovery experiments to investigate the effects of particle size and mixture stoichiometry on the reaction response [2]. Three different powder morphologies were investigated: *fine* powders of spherical Ni (3-7 μm) and Al (10-20 μm), *coarse* powders of spherical Ni (45-70 μm) and Al (45-150 μm), and *flaky* powders of flake Ni (-325 mesh) and spherical Al (10-20 μm) [2]. Each morphology was mixed to three different stoichiometries: 3Ni:Al, Ni:Al, and Ni:3Al [2]. The powders were then packed to $\sim$ 65% TMD in a Sandia recovery fixture and compacted.

Figure 2.19 shows the compacted microstructures of the *coarse* (a), *fine* (b), and *flaky* (c) system along with a micrograph of a typical fully reacted zone (d). The fully reacted zone is seen to have many pores, possibly the result of shrinkage from the melt or even gas emission [2]. The *flaky* mixture exhibits more pronounced deformation of the constituents due to the morphology of the Ni particles. With a flake geometry, both constituents can laterally deform simultaneously, leading to more thorough mixing. These findings support the conclusions drawn by Song and Thadhani [9, 71] and explain the increased reaction response seen in the *flaky* mixture for all stoichiometries [2]. In the *fine* and *coarse* mixtures, the Ni is seen to retain

its shape, acting as an anvil as the aluminum deforms around it [2]. In spherical mixtures, the reaction response was seen to depend on the Ni concentration and particle size. The *fine* mixture showed some reaction in all three stoichiometries, with the most in the 3Ni:Al mixture. In contrast, the *coarse* mixtures only reacted for the 3Ni:Al system. These observations highlight the importance of surface area per unit volume and material mixing on reaction initiation. With increasing particle size, the surface area for reaction decreases, lowering the likelihood of reaction. Additionally, as the concentration of Ni increases, more flow is observed in the Al, since there are more Ni particles to act as anvils. This produces more intimate mixing between the constituents and increases the reaction yield.

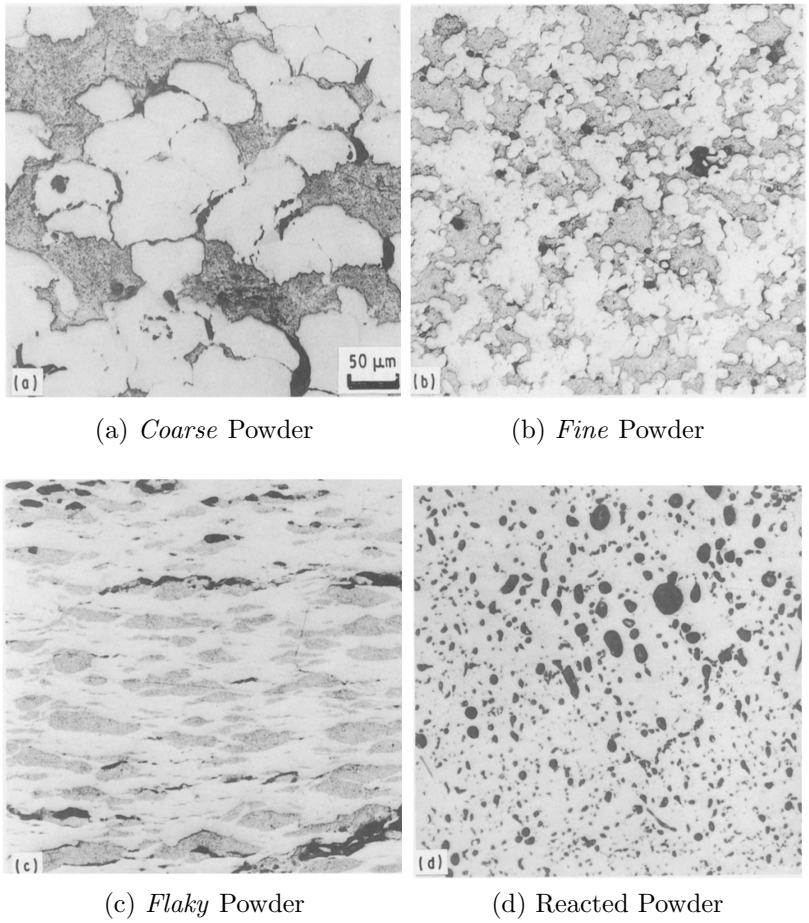

(a) *Coarse* Powder (b) *Fine* Powder

(c) *Flaky* Powder (d) Reacted Powder

Figure 2.19: Optical micrographs of the compacted regions of the *coarse* (a), *fine* (b), and *flaky* (c) mixtures along with a fully reacted region (d) [2].

Dunbar *et al.* [2] used the unreacted regions from these compacts to quantify the effect of morphology and stoichiometry on the pre-ignition behavior of each system using DTA analysis, similar to the work done by Hammetter *et al.* [2]. The results of the DTA scan for each powder mixtures for the 3Ni:Al stoichiometry are shown in Figure 2.20, since it was the only stoichiometry to exhibit any notable pre-ignition behavior [2]. The DTA traces in Figure 2.20 show that the pre-ignition exotherm is tied to the degree of mixing in the composite.

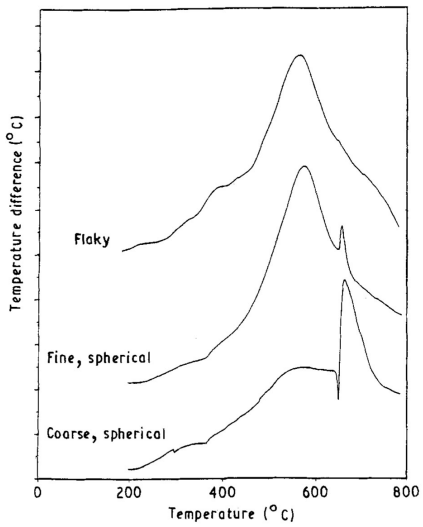

Figure 2.20: DTA traces for the *flaky*, *fine*, and *coarse*, mixtures for the 3Ni:Al stoichiometry. The results show that all mixtures exhibit a pre-ignition exotherm, with the *flaky* mixture having the largest [2].

2.2.1.2 Time-Resolved Experiments

In the previously mentioned studies, the location of reaction in areas experiencing the highest temperatures suggests a diffusion-enhanced mechanisms characteristic of a shock-assisted reaction. In order to identify a shock-induced reaction, time-resolved diagnostics must be used. Unfortunately, the detection of a shock-induced reaction is often difficult due to the relatively small changes in bulk material properties generated. It has been suggested that the best method to identify these reactions is through the rapid temperature increases that accompanies many of these reactions

[64]. However, temperature measurements with radiation pyrometry are difficult. As a result, other experimental methods have been developed to infer reaction.

Bennett *et al.* [72] utilized a manganin gauges to obtain a time resolved stress response for a Ni/Al powder to identify reaction. They performed recovery experiments on 20 μm Al and 3-7 μm Ni powders compacted to 55% TMD on a gas gun. The manganin gauge was positioned on the back side of the powder compact to record the propagated stress profile. The experiment was designed such that the powder would be activated by the initial propagating shock wave. This shock wave then reflected off the stainless steel container reacting the powder [72]. Their experiments found that reaction could be observed in this configuration through the detection of an "excess pressure" in the bulk response ($\sim$ 5 GPa), as seen in Figure 2.21. This response was attributed to a thermal pressure resulting from the heat released and corresponding volume expansion during the ultra-fast reaction.

Yang *et al.* later extended this work to investigate the mechanism behind these reactions. They performed similar experiments to identify if there was a threshold energy, as proposed by Krueger and Vreeland [73], for reaction initiation [74]. By adding an Al layer behind the powder, the reflected shock structure was changed from one step to two. This changed the structure of the wave, but not the overall energy. Yang *et al.* found no "excess pressure" with the two step wave, as seen in Figure 2.21. These findings showed that an energy threshold for reaction was inadequate and that a mechanochemical description was more appropriate [74].

Graham *et al.* were also able to infer reaction in Ni/Al and Ti/Si powders by noting a volume expansion at constant pressure of the material relative to the fully dense state, which they termed the "ballotechnic model"[75]. While these reactions often proceed from low to high densities, or to lower volume states, the heat release from the reaction process can cause a net increase in volume [13], allowing for identification of reaction. In this model, the expansion in volume at constant pressure, as seen in

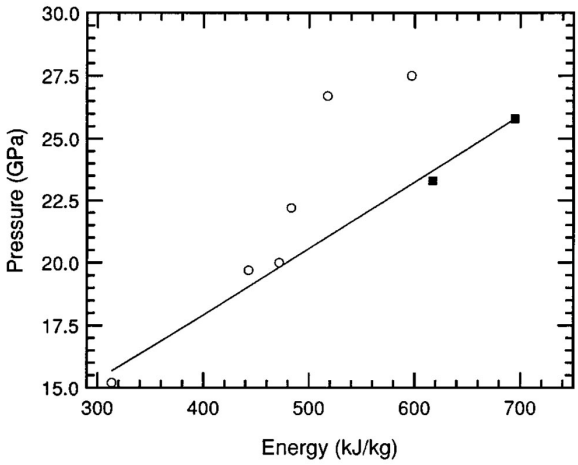

Figure 2.21: The P-E relations for various impact velocities on Ni/Al powders represented by the open circles. The circles are seen to lie above the inert material response (solid line) signifying an over pressure resulting from an exothermic reaction. The solid rectangles show no signs of reaction and indicate experiments in which the wave structure was changed from one step to two. This result suggests that the reaction is a mechanochemical process [74].

Figure 2.22a, can be described using the heat of reaction [75].

$$\Delta V = (V_{00} - V) + \frac{\beta Q}{C_p} \tag{2.86}$$

Here, V_{00} is the specific volume of the unshocked powder, β is the coefficient of thermal expansion, and Q is the heat of reaction. The ballotechnic model can also be viewed in U_S-U_P space, as shown in Figure 2.22b. Under this model, an increase in volume at constant pressure results in an increase in the slope of the Rayleigh line, raising the shock speed over the inert response. Bennett and Horie [76] later built upon the ballotechnic model to develop equations for the determination of the Hugoniot of a reacted powder system using both constant volume and constant pressure adjustments.

Eakins and Thadhani [27, 1] used time-resolved diagnostics to investigate reaction formation during parallel plate impact experiments on various Ni/Al powder compacts based on the concepts of the ballotechnic model. While they found no signs of reaction in micron or nano-sized spherical powder composites, reaction was observed in 45%

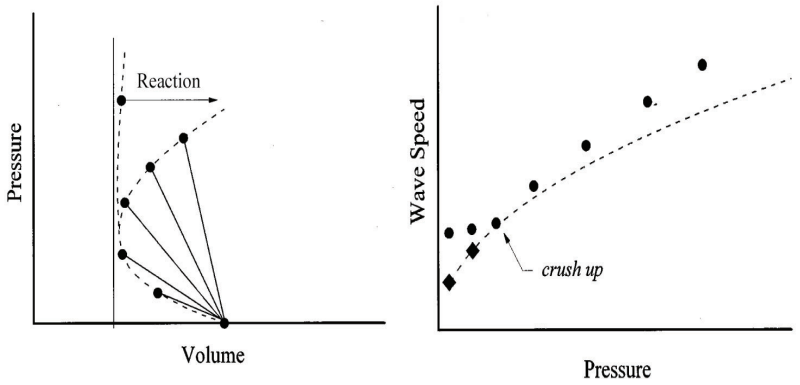

(a) P-V Curve (b) U_S-P Curve

Figure 2.22: The ballotechnic model suggests an increase in volume (a) and wave speed (b) at a fixed pressure due to an exothermic reaction [14].

TMD, -325 mesh flake Ni and spherical Al compacts [1]. This reaction was identified through an increase in the resulting shock speed, consistent with the ballotechnic model, as shown in Figure 2.23. Using two-dimensional simulations, Eakins and Thadhani [11] were able to attribute this elevated reaction response to the increased lateral deformation of the Al, similar to that found by Dunbar *et al.* [2] and shown in Figure 2.19c.

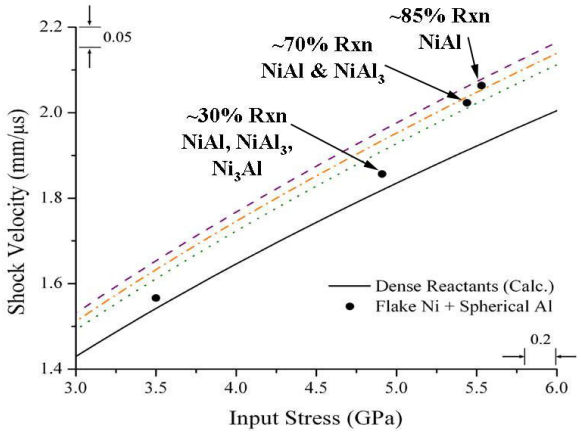

Figure 2.23: U_S-P curve for 45% TMD flake Ni and spherical Al mixtures up to 6 GPa showing the degree of reaction and possible product phases [1].

For the experiments showing signs of reaction, Figure 2.23 also provides estimates of the degree and possible products of the reaction. Eakins and Thadhani obtained

these estimates through volume averaging the material shock speeds for the three proposed product phases: AlNi, Al_3Ni, and $AlNi_3$ [1].

$$X^{rxn} = \frac{U_S^{rxn} U_S^0}{U_S^{obs}(U_S^0 - U_S^{rxn})} - \frac{U_S^{rxn}}{(U_S^0 - U_S^{rxn})} \tag{2.87}$$

In the above, X^{rxn} is the degree of reaction, U_S^0 is the inert mixture shock velocity, and U_S^{obs} is the experimentally measured shock velocity. The shock velocity of the reaction products, U_S^{rxn} can then be determined from the volume fractions and shock velocities of the three assumed reaction products, designated β, δ, and γ [1].

$$U_S^{rxn} = \frac{U_S^\beta U_S^\delta U_S^\gamma}{X^\beta U_S^\delta U_S^\gamma + X^\delta U_S^\beta U_S^\gamma + X^\gamma U_S^\delta U_S^\beta} \tag{2.88}$$

With these equation, Eakins and Thadhani were able to construct a reaction product composition diagram for each experiment exhibiting an increased shock velocity, as shown in Figure 2.24 [1].

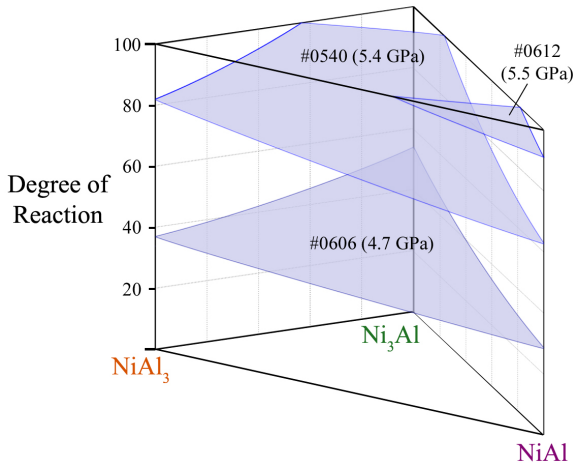

Figure 2.24: Composition diagram showing the possible combinations of reaction products for each experiment in Figure 2.23 with an elevated U_S [1].

2.2.1.3 Proposed Reaction Mechanisms in Porous Systems

While a deviation from the Hugoniot curve suggests that shock-induced reaction has likely occurred, it still does not provide any insight into the specific mechanisms of the reaction. Models based on the melting of either or both constituents seem logical

and have been proposed in the past [17]. However, Vandersall and Thadhani have shown experimentally that melting inhibits shock-induced reaction initiation, leading to restricted intermixing between constituents [3]. In addition, the work done by Yang *et al.* [74] has shown that the reaction process is most likely mechanochemical. As a result, a number of mechanochemical reaction mechanisms have been proposed.

One of the first mechanochemical models proposed was the Roller model developed by Dremin and Bruesov [77]. A schematic of the model is given in Figure 2.25a. In this model, the relative motion of the interface between two constituents results in the nucleation of the product phase in a continuously-layering, or snowball-like, fashion. Dremin and Bruesov estimated the size of the nucleated product phase to be $\sim 3\mu m$ [77]. For this mechanism to work, significant interparticle shear must be present and lead to reaction initiation. Intense shear is expected during the consolidation of voids and has been shown computationally [78] and experimentally [15, 17, 79] to initiate reaction.

Another shock-induced reaction model was proposed by Batsanov *et al.* [12, 13]. In this model, the increased material mixing during shock consolidation was attributed to the varying material velocities in each constituent. A schematic of this process is shown in Figure 2.25b. If the disparity in material velocities is large enough, inter-penetration of one material into another occurs, leading to ultra-fast material mixing [12]. This inter-penetration is aided by scuffing, fragmentation, and spallation during the compaction process which generates small particles. These particles can be as small as 10 nm and obtain fresh surfaces at elevated temperatures during inter-penetration, promoting reaction [13]. The intermixing continues until a characteristic time, $\tau = \frac{2\bar{d}}{\Delta U}$, is reached, where $\bar{d}$ is the average particle diameter and ΔU is the disparity between material velocities [13]. Batsanov *et al.* calculated that, if the reaction occurs only at material surfaces and the particles are $\sim$ 10 nm, reaction yields around 20% can be obtained.

While the previous models try to physically explain the reaction process, Graham [80] developed a simple conceptual description of the reaction process termed the CONMAH (**CON**figuration change, **M**ixing, shock **A**ctivation, and **H**eating) model. The model, shown schematically in Figure 2.25c, is based on the idea that shock-induced reactions are driven by deformation caused by the heterogeneities of the mixture (*e.g.* intrinsic material properties, voids, and particle shape). The compaction process then rearranges and deforms the particles during mixing. This mixing cleanses material boundaries and generates defects (*e.g.* dislocations, vacancies, stacking faults, grain boundaries, cracks), that activate the composite through enhanced mobility. While the CONMAH model does not explain the reaction process it does qualitatively describes the importance of starting mixtures properties on the reaction response.

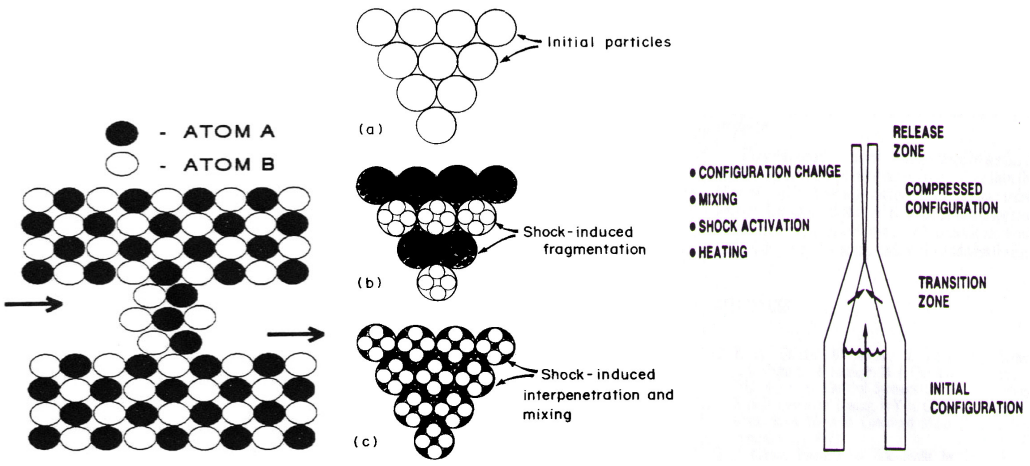

(a) Roller (b) Batsanov Model (c) CONMAH

Figure 2.25: Illustrations of the various mechanochemical reaction models proposed. Dremin and Breusov's Roller model (a) [27] shows the nucleation of a small product phase as a result of interfacial shear. Batsanov's model (b) [13] relies on the disparity in material velocities to generate mixing and reaction. Graham's CONMAH model (c) [27] qualitatively describes the reaction through various mixing mechanisms in the transition zone.

In all of these models, both the intrinsic and extrinsic properties of the starting mixture influence the degree of reaction. To provide a more visual representation

of how material properties effect the reaction response, Eakins developed a material properties map, shown in Figure 2.26 [27]. The map plots the difference in yield strength along the abscissa and the difference in impedance along the ordinate. In addition, the size of each datum point corresponds to the largest intermetallic heat of formation for the system. The map allows for easy comparisons of various intrinsic property differences for each mixture that have been suggested to influence the reaction response. Using past research, Eakins was able to define an inhibited zone in which the material properties were too different to enable adequate mixing to promote reaction at modest pressures [27]. Based on the map shown in Figure 2.26, the Ni and Al system may not react at modest pressure, due to the large discrepancies in intrinsic properties. However, it has been shown by numerous authors that the reactivity of the Ni and Al system can be increased by changing the shape of the Ni particles to a flake geometry [27, 2, 9, 70, 71]. Such changes in the extrinsic properties of the mixture can enable more mixing modes and promote reaction. Using this result, Eakins defined a termed called the "eccentricity", Δe, to encapsulate the extrinsic properties of the mixture [27]. Eakins concluded that by changing the extrinsic properties of the mixture the boundaries of this inhibited zone could be moved, as seen in Figure 2.26, to represent the occurrence of reaction at lower thresholds [27].

2.3 Computational Investigations of the Shock Compression of Reactive Mixtures

Computer simulations at the meso-scale, or particle level, have been employed to investigate a variety of material responses. For example, Lee *et al.* [81] used finite element simulations to study the stresses around pores in a high-pressure, die-cast AM50 magnesium alloy. In a similar fashion, meso-scale simulations can be used to understand the response of materials under high strain rate loading. There have been numerous studies focusing on the dynamic response of materials at the meso-scale. These efforts have helped in understanding and visualizing wave interactions and

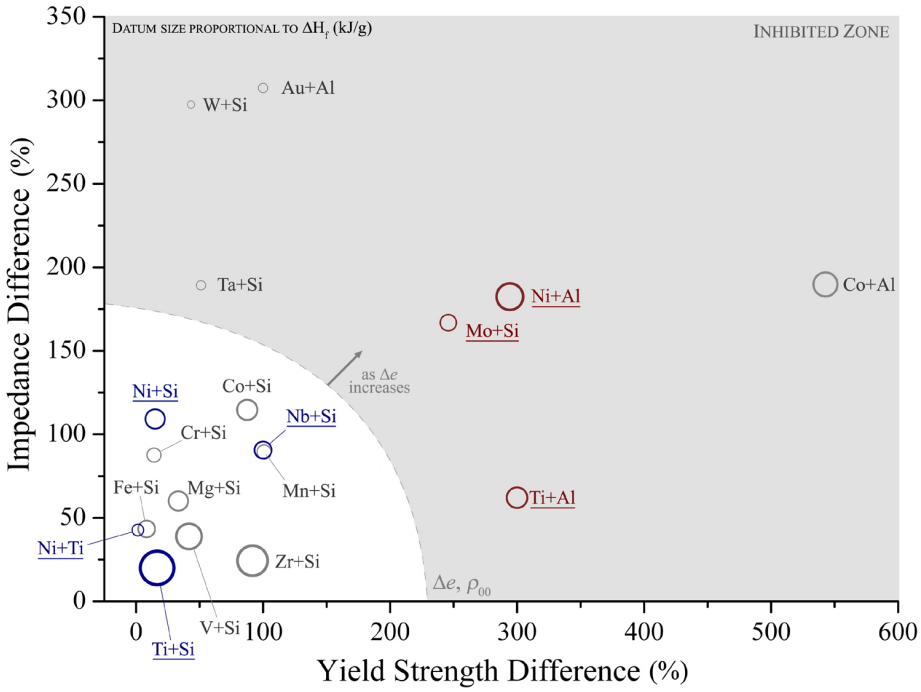

Figure 2.26: Intrinsic property map for various binary reactive systems [27]. The datum size corresponds to the largest intermetallic heat of formation of each system. Reactions tend to occur more easily in systems with similar properties. However, variations in the extrinsic properties of the mixture, quantified by Δe, can lower reaction initiation thresholds and move the inhibited zone boundary.

material deformation in complex systems, such as porous powder compacts. This section focuses on some relevant computational studies on the shock compression of powder systems. However, it does not provide any background on the underlying numerics inherent in these methods. For a more in-depth review of numerical methods in hydrocodes, the reader is referred to Benson [82] or Zukas [83].

Williamson is generally credited with the first numerical particle level shock compression simulation [84]. He simulated the compaction of spherical 304 stainless steel particles and showed that interparticle contacts and void collapse play an important role in local heating of nascent particle surfaces [84]. While insightful, the small computational domain in Williamson's work limited the amount of information that could be obtained from the system. Simulations on larger collections of particles were later performed by Benson on various morphologies of idealized Cu particles [85, 86] in the

two dimensional, multi-material, reaction capable, Eulerian Hydrocode RAVEN [87].

Benson generated two unique microstructures of spherical and rectangular particles through the "pseudo-gravity" method, which arbitrarily drops particles into the model space [85, 86]. Each microstructure was then simulated at a variety of impact velocities. The results for the spherical particles are presented in Figure 2.27 [85]. The simulations performed by Benson [85] showed that particle morphology has a drastic effect on the material deformation resulting from void collapse. In particular, Benson was able to show that flow modes, such as vortexing and jetting, increased with particle velocity. While this behavior is highly dependent on the constitutive relations used, the simulations still provide valuable insight into the particle level phenomena during shock compaction that can not be observed experimentally.

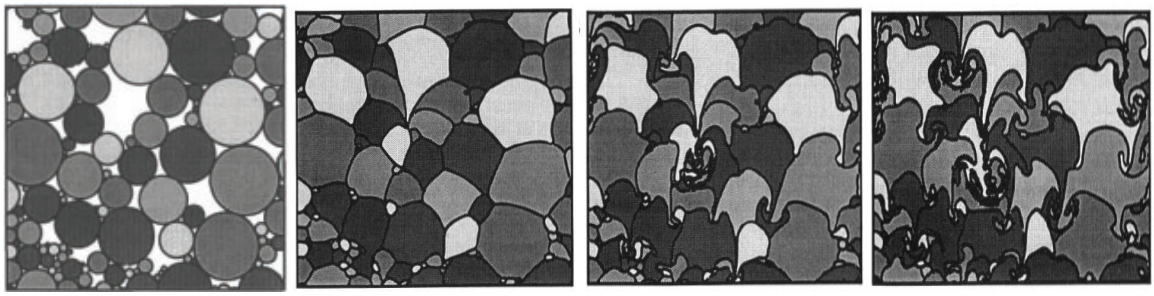

(a) Initial (b) 0.25 km/s (c) 1.00 km/s (d) 2.00 km/s

Figure 2.27: Simulated impact on copper particles (a) at 0.25 km/s (b), 1.00 km/s (c), and 2.00 km/s (d) by Benson [85]. The results show that greater impact velocities lead to greater particle mixing and stronger flow phenomena, such as jetting and vortexing.

Austin *et al.* [7] also used RAVEN to investigate the shock compression response of a composite of Al+Fe_2O_3 in 20 wt% epoxy at different impact velocities. The initial and compacted microstructures at an impact velocity of 1 km/s are shown in Figure 2.28. In addition to visualizing the particle level deformation, Austin *et al.* [7] were able to predict the bulk material response as well as various particle level phenomena, such as melt fractions. The simulated bulk response was found to provide

good agreement with experimental measurements, highlighting the ability of meso-scale simulations to accurately describe the shock compression of highly heterogeneous systems. This makes simulations an ideal tool for performing parametric studies to understand the influence of the microstructure on the mechanical and reaction response in composite systems.

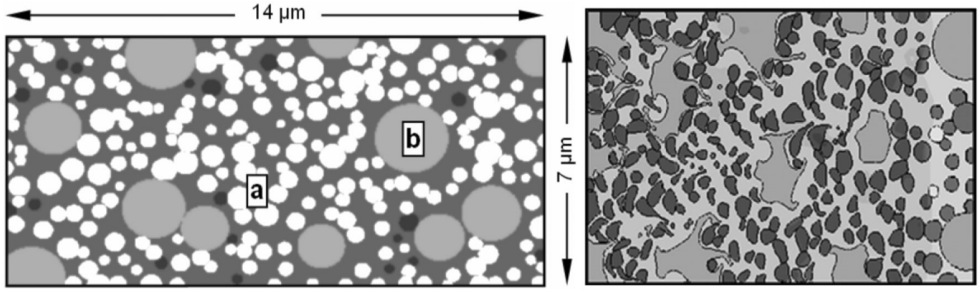

(a) Initial (b) Compacted

Figure 2.28: Initial (a) and compacted (b) microstructures of a composite of Al+Fe_2O_3 in 20 wt % epoxy impacted at 1 km/s. The white particles, labeled a, are the Fe_2O_3. The light grey particles, labeled b, are Al, and the dark grey particles are void space. The impacted microstructure shows extensive deformation of both the Al and Fe_2O_3 particles and the complete elimination of the void space in the shocked region [7].

The simulations performed by Benson [85, 86] and Austin [7] were on idealized microstructures. In powder compacts, the particles are often highly heterogeneous, and these irregularities in shape can greatly affect the particle level and bulk material response. In order to understand the effects of these irregularities, Eakins and Thadhani [10, 11] incorporated real, heterogeneous, two-dimensional microstructures into CTH, a multi-material, finite volume, Eulerian Hydrocode developed by Sandia National Laboratories [88]. These simulations utilized two different Ni and Al powder morphologies: spherical Al and Ni and spherical Al with flake Ni. Their simulated results correlated well with experimental data and provided valuable insight into the particle level phenomena driving the differing responses. These particle level simulations were able to identify and characterize numerous material mixing modes, such as vortexing, focused flow, and flattening [10, 11]. Examples of each mixing mode are

shown in Figure 2.29.

Eakins and Thadhani also identified a fourth mixing mode, termed particulation, which is the generation and dispersion of small Ni fragments into the Al matrix, as seen in Figure 2.29a. This mixing method was hypothesized by Batsanov [12, 13] (presented in Section 2.2.1.3) and is most likely present experimentally. However, in the simulations done by Eakins and Thadhani, no failure models were employed. As a result, the particulation in these simulations is solely a numeric artifact from advection, and may not be an accurate description of the fragmentation process.

Eakins and Thadhani were able to relate these deformation modes to the varying degrees of reaction seen in each mixture [10, 11]. In particular, they saw that the flattening, characteristic of only the flake morphology of Ni, induced more lateral flow of both constituents. This caused increased mixing, which was attributed to the increased reaction response seen experimentally in the flake Ni mixture [1]. In contrast, the Ni particles in the spherical powders acted as anvils, focusing the deformation in only the aluminum and limiting mixing and reaction. The computational results are in agreement of the past observations by Dunbar *et al.* and Song and Thadhani [9, 71] and highlight how coupling experiments and simulations can provide a deeper understanding of such highly heterogeneous systems.

The two dimensional approximation used in the above studies is not always appropriate and can lead to discrepancies between the simulated and experimental response. In two dimensions, the particles are essentially infinite rods of material and this approximation can lead to unrealistic material responses, such as higher deformation rates. This has lead to efforts to simulate a 3D microstructure. Baer [89] conducted three dimensional microstructural simulations on a network of idealized HMX (octahydro-1,3,5,7-tetranitro-1,3,5,7-tetraocine) crystals in CTH [88]. The simulations were designed to understand the various particle level interactions that

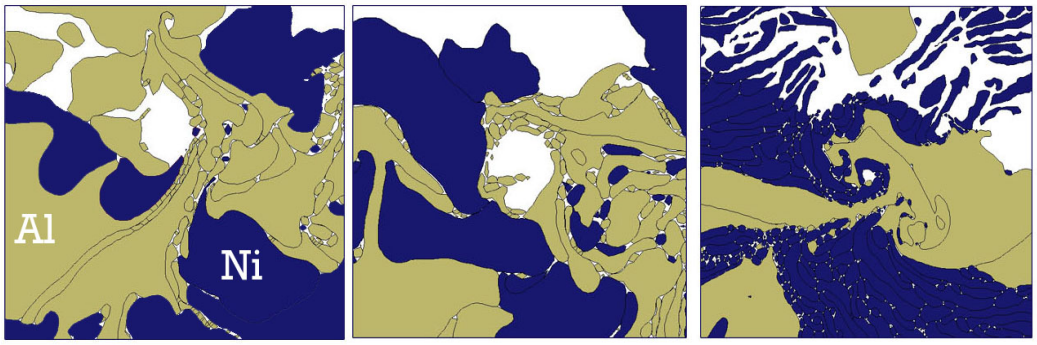

(a) Focused Flow (b) Vortex Formation (c) Flattening

Figure 2.29: Images showing the mixing mechanisms present in various particle compacts of Ni and Al. The spherical compacts are seen to undergo focused flow (a) and vortex formation (b). The flake Ni and spherical Al powders are seen to undergo flattening (c), which increases the lateral deformation of both phases. This increases mixing between constituents and was attributed to the increased reaction response of the flake Ni mixture [11].

could explain the differing sensitivities between HMX networks. The simulation results captured the localized particle interactions that lead to the creation of areas of elevated temperature and pressure, called "hot-spots", for reaction initiation, as seen in Figure 2.30. The formation of these "hot-spots" was seen to be heavily influenced by the crystal structure of the composite [89], showing how simulations can provide a deeper understanding of experimentally obtained data.

With the exception of the simulations by Baer [89], none of these computations attempted to model the reaction response directly. The modeling of a reaction response is a difficult problem in an Eulerian description, due to the complexities of resolving material interfaces in mixed cells. However, there have been a number of attempts to model the reaction response of reactive and energetic materials. Baer and Nunziato [90] developed a model based on the continuum theory of mixtures to describe the reaction response of a bed of granular explosives that has proven to be quite accurate. Do and Benson [91] implemented a model into RAVEN to simulate the shock-induced reaction response of the Nb+2Si system. The model was built on an Arrhenius reaction rate with the simple form of A+B $\rightarrow$ C. Using this approach,

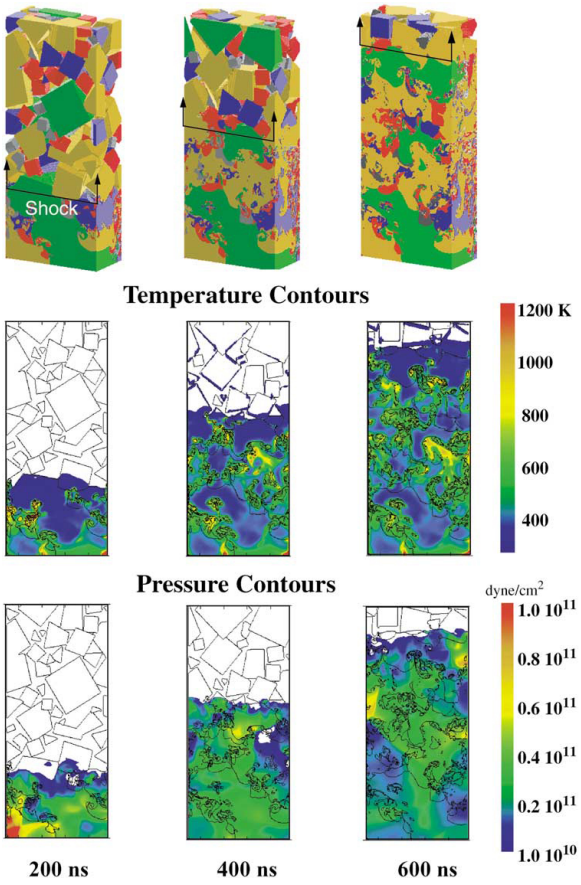

Figure 2.30: Simulated results obtained by Baer on HMX crystals impacted at 1000 m/s. Temperature and pressure profiles show the areas of elevated pressure and temperature, or "hot-spots", responsible for reaction initiation in the material [89].

Do and Benson were able to simulate the reaction response of 60% TMD compact of Nb+2Si at an impact velocity of 1 km/s, as shown in Figure 2.31.

A homogeneous reaction model, like the one used by Do and Benson [91], must have a specified transport model. Without a transport mechanism, reaction is limited to mixed cells containing both A and B. After that cell reacts, it creates a barrier separating both phases and inhibiting further reaction. The transport model simulates the migration of each phase through the reaction products in order to continue the reaction. For simplicity, Do and Benson assumed an infinite transport rate, meaning the materials diffuse at the rate necessary to continue the reaction [91]. This assumption is not accurate and leads to the model over-predicting the extent of reaction.

In contrast to the models of Do and Benson [91], experimental observations have shown that reaction often initiates heterogeneously at "hot-spots" created through particle interactions and void collapse. To accurately capture this phenomenon, there have been attempts to develop heterogeneous reaction models. Reding and Hanagud [92] developed a heterogeneous granular level reaction (GLR) model to interface with RAVEN. More recently, attempts have been made to develop a stochastic approach to modeling reaction in heterogeneous media by Baer *et al.* [93]. Efforts to develop more accurate reaction models for heterogeneous systems, like these, are part of an active area of research.

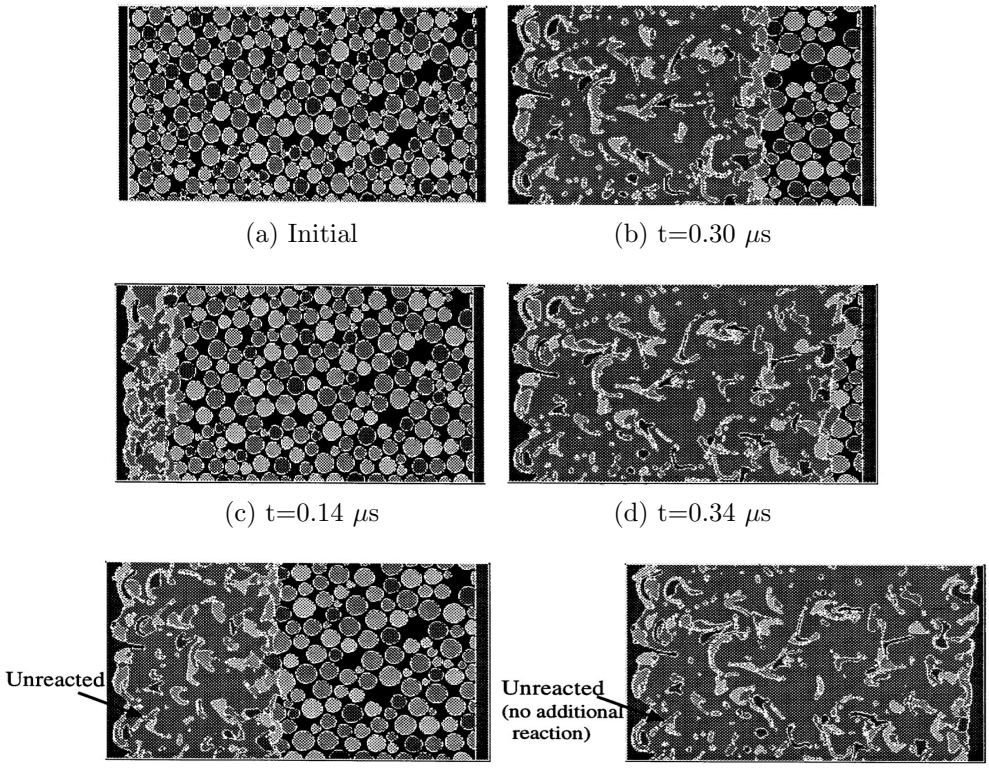

(a) Initial (b) t=0.30 μs

(c) t=0.14 μs (d) t=0.34 μs

(e) t=0.24 μs (f) t=0.36 μs

Figure 2.31: Simulated reaction response of an idealized 60% TMD compact of Nb+2Si at an impact velocity of 1 km/s [91]. The results show near complete reaction in the shock front, due to the infinite transport mechanism.

2.3.1 Constitutive Response in Hydrocodes

The simulation results presented above display extensive material deformation and mixing during the compaction process. While material flow is expected during dynamic compaction, the resulting degree of deformation in the simulations (Figure 2.27) exceeds that seen experimentally (Figure 2.19). The extensive deformations can be attributed to the two-dimensional approximation and limitations in the constitutive models. In 2D, the out-of-plane degrees of freedom are constrained forcing the material to deform more in the plane simulated. This causes increased material deformation in distended systems.

Any computational investigation is also going to depend heavily on the material models chosen. When performing any computational study, an understanding of the underlying assumptions and limitations of the models used must be kept in mind. To determine the thermodynamic relationships of the material, an equation of state is used. To model the the deviatoric components of the stress, and constitutive model is employed. Constitutive strength models are crucial for obtaining the proper deformation response of a material. In its simplest form, a constitutive model only needs to describe a yield strength and Poisson's ratio of the material. This would define an elastic-perfectly-plastic material response. For many instances, this is not an accurate representation of the material behavior. As a result, there have been many different constitutive models proposed to represent material behavior under finite strain. The following section describes a few models employed for high strain rate deformation of metals: Johnson-Cook [94], Steinberg-Guinan-Lund [95, 96], Zerilli-Armstrong [97], and Austin-McDowell [98, 99].

2.3.1.1 Johnson-Cook Model

The simplest of the constitutive models described in this section is the Johnson-Cook model [94]. This model is entirely empirical and relates the von Mises yield stress,

σ_Y, to the strain, ϵ, strain rate, $\dot{\epsilon}$, and temperature, T, through the following relation.

$$\sigma_Y = (A + B\epsilon^n)\left(1 + C\ln\dot{\epsilon^*}\right)(1 - T^*) \tag{2.89}$$

Here A, B, C, n, and m are experimentally determined material constants. The term $\dot{\epsilon^*}$ is a non-dimensionalized strain rate, and T^* is the homologous temperature, defined as the following [94].

$$T^* = \frac{(T - T_{ref})}{(T_{melt} - T_{ref})} \tag{2.90}$$

The simplicity of the Johnson-Cook model makes it very easy to match experimental data and implement in computer codes.

2.3.1.2 Zerilli-Armstrong Model

The Zerilli-Armstrong model [97] has a similar form to the Johnson-Cook model [94], but utilizes thermally activated dislocation glide mechanics. The model accounts for grain size effects, strain hardening, strain rate hardening, and thermal softening. The Zerilli-Armstrong model consists of the following equation.

$$\sigma = \Delta\sigma'_G + (c_1 + c_2\epsilon^{1/2})exp\left(-c_3T + c_4T\ln\dot{\epsilon^*}\right) + +c_5\epsilon^n + kl^{-1/2} \tag{2.91}$$

The parameters c_1 through c_5 and n are material constants and can be set to yield behavior representative of FCC or BCC metals. For BCC metals, it is assumed that the effects of temperature and strain rate dominate the athermal stress response, such that the effects of strain are negligible. This is achieved by setting $c_2 = 0$ and accounting for strain hardening with a simple power law dependence. In contrast, the response of the athermal stress in FCC metals is assumed to depend on the square root of the strain, making $c_1 = c_5 = 0$. The term $\Delta\sigma'_G$ represents any additional stress present in the material, such as from an initial dislocation density. The last term in Equation 2.91 accounts for any increase in stress resulting from transmission of plastic flow between grains, which is done by using a microstructural stress intensity factor, k, and the average grain diameter, l.

2.3.1.3 Steinberg-Guinan-Lund Model

The Steinberg-Guinan-Lund [95] model describes the material's constitutive response through the equivalent plastic strain, ϵ, and the pressure and temperature dependence of the shear modulus, G. In order to accomplish this, the pressure dependence of the yield strength, Y, is related to that of G with the following relation [95].

$$\frac{1}{Y_0}\left.\frac{dY}{dP}\right|_0 \sim \frac{1}{G_0}\left.\frac{dG}{dP}\right|_0 \tag{2.92}$$

Using this approximation, the pressure dependence of Y and G can be obtained through the extrapolated response of G at extremely high pressures [100].

$$G = G_0 + \left.\left(\frac{dG}{dP}\right)\right|_0 \frac{P}{\eta^{1/3}} \tag{2.93}$$

Here, $\eta = \frac{V_0}{V}$ is the material compression and the 1/3 comes from the Thomas-Fermi statistical model of the atom and is only truly accurate at extremely high compressions (*i.e.* $\eta \sim 15$) [100].

With these relations, the rate independent Steinberg-Guinan-Lund model can be express using the following equation [95], subject to a limitation on the amount of strain hardening possible.

$$Y = Y_0\left[1+\beta\left(\epsilon+\epsilon_i\right)\right]^n\left[1+\left.\left(\frac{\frac{\partial Y}{\partial P}}{Y_0}\right)\right|_0 \frac{P}{\eta^{1/3}} + \left.\left(\frac{\frac{\partial G}{\partial T}}{G_0}\right)\right|_0 (T-T_{ref})\right] \tag{2.94}$$

$$G = G_0\left[1+\left.\left(\frac{\frac{\partial G}{\partial P}}{G_0}\right)\right|_0 \frac{P}{\eta^{1/3}} + \left.\left(\frac{\frac{\partial G}{\partial T}}{G_0}\right)\right|_0 (T-T_{ref})\right] \tag{2.95}$$

In the above, β and n are work hardening constants, ϵ_i is the initial strain, and T_{ref} is a reference temperature.

The above model was later expanded by Steinberg and Lund to hold for lower strain rates by accounting for rate effects [96].

$$Y = \left[Y_T(\dot{\epsilon},T) + Y_A f(\epsilon)\right]\left.\left[\frac{G(P,T)}{G_0}\right]\right|_0 \tag{2.96}$$

The thermally activated part of Equation 2.96, $Y_T(\dot{\epsilon}, T)$, can be expressed using dislocation mechanics as the following [96].

$$\dot{\epsilon} = \left\{ \frac{1}{C_1} exp \left[\frac{2U_k}{kT} \left(1 - \frac{Y_T}{Y_P} \right)^2 \right] + \frac{C_2}{Y_T} \right\} \tag{2.97}$$

Here, $2U_k$ is the energy necessary to form a pair of kinks in a dislocation of length L, k is Boltzmann's constant, and Y_P is the Peierls stress. The constants C_1 and C_2 are described with the following relations [96].

$$C_1 = \frac{\rho L a b^2 \nu}{2\omega} \tag{2.98}$$

$$C_2 = \frac{D}{\rho b^2} \tag{2.99}$$

In these equations, ρ is the dislocation density, a is the distance between Peierls valleys, b is the Burger's vector, ν is the Debye Frequency, ω is the width of a kink loop, and D is the dislocation drag coefficient. The final condition for the rate-dependent approximation for the Steinberg-Guinan-Lund model is that $Y_T \ll Y_P$.

2.3.1.4 Austin-McDowell Model

Austin and McDowell developed a constitutive model using a dislocation based approach to describe the high strain rate behavior ($10^4 - 10^8 s^{-1}$) of FCC metals below the material twinning threshold ($\sim$ 15 GPa) [98, 99]. The model describes the kinetamics of slip through a generalized Orowan equation. Both the immobile and mobile dislocation densities are stored as internal state variables and evolved through equations for nucleation, annihilation, multiplication, and trapping. Additionally, the dislocation glide kinetics are described both for the thermally assisted and dynamic regimes, with the dynamic regime accounting for phonon drag and relativistic effects. A detailed numerical description of the model is not presented here, but can be found in reference [98]. While the model is sensitive to the time step, it has proven to yield a more realistic deformation response for porous powder composites in two-dimensions

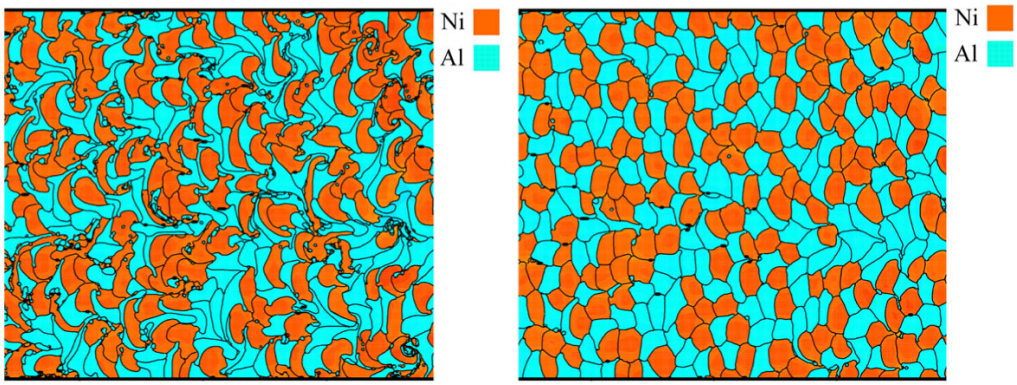

(a) Steinberg-Guinan-Lund Model (b) Austin-McDowell Model

Figure 2.32: Comparison of the predicted particle deformation in a idealized mixture of Ni and Al at 1000 m/s by the Steinberg-Guinan-Lund rate-independent model [95] (b) and the rate-dependent, dislocation based Austin-McDowell model [98, 99] (c). The results show that, for distended materials in 2D, the Austin-McDowell rate-dependent viscoplastic model tends to more accurately predict the deformation response [102].

than the Steinberg-Guinan-Lund rate-independent model [95], as seen in Figure 2.32 [101, 102].

2.4 Reaction and Mechanical Response of Laminated Multilayer Composites

While the reaction responses of a variety of metal/metal binary systems have been investigated [22, 103, 104, 105, 106], this section focuses on the Ni-Al multilayer system. For a more in depth review of work in other metal/metal systems, the reader is referred the review by Munir and Anselmi-Tamburini [22].

The structure of a multilayer composite is strongly dependent on its fabrication technique. There are numerous ways to make multilayer composites, each with its own advantages and disadvantages. A common way to make multilayers with nanometer sized layers, often called nanofilms, is through physical vapor deposition (PVD). This can be done with sputter deposition [25, 107, 108, 20, 109] or electron beam evaporation [110, 111]. These methods enable the production of very precise, uniform layers

as small as a few nanometers. Figure 2.33 shows an SEM image of a sputter-deposited multilayer with two different bilayer spacings. The bilayer spacing is the average distance between the centers of neighboring layers of the same material. Since these are binary systems, the length scale used to describe them must capture both materials. While these methods enable precise control, they also have the limitation of only producing very thin samples on the order of tens of μm thick. In addition, there is an inherent intermixed region that is formed between layers during sputter deposition. Given the small bilayer spacings in these vapor deposited films, the intermixed region can have a dramatic effect on the reaction response of the multilayers [25].

Another complication can arise from the sputter deposition of Ni. In order to make Ni non-magnetic and the deposition process easier, the Ni is often alloyed with 7 wt% V [108]. This leads a concentration of V in the final multilayer composite which is not insignificant (identical Al and Ni-V layer thicknesses yield a $Al_{50}Ni_{46}V_4$ composite) [108].

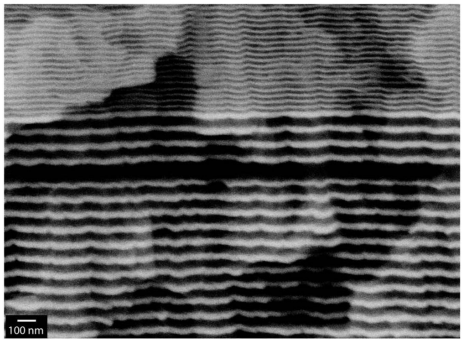

Figure 2.33: Cross sectional image of a sputter deposited foil showing two distinct bilayer spacings. Sputter depositing enables the creation of very small, uniform, bilayers [107].

Multilayer composites can also be fabricated through mechanical means. This is often done by cold-rolling and folding [26, 112, 113, 114, 115] or by mechanical pressing [116, 117, 118]. Both of these methods allow for the creation of large samples. Mechanical pressing yields very uniformly layered structures, while cold-rolling and

folding generates very heterogeneous microstructures. However, through repeated rolling and folding, large scale composites with bilayer spacings under a micron can be made [114]. In addition, unlike other mechanical processing techniques, such as ball milling [119, 120], cold-rolling does not lead to the formation of a significant amount of any intermetallic phase [114]. This makes it an attractive method for producing reactive mixtures with a laminar microstructure.

2.4.1 Reaction Studies in Ni-Al Multilayer Composites

Depending on the fabrication method and stoichiometery, the initiation of thermally induced reaction in multilayer composites can differ. Blobaum *et al.* found that reaction initiated with the formation of metastable Al_9Ni_2 in sputter-deposited foils [20]. This was dependent on the bilayer spacing, and for small bilayer spacing (< 12.5 nm), the formation of Al_3Ni was observed first [20]. Blobaum *et al.* were able to attribute this behavior to the composition and size of the intermixed regions [20]. However, most investigators have found that reaction initiates with the formation of Al_3Ni [26, 104, 112, 113, 114, 115]. This is the case for cold-rolled multilayers, were the deformation from rolling provides limited mixing, which, according to 3D atomic probe analysis, favors the formation of Al_3Ni [113]. Since these are diffusion driven reactions, they are seen to initiate with the formation of an Al rich phase. As discussed in Section 2.2, under shock compression, reaction has been found to initiate with Ni rich phases [9]. Therefore, dynamic loading could potentially provide a unique reaction pathway for the Ni/Al multilayers.

Under thermal ignition, the multilayer composites have been found to follow a two stage reaction process, first proposed by Coffey *et al.* [105]. A schematic of this two-stage reaction process is shown in Figure 2.34. Reaction initiates at specific locations on the material interface, which then grow laterally along the interface. Once the interfacial area is consumed, the product phase then grows perpendicularly

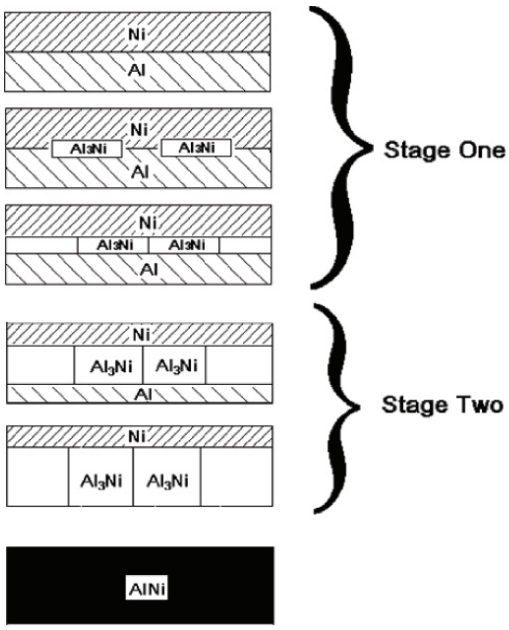

Figure 2.34: Thermal reaction process proposed by Coffey *et al.* [105] in Ni+Al multilayers [115].

from the interface until both constituents are consumed. This reaction process has been extensively documented in Ni/Al multilayers with DSC traces and SEM images [115, 26]. A DSC trace showing the signature of this two stage reaction for multilayers having undergone differing amounts of rolling is presented in Figure 2.35 [26]. SEM images of this two stage reaction process are also provided in Figure 2.36 [26].

The first trough in the DSC trace corresponds to the lateral formation of Al_3Ni along the Al/Ni interface, which can be seen in Figure 2.36b. The second trough then corresponds to the perpendicular growth of this phase, which can be seen in Figures 2.36c and 2.36d. Figure 2.35 also shows the magnitude of the first DSC trough increasing and that of the second trough decreasing with increasing rolling passes. Since more rolling passes yield smaller bilayer spacings, there is more interfacial surface area available for the initial lateral stage of growth, leading a larger initial trough [26]. Consequently, a smaller bilayer spacing means less room for perpendicular growth, shrinking the second trough [26]. Both of these troughs are also seen to occur at lower temperatures as the number rolling cycles increases [26]. With

more rolling passes, higher defect concentrations are generated, aiding diffusion, and lowering the reaction threshold.

There is also evidence to suggest the reaction process is more complex than the simple two stage growth of Al_3Ni proposed by Coffey *et al.* [105]. Battezzeti et al. found evidence of the formation of Al_3Ni_2 and $AlNi_3$, showing a progression from Ni rich and Al rich phases to the stoichiometric AlNi phase [26], as shown in Figure 2.37. This result is closely tied to the underlying microstructure of these multilayer composites and highlights how important the microstructure is in determining the reaction response.

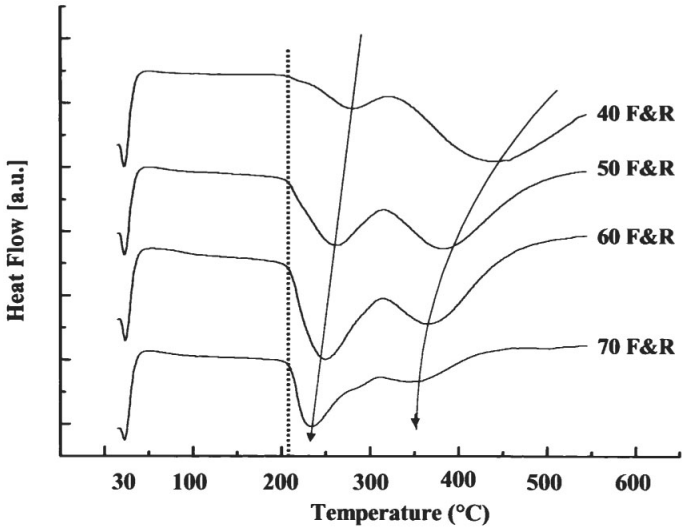

Figure 2.35: DSC trace exhibiting two troughs corresponding to the lateral then perpendicular formation of Al_3Ni [115]. With increasing rolling passes, the bilayer spacing decreases, leading to more interfacial area. This causes the first trough to increase and the second trough to decrease.

The reaction response in multilayer systems also depends heavily on the degree of component mixing and the bilayer spacing. Gavens *et al.* investigated the effects of both bilayer spacing and intermixing on the flame speed in sputter-deposited multilayers [25]. Their results showed that the flame velocity increased with decreasing bilayer spacing and intermixing. Gavens *et al.* found that when the intermixed region becomes a significant portion of the layer thickness, it acts as a diffusion barrier,

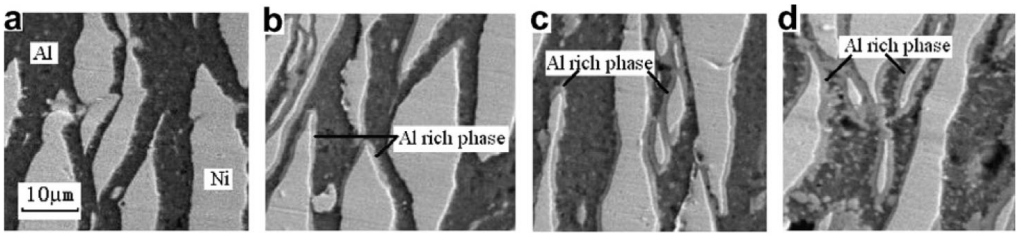

Figure 2.36: SEM image showing formation of an Al rich phase in Ni/Al multilayers (a) initially beginning laterally (b) and then perpendicularly (c-d) from the interface [115].

explaining the lower flame speed [25]. The effects of bilayer spacing on the heats of reaction and flame speed in vapor deposited multilayers were also investigated by Knepper *et al.* [107]. In this study, multilayers with a fine and coarse bilayer spacings were fabricated, along with a multilayer containing both bilayers (Figure 2.33). The results showed that, for multilayers with multiple bilayers, a number average of the bilayer spacing was appropriate for predicting heats of reaction, while a volume average was better suited for estimating reaction velocities [107]. All of these studies, once again, illustrate how important the underlying microstructure is on the resulting reaction response in multilayer composites.

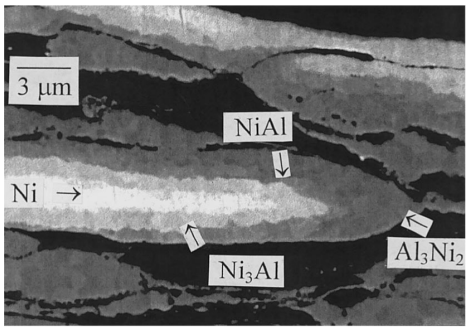

Figure 2.37: SEM image showing the progressing of Al and Ni rich phases in forming stoichiometric AlNi [26].

2.4.2 Mechanical Response of Multilayered Composites

Multilayer composites composed of materials with large differences in their elastic and plastic properties comprise a system dominated by the periodic heterogeneities

of their interfaces. In multilayers with nanometer sized layers, the interfaces dominate the plasticity mechanisms, leading to very high flow strengths that are stable at large strains [121, 122]. In bulk laminated composites, the impedance difference at the material interfaces can cause numerous stress wave reflections and interactions, which lead to changes in the propagating wave structure. The changes in the stress wave can be attributed to two factors: geometric dispersion and spatial dissipation. Geometric dispersion is a spreading of the wave energy, which changes the shape of the stress pulse. Spatial dissipation alters the stress pulse as a result of the deposition of the wave energy irreversibly into the material. The effects of both of these factors on a propagating stress wave have been extensively investigated in the past.

Past experimental work on the shock compression response of laminated composites has focused on systems with the layers oriented perpendicular to the direction of shock wave propagation. Lundergan and Drumheller [123] looked at plastic wave propagation through a laminated composite consisting of 10 bilayers of Epon 828 epoxy and 304 stainless steel. They used experiments along with one-dimensional computations to understand the effect of material interfaces on the propagation of the shock wave. The results showed that laminated media experienced oscillations in the particle velocity profile. While the velocity profiles showed changes over time, its perturbations were periodic, enabling it to be considered a steady wave. Their experimental results along with the computational results using a simple elastic wave model implemented in the 1D, Lagrangian finite-difference code, WONDY III, are shown in Figure 2.38 [123].

Additional studies by Oved, Luttwak, and Rosenberg [124] looked at a similar multilayer composite made of PMMA (polymethyl methacrylate) and Cu at higher strain rates. They compared the results of their experiments with one-dimensional hydrocode analysis, which is seen in Figure 2.39. Similar to the findings of Lundergran and Drumheller [123], their composite exhibited oscillatory behavior in the pressure

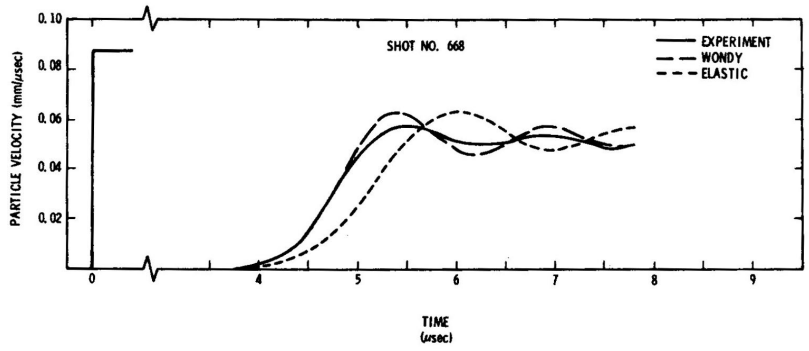

Figure 2.38: Comparison of experimental and computational results for low impact velocity experiments on 10 bilayers of Epon 828 epoxy and 304 stainless steel performed by Lundergran and Drumheller[123].

pulse, resulting from multiple wave interactions [124]. Oved *et al.* concluded that these interactions were the main source of attenuation observed in the multilayer composite [124].

More recent work done by Zhuang, Ravichandran, and Grady [125] on multilayer composites of polycarbonate/T-6 6061 aluminum, polycarbonate/304 stainless steel, and polycarbonate/glass have also revealed oscillatory behavior in the pressure pulse. Their results showed that the pressure oscillations increase with increasing impedance mismatch between constituent. This can be seen by comparing the results for the polycarbonate/304 stainless steel (Figure 2.40a) and polycarbonate/glass (Figure 2.40b) composites at various impact velocities. Zhuang, Ravichandran, and Grady [125] also found that the strain rate was proportional to the square of the shock speed for layered media, suggesting they have more shock viscosity than homogeneous materials, which scale to the fourth power [125].

There have also been investigations of the static and dynamic failure of cold-rolled multilayer composites by Vitali *et al.* [126]. In this work, laser shock loading coupled with computational analysis was able to highlight the importance of material bonding and layer spacing on the corresponding spall strength of cold-rolled Ni/Al multilayers [126].

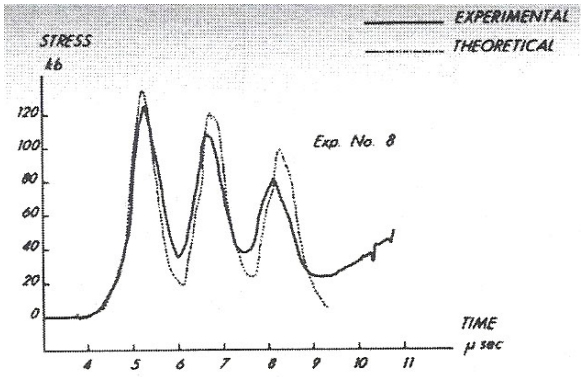

Figure 2.39: Experimental and theoretical stress profiles for a multilayer of PMMA and Cu. Both results show large oscillatory behavior in the shock pulse [124].

Extensive analytical work has also been performed to understand the shock propagation response in multilayer composites. Barker [127] developed a model for shock wave propagation perpendicular to the layers in laminated media. Noting that the dissipative effects of laminated media are similar to a viscoelastic material, Barker developed a viscous model to predict the wave structure of a multilayer composite. Comparing his model to experimental findings, Barker showed that, while the model was able to predict the gross wave characteristics, it failed to capture the oscillatory behavior of the shock wave [128]. Curran, Seaman, and Austin [129] used a similar approach and derived a dissipative model utilizing the artificial viscosity already present in 1D hydrocodes. Drumheller and Sutherland [130] also developed a model for plastic wave motion in a fiber reinforced composite with the wave traveling perpendicular to the fibers. The Drumheller and Sutherland model is non-dissipative and assumes geometric dispersion is the result of the periodicity of heterogeneities and not their structure. In this sense, the heterogeneities can then be redistributed in a laminated format to match the dispersive character of any composite. Drumheller and Sutherland [130] compared their lattice model to some low velocity impact data and obtained a slight over prediction of the oscillatory wave structure, as seen in Figure 2.41.

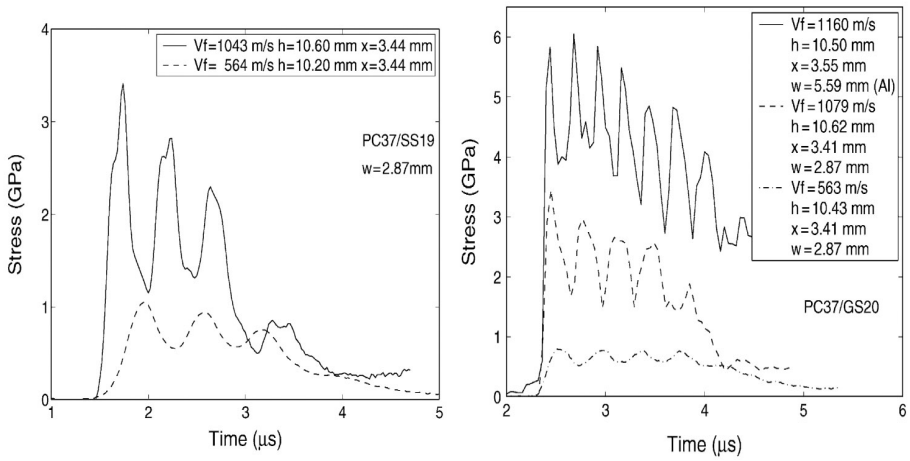

(a) PC37/SS19 (b) PC37/GS20

Figure 2.40: Experimentally obtained stress profiles in a layered composite of 0.37 mm polycarbonate and 0.19 mm 304 stainless steel (a) and 0.37 mm polycarbonate and 0.20 mm glass (b). The two composites exhibit varying degrees of pressure oscillations due to the differing impedance mismatch between the layers [125].

The propagation of stress waves in the direction of the layering has also been investigated. The analysis of time-harmonic elastic stress waves along the layering has been studied by both Sun *et al.* [131, 132] and Achenbach and Hermann [133] through the development of effective stiffness theory. Effective stiffness theory involves using representative elastic moduli for each phase to obtain an effective stiffness of the composite. This enables the bending, shear, and extensional stiffnesses to be accounted for in the strain energy [132]. Additional work by Peck and Gurtman [134] focused on understanding the dispersion of a wave propagating laterally through stratified media. Their analysis uses the head-of-pulse approximation to quantify a dispersion time that could simply describe the dispersion in the system.

Tsou and Chou [135] developed a theoretical model for a shock wave propagating longitudinally in a fiber reinforced composite. Their model was limited to a two-dimensional cross-section of the composite, which presents a microstructural configuration identical to a multilayer composite with a shock wave propagating parallel to the layers. The model focused on the hydrodynamic regime, with steady, isothermal

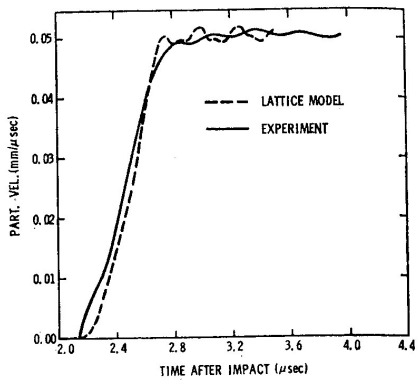

Figure 2.41: Comparison of Drumheller and Sutherland's lattice model to experimental results for an Al-W fiber-reinforced composite. [130].

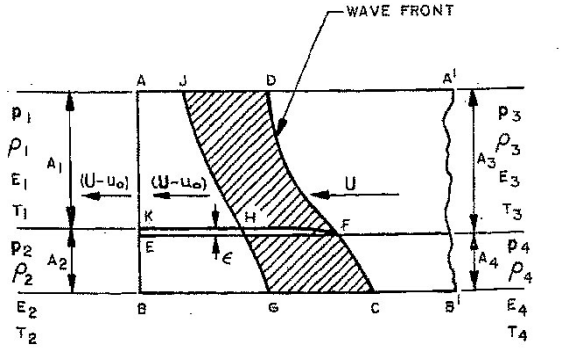

Figure 2.42: Schematic of a shock front in a laminated composite [135].

flow and perfect bonding between constituents. Using a control-volume approach, they re-derived the Rankine-Hugoniot conditions to account for the compression of the fibers, as seen in Figure 2.42, which is a two-dimensional effect [135].

$$\rho_1(\sigma - \sigma^*)(U - u_o) = \rho_3 \sigma U \tag{2.100}$$

$$\rho_2(1 + \sigma^*)(U - u_o) = \rho_4 U \tag{2.101}$$

$$(\sigma\rho_3 + \rho_4)U^2 \left(\frac{u_o}{U}\right) - (1 + \sigma)(P_1 - P_3) = 0 \tag{2.102}$$

$$\frac{\sigma\rho_3}{\rho_4}(E_1 - E_3) + (E_2 - E_4) - \frac{1}{2}\left(\frac{\sigma\rho_3}{\rho_4} + 1\right)u_0^2 - (\sigma + 1)\frac{P_3}{\rho_4}\frac{u_0}{U} = 0 \tag{2.103}$$

Here, Equations 2.100 and 2.101 represent the conservation of mass, Equation 2.102 the conservation of momentum, and Equation 2.103 the conservation of energy. In

these equations, A refers to the layer area, U the shock velocity, and u_0 the particle velocity. The parameters σ and σ^* are represented with the following [135].

$$\sigma = \frac{A_3}{A_4} \tag{2.104}$$

$$\sigma^* = \frac{\epsilon}{A_4} = \frac{A_3 - A_1}{A_4} = \frac{A_2 - A_4}{A_4} \tag{2.105}$$

In this description, the subscripts 1 and 3 refer to initial and final states of component A, while the subscripts 2 and 4 refer to the initial and final states of component B. Tsou and Chou [135] also developed equations for the shocked temperature, T, and interfacial shearing force, F, in the composite assuming a steady-state ($P_3 = P_4$), isothermal flow ($T_3 = T_4$).

$$T = \frac{1}{1 - \frac{E - E_a}{\mathcal{A}}} \left[T_0 + \frac{1}{C_p} \left\{ (E - E_0) + P_0 \left(\frac{1}{\rho} - \frac{1}{\rho_0} \right) \right\} \right] \tag{2.106}$$

$$\frac{F}{(A_3\rho_3 + A_4\rho_4)U^2} = \left(\frac{1}{1 + \frac{1}{\sigma}\frac{\rho_4}{\rho_3}} \right) \left(\frac{(P_1 - P_3)\sigma - P_1\sigma^*}{\rho_3\sigma U^2} - \frac{u_0}{U} \right) \tag{2.107}$$

Here, the subscript 0 refers to the reference state of either constituent, C_p is the constant pressure specific heat, and $\mathcal{A}$ is represented with the following,

$$\mathcal{A} = \left(\frac{\partial E}{\partial P} \right)_\mu \left[P - \frac{\rho^2}{\rho_0} \left(\frac{\partial E}{\partial \mu} \right)_P \right] \tag{2.108}$$

where $\mu = \frac{\rho}{\rho_0} - 1$ is the compression. The results were then applied to determine the bulk response of a theoretical polyethylene/beryllium composite. Tsou and Chou [136] later extended the model to a macroscopically homogeneous composite of any geometry.

Torvik [137] took the fiber reinforced composite model of Tsou and Chou [135, 136] and modified it for the case when there was no bonding between the constituents. His model used the pressure differential in each layer to maintain a steady shock wave. Application of the model to a composite of PMMA and Al showed the potential for a composite to have a lower bulk sonic velocity then either constituent [137]. Munson and Schuler [138] also followed the development of Tsou and Chou [135, 136]

to develop a mechanical model based on steady wave analysis for laminated media. While being simpler and applicable to both longitudinal and lateral wave motion, it proved to be less accurate than the Tsou and Chou model [135, 136], since it does not account for material geometry.

More recently, efforts have been made to numerically account for the multiple wave interactions and reflections in laminated medium [139]. This work is based on Floquet theory [140] applied in both the elastic and hydrodynamic regimes. The analysis is able to capture the oscillatory behavior of a simple, idealized multilayer composite showing the effect of material properties and layer structure on the propagating wave [141]. While this work is interesting, the need for analytical models of wave propagation through laminated media is becoming less necessary as access to even moderate computational resources enable more exact computational solutions. Additionally, computational analysis eliminates the need to stay with idealized laminated media. As a result, computational analysis allows for more complex systems with non-uniformities and non-continuous layers to be investigated.

2.4.2.1 Mechanical Initiation of Reaction in Laminated Media

In addition to the studies on the thermal ignition of the multilayer foils, there have been a few studies focused on mechanical ignition. Spey investigated the ignition of Ni/Al multilayers using a drop weight attached to a lever arm [142]. This method enabled a determination of the energy necessary to ignite the Ni/Al multilayers. It was found that the mechanical initiation of the multilayers became harder with increasing bilayer spacing and intermixing [142]. Wei *et al.* investigated the ignition of Ni/Al multilayers through high-intensity laser shock loading [143]. Their results showed that a shock-assisted reaction could be initiated at the material interfaces with sufficient laser energy ($1.23e13\ Wcm^{-2}$) and duration (8 ns) to induce melting of Al. However, the reactions were not able to propagate in a self sustaining manner,

most likely due to the rapid cooling of the transient high temperatures generated by the laser [143].

There have also been computational efforts to model the mechanical ignition of reaction in mutlilayers of Ni and Al. Molecular dynamics (MD) simulations of Ni/Al nanofilms under shock loading ($U_P = 2$ km/s) have been performed by Zhao, Germann and Strachan [144, 145]. These efforts utilize nonequilibrium MD calculations to describe the shock loading state and constant volume and energy MD methods for longer time phenomena [144, 145]. Both perfect and porous nanofilms with layers oriented perpendicular to the propagating shock pulse were investigated [144, 145]. The presence of voids was found to lead to both higher temperatures and increased levels of intermixing. This accelerated the alloying process [144] and aided reaction, which was shown to be dependent on the melting of both constituents [145].

CHAPTER III

MATERIAL SYSTEM

3.1 The Nickel and Aluminum Binary System

Ni and Al are both FCC metals, but they have vastly different material properties. Some of these material properties are listed in Table 3.1. It is clearly seen that Ni has a much larger density, strength, melting point, and moduli than pure Al. In contrast, Al is seen to have larger longitudinal and shear wave speeds. These differing properties are important to consider in any analysis on composites of Ni and Al. This is particularly true for shock compression, where large discrepancies in material properties can create complex loading scenarios and wave interactions.

Table 3.1: Elemental properties of Ni and Al [146, 147].

Element	Density ($\frac{g}{cm^2}$)	E (GPa)	G (GPa)	σ_y (MPa)	ν	c_L ($^m/_s$)	c_S ($^m/_s$)	T_M (°C)
Al	2.6989	62	25	15-20	0.33	6200	3044†	660.4
Al-5052-O	2.68	69	26	90	0.33†	6142†	3115†	649
Ni	8.902	207	76	59	0.31	4700	2922†	1453

†Calculated assuming an isotropic, homogeneous solid.

As stated previously, there is significant interest in the Ni/Al system due to the exothermic nature of its reactions. The Ni/Al system has six stable intermetallic phases, which are identified on the phase diagram presented in Figure 3.1. The structural and thermal properties of these intermetallic phases are listed in Table 3.2, which clearly shows that all of the intermetallic phases of Ni/Al undergo exothermic reactions with AlNi having the highest heat of reaction. There has also been evidence of metastable phase formation in the Ni/Al system [20], providing further interest for study.

The heats of formation presented in Table 3.2 are dependent on the composition.

This dependence is shown graphically in Figure 3.2, which provides the enthalpy of formation for most of the intermetallics of Ni/Al over their entire composition range on the phase diagram (Figure 3.1).

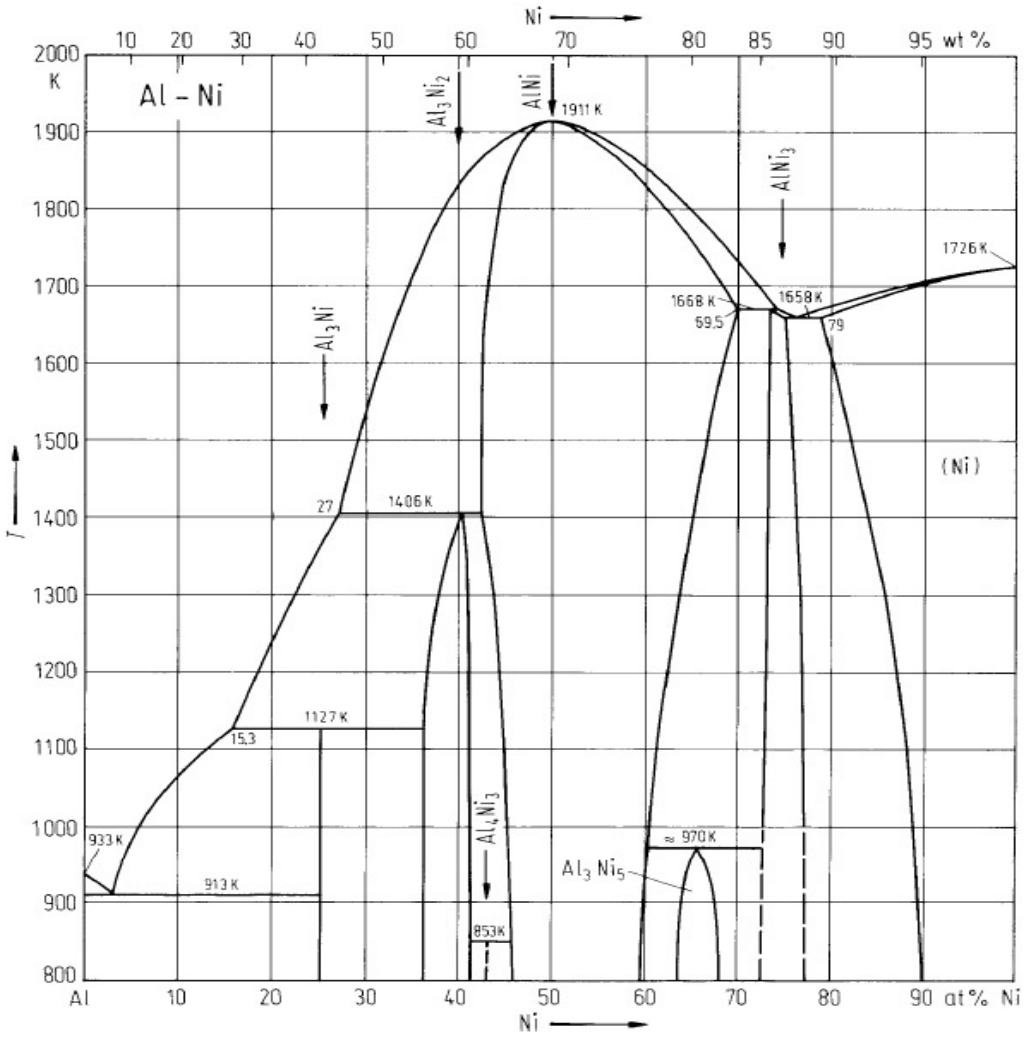

Figure 3.1: The phase diagram of the Ni/Al system [147].

3.2 Multilayer Composite Structure and Fabrication

The current research utilizes Ni/Al multilayered composites fabricated by Dr. Timothy P. Weihs at Johns Hopkins University [151]. The composites are made by cold-rolling individual Ni 201 (99.6% Ni) and Al 5052 H19 (2.5% Mg and 0.25% Cr) foils. The properties of Ni 201 are assumed to match those of pure Ni given in Table 3.1.

Table 3.2: Structural and thermal properties for the intermetallic phases of Ni and Al [147, 148, 149, 150].

Phase	Structure [147]	Space [148] Group	a [147] (nm)	b [147] (nm)	c [147] (nm)	Density [148] ($^{g}/_{cm^2}$)	ΔH^f [149, 150] ($^{kJ}/_{g}$)
Al_3Ni	orth.	Pnma	0.6612	0.73767	0.4812	3.82	-1.084
Al_3Ni_2	rhomb.	$P\bar{3}m1$	0.4363 †	-	0.4900 †	4.14	-1.489
Al_4Ni_3	cub.	$Ia\bar{3}d$	1.1408	-	-	5.083	-
AlNi	cub.	$Pm\bar{3}m$	0.2887	-	-	5.956	-1.673
Al_2Ni_3 ‡	bct	-	0.2668	-	0.3244	-	-0.983
Al_3Ni_5	orth.	Cmmm	-	-	-	6.627	-0.859
$AlNi_3$	cub.	$Pm\bar{3}m$	0.357	-	-	7.474	-0.755

†Hexagonal Parameters

‡Metastable Phase

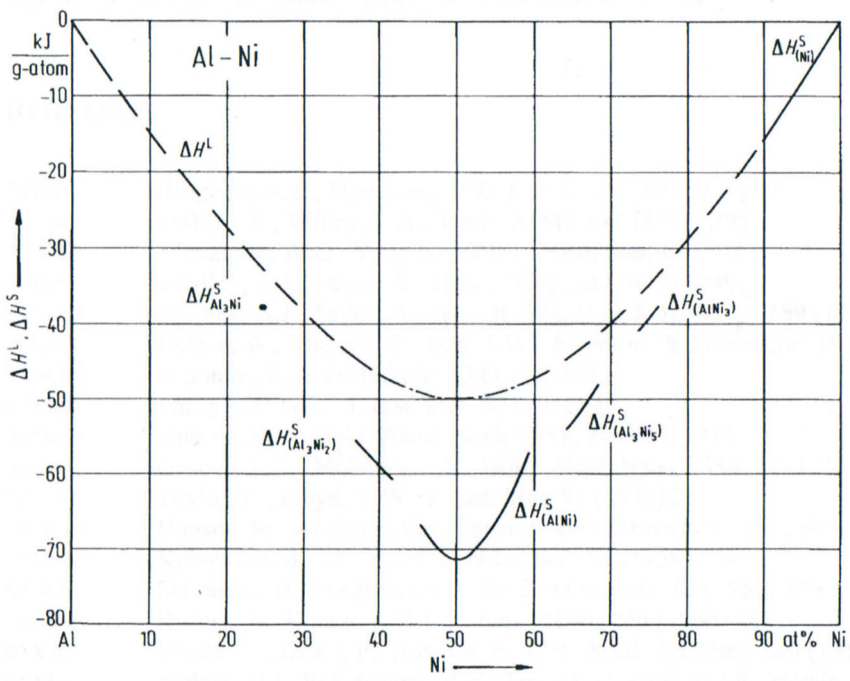

Figure 3.2: Enthalpy of mixing for liquid alloys of Ni and Al at 1873 K (dashed line) along with enthalpies of formation at standard temperature and pressure conditions for many intermetallic phases (solid lines) [147].

The properties of Al 5052 O are also listed in Table 3.1 and are fairly similar to those of pure Al, except in yield strength. The use of the extensively strain hardened Al 5052 H19 over a commercially pure Al alloy is done to improve the rolling process, which is most effective when the two constituents have similar hardnesses.

The fabrication process for these cold-rolled multilayers is described in Figure 3.3. To create these composites, individual foils are chosen and stacked to achieve the desired stoichiometry (Figure 3.3a). The stacked foils are then rolled to a 50% reduction in thickness (Figure 3.3b). This rolled sheet is then cut in half, and the halves are stacked on top of each other to regain the original thickness (Figure 3.3c). Finally, the stacked halves are rolled once more to a 50% reduction in thickness (Figure 3.3d). This whole process constitutes one rolling cycle. The more rolling cycles the multilayer endures, the larger the deformation induced in the materials and the smaller the bilayer spacing, λ. As mentioned earlier, the average bilayer spacing is an

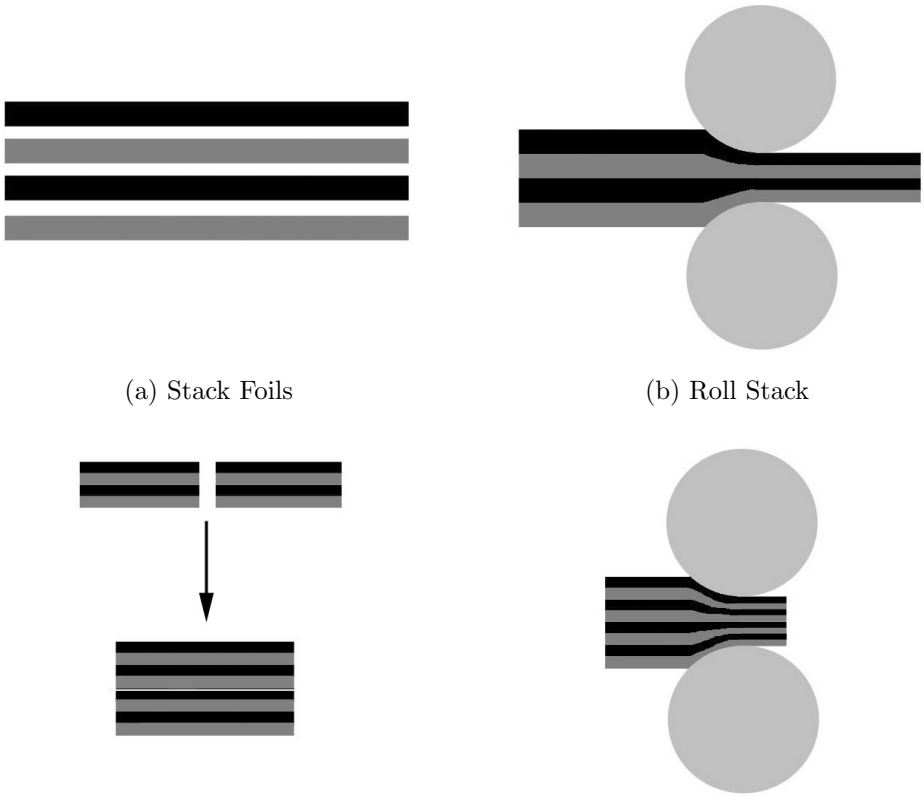

(a) Stack Foils

(b) Roll Stack

(c) Cut and Re-stack

(d) Re-roll Stack

Figure 3.3: Rolling process used for the fabrication of the cold-rolled multilayer composites. First, foils of Ni and Al are stacked (a) and then rolled to half of the original thickness (b). This rolled material is then cut in half, re-stacked (c), and rolled once more(d).

important microstructural parameter that effects the reaction response under thermal ignition [22, 25, 107]. The bilayer spacing can also be controlled to a limited extent through variations in the starting foil thicknesses. A more detailed description of the multilayer composite fabrication is outlined in U.S. patent application 20110027547 [151].

The multilayer composite used in this work was fabricated with Ni and Al foils initially 178μm and 127μm thick, respectively. The foils were stacked to achieve a 1:1 stoichiometric ratio (60% Al and 40% Ni by volume) and the composite underwent 3 rolling cycles. An optical micrograph of a hand-polished cross-section of

the Ni/Al multilayer is shown in Figure 3.4. The multilayer composite was hand-polished to minimize delamination and pitting in the microstructure. The optical micrograph shows a microstructure with intimate and continuous particle contacts and very limited void space ($\sim$ 0.25%, possibly a result of delamination or pitting due to polishing). As a result, the multilayered Ni/Al composite is considered fully dense and the effect of any porosity is ignored.

The resulting composite has a final total thickness of $\sim 650\mu$m and an average bilayer spacing, within 95% confidence, of 28.2 $\pm$ 4.2 μm. A histogram showing the variation in bilayer spacing for these multilayers is shown in Figure 3.5. The large spread of the histogram highlights the large degree of heterogeneity in the cold-rolled multilayer microstructure. While the bright contrast Al layers in the optical micrograph are almost continuous along the length of the composite, the darker contrast Ni layers are discontinuous as a result of necking during the rolling process. This leads to the large variation in the average bilayer spacing.

The micrograph presented in Figure 3.4 corresponds to the longitudinal cross-section, meaning the normal to the image plane is in the longitudinal direction. In rolled materials, the microstructure often varies depending on the orientation of the sectioning plane relative to the rolling direction. This is the case for the multilayer composite investigated here. Figure 3.6 shows the cross-sections for the long and short transverse directions. Unlike the longitudinal cross-section, the long transverse cross-section does not exhibit the long, continuous Al layers and show signs of shear banding due to rolling. This difference in the longitudinal and long transverse cross-sections is dependent on the number of rolling cycles [143]. With more rolling cycles, the long transverse and longitudinal cross-sections eventually become indistinguishable. With only three rolling cycles, the multilayer composite used in this work has not undergone enough rolling to have similar longitudinal and long transverse cross-sections.

The work presented here focuses only on the longitudinal cross-section for two

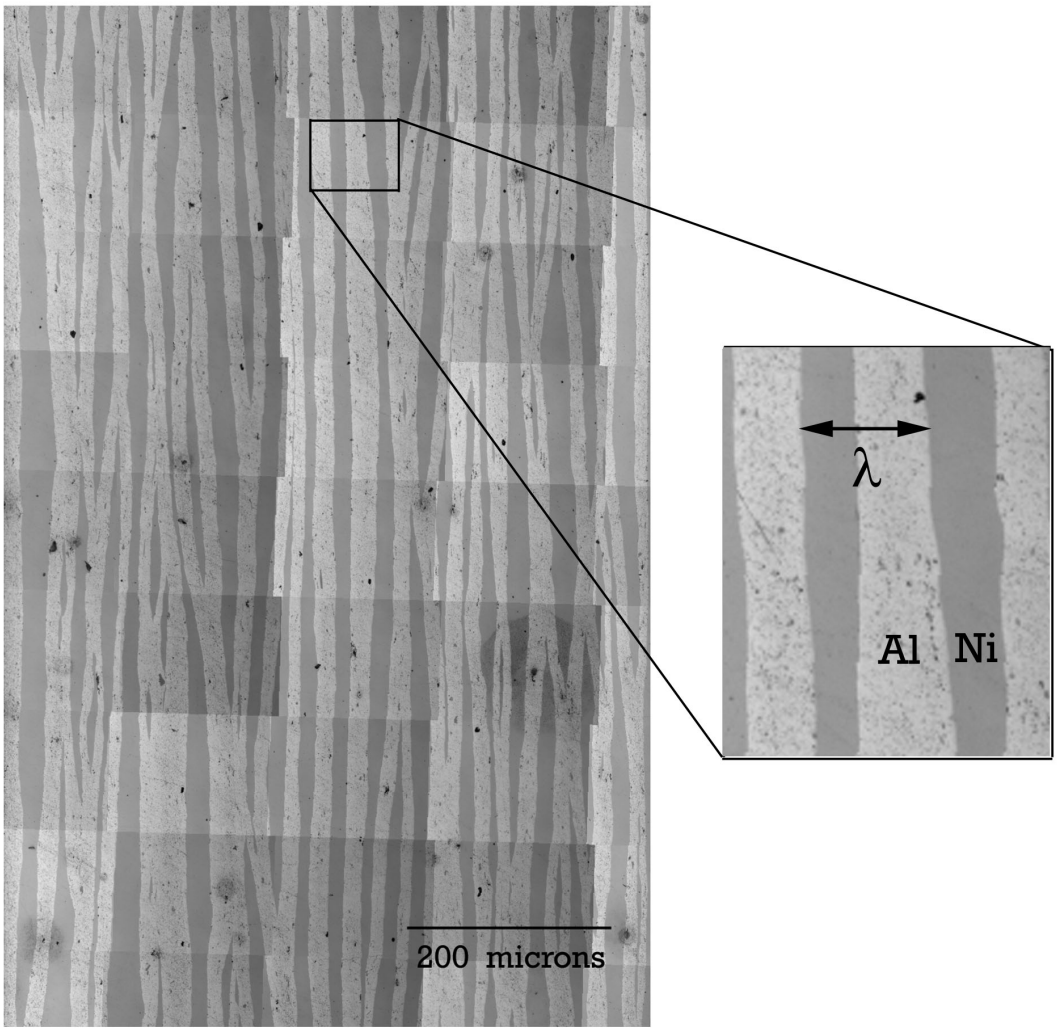

Figure 3.4: Optical micrograph of the longitudinal cross-section of the Ni/Al multilayer composite.

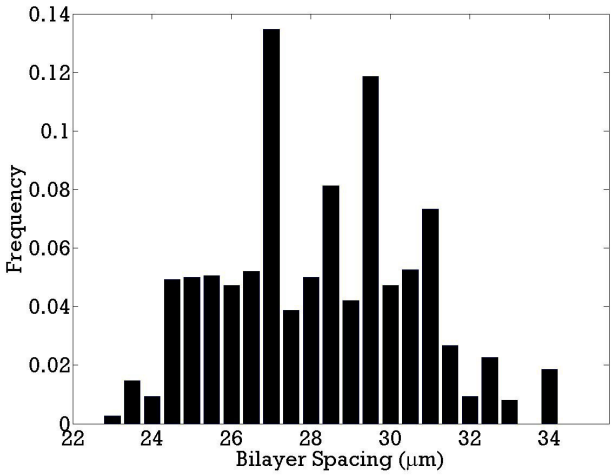

Figure 3.5: Histogram showing the variation in bilayer spacing for the longitudinal multilayer cross-section shown in Figure 3.4.

main reasons:

- To be representative of multilayers that underwent more rolling cycles. The long transverse cross-section eventually becomes similar to the longitudinal cross-section with more rolling cycles. This allows for correlations to be made to multilayers with smaller bilayer spacings through a simple scaling of the microstructure shown in Figure 3.4.

- To strengthen comparisons between the results presented here and previous experimental results on idealized perfect laminated microstructures. The longitudinal cross-section presents the most idealized laminar microstructure for the multilayers.

Even when focusing on one cross-section, it is important to remember that these composites can only be approximated as laminar materials. Their underlying microstructure is truly three-dimensionally varying and highly heterogeneous. Any analysis on these systems must account for these heterogeneities for accurate results, which is done in this work.

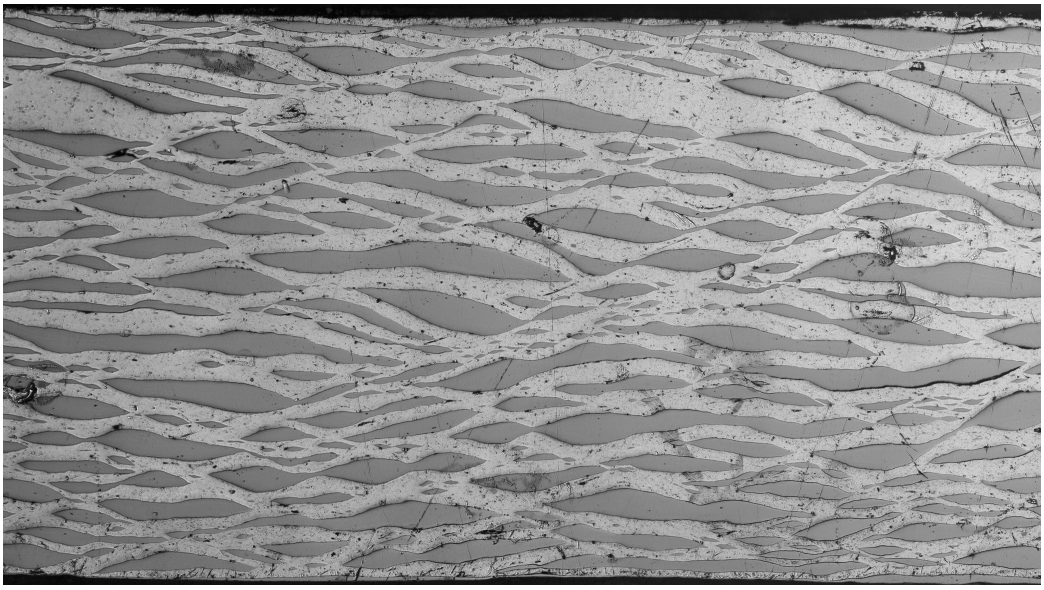

(a) Transverse

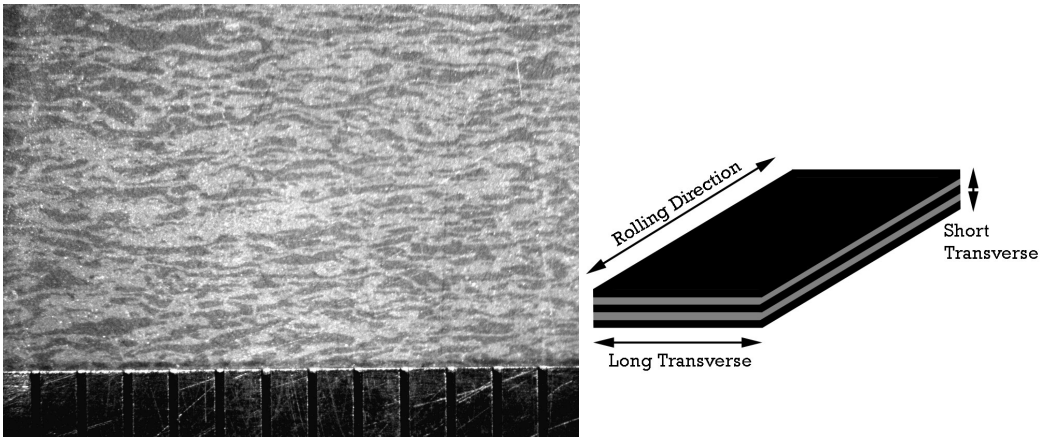

(b) Short Transverse

Figure 3.6: Optical micrograph of the long transverse (a) and short transverse (b) cross-section in the multilayer composite

3.3 Properties of the Multilayer Composites

3.3.1 Multilayer Composite Composition

Excessive deformation is known to induce reaction in the Ni/Al system due to solid-state defect-enhanced diffusion. This has been observed in ball milled powders [119, 120]. In addition, intermixing in sputter or vapor deposited multilayers is known to have a significant effect on the reaction response, as stated in Section 2.4.1 [25, 107, 152]. The past work of Battezzati *et al.* on cold-rolled multilayers reported no significant intermixing even after 75 rolling cycles [26]. Sauvage *et al.* did find some evidence of very limited intermixing with 3D atomic probe analysis in cold-rolled multilayers, but not to a degree that would be visible through X-ray diffraction (XRD) analysis [113]. Based on these past studies, intermixing is not expected to be present in the multilayer composites investigated here. However, if it is present, it can affect the response of cold-rolled composites. An XRD trace was taken to verify if any significant intermixing is present in the multilayers used in this work.

Another reason for obtaining an initial XRD trace comes from the choice of Al 5052 H19 for the fabrication of these multilayers. Past studies on intermetallic formation in cold-rolled multilayers [26, 113, 114] utilized high purity elemental foils. Al 5052 has 2.5% Mg. An XRD trace can help determine if the Mg content needs to be considered. The XRD analysis was done on a Panalytic X'Pert PRO MPD XRD machine using CuKα_1 radiation and a solid state scanning X'Celerator detector. The XRD trace obtained is shown in Figure 3.7. The trace is seen to have only Ni and Al peaks. Since no peaks from Mg or an intermetallic were observed, the multilayer composite was treated as initially composed of pure Al and Ni.

3.3.2 Volume Fraction and Surface Area Measurements

The multilayer microstructure shown in Figure 3.4 was manually thresholded into a binary image of the phases. This was done for two reasons: to aid in the computational

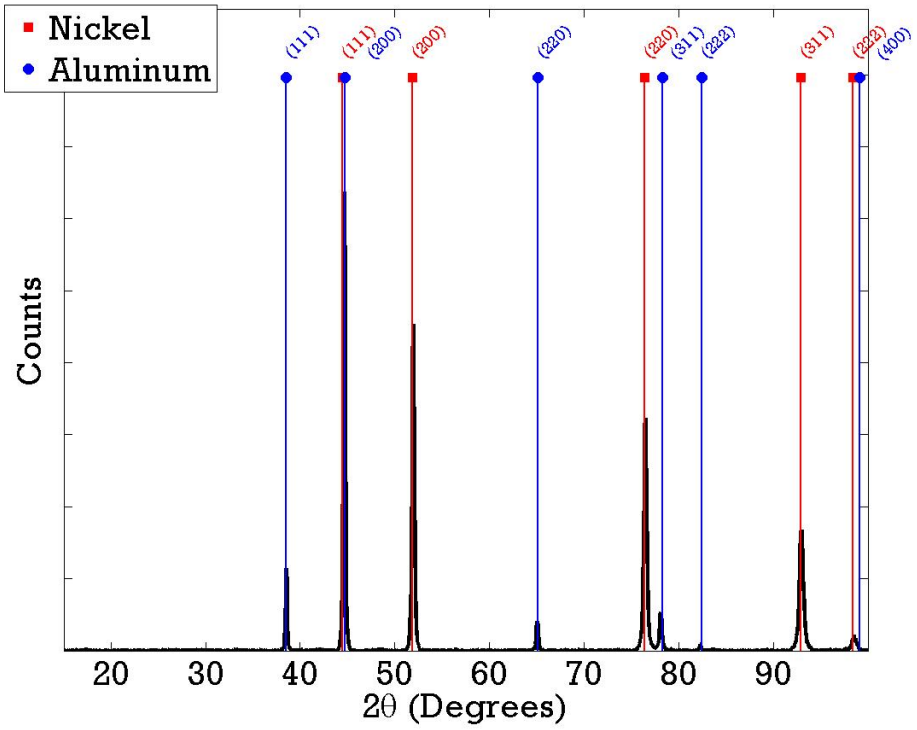

Figure 3.7: XRD trace for the multilayer composite used in this study showing only Ni and Al peaks.

investigations, described later in Chapter 4, and to obtain an estimate of the volume fractions of each phase through point counting [153]. The manually thresholded image is shown in Figure 3.8, and clearly captures the layer heterogeneities. The lighter gray corresponds to the Al, while the darker gray corresponds to Ni. Using this image, the volume fraction of each constituent can be equated to the fraction of pixels representing each phase. Using this method, the volume fractions obtained were 60.7% for Al and 39.3% for Ni.

Since the multilayers are rolled from sheets, the plastic deformation can be treated as volume conserving. This allows the thicknesses of the starting foils to also be used to estimate the volume fraction of each constituent. Using the values given in Section 3.2, the percentages of Al and Ni per volume are estimated to be 58.4% and 41.6%, respectively. The volume fractions from both methods are seen to be similar and suggests that the binary image generated from Figure 3.4 is accurate and representative of the multilayer composite.

Surface area per unit volume, S_V, can be measured in an unbiased manner in an anisotropic microstructure by using the trisector method outlined by Gokhale and Drury [154]. The trisector method enables the estimation of S_V to within an error of 5% with the fewest possible planes and without making any assumptions about the microstructure. The method first involves the determination of a vertical axis in the material, such that at least 90% the surfaces of interest are not aligned with the chosen axis [154]. Three sections containing the vertical axis and oriented 120 degrees apart are then cut into the material. This set of three planes is termed the trisector. On each plane in the trisector, a series of cycloid test lines are placed with their minor axes aligned with the vertical axis. The average intersections per unit length over all of these cycloids test lines, $\bar{P}_L^C$, can then be used to determine S_V with the following equation.

$$S_V = 2[\bar{P}_L^C]_3 \tag{3.1}$$

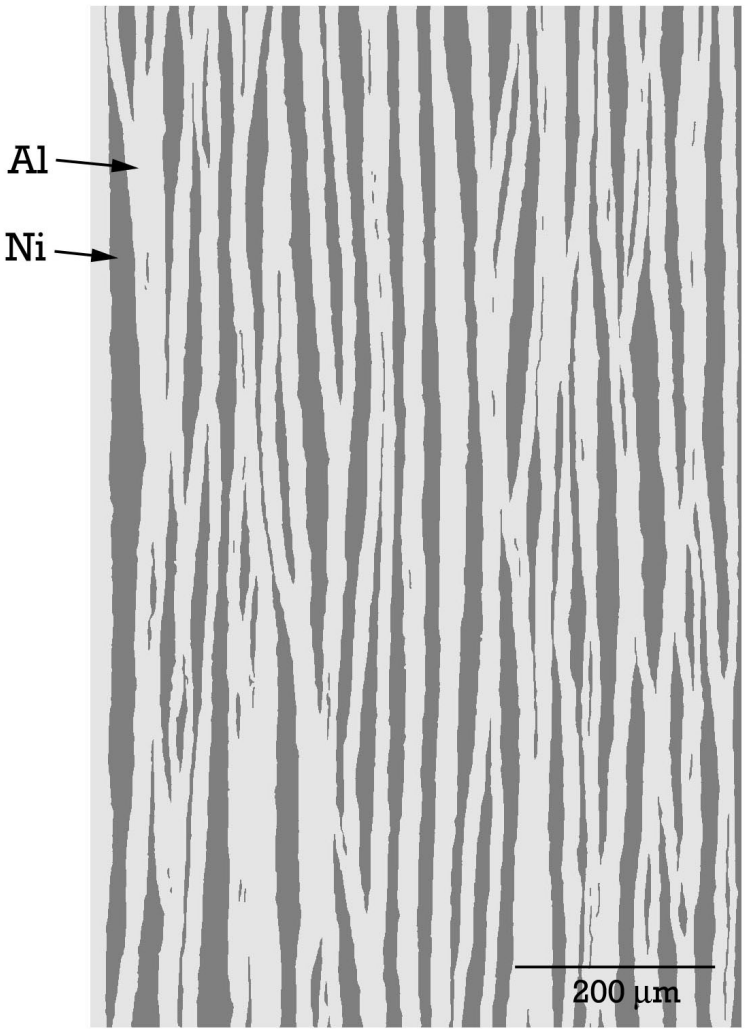

Figure 3.8: Manually sectioned image of the optical micrograph shown in Figure 3.4. The light gray and dark gray areas correspond to Al and Ni, respectively.

Taking the vertical axis for these multilayers along the short transverse direction, S_V, within 5% error, was found to be $S_V = 76.1\frac{1}{mm}$.

Given the laminar nature of the multilayer composites, it is also possible to develop an analytical approximation of S_V [155]. This is accomplished by noting that for every bilayer there are two interfaces. This means that the number of internal interfaces in a laminar structure can be defined as $2N-1$, where N is the number of bilayers. The number of interfaces can then be divided by the thickness, $N\bar{\lambda}$ to obtain S_V [155].

$$S_V = \frac{2N-1}{N\bar{\lambda}} \tag{3.2}$$

This expression is accurate to within 1% for laminar materials with more than 7 bilayers. In the limit of an infinite number of bilayers, S_V is seen to converge to $\frac{2}{\bar{\lambda}}$ [155]. Using this result, S_V for a perfectly layered composite with the same bilayer spacing as the multilayers investigated is 71.4 $\frac{1}{mm}$. This value is lower than that for the cold-rolled multilayers, since the irregularities imparted during rolling increase the surface area. However, this increase is not large, showing that the cold-rolled multilayers are still fairly laminar.

3.3.3 Multilayer Composite Density

The density of the multilayer composite was found by taking Arrhenius density measurements on five individual samples. The Arrhenius method involves the measurement of the material mass in air and submerged in water in order to relate the sample density to that of water.

$$\rho = \rho_{water}\frac{m_{dry}}{m_{dry} - m_{wet}} \tag{3.3}$$

All measurements on the multilayer composites were taken on a scale with 0.001g accuracy. Measurements on five individual samples were obtained yielding a density for the multilayer composites, within 95% confidence, as $\rho_{mult} = 5.300 \pm 0.047\frac{g}{cm^3}$. The measured density can be checked against the volume fraction of the constituents. Assuming the deformation is volume conserving, the starting foil thicknesses can be

used to estimate the composite density as $5.268 \frac{g}{cm^3}$, which is within the error of the measured value.

3.3.4 Multilayer Composite Sound Speed Measurement

The longitudinal and shear wave speeds for the multilayer composite were measured using a Tektronix® DP0 5104 1 GHz digital phosphor oscilloscope and Olympus 5072PR pulser/receiver. The longitudinal sound speed measurements were made with Ultran WC50-2 transducers, while the shear wave measurements were made with Ultran SWC50-5 transducers.

The thickness of the multilayer composites ($\sim 650\mu$m) made direct measurement of the sound speeds difficult. In order to obtain measurements of the wave speeds, the multilayers were adhered to the back surface of a Cu disk with Loctite® Hysol Thin Film Epoxy (RE2038 resin and HD3475 hardener). The Cu disk was lapped flat on both sides and measured to be parallel within ± 0.0005 inches. With the multilayer adhered to the Cu, the difference in the wave transit times between the Cu and multilayer/Cu composite was used to determine the sound speeds in the multilayer.

The transit times through the Cu and multilayer/Cu composite were measured at 4 different locations on two samples. The resulting values for each sample are given in Table 3.3. To obtain an accurate measure of the multilayer sound speeds, the transit time though the epoxy layer must be accounted for. The maximum thickness of the epoxy layer was determined from the measurements of the Cu, multilayer, and multilayer/Cu assembly. This maximum thickness was divided in half to define an average thickness. Consequently, the error associated with the epoxy layer was set equal to the average thickness. This allows for the possibility that the multilayer and Cu are in direct contact at the point of measurement. This necessitated additional measurements to determine the longitudinal and shear wave speeds of the Hysol epoxy: $c_L = 2.442 \pm 0.006 \frac{km}{s}$ and $c_S = 1.177 \pm 0.003 \frac{km}{s}$.

The transit time through the epoxy, t_{epoxy}, was found by dividing the average layer thickness by the corresponding wave speed (*i.e.* either the longitudinal or shear). The wave transit time through the sample was then determined with the relation: $t_{sample} = t_{total} - t_{Cu} - t_{epoxy}$. The wave speeds for the multilayers were then found by dividing the multilayer thickness by the wave transit time.

$$c = \frac{\Delta X_{sample}}{t_{sample}} \tag{3.4}$$

These values are given in Table 3.3, and the errors were found using Equation 5.34 for independent errors given in Section 5.4. Lastly, the two individual measurements were combined to yield a more accurate estimate of the sound speeds, which are given in Table 3.4.

Table 3.3: Measurements for longitudinal and shear sound speeds of the multilayer composite.

	Sample 1	Sample 2
Sample Thickness, ΔX_{sample} (mm)	0.71191 ± 0.01179	0.6581 ± 0.0067
Copper Thickness, ΔX_{Cu} (mm)	2.17348 ± 0.01245	2.0819 ± 0.0066
Epoxy Thickness, ΔX_{epoxy} (mm)	0.01143 ± 0.01143	0.0053 ± 0.0053
Longitudinal Wave		
Transit Time in Cu, t_{cu} (μs)	0.8345 ± 0.008812	0.8115 ± 0.009933
Transit Time in Epoxy, t_{epoxy} (μs)	0.00468 ± 0.00468	0.00217 ± 0.00217
Total Transit Time, t_{total} (μs)	0.9939 ± 0.007422	0.9689 ± 0.01791
Transit Time in Sample, t_{sample} (μs)	0.15472 ± 0.01240	0.1552 ± 0.0206
Longitudinal Wave Speed, $c_L(\frac{mm}{\mu s})$	4.601 ± 0.377	4.240 ± 0.564
Shear Wave		
Transit Time in Cu, t_{cu} (μs)	1.399 ± 0.026	1.367 ± 0.021
Transit Time in Epoxy, t_{epoxy} (μs)	0.00971 ± 0.00971	0.00453 ± 0.00453
Total Transit Time, t_{total} (μs)	1.680 ± 0.022	1.651 ± 0.0150
Transit Time in Sample, t_{sample} (μs)	0.271 ± 0.0354	0.2790 ± 0.0262
Shear Wave Speed, $c_S(\frac{mm}{\mu s})$	2.624 ± 0.345	2.359 ± 0.223

The measured longitudinal and shear wave speeds can be used to obtain the bulk wave speed, c_b, of the multilayer.

$$c_b = \sqrt{c_L^2 - \frac{4}{3}c_S^2} \tag{3.5}$$

In addition, the bulk, K, and shear, G, moduli for the composite can be determined.

$$K = c_b^2 \rho \tag{3.6}$$

$$G = c_S^2 \rho \tag{3.7}$$

The resulting bulk wave speed, bulk modulus, and shear modulus for the multilayer composite are given in Table 3.4.

Table 3.4: Sound speeds and bulk and shear moduli of the multilayer composite.

Longitudinal Wave Speed, $c_L(\frac{mm}{\mu s})$	4.421 ± 0.339
Shear Wave Speed, $c_S(\frac{mm}{\mu s})$	2.492 ± 0.206
Bulk Wave Speed, $c_b(\frac{mm}{\mu s})$	3.356 ± 0.491
Bulk Modulus, K (GPa)	59.694 ± 17.511
Shear Modulus, G (GPa)	32.914 ± 5.449

3.3.5 Multilayer Composite Stiffness Tensor

If a material is assumed to be isotropic and homogeneous, the Young's modulus, Lamé's constant, and Poisson's ratio can also be estimated from the sound speeds. For the multilayered composites investigated, such an assumption can not be made. However, the stiffness tensor of the multilayer can be estimated through effective modulus theory [133, 156, 157], which assumes a layered composite with homogeneous, isotropic layers. Using this assumption, the composite can then be described as a transversely isotropic material.

Postma [157] used effective modulus theory to estimate the stiffness tensor of a composite composted of alternating layers of materials 1 and 2, as shown in Figure

3.9. The resulting stiffness tensor of such a composite is described with the following.

$$\begin{vmatrix} c_{11} & c_{12} & c_{13} & 0 & 0 & 0 \\ c_{12} & c_{22} & c_{13} & 0 & 0 & 0 \\ c_{13} & c_{13} & c_{33} & 0 & 0 & 0 \\ 0 & 0 & 0 & c_{44} & 0 & 0 \\ 0 & 0 & 0 & 0 & c_{44} & 0 \\ 0 & 0 & 0 & 0 & 0 & \frac{1}{2}(c_{11} - c_{12}) \end{vmatrix} \tag{3.8}$$

If the materials are assumed to have thicknesses of d_1 and d_2 and Lamé constants λ_1, μ_1, λ_2, and μ_2, expressions for each stiffness component can be developed [157].

$$c_{11} = \frac{1}{D}\left\{(d_1+d_2)^2(\lambda_1+2\mu_1)(\lambda_2+2\mu_2) + 4d_1d_2(\mu_1-\mu_2)\right\} \\ [(\lambda_1+\mu_1)-(\lambda_2+\mu_2)] \tag{3.9}$$

$$c_{12} = \frac{1}{D}\left\{(d_1+d_2)^2\lambda_1\lambda_2 + 2(\lambda_1 d_1+\lambda_2 d_2)(\mu_2 d_1+\mu_1 d_2)\right\} \tag{3.10}$$

$$c_{13} = \frac{1}{D}\left\{(d_1+d_2)\left[\lambda_1 d_1(\lambda_2+2\mu_2)+\lambda_2 d_2(\lambda_1+2\mu_1)\right]\right\} \tag{3.11}$$

$$c_{33} = \frac{1}{D}\left\{(d_1+d_2)^2(\lambda_1+2\mu_1)(\lambda_2+2\mu_2)\right\} \tag{3.12}$$

$$c_{44} = \frac{(d_1+d_2)\mu_1\mu_2}{d_1\mu_2+d_2\mu_1} \tag{3.13}$$

$$D = (d_1+d_2)\left[d_1(\lambda_2+2\mu_2)+d_2(\lambda_1+2\mu_1)\right] \tag{3.14}$$

For the multilayer composites used in this work, the average thickness of the Al and Ni layers can be estimated from the bilayer spacing and volume fractions found in Sections 3.2 and 3.3.2. Choosing Al as material 1 and Ni as material 2, d_1 and d_2 can be defined as 16.35 and 11.65 μm, respectively. Using the values given in Table 3.1 and assuming the layers are homogeneous, isotropic materials, the Lamé constants for Ni and Al 5052 can be estimated as $\lambda_1 = 49.1$ GPa, $\lambda_2 = 199$ GPa, $\mu_1 = 26$ GPa, and $\mu_2 = 76$ GPa . Estimates of the stiffness tensor components for the multilayer composite can then be calculated and are listed in Table 3.5.

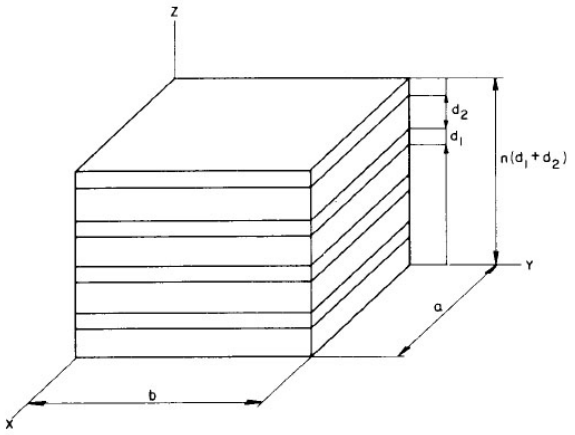

Figure 3.9: Volume element of uniformly layered composite of materials 1 and 2 [157].

Table 3.5: Theoretical stiffnesses of the multilayer composites based on effective modulus theory.

c_{11} (GPa)	c_{12} (GPa)	c_{13} (GPa)	c_{33} (GPa)	c_{44} (GPa)
183	90	75	144	36

No effort was made in this work to experimentally verify the stiffnesses given in Table 3.5. There have been some quasi-static tensile tests performed on the cold-rolled multilayer composites by Vitali *et al.* [126], but that work yielded no reliable measurement of the elastic modulus. The quasi-static experiments performed by Vitali *et al.* [126] were on the longitudinal and short transverse directions of two different cold-rolled multilayer composites: the composite investigated in this work (thicker bilayer) and a composite with a bilayer spacing of $\sim 5\mu m$ (thinner bilayer). The setup used for these tests is shown in Figure 3.10, while the results obtained are shown in Figure 3.11.

It can be seen from the quasi-static tensile tests that, in the longitudinal direction, the materials exhibit limited plastic deformation in both composites (red and black lines). In the transverse direction, the material exhibits what appears to be extensive plastic deformation. This deformation actually results from the gradual delamination

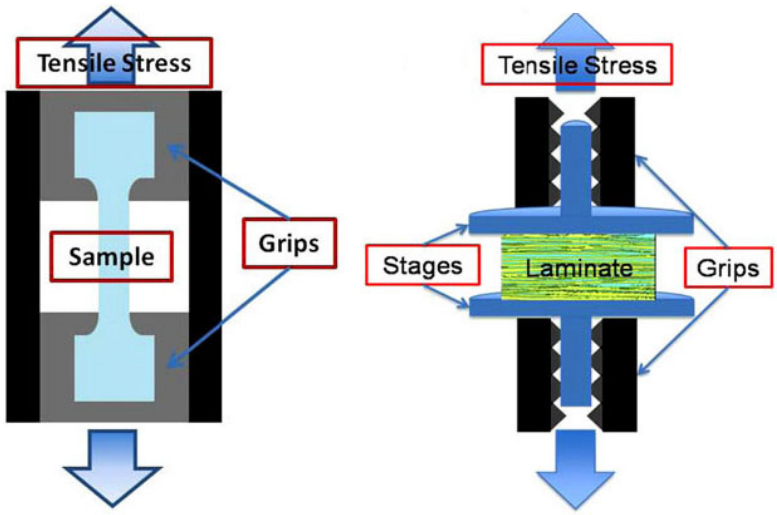

(a) Longitudinal (b) Short Transverse

Figure 3.10: Schematic of the (a) longitudinal and (b) short transverse quasi-static tensile tests performed on the multilayer composites [126].

of the composite. Additionally, the experiments show that the thinner bilayer composite exhibits lower failure stresses than the thicker bilayer composite in the short transverse direction. This can be attributed to the higher defect concentrations in the thinner bilayer composite as a result of the additional rolling cycles.

3.3.6 Effective Strain Hardening of Multilayer Composites

Cold-rolling the multilayers imparts a large amount of strain hardening during fabrication. To meaure this strain hardening, fifteen Vickers hardness measurements, using a 25g load, were take in the individual layers of Ni and Al to estimate the work hardening of each constituent. The hardnesses measured for Ni and Al, within 95% confidence, were 262 ± 30 HV and 144 ± 16 HV, respectively. The relatively high error in the measurements stems from the non-uniform deformation of the materials during rolling.

The hardness of each material can be used to estimate the work hardening of each material in terms of a change in yield strength through the following relation.

$$\sigma_y = \frac{1}{3} HV(MPa) \tag{3.15}$$

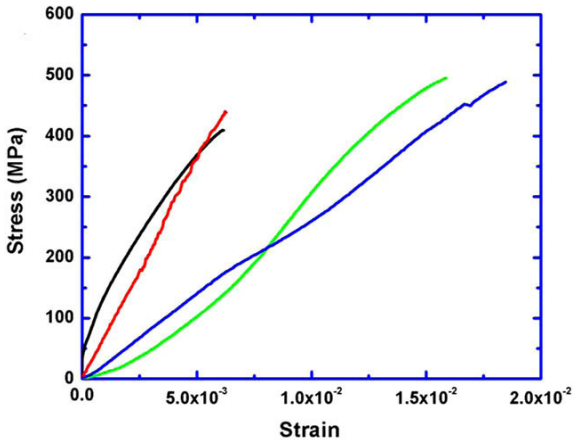

(a) Longitudinal

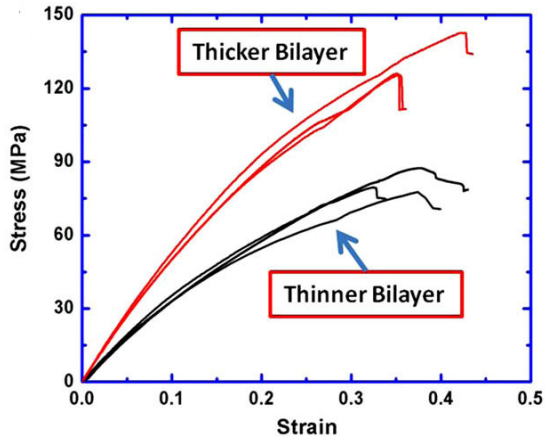

(b) Short Transverse

Figure 3.11: Stress vs. strain curves for the (a) longitudinal and (b) short transverse directions of the multilayer composites obtained through quasi-static tensile tests [126]. In the longitudinal direction, both the thick (red) and thin (black) multilayers are seen to endure little deformation. No identification was given for the two sets of longitudinal curves (green and blue) by Vitali *et al.* [126]. In the short transverse direction, both the thick and thin multilayers undergo delamination until failure. In addition, the smaller bilayer spacing is seen to exhibit a lower failure stress due to higher defect concentrations.

Here, $HV(MPa)$ is the measured hardness in MPa. The yield strength determined for Ni was 856.45 ± 98.07 MPa, while that for Al was 469.84 ± 52.30 MPa. Modeling the strain hardening with the Steinberg-Guinan-Lund model described in Section 2.3, the yield strength can be used to estimate the strain in each material. For Al, the strain is estimated as 1.15, while for the Ni it is 0.64.

3.4 Determining the Representative Volume Element of the Multilayer Composites

When modeling a heterogeneous microstructure, like the one shown in Figure 3.4, it is important to determine the minimum computational domain necessary to statistically represent the features of interest. Heterogeneous microstructures contain a variety of points, lines, and volumes with various orientations, spatial distributions, and locations. It is necessary to accurately capture the statistical variation of these features in any computational domain.

The spatial statistics of a microstructure can be found through various techniques, such as n-point correlation functions [158], lineal path distributions [159], or nearest neighbor distributions [160]. Another technique that has been applied for the efficient determination of the representative volume element (RVE) for a binary, two-dimensional, heterogeneous microstructure is the multi-scale analysis of area fractions, or MSAAF, technique developed by Spowart *et al.* [161]. This method determines the length scale necessary to statistically capture the variation in material area fractions, termed the homogeneous length scale, L_H. This ensures that any square domain equal or larger in size than L_H is representative, regardless of where that domain is chosen.

The MSAAF technique is based on Poisson statistics and divides the microstructure into smaller sub-areas, termed quilt areas, of dimension Q to determine the homogeneous length scale. Computationally, this is achieved by essentially coarsening the microstructure image. After dividing the image into quilt areas, the image is re-sampled by averaging the pixel values in each quilt area. This essentially creates

a larger pixel with a value equal to the area fraction of that quilt area. This process is repeated with continually increasing quilt areas, as shown in 3.12a.

Since the quilt area values are determined from the area fraction, the variation in their values can be used to determine the homogeneous length scale. The quilt dimension, Q, at which the variation in quilt area values drops below an acceptable tolerance represents the homogeneous length scale. Often times, the image used is not large enough to be divided into representative quilt areas. To solve this problem, a MSAAF plot can be used, which compares the variation in quilt area values normalized by the total phase area fraction, $\frac{\sigma_{A_f}}{A_f}$, against the quilt dimension, Q, on a log-log scale. An example MSAAF plot is shown in Figure 3.13.

The MSAAF plot data can be fit with the following equation [162].

$$\frac{\sigma_{A_f}}{A_f} = \frac{1}{\sqrt{\frac{A_f}{1-A_f} + \alpha(Q-1)^{-2*\xi}}} \tag{3.16}$$

In the above equation, α and ξ are fitting parameters and Q is expressed in pixels. This equation can also be expressed in linear dimensions, by defining a length per pixel, χ.

$$\frac{\sigma_{A_f}}{A_f} = \frac{1}{\sqrt{\frac{A_f}{1-A_f} + \alpha^*(Q-\chi)^{-2*\xi}}} \tag{3.17}$$

$$\alpha^* = \frac{\alpha}{(\chi)^{-2*\xi}} \tag{3.18}$$

With this equation, the data can then be extrapolated to larger quilt dimensions, allowing for easy determination of the homogeneous length scale for any desired tolerance, as shown in Figure 3.13.

The isotropic MSAAF technique described above is ideal for particles in a matrix. For laminar materials, that exhibit periodic microstructures, the direction MSAAF technique developed by Tschopp *et al.* is more appropriate [162]. The directional technique follows the same procedure as the isotropic method except that the subareas are lines not squares. The lines are oriented at 0 and 90 degrees in order

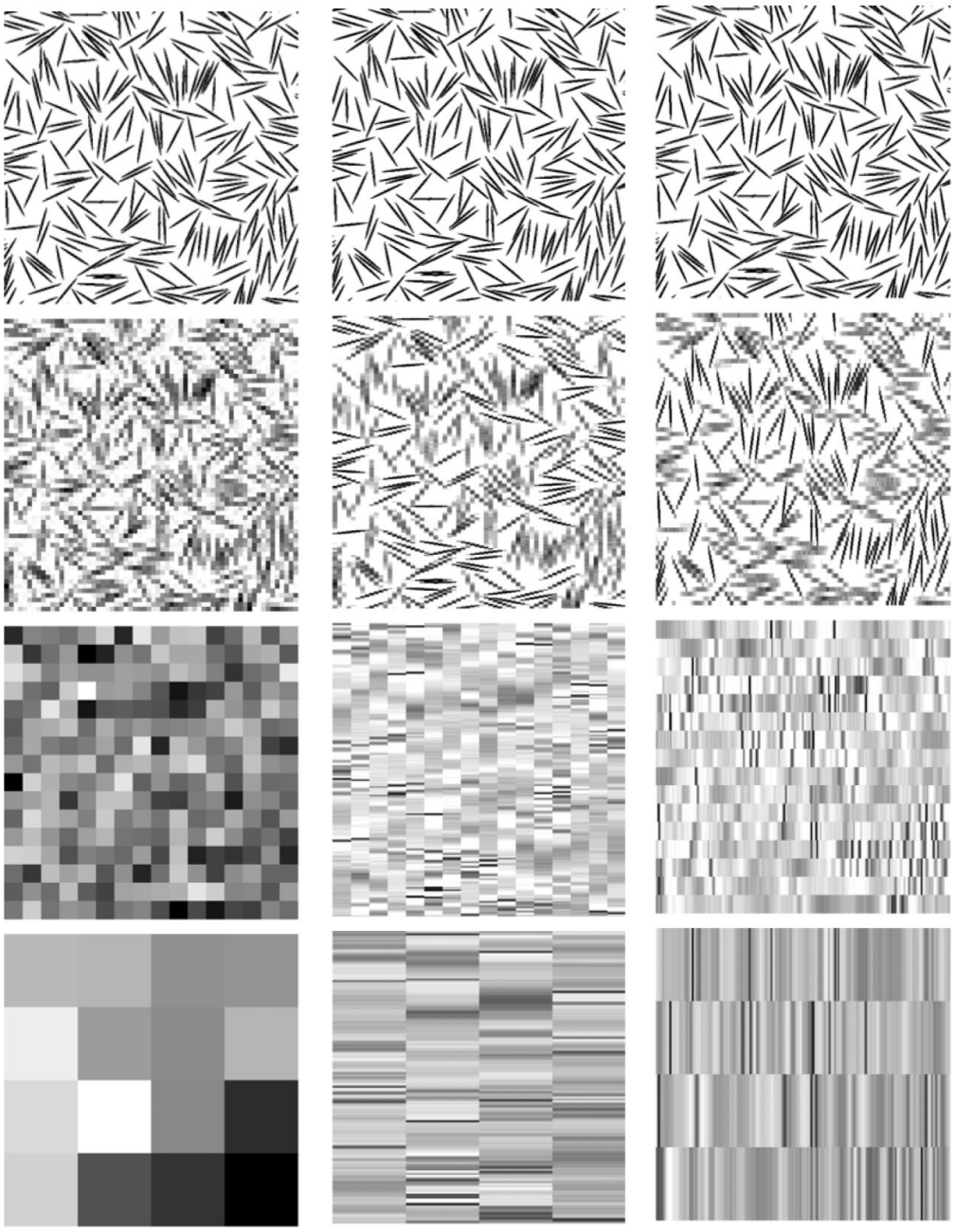

(a) Isotropic (b) X Directional (c) Y Directional

Figure 3.12: Graphical representation of the isotropic (a), X directional (b), and Y directional (c) MSAAF techniques [162].

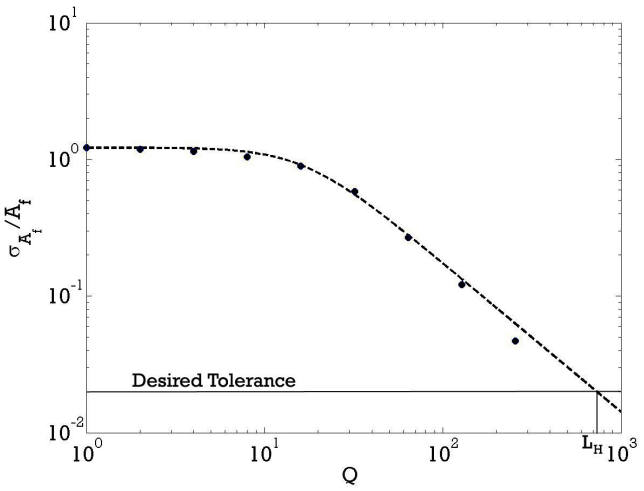

Figure 3.13: Typical MSAAF plot used to determine the homogeneous length scale of a microstructure.

to determine the homogeneous length scales of the microstructure in both the x and y directions. This essentially finds the 1D homogeneous length scale of the microstructure in the x direction (Figure 3.12b) and the y direction (Figure 3.12c).

For the multilayer composites, the directional MSAAF technique applied perpendicular to the layers is the most appropriate way to determine the RVE of the microstructure, due to the periodicity. If applied parallel to the layers, the results would not converge, yielding an infinite L_H. This lack of convergence parallel to the layers also leads to unreasonably large L_H values for the isotropic MSAAF technique. As a result, the only meaningful homogeneous length scale for layered media is that perpendicular to the layers, which, due to the periodicity, can be expressed solely in terms of bilayers.

The periodicity of the multilayers also enables an analytical estimation of L_H. In the case of an idealized multilayer with uniform layering, the microstructure becomes 1D. The homogeneous length scale is then the number of bilayers necessary such that adding one additional material layer changes the area fractions by less than the desired error. Consider a multilayer of two components with thicknesses, t_1 and t_2. The bilayer spacing in this multilayer is then $\lambda = t_1 + t_2$, and each bilayer has a

constant area fraction. The homogeneous length scale for material 1 can then be found with the following equation.

$$\frac{\sigma_{A_f}}{A_f} = \frac{Nt_1}{(N-1)\lambda + t_1} - \frac{t_1}{\lambda} \tag{3.19}$$

In the above equation, each point is taken at the center of the bilayer and N is the number of bilayers already considered. Given a specific tolerance in the area fraction, $\frac{\sigma_{A_f}}{A_f}$, Equation 3.19 can easily be solved for the number of bilayers necessary, N. Equation 3.19 can also be easily changed to determine the length scale of material 2 by switching t_2 for t_1.

Both the directional MSAAF technique and the analytical solution were used to characterize the number of bilayers necessary to accurately represent the multilayer composite. The application of the directional MSAAF technique perpendicular to the layers (x direction) was done on a 512 x 512 pixel (341μm x 341μm) image for both the Ni and Al phases. The analytical solution was solved assuming an Al thickness of $t_1 = 17\mu$m and a Ni thickness of $t_2 = 11\mu$m. The length scales with a 10% and 1% variation in area fraction along with the fitting parameters used for Equation 3.17 are presented in Table 3.6.

Table 3.6: The homogeneous length scale perpendicular to the layers found using the directional MSAAF technique and analytical solution.

	Directional MSAAF				Analytical	
	$L_{H_x}(0.1)$	$L_{H_x}(0.01)$	α^*	ξ	$L_{H_x}(0.1)$	$L_{H_x}(0.01)$
Al	2.8λ	24.6λ	0.01736	-0.9559	2.8λ	24.2λ
Ni	4.1λ	35.7λ	0.00809	-0.9520	3.0λ	24.5λ

The analytical method is shown to provide a fairly accurate estimate of the length scale necessary to represent the microstructure when compared to the directional MSAAF technique, particularly for Al. This was attributed to the higher volume fraction and more uniform layering of the Al, which extend over the whole microstructure. The necking in the Ni, due to rolling, broke those layers into essentially long,

elongated particles. This causes the geometry of the Ni layers to deviate more from the 1D ideals of the analytical solution than Al. As a result, the analytical solution is seen to under predict L_H for Ni. However, the deviation is not too large, and the analytical method can be used as a first approximation for the composite RVE.

Previous work on these cold-rolled multilayer composites has shown that the longitudinal cross-section of the microstructure has similar characteristics regardless of the number of rolling cycles endured [143]. This fact enables microstructures with differing bilayer spacings to be treated as scaled version of each other, with L_H scaling accordingly. Consequently, the number of bilayers necessary to statistically represent the microstructure does not change with bilayer spacing. This fact is used in Section 4.2, when investigated the effect of interfacial density on the shock compression response of the cold-rolled multilayers.

3.5 Fully Dense Ni/Al Particle Composites

In addition to Ni/Al multilayer composites, the shock compression response of a fully dense powder compact of Ni and Al was also investigated. The fully dense powder composite and its nearly isotropic microstructure of roughly spherical particles provides a bridge for comparison between the multilayer composites and the past work on distended powder compacts.

Fully dense composites of Ni and Al powders were generated through shock consolidation. The experimental assembly for this has been extensively characterized [163, 164] and is shown in Figure 3.14. High purity (99.8%), elemental, -325 mesh powders with a spherical geometry were mixed in an equivolumetric ratio [165]. The powder was loaded in stages into the center tube of the compaction fixture to avoid a gradient in the compact density. A larger steel cylinder was then placed around this, creating a two walled structure. Ammonium nitrate/fuel oil (ANFO) explosive, with a detonation velocity of 2.6 km/s, was then used to accelerate the outer cylinder into

the inner cylinder at $\sim$ 300 m/s to compact the powder [165]. The Al mandrel in the center is used to ensure that no powder is subjected to the high pressure Mach stem, which can cause material failure and induce reaction [163, 164].

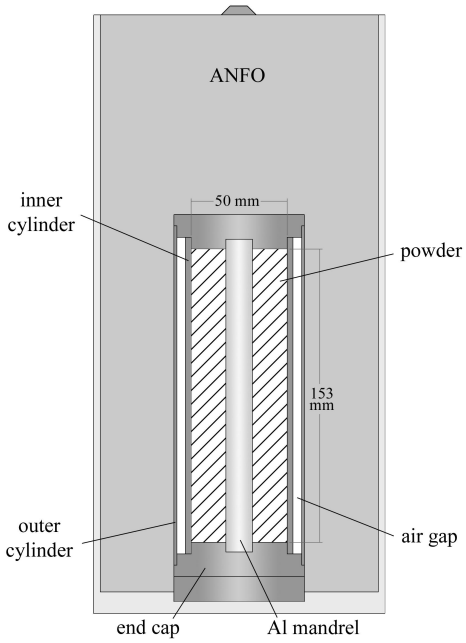

Figure 3.14: Schematic of the shock compression cylinder [165].

An optical micrograph of the shock compacted Ni/Al microstructure taken from the top of the compact is given in Figure 3.15. The compaction process is seen to generate a microstructure consisting of Ni particles suspended in an Al matrix. The areas in Figure 3.15 out of focus correspond to pull-out of the Ni particles during polishing. These particles were artificially inserted during the creation of a binary image of the compact to more accurately represent the true volume fraction of constituents.

Similar to the multilayer composites, various material parameters of the shock compacted microstructure were measured to quantify the composite characteristics. The density of the shock compacted composite has a slight variation over the height of the compact, but, for the top section, where Figure 3.15 was taken, it has been previously reported as 5.527 g/cm^3 [165]. Using a binary image of Figure 3.15, the volume fraction of the constituents, compensating for particle pull-out, was found

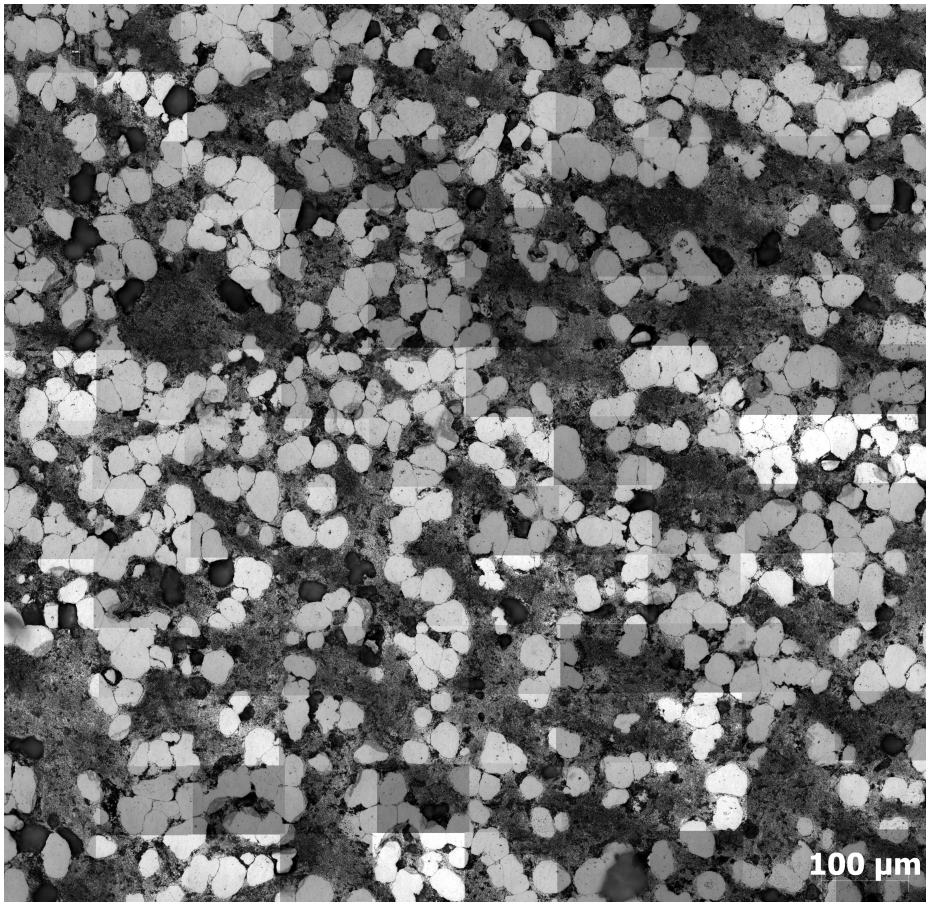

Figure 3.15: Optical micrograph of the shock compacted microstructure showing spherical Ni particles in an Al matrix.

to be 55.26% for Al and 44.74 % for Ni. The compact is not equivolumetric as intended, but has a composition that lies between equivolumtric and stoichiometric. The isotropic MSAAF technique, described in Section 3.4, was used to determine the homogenous length scale of the shock-compacted composite as $\sim 400\mu m$. Lastly, hardness measurements were taken to characterize the strain hardening induced in each material during compaction. Using a 10g load, the yield strength of Al and Ni were measured to be 129.84 ± 26.77 and 840.10 ± 127.51 MPa, respectively.

CHAPTER IV

COMPUTATIONAL INVESTIGATION

The analysis described in this chapter uses parallel, two-dimensional computations to understand the structure of a propagating shock wave in cold-rolled Ni/Al multilayer composites. The non-uniformity of layering in the multilayer composites presents a complex microstructure with deviations in the periodicity of the system. Hence, the analysis of the effect of these heterogeneities on the propagation of a shock wave is complicated and lends itself to the use of two-dimensional computations. This chapter focuses on the effect of various microstructural changes in the multilayered composites on the dissipation and dispersion of a shock wave. In particular, microstructural aspects controlled through fabrication and implementation are investigated. First, the effects of interfacial orientation on the resulting shock compression response are discussed. Building on these results, the chapter then examines the effects of interfacial density, interfacial structure, interfacial strength, and material strain hardening on the propagating shock wave. Lastly, the response of a shock compacted composite is presented for comparison to the multilayer composites.

4.1 Effect of Orientation on the Shock Compression Response of Cold-Rolled Multilayers

In this section, the effect of 0^o, 45^o, and 90^o interfacial orientations with respect to the direction of shock wave propagation on the local pressure, temperature, and strain response during shock compression is investigated. The material response is then related to different microstructural factors affecting the shock wave propagation through the multilayered material. The results show that the orientation of the layers with respect to the direction of shock front propagation and the heterogeneities

introduced through cold-rolling have a marked effect on the overall shock compression response of the multilayered composite system.

4.1.1 Computational Methodology and Microstructure Generation

The microstructure of the multilayered Ni/Al composite, shown in Figure 3.8, was imported into the multi-material, finite volume, Eulerian hydrocode CTH, developed by Sandia National Laboratories [88], using a MATLAB code. The MATLAB code was developed specifically to incorporate real, heterogeneous microstructure into CTH, and is described in Appendix B. This method of microstructure importation has proven to be very reliable and efficient for clearly capturing the heterogeneous nature of the individual layers, while maintaining the area fraction of the constituents to within an error of ± 2% (*i.e.* $\frac{\sigma_{V_V}}{V_V} \leq 0.02$).

Simulations were performed on three orientations of the layers relative to the direction of the shock front propagation: a) 90 degrees (to be referred to as the "perpendicular orientation"), b) 45 degrees (to be referred to as the "angled orientation"), c) 0 degrees (to be referred to as the "parallel orientation"). The CTH renderings of each orientation investigated are seen in Figure 4.1 and clearly capture the heterogeneities in the system. The different orientations were created by simply rotating of the original multilayer composite micrograph. To facilitate the rotation, an enlarged microstructure was created by artificially extending the original microstructure. Due to the periodicity of the multilayer composite, it was assumed that extending the microstructure would not appreciably alter the overall response.

The area fractions of the reactants in the CTH rendering are $\sim$ 39% Ni with the remainder essentially all Al. The perpendicular simulations do include void space with a total area fraction of $\sim$ 0.25%. Given its extremely low area fraction, the void space was assumed to have little effect on the results and was removed for the parallel and angular orientations. The surface areas per unit volume of the CTH renderings

were also calculated by finding the length per unit area, L_A, of the microstructure, which is the total perimeter of all the Ni layers divided by the domain area. This can then be related to S_V with the following relation [155].

$$S_V = \frac{4}{\pi} L_A \tag{4.1}$$

Here, $\frac{4}{\pi}$ is a geometric term that compensates for the random orientations of the surfaces to the sectioning plane. For the multilayers, the interface orientations are not random and are all roughly perpendicular to the sectioning plane, making the multilayer microstructure essentially 2D. This means that for the multilayers the geometric term does not apply, and S_V is equal to L_A. The S_V found for the CTH rendering was $79.2 \frac{1}{mm}$. This value matches closely to that found in Section 3.3.2, and helps prove the method of microstructural incorporation into CTH is accurate.

Impact by a semi-infinite copper piston from the left of the multilayer composite, shown in Figure 4.1, was modeled at five different impact velocities: 500, 750, 1000, 1250, and 1500 m/s. The multilayer constituents were modeled as Al 1100 (*i.e.* commercially pure) and pure Ni, while the piston was modeled as pure Cu. Al 1100 was found to provide an excellent approximation of Al 5052 in both the equation of state and constitutive behavior in the rolled state. The rational behind this choice is elaborated on in Section 4.1.1.1 to follow. The EOS responses for all the materials were modeled using the Mie-Grüneisen equation of state. For the constitutive behavior of Cu, the Johnson-Cook model [94] was used assuming an essentially infinite yield strength. This ensured the Cu impactor was rigid and provided a smooth impact surface without any spurious wave phenomena, which can occur when specifying a moving reflective boundary condition. For Ni and Al, the Steinberg-Guinan-Lund [95] model was chosen to represent their constitutive behavior. To account for the work hardening imparted during cold-rolling, the yield strengths of the layers were changed to the values given in Section 3.3.6. The yield strengths of each material were the only model parameters, either EOS or constitutive, not taken from the CTH

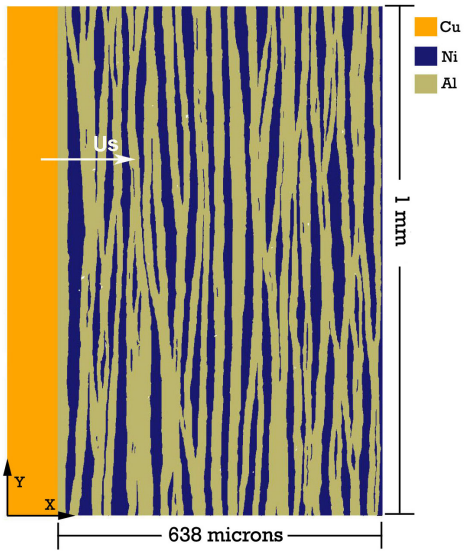

(a) Perpendicular Orientation

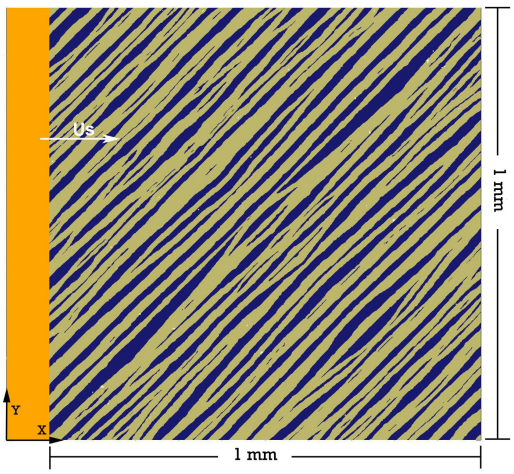

(b) Angled Orientation

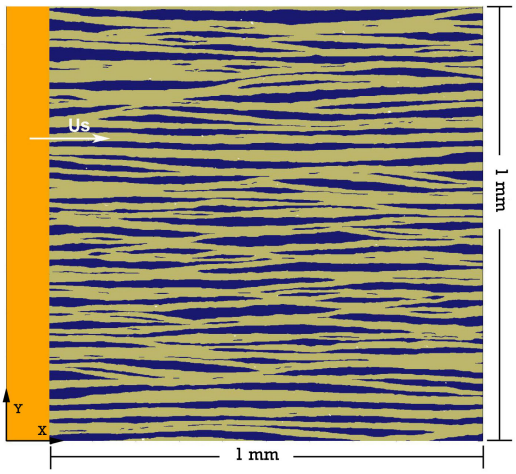

(c) Parallel Orientation

Figure 4.1: Perpendicular (a), angled (b), and parallel (c) oriented multilayer composites showing the Al and Ni layers along with the Cu piston used to generate a shock wave propagating in the positive x direction.

database [88].

Stress based fracture was modeled for both the Al and Ni. This simplified approximation was assumed to be sufficient, since both materials are FCC and no significant tensile stresses are expected in the simulations. Additionally, heat conduction for each material was incorporated through tabular data to more accurately describe the shock heating.

A square mesh was chosen for all simulations. The mesh resolution was found to converge at a resolution of 0.8 μm/cell. This gives an average of approximately 17 cells across each layer. The mesh size was graded from 0.8 μm/cell to 2 μm/cell in the Cu impactor. This was done to save computational resources and ensure that there would be not spurious reflections at the impactor/sample interface due to large aspect ratio changes in the cells. Periodic boundary conditions were used along the boundaries in the y-direction, while the boundaries in the x-direction were modeled as sound speed-based absorbing to approximate semi-infinite materials.

In order to understand the bulk shock compression response of the multilayer composites as a function of the various orientations, the particle velocity (U_P) and shock velocity (U_S) relationships were determined. The particle velocity can not be obtained from the specified impact velocity, since it is not constant and controlled by the impedance mismatch (*i.e.* conservation of momentum) between the impactor and sample. Hence, to obtain the particle velocity, 10 Lagrangian tracer points were located along a plane 20 μm from the impact face in the Cu driver. The particle velocity was found by determining the average steady state velocity of the tracer points through the duration of the simulation. This allowed for determination of the particle velocity to within a standard deviation of roughly $\pm$ 1%. The location of the tracer points was found not to affect the results, since simulations performed with tracer points on the impact plane yielded identical velocities.

To determine the shock velocity, a MATLAB script was used to obtain an average

pressure along the length (at each x location) of the multilayer composite, referred to as a pressure trace. Example pressure traces are shown in Figure 4.2. The shock front was first identified by finding the location in the pressure curve considered to be above the noise of the simulation, chosen in this work to be 0.1 GPA. The MATLAB script then located the shock wave peak and impact face in order to calculate the steady state pressure by averaging the pressure values in that interval. To obtain a more accurate answer, the first and last 15% of this interval was excluded to remove any oscillatory behavior at the shock peak and impact face. Locations in the rise corresponding to 25%, 50%, and 75% of the steady state pressure were identified and tracked every 20 ns of the simulation. This process is shown graphically in Figure 4.2, which shows the tracking of each of these features at 80 and 100 ns after impact. Comparing the 25%, 50% and 75% values in the rise at each time interval gave three measures of the shock velocity. An average of all of these shock speeds was used to determine the shock velocity for each simulation. The MATLAB script used for these U_S calculations is provided in Appendix C.

The first value was taken at 25% to exclude any elastic precursor present in the response. In addition, intervals of 20 ns were chosen to smooth out any variation due to mesh resolution. At a shock velocity of 4 km/s, the shock wave travels 80 μm in 20 ns. Given the resolution of the simulations, this corresponds to 100 cells. As a result, the discritization of the pressure values to the cell centers generates an error in the shock front location of less than 1%.

The above method gave very good results for the perpendicular and angled configurations. However, it did not work well for the parallel configuration, due to extensive two-dimensional effects which lead to large amounts of dissipation and dispersion. The dispersion and dissipation smear the shock front, leading to changes in the shock velocity as the wave propagates through the composite. As a result, the shock velocity measured depends on which point in the rise is chosen. In order to

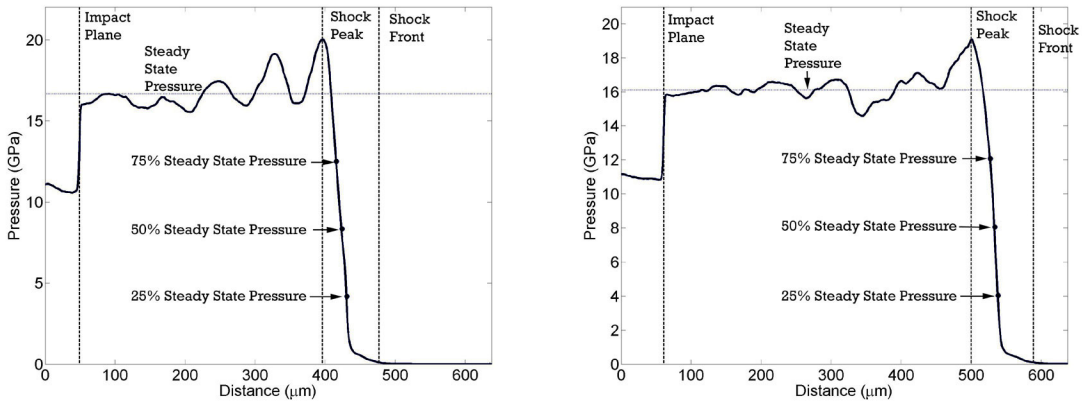

(a) Pressure Trace 80 ns After Impact

(b) Pressure Trace 100 ns After Impact

Figure 4.2: Pressure traces 80 ns (a) and 100 ns (b) after impact with the locations of the shock front, shock peak, and impact plane labeled. The pressure values between the shock peak and impact plane are averaged to obtain the steady state pressure, which is also labeled. Points corresponding to 25, 50, and 75% of the steady state pressure in the shock rise are then located at each time interval to determine the shock velocity.

facilitate comparison, a consistent point needed to be used. For that reason, a wave front velocity, U_W, corresponding to 25% of the steady state pressure was chosen for defining the bulk parameters of the parallel configuration. While this single metric can not represent all of the complexities occurring in the shock front, it does allow for comparisons to the perpendicular and angled configurations, since their calculated shock and wave front velocities were similar.

To further understand the differences between the characteristics of shock wave propagation in each configuration, simulations were preformed with increased resolution to capture the interfacial effects on shock wave propagation. This was done with adaptive mesh refinement (AMR) to resolve a small section in the center of the multilayer to a resolution of ~ 200 nm per cell, while the resolution of the multilayer outside this window was kept at 0.8 μm per cell for consistency. All of these simulations were run with an impact velocity of 1000 m/s and contained Lagrangian tracers in each phase to capture the individual material responses.

4.1.1.1 Comparison Between the EOS and Constitutive Behavior of Al 5052 and Al 1100

The decision to use Al 1100 for the multilayer composite simulations was made after careful consideration. The EOS responses of various Al alloys are not significantly different (*i.e.* all parameters are within a few percent), which makes Al 1100 an appropriate choice for the EOS response of Al 5052. However, determining if Al 1100 was an acceptable analog for the constitutive behavior of Al 5052 needed further analysis.

In order to determine if a modified Al 1100 strength model would be an appropriate choice for Al 5052 H19, the alloy behaviors were compared using the Steinberg-Guinan-Lund [95] formulation. Recall, the Steinberg-Guinan-Lund model is dependent on density, temperature, strain, and strain rate. For this comparison, only the strain hardening section of the model needs to be analyzed for two reasons:

- The temperature dependence of the yield strength does not very significantly between Al alloys.
- A rate independent model was used.

The stress-strain behavior of Al 5052 O is shown in Figure 4.3. Since Al 5052 H19 is only strain hardened and not heat treated, it is assumed that the yield behavior follows that of Al 5052 O. The only change expected is in the initial yield point. Using the curve in Figure 4.3, the strain hardening can be described using the first component of Equation 2.94, assuming $\epsilon_i = 0$.

$$\sigma_Y = \sigma_{Y_0}[1 + \beta\epsilon]^n \tag{4.2}$$

The fit obtained for Al 5052 O gives $Y_0 = 70.23MPa$, $\beta = 270.2$ and $n = 0.3309$.

The only thing now left to consider is the influence of the cold working endured by the Al during fabrication on its constitutive response in the simulations. The cold

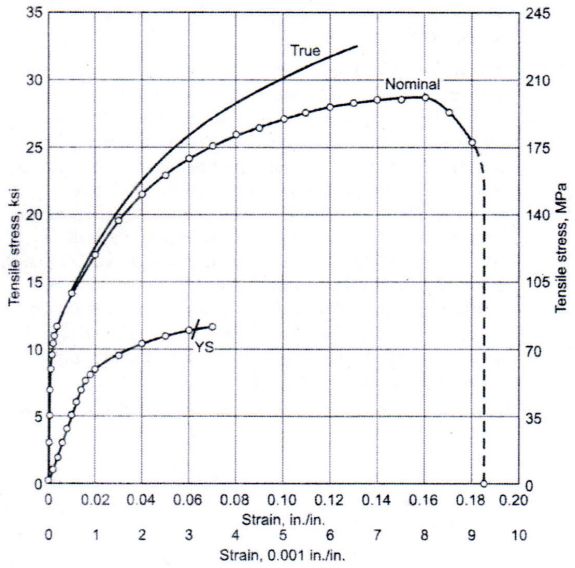

Figure 4.3: Stress vs. strain curve for Al 5052 O [166].

working increases the starting yield strength and significantly decrease the amount Al strain hardens in the simulation. The Steinberg-Guinan-Lund model imposes a maximum yield strength achievable by a material through strain hardening, which, for Al alloys, is assumed to be around 500 MPa. Given the initial yield strength estimated as 470 MPa through hardness measurements, as described in Section 3.3.6, the Al 5052 is essentially already strain hardened to its limit. Using Equation 4.2, the maximum amount of additional strain expected for both Al 5052 and Al 1100 under such conditions is ~ 0.003 and the yield strengths of each alloy over this range differ by less than 1%. Simulations with a maximum yield strength of 1 GPa were performed to investigate this limit in the strain hardening, and essentially identical results were obtained. From these considerations, it was concluded that the choice of the Al 5052 constitutive model is not crucially important and can be accurately modeled as Al 1100, or any other Al alloy.

4.1.2 Perpendicular Configuration

Prior work of Oved *et al.* [124], Lundergran and Drumheller [123], Barker [128], and Zhuang *et al.* [125] has conclusively shown that shock wave propagation through a perpendicularly oriented, uniform multilayer composite produces a steady pressure response with oscillatory behavior. The oscillations result from multiple wave interactions generated by the material interface and are controlled by the material impedances and thicknesses [141]. The oscillations are dispersive and diminish over time, but the initial wave structure remains periodic during its propagation through the multilayer composite, making it a steady wave. The cold-rolled multilayer composites are not uniform in terms of their inter-layer characteristics like the composites used in these past studies. These non-uniformities in the composite structure produce complex wave interactions that affect the overall shock compression response.

The simulation performed at an impact velocity of 1000 m/s, corresponding to a particle velocity of 597 m/s, was used to illustrate the effects of these non-uniformities on a shock front propagating perpendicular to the composite layers. The pressure response under these conditions at 80 ns and 100 ns after impact is shown in Figure 4.4. The corresponding pressure traces showing the average, maximum, and minimum pressures across the composite are given in Figure 4.5. The shock wave is seen in Figure 4.5 to have an equilibrium pressure around 16.7 GPa and a rise time of about 15 ns. The pressure response is seen to fluctuate around this equilibrium value in a random fashion. These fluctuations occur not only in space, as seen in Figure 4.4, but also in time. In addition, the perturbations diminish quickly, which is easily seen by comparing Figures 4.5a and 4.5b.

While the cold-rolled multilayer composites exhibit similar oscillatory behavior seen in past experimental investigations [123, 125, 124, 128], the non-uniformity of the layers causes variability and faster attenuation of the oscillations. These heterogeneities in the layering induce perturbations in the transverse direction which tend

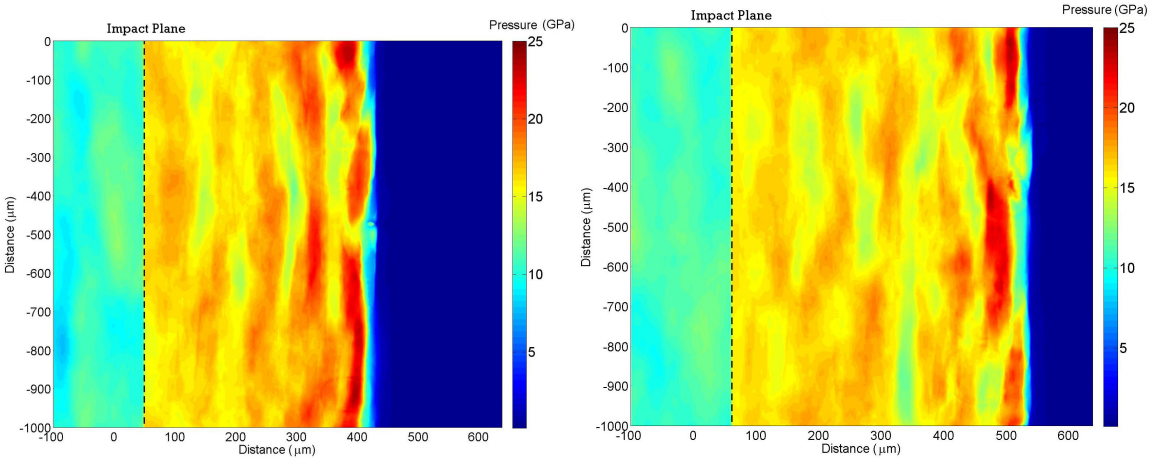

(a) Pressure Profile 80 ns After Impact

(b) Pressure Profile 100 ns After Impact

Figure 4.4: Pressure profiles at 80 (a) and 100 (b) ns after impact at 1000 m/s illustrating that the high-pressure areas are not periodic and fluctuate in time and space.

to carry away the oscillatory behavior of the initial wave train. This leads to the development of a quasi-steady shock wave in the multilayers, which no longer has the periodic, predictable oscillations of a steady shock wave.

The simulation on a uniformly layered multilayer composite with identical bilayer spacing, constituent ratio, and material properties can be used to further highlight the effect of these non-uniformities. The one-dimensional pressure response obtained in the same manner 180 ns after impact at 1000 m/s in the idealized, uniformly layered multilayer composite is shown in Figure 4.6. In these simulations, the maximum, minimum, and average pressures are identical, due to the idealized, 1D nature of the microstructure. While the oscillations observed in the shock wave are non-uniform, they are periodic with deviations remaining in consistent locations along the multilayer composite. This means the uniformly layered composite supports a steady wave, similar to previously obtained experimental results [124, 123, 128, 125].

The computed shock properties of the uniform multilayer composite are similar to those of the non-uniform multilayer composite, except for the rise time. This suggests that the non-uniformities greatly affect the structure of the wave, which can lead to

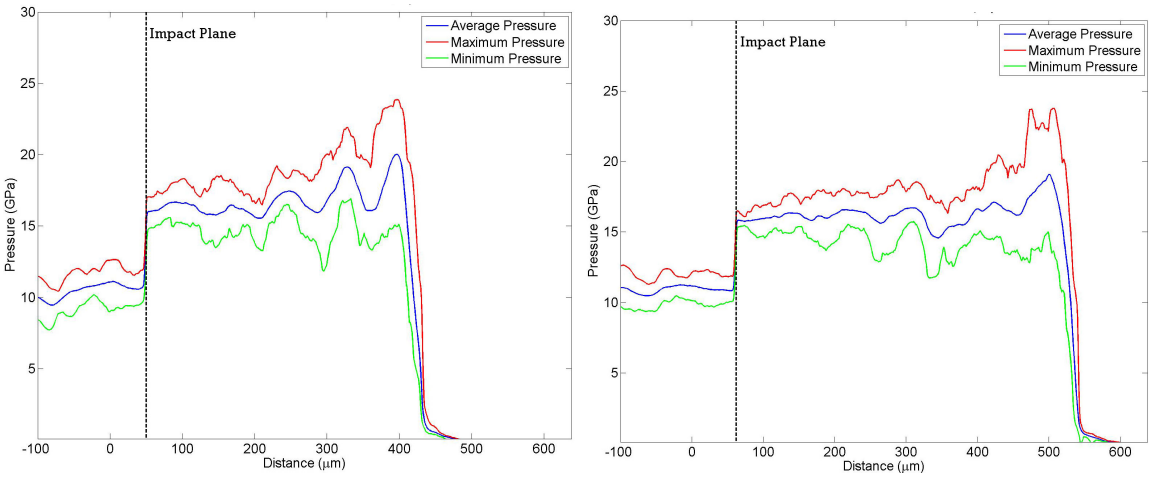

(a) Pressure Trace 80 ns After Impact

(b) Pressure Trace 100 ns After Impact

Figure 4.5: Pressure traces at 80 (a) and 100 (b) ns after impact showing the maximum, minimum, and average pressure profiles along the perpendicular multilayer composite. The trace at 80 ns shows characteristic oscillations in the average pressure similar to what has been seen in previous studies [123, 125, 124, 128]. The average pressure trace at 100 ns shows that these oscillations are not steady and attenuate rapidly due to the non-uniformity of the layers.

larger attenuation and apparent viscosity. The viscosity increase is evident in the 20% decrease in the rise time for the uniform multilayer composite as compared to the cold-rolled multilayer composite. The heterogeneities in the cold-rolled multilayer composites clearly produce more geometric dispersion and dissipation than an idealized multilayer composite, and the effects of this are further examined in Section 4.2

Figure 4.7 shows high-resolution images of the computed material deformation, temperature, and strain response of a small section of the multilayer composite. The temperature difference between the Ni and Al, Figure 4.7b, is small but well defined. This can be explained by the time scale of the simulation and the strain response. First, the time scale of the simulations is not enough to allow for sufficient heat conduction immediately after the passage of the shock front to equilibrate the temperature. This helps produce the steep gradient in temperature observed. Secondly,

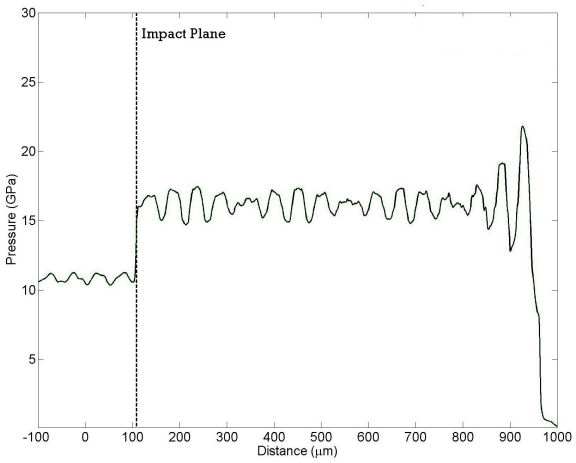

Figure 4.6: Pressure traces 180 ns after impact of a uniform multilayer composite. The traces show that while the oscillations are variable, they are also periodic. This means that a uniform multilayer composite can support a steady shock wave as previously seen experimentally [124, 123, 128, 125].

as seen in Figure 4.7c, the strain values are on the order of 10% and localized exclusively in the softer Al layers. There is little shear along the interface that could otherwise create areas of high temperature, making compression the only means of energy dissipation. Correspondingly, only temperatures around 450 to 500 K are reached in the Al layers, with a sharp gradient between the adjacent, cooler Ni layers. This suggests that the behavior of the perpendicular laminate is dominated by wave dispersion phenomena, with little effect from dissipative processes.

It deserves noting that in these simulations there is no continuity in pressure between the Cu piston and the sample, as seen in Figure 4.6, due to the rigid, incompressible nature of the Cu piston. The rigid assumption leads to large stress deviators and prohibits the equilibration of the pressure between the two bodies. This only affects the response of the Cu piston, which is not of interest. This was verified with an identical computation using the true properties of Cu, which produced no variation in the multilayer response.

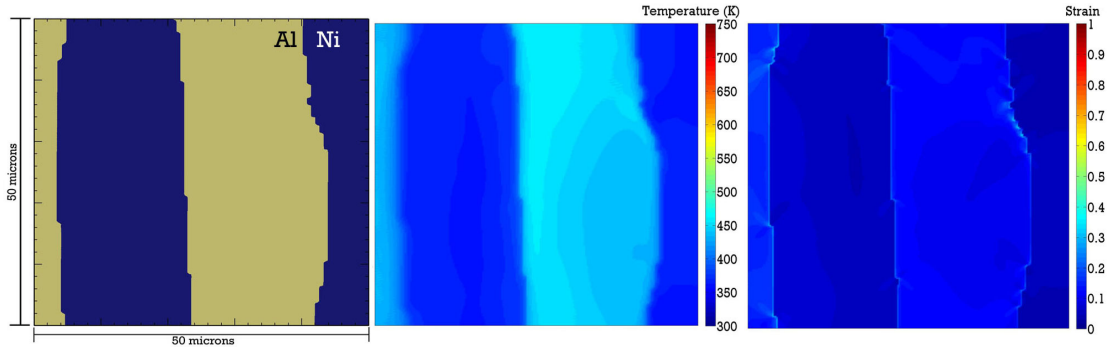

(a) Materials (b) Temperature (c) Strain

Figure 4.7: High resolution simulation showing the material deformation (a), temperature (b), and strain (c) in the perpendicular configuration. The temperature profile shows more heating in the Al and a sharp temperature gradient between layers. This is a result of the low interfacial strain associated with this configuration and the short time scale. Most deformation is normal to the interfaces allowing for limited shear, making compression the main means of energy deposition.

4.1.3 Angled Configuration

The multilayer composite microstructure was rotated to an inclination of 45^o relative to the direction of shock wave propagation and simulated at an impact velocity of 1000 m/s ($U_P = 596$ m/s). In this orientation, the one-dimensional strain approximation is lost, due to areal changes of each layer under the compression of the shock wave. While this deviation from the one-dimensional ideal is not large, it is significant enough to be considered when looking at the overall shock compression response, and becomes more important when discussing the bulk properties of the cold-rolled multilayer composite in Section 4.1.5.

The pressure response of the angled configuration can be seen in Figure 4.8a. The steady state pressure is found to be around 16.2 GPa, which is essentially the same as the perpendicular configuration. This is expected as the pressure depends mostly on the ratio of constituents. The feature of most interest is the markedly uniform pressure response, similar to what would be expected from a homogeneous solid. There is no oscillatory behavior as observed in the perpendicular configuration.

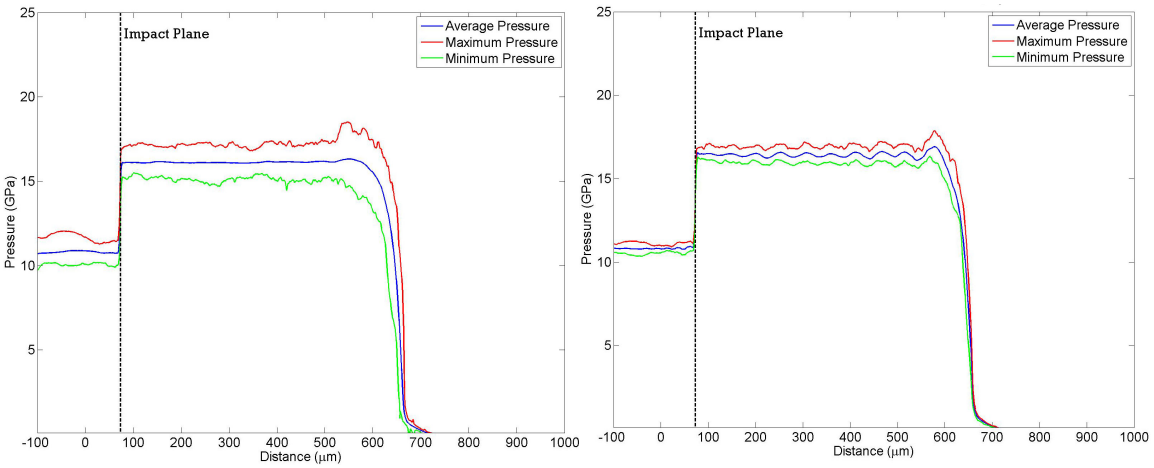

(a) Cold-Rolled Composite (b) Uniformly Layered Composite

Figure 4.8: Maximum, minimum, and average pressure profiles along the length of the cold-rolled (a) and uniformly layered (b) angled multilayer composite 120 ns after impact at 1000 m/s. The cold-rolled composite is seen to exhibit a markedly uniform pressure response, while the uniformly layered composite exhibits low level oscillations.

Consequently, the angled configuration can be considered to exhibit a steady shock wave. This results from the angle of inclination and the non-uniformity of the layers and is more clearly understood by looking at the response of an analogous uniformly layered multilayer structure.

A uniform multilayer composite oriented 45^o to the direction of shock wave propagation with the same material properties, constituent ratio, and bilayer spacing was simulated at an identical impact velocity. Figure 4.8b shows the pressure response of this uniform multilayer composite. Due to the method utilized to obtain these pressure traces, in the uniformly layered angled composite the maximum pressure response corresponds to the Ni layers, while the minimum corresponds to the Al layers. Low amplitude steady oscillations are observed in the average pressure response shown in Figure 4.8b. The inclination of the material interfaces leads to transverse wave motion, or geometric dispersion, reducing the amplitude of these oscillations when compared to the perpendicular configuration. The cold-rolled multilayer composites have a variety of angles of inclination with average at 45^o, which leads to

wave reflections in a multitude of angles. The range of angles increases the geometric dispersion, quickly equilibrating the pressure and providing a uniform pressure response.

The inclination of the layers also leads to an increase in the viscosity of the multilayer composite. This is seen in the larger 30 ns rise time observed for the cold-rolled angled configuration, which is twice the rise time of the perpendicular configuration. The increase in viscosity can be explained through the presence of two-dimensional effects. The shock wave exists in both materials independently, leading to shearing forces at the interface to maintain the coherency, which dissipates energy. This increase in viscosity is also aided by the dispersion induced by the non-uniformity of the layers, which is evident in the lower rise time for the uniform angled multilayer composite.

The temperature and strain response exhibited in the higher-resolution simulations are shown in Figure 4.9. It can be seen that the Al exhibits a much larger temperature and strain, as expected. The interesting aspect of this configuration is the increased temperature and strain along the Al and Ni interfaces, in particular the ones in which the wave travels from Al into Ni. This can be explained by the impedance mismatch between the two materials. The impedance of Al is roughly 36% of Ni. Hence, as the wave moves from Al into Ni, the reflected compression wave leads to the generation of higher pressures and transverse motion that increase interfacial strain. This leads to larger dissipation as seen in the interfacial temperatures ($\sim 600K$), which are significantly higher than in the perpendicular orientation. This suggests that strain plays a large role in the dissipation of the shock wave energy. It is also interesting to note that the elevated strains are almost exclusively localized along the sections with a smooth surface. A bulge in the Al layer, seen in Figure 4.9c, exhibits different wave interactions that produce lower strain and temperature values. This suggests that multiple wave interactions at a bulge disperse the wave energy.

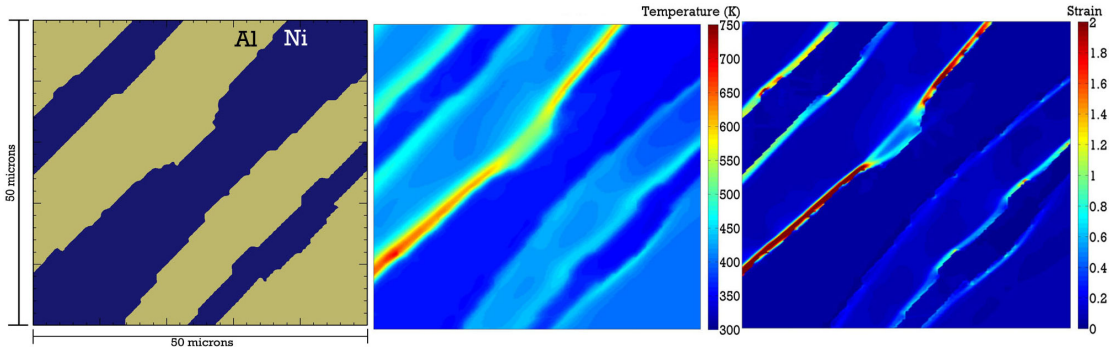

(a) Materials (b) Temperature (c) Strain

Figure 4.9: High resolution simulation showing the material deformation (a), temperature (b), and strain (c) profiles in the angled configuration. The large amount of interfacial heating results from large strains along the interface, due to transverse wave motion.

This causes the energy to be dissipated over the entire area, instead of the interface, thereby reducing the interfacial shear and the total amount of energy dissipated.

4.1.4 Parallel Configuration

The final set of simulations involved a microstructure with the layers oriented parallel to the direction of shock wave propagation, giving a configuration with no interfaces to impede the wave motion. The simulation performed at an impact velocity of 1000 m/s, corresponding to a particle velocity of 595 m/s, is discussed. The complication with this configuration is the loss of a one-dimensional strain approximation. With the layers parallel to the shock wave, the compression resulting from the shock wave leads to a change in area of each layer. The areal change must occur in the shock rise time, causing an inherent increase in viscosity for this configuration. In addition, the configuration itself leads to attenuation of the wave as a result of geometric dispersion, which has been previously shown with elastic waves by Peck [134].

In a parallel configuration, the shock wave propagates across each material independently, and provides a unique shock velocity for each constituent. However, due to the coherency of the interface, a sinusoidal behavior at the wave front develops,

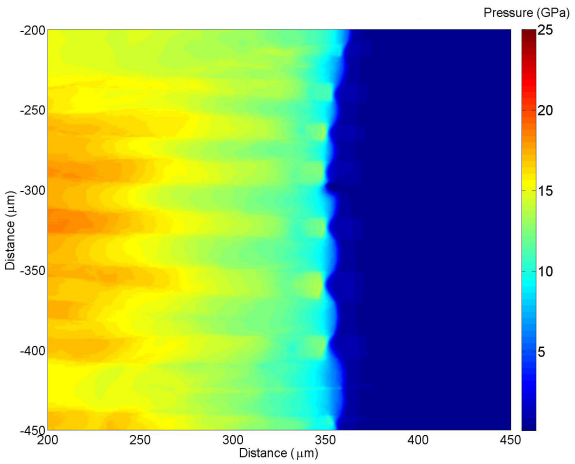

Figure 4.10: Oscillatory wave front seen in the parallel CTH simulations.

as seen in Figure 4.10. This fact has been used by Tsou and Chou [135] and Torvik [137] for the development of their analytical models, as discussed in Section 2.4.2. The one dimensional pressure trace shown in Figure 4.11a illustrates that the wave profile slowly rises to a steady state pressure of 16.2 GPa, which is essentially the same as that for the other configurations. What is of note is the large rise time in this orientation, which increases as the wave propagates through the composite. Figure 4.12 shows the pressure traces of the multilayer composite at 20, 60 and 100 ns after impact at 1500 m/s. It is clearly seen that the initial shock front slowly attenuates and smears as the wave propagates. This is a result of dissipative and dispersive wave phenomena in this configuration that is more clearly seen with an idealized multilayer composite.

The pressure trace of a uniform multilayer composite with the same orientation, material properties, and bilayer spacing at an identical impact velocity is shown in Figure 4.11b. A dual-wave front is clearly seen to exist, since the shock wave moves across each material at differing speeds. The leading wave corresponds to the lower impedance material, which, in this case, is Al. This wave causes the initial rise in pressure in Figure 4.12. The wave in the higher impedance material, in this case Ni, lag behinds this initial wave. The separation of the shock waves in each material

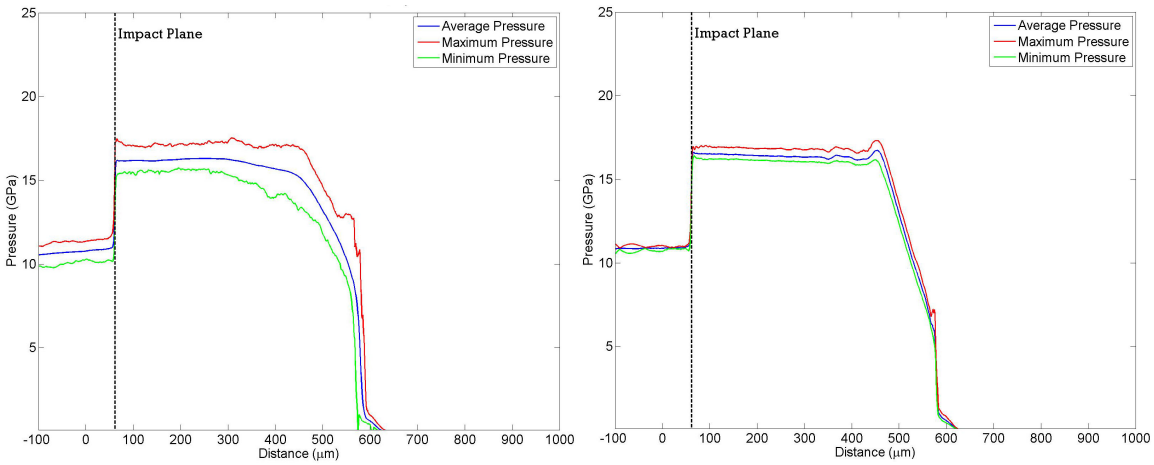

(a) Multilayered Composite (b) Uniformly Layered Composite

Figure 4.11: Maximum, minimum, and average pressure traces along the length of a cold-rolled (a) and uniformly layered (b) parallel multilayer composite 100 ns after impact at 1000 m/s.

leads to increases in dissipation and dispersion, and can be thought of as an increase in viscosity. The shock front must be bound by these two material dependent shock waves. Since the layer area is gradually changing between them, they define the transition from the initial and final states. The different wave velocities in each constituent lead to an increase in separation between both wave fronts over time, causing a smearing of the shock front. This can be seen in the increasing rise times in Figure 4.12. The microstructure modeled also assumes perfectly bonded interfaces. The specified interfacial coherency causes extensive energy dissipation, due to the disparity in particle velocities. The dissipation works in concert with the geometric dispersion caused by the non-uniformities in the cold-rolled multilayer composite, causing the waves to attenuate and dissipate at an accelerated rate, as seen in Figure 4.12. The parallel configuration can, therefore, not support a steady shock wave over the domain investigated. In addition, the extensive dispersion and dissipation leads to an interesting bulk shock compression response, which is discussed later in Section 4.1.5.

High resolution simulations were used to investigate the interfacial temperature

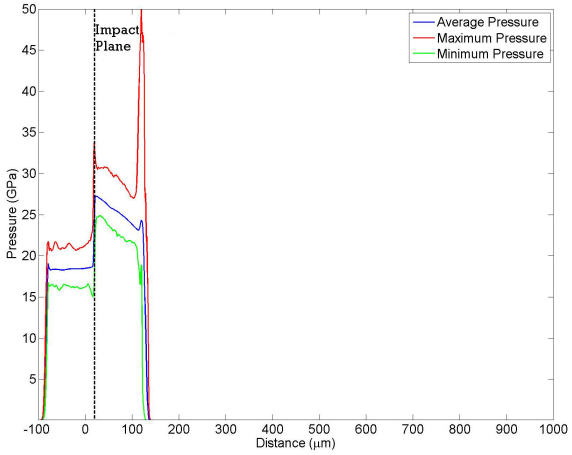

(a) Pressure Trace at 20 ns

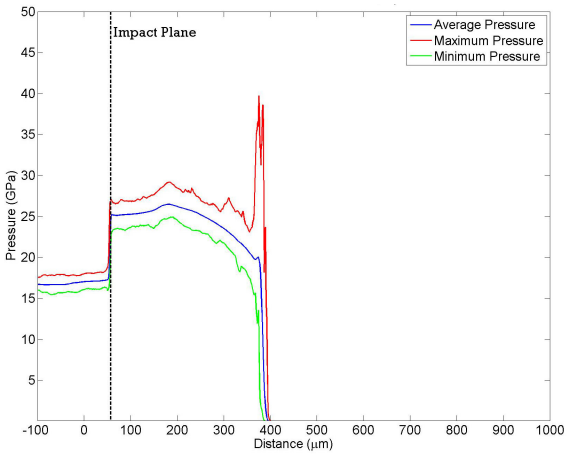

(b) Pressure Trace at 60 ns

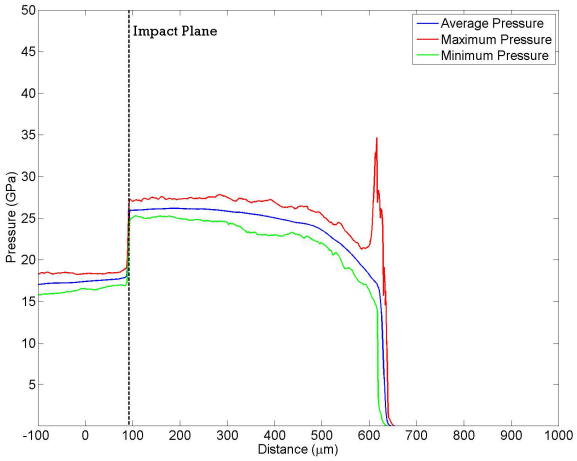

(c) Pressure Trace at 100 ns

Figure 4.12: The pressure traces 20 (a), 60 (b), and 100 (c) ns after impact at a velocity of 1500 m/s. The initial shock wave in Al is seen to develop at 20 ns, with a slow rise to the pressure of the trailing shock wave in Ni. The pulses are seen to attenuate and smear as energy is dissipated from the system, increasing the rise time.

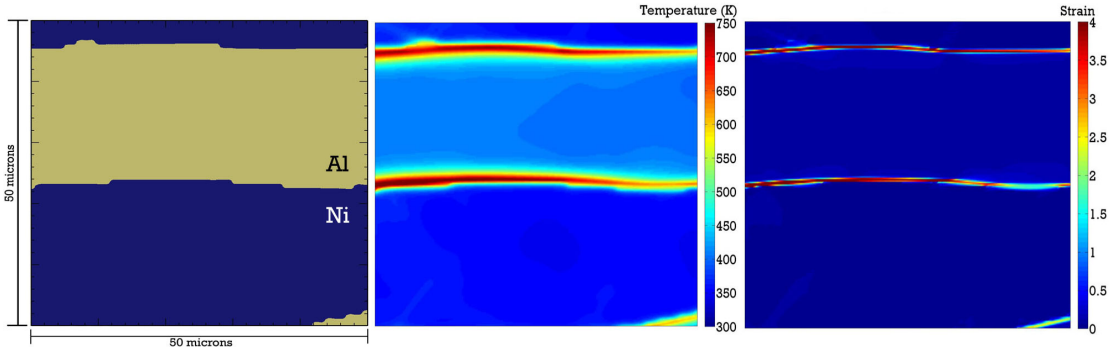

(a) Materials (b) Temperature (c) Strain

Figure 4.13: High resolution simulation showing the material deformation (a), temperature (b), and strain (c) response for the parallel configuration. The results show large heating at the interface. This is the result of large strains and shearing forces generated at the interface due to the large discrepancy between the particle velocities in each of the individual layers.

and strain responses in this configuration, as seen in Figure 4.13. Figure 4.13b shows that the temperatures along the interfaces are elevated to around $800K$, which is close to the melting point of Al at zero pressure. The elevated temperature is due to large interfacial strains, which are seen in Figure 4.13c. These large strains result from the coherency of the material interfaces. Since each layer has a characteristic material velocity, large shearing forces develop at the material interfaces. This produces the large strains, dissipating energy as the particle velocities in each layer are brought to equilibrium. Figure 4.14 shows the velocity in the center of each material layer over time. The particle velocity in the Al is initially much higher, but eventually equilibrium is reached over the rise of the shock wave as the interfaces dissipate the shock energy. Due to these large interfacial strains, the parallel configuration is the most dissipative of all the orientations. In addition, the disparity in particle velocities concentrates the energy deposited at the interfaces, which is ideal for reaction initiation. Based on these factors, the parallel configuration presents the most likely configuration for inducing reaction.

A source of error that was investigated in this configuration was the temperature

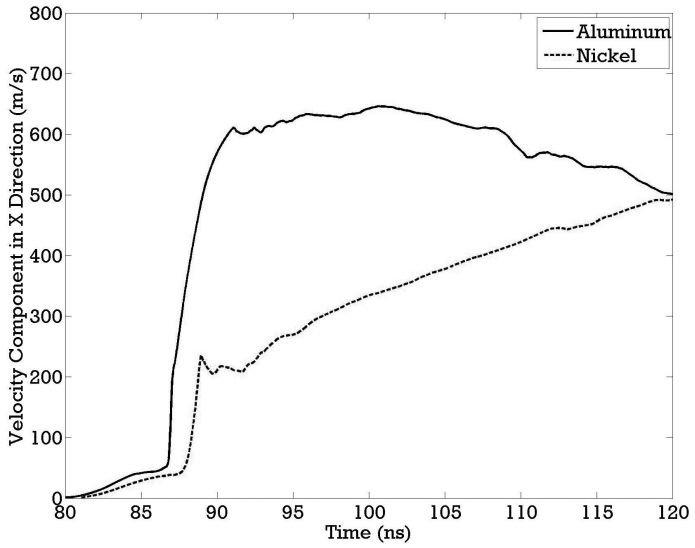

Figure 4.14: The x component of the velocity in each material over time showing that continuity in the particle velocity is achieved over the rise of the shock pulse, due to the interfacial coherency.

response. CTH calculates temperature using the Mie-Grüneisen equation of state approximation. This assumes a constant specific heat, which is not accurate. While this casts some doubt on the absolute values of the temperature, the overall distribution of temperatures is what is most important. The temperature distribution is controlled by the advection method. Given the resolution of the mesh, the low level of deformation, and the validity of the Mie-Grüneisen equation of state in this pressure regime, the energy error can be assumed small. Regardless, the advection scheme was changed to obtain bounds for the temperature distribution.

There are two advection methods commonly employed. The first, which was used for this work, advects internal energy and momentum through the mesh at each time step. This provides the most accurate estimation of temperature, which is determined from the internal energy. The second method, which was used for comparison, advects momentum and total energy (*i.e.* the sum of the kinetic and internal energies). The kinetic energy is then determined from the momentum and subtracted from the total energy to obtain the internal energy. This method generates a kinetic energy error,

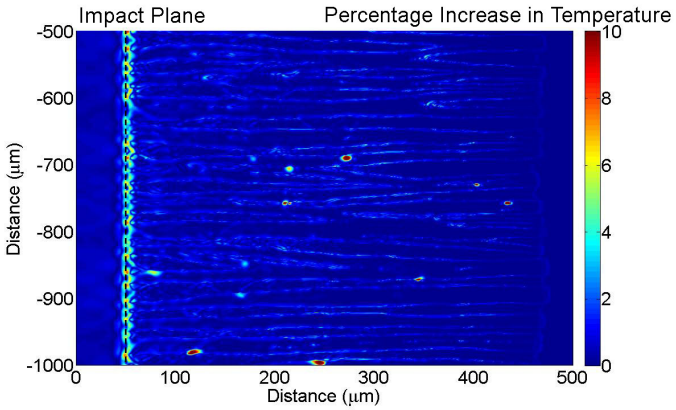

Figure 4.15: Temperature difference profile 80 ns after impact at 1000 m/s. The few voids in the multilayer and the impact interface are seen to cause the largest temperature differences between the two convection schemes. The rest of the multilayer shows temperature differences less than 5%.

which is added to the internal energy and produces higher temperatures.

The parallel configuration was chosen for this analysis, since it exhibits the highest temperatures. The difference in temperature as a percent between the two methods is shown in Figure 4.15. The error is seen to be mostly under 5%, with elevated pockets around 10-15%, mainly at the impact interface. With such a small deviation overall, the advection method is not assumed to be a significant source of error in this work.

4.1.5 Bulk Response of the Multilayer Composites

The results of the simulations at impact velocities of 500, 750, 1000, 1250 and 1500 m/s were used to understand the bulk response of the shock compressed multilayer composite at various orientations. Particularly, the results were used to develop an equation of state relating the shock velocity to the particle velocity. For this analysis, the composites were all assumed to follow the standard linear equation of state (*i.e.* $U_S = C_o + S_1 U_P$). The values of the constants C_0 and S_1 for the perpendicular, angled, and parallel configurations are given in Table 4.1, along with the values predicted considering a homogeneous Ni and Al mixture based on McQueen mixture theory [45] (obtained with the GTShock code [27]). The results of the U_s-U_P relation

Table 4.1: Equation of state parameters for various multilayer composite orientations.

Orientation	C_o (m/s)	S_1
Perpendicular	4419	1.559
Angled 45^o	4392	1.624
McQueen Mixture Theory	4943	1.508
Parallel 0^o	4459	1.952 †

†Valid for $U_P < 1000$ m/s

for the perpendicular and angled configurations are plotted in Figure 4.16, clearly showing that the bulk sound speeds of the perpendicular and angled configurations are very similar and within 1% of each other. McQueen mixture theory is seen to yield a larger inert sound speed (about 11% higher), which is expected since McQueen mixture theory assumes a homogenous composite with no phase boundaries to inhibit wave motion. This gives the homogenous mixture a lower impedance, causing a shift upward in U_S-U_P space. Based on these results, the number of interfaces is seen to affect the bulk sound speed, while the orientation seems to have a minimal influence. This would suggest that geometric dispersion is a bulk factor and not affected by orientation at these strain rates.

The other conclusion drawn from these simulations is that the material constant, S_1, is seen to change slightly between the perpendicular and angled configurations. The results of McQueen mixture theory and the perpendicular configuration are within about 2%. However, the angled configuration exhibits a small change, which is attributed to the two-dimensional effects beginning to influence the shock compression response. This shows that the dependence of the shock speed on the particle velocity is not necessarily just dependent on the ratio of constituents, and can clearly be altered by the microstructure inducing two-dimensional strain effects.

The bulk wave propagation response of the parallel configuration can not be viewed with a linear EOS in the manner that was done with the perpendicular and angled configurations. The extensive dispersion and dissipation does not produce a steady or

quasi-steady shock wave, causing the shock, or wave, velocity to be heavily dependent on propagation distance. This causes a deviation from the linear EOS approximation, and the need for extremely large impact velocities to obtain a coherent shock response in the 1 mm domain studied. The effect is clearly seen with Figure 4.17, which shows the EOS of the constituents, Al ($U_S = 5380 + 1.34U_P$) and Ni ($U_S = 4590 + 1.44U_P$) [56], along with the simulated wave front velocity data for the parallel Ni-Al multilayer composite configuration. Only portions of the EOS response of the parallel configuration can be expressed through a linear EOS. This approximation for particle velocities below 1000 m/s is provided in Table 4.1.

The effects of attenuation and viscosity are more evident when simulations are done at higher impact velocities (2000, 2500, 3000, 3500, 4000, 4500, and 5000 m/s) to ensure a coherent shock wave persists through the entire computational domain. The results are presented in Figure 4.17 and help to illustrate how the response of the multilayer composite is controlled by the constituents. At lower velocities, the wave front follows very closely to the EOS of Ni. This dominance of the higher impedance material at lower impact velocities is expected given the presented method for determining shock speed. The wave in the lower impedance material, Al, has attenuated by the time the first measurement is taken 20 ns after impact. As a result, the wave in Ni is the one tracked through the multilayer. As the particle velocity increases, the Al wave is able to sustain itself for longer periods, increasing its contribution to the measured bulk responses. This causes the slow shift of the data to the Al EOS at larger particle velocities. Eventually, the material follows the Al EOS, since the Al no longer attenuates over the computational domain. At impact velocities over 4000 m/s, the material response is seen to move to the center of both materials. At this large of a particle velocity, the waves remain close enough to be considered essentially a coherent, one-dimensional shock over the whole domain, causing the response to be averaged.

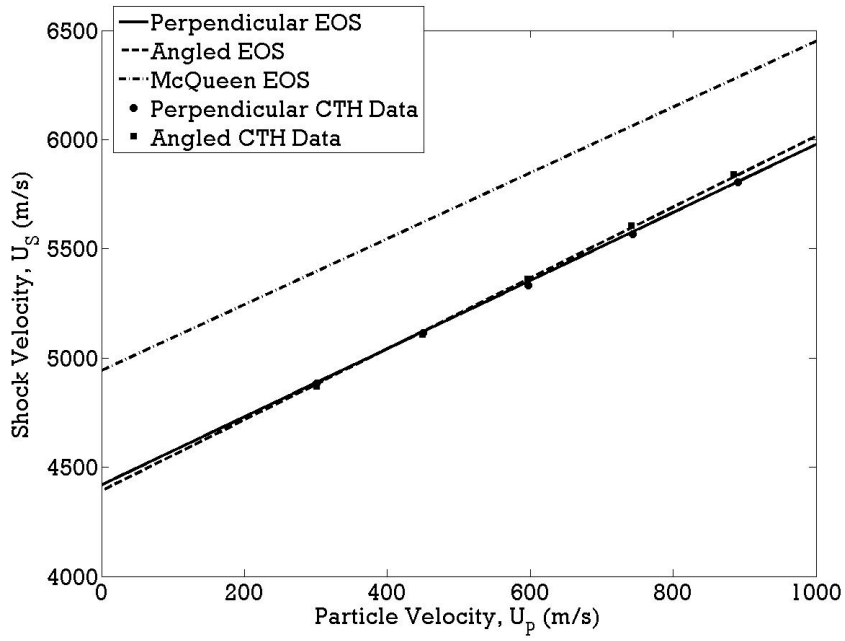

Figure 4.16: U_S vs. U_P curve for the perpendicular and angled configurations along with EOS predicted by McQueen mixture theory.

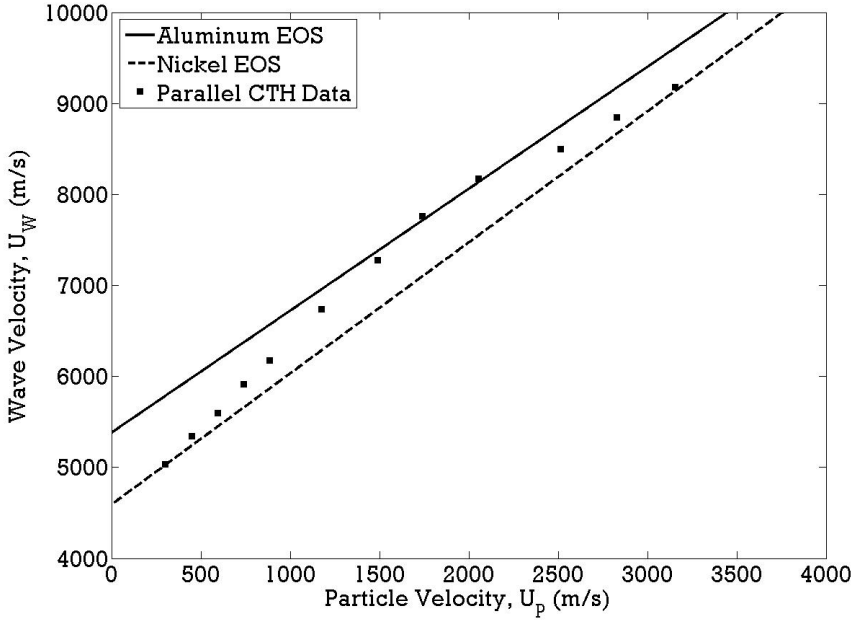

Figure 4.17: U_W vs. U_P plot for the parallel configuration along with the EOS for Al and Ni. The response of the parallel configuration is seen to transition from being dominated by the response of the Ni to that of Al as U_P increases.

It is important to note that these simulations were only done to illustrate how the constituents determine the bulk response in the parallel configuration. The simulations are in no way intended to truly represent the material response at such large particle velocities. The materials were modeled with the Mie-Grüneisen equation of state, which does not allow for phase changes, such as melting or chemical reactions between the constituents. For a true representation of the material response at such large particle velocities, phase changes need to be considered.

Comparisons in U_S-U_P space show drastic differences between the parallel, angled, and perpendicular orientations. As alluded to previously, all the orientations had similar steady state pressures. A comparison of all three orientations in P-U_P space shows very similar responses for each configuration, as seen in Figure 4.18. While the pressure does decrease in the parallel configuration as the wave propagates, this decrease was not large enough over the time scale of the simulations to exclude this sort of comparison. From Figure 4.18, it is clearly evident that all the configurations exhibit similar equilibrium responses. It is important to remember that the p-U_P response shows only the final equilibrium state of the materials and does not capture the two dimensional effects in the rise of the shock pulse. Consequently, the P-U_P response is not fully representing the material response under shock loading. These reasons dictated the use of the pressure traces and interfacial simulations to characterize the true shock loading response of these materials.

There are several conclusions that can be drawn from the bulk response of these multilayer composites. First, the shock compression response of the cold-rolled multilayer composite is dominated by the dissipation induced from two-dimensional strain effects and the interface coherency. This causes the variations in wave speed for the parallel orientation. It also is why representations based on the final equilibrium state, such as the P-U_P response, does not fully represent the shock response. In addition, it was also seen that geometric dispersion is a bulk property and is not influenced by

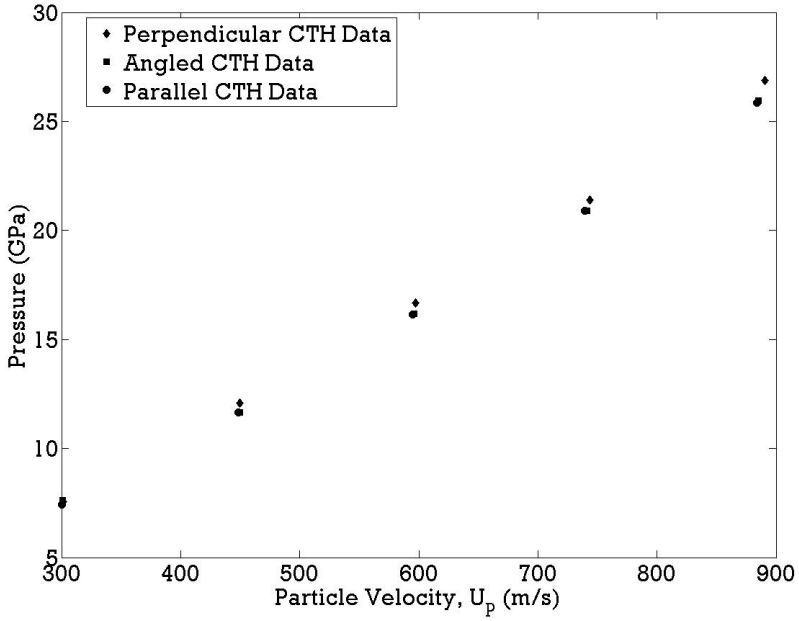

Figure 4.18: P-U_P curves for all three orientations: perpendicular, angled, and parallel.

layer orientation over the conditions and domain size simulated.

4.2 Effect of Interfacial Density and Material Properties on the Dispersion and Dissipation in the Parallel Configuration

In the previous section, two dimensional effects were seen to cause increased dispersion and dissipation in the parallel orientation. These factors make the parallel orientation the most promising for reaction initiation, since elevated temperatures and large strains are generated at the material interfaces. These properties could also be used for the attenuation of a wave, such as in an armor application. Building on these results, it was desired to examine the effects of various microstructural parameters on the dispersion and dissipation of the shock wave in the parallel configuration. Through microstructural variation, the parameters necessary to optimize the microstructural response can be determined. To this end, the microstructural

parameters controllable through fabrication in Ni/Al multilayer composites were investigated. These microstructural features can be classified in two main categories: interfacial parameters and material properties.

The effects of interfacial density, structure, and strength on the propagating shock wave were independently investigated. To isolate the influence of these interfacial parameters, the material properties were kept identical to those used in the previous section on orientation effects. The role of interfacial density was examined by comparing the responses of multilayered composites with bilayer spacings ranging from 14 to 112 microns. As stated in Section 3.2, interfacial density is a parameter easily varied during fabrication through changes in the starting foil thicknesses or the number of rolling cycles. The effect of interfacial structure was investigated by looking at the response of a uniformly layered composite compared to that of a cold-rolled composite. This analysis is similar to that performed in the orientation study and allows for a comparison between the responses of hot pressed and cold-rolled multilayer. Lastly, the assumption of perfectly bonded interfaces, which generate large amounts of interfacial shear and dispersion, is studied. Since the amount of energy dissipated largely depends on the interfacial coherency, simulations were run with no interfacial strength to obtain bounds for the composite response.

The variations in material properties focuses on the strain hardening. By varying the number of rolling cycles or performing low temperature anneals, the strain hardening in these multilayers can be controlled. For this section, the initial yield point of both Ni and Al were varied, while the geometry of the simulations was kept the same to isolate the effects of strain hardening on the dispersion and dissipation of the shock wave.

4.2.1 Microstructure Generation and Computational Method

As stated in Section 3.2, the longitudinal cross section of these cold-rolled multilayer composites have similar characteristics regardless of the number of rolling cycles endured. Utilizing this fact, the optical micrograph shown in Figure 3.4 can be used for the generation of microstructures with various bilayer spacings through simple scaling. For bilayer spacings under 28 microns, the periodicity of the multilayers can be used to artificially extend the microstructure through mirroring. For bilayer spacing larger than 28 microns, the microstructures can be taken from a smaller section of the scaled, original microstructure. This procedure enabled the generation of identical domain sizes of microstructures with average bilayer spacings of 14, 28, 42, 56 and 112 microns.

4.2.1.1 Statistical Variation of Microstructures

There is an important consideration that must be made when scaling the microstructure. As shown in Section 3.2, the multilayer composites are highly heterogeneous systems. Similarly, as argued in Section 3.4, any computational domain must statistically capture these heterogeneities to provide accurate results. Consequently, the bilayer spacing can only be increased to a certain amount before the microstructure is not statistically representative over the 1mm domain investigated.

The CTH renderings for the 14, 42, 56, and 112 micron multilayers are provided in Figure 4.19. The CTH rendering of the 28 micron composite was presented in Figure 4.1c. Using the average bilayer spacing and the known computational domain, the average number of layers represented in each variation can be determined and are listed in Table 4.2. Recall from Section 3.4, the MSAAF technique was used to determine the homogeneous length scale for the multilayer composites, which could be expressed solely in terms of bilayers. Using the computational fit to the MSAAF data provide through Table 3.6 and Equation 3.17, the variation in area fractions for each

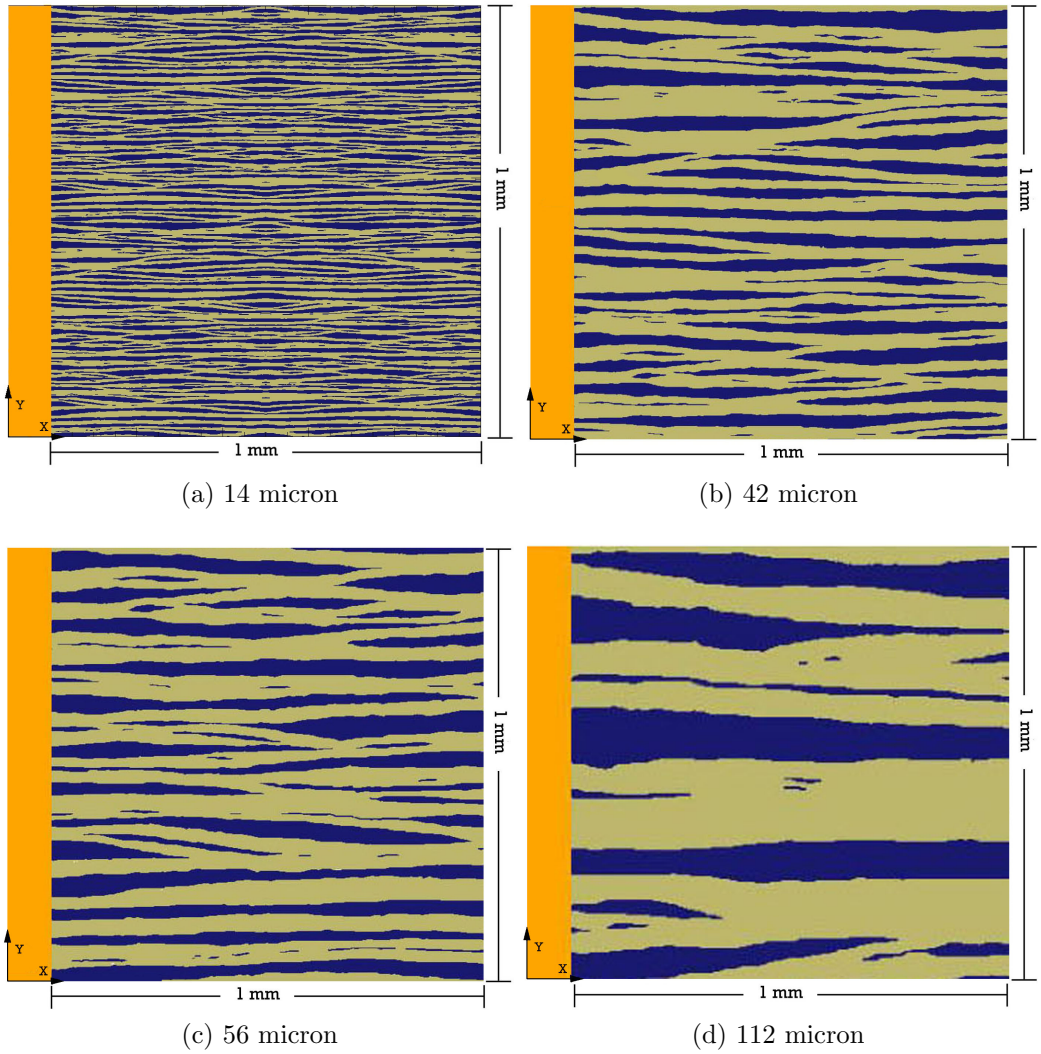

(a) 14 micron (b) 42 micron

(c) 56 micron (d) 112 micron

Figure 4.19: CTH renderings for the 14 (a), 42 (b), 56 (c) and 112 (d) micron composites.

material over a quilt length of 1mm can be obtained for each bilayer spacing. This is provided in Table 4.2. It was desired to keep the variation of these microstructures to within $\sim 5\%$, to ensure that the domains were representative. The results in Table 4.2 show that 9 bilayers are the minimum required to statistically capture these multilayer systems within the allowable tolerance, which set the upper maximum for bilayer spacing in this work at 112 microns.

The estimations in Table 4.2 can be checked against the actual values rendered in CTH. If the domains are representative, the area fractions should all be within 5%

Table 4.2: Results of x directional MSAAF method for each bilayer spacing investigated.

Average Bilayer Spacing	Average Number of Layers in 1mm	$\frac{\sigma_{A_f}}{A_f}(Al)$	$\frac{\sigma_{A_f}}{A_f}(Ni)$
14 micron	71.4	0.53	0.80
28 micron	35.7	1.03	1.55
42 micron	23.8	1.52	2.28
56 micron	17.9	1.99	2.99
112 micron	8.9	3.89	5.82

of that measured in Section 3.3.2. In addition, S_V for each configuration should scale with the bilayer spacing. These values for each CTH rendering are given in Table 4.3. All of the area fractions are seen to remain within $\sim 5\%$ to that measured for the multilayer composite given in Section 3.3.2. The S_V for each configuration is also seen to scale with the bilayer spacing, helping to prove that each rendered microstructure is representative.

Table 4.3: Area fraction and S_V values for the CTH renderings of each bilayer spacing.

Average Bilayer Spacing	$V_{f_{Ni}}$	S_V $(\frac{1}{mm})$
14 micron	38.9	157.5
28 micron	38.9	79.2
42 micron	38.9	52.2
56 micron	38.7	41.4
112 micron	36.8	16.7

4.2.1.2 Simulation Parameters

The effect of various microstructural parameters on the parallel configuration were investigated utilizing essentially the same computational method described in Section 4.1.1. To isolate the effects of interfacial density, the material and simulation parameters were kept constant and identical to those of the orientation study. For clarity, each microstructure is referred to by its bilayer spacing (*i.e.* 14, 28, 42, 56, and 112 micron configurations). To investigate the effect of interfacial structure and strength, the 28 micron simulation was used as a standard. A composite with uniform layers,

termed the uniform configuration, was generated with the same bilayer spacing, constituent ratio, and material properties as the 28 micron simulation. This enabled the effects due to rolling to be isolated and compared. For interfacial strength, bounds for the composite response were obtained by simulating the 28 micron composite with no interfacial strength, termed the non-bonded configuration, and comparing it to the perfectly bonded case (*i.e.* 28 micron configuration). Lastly, the effects of strain hardening were assessed in the 28 micron configuration. The initial yield strengths of each material were altered generating two cases for comparison to the fully hardened, 28 micron configuration: zero and half the strain hardening. To simulate no strain hardening, to be referred to as the pure configuration, the properties for nascent Al and Ni where used. For half the strain hardened simulations, to be referred to as the half configuration, yields strengths half way between those measured and those for the pure materials were used.

For the bilayer spacing study, special considerations must be given to the computational mesh. This is the only parameter that was changed from the computational method outlined in Section 4.1.1. Even though the microstructures are scaled versions of each other, the mesh resolution can not be scaled accordingly. CTH is a scale independent code. This means the cell dimensions have little effect on the provided results. If the cell size scales with the microstructure, the simulations would be essentially just various domain sizes of the same microstructure. Since the microstructures were chosen to be statistically representative, no significant variations in the results would be observed. As a result, the cell size must be kept constant for each simulation and correspond to that which provides convergence for the smallest bilayer spacing.

The smallest bilayer spacing for the orientation study is 14 microns, which was obtained by scaling the original microstructure by one half. The converged mesh for the orientation study can also be halved, providing a resolution of 0.4 μm/cell for the bilayer spacing study. Keeping the mesh resolution constant means the number of

cells across each layer is increasing as bilayer spacing increases. This could be argued as an increase in the mesh resolution for the larger bilayer spacings, which should not yield significant variations in the results for a converged mesh. However, this is not an accurate description. While the number of cells is increasing across the layers, the simulations are maintaining a similar time step and a consistent thermal length scale. This minimizes numerical artifacts and enables the variations in response to be attributed to the interfacial density.

The extensive two dimensional effects in the parallel configuration have been previously shown to induce large amounts of dispersion and dissipation. The dispersive and dissipative characteristics were characterized for each configuration by looking at both the bulk material and interfacial properties. The particle level simulations are particularly important for understanding how the various microstructural changes affect the observed bulk response. These interfacial responses were obtained using high resolution AMR simulations on each configuration at an impact velocity of 1000 m/s. Following the same procedure for the AMR simulations outlined in Section 4.1.1, a small section of each composite was resolved to 100 nm/cell in order to understand the microstructural changes in temperature and strain at the interface. Once again, this is half the resolution used in the orientation study. These interfacial simulations enable a clear understanding of the microstructural phenomena that lead to changes in the dispersion and dissipation between material configurations investigated in this section.

4.2.1.3 Quantification of Bulk Dispersion and Dissipation

To aid in the comparison between each configuration, metrics were developed to represent the various dispersive and dissipative behaviors. The quantification of the dispersion in a material is best viewed by looking at the rise of the shock pulse. As dispersion increases, the shock rise time also increases, spreading out the wave front.

While the energy dissipated in the shock front also effects the rise time, dispersion is the dominant factor in determining its shape. This fact enables the method for generating 1D pressure traces outlined in Section 4.1.1 to be utilized for quantifying the observed bulk dispersion of these simulations. The main dissadvantage of this method is that it provides no insight into the dispersion perpendicular to the propagating shock wave. However, since this study focuses on the parallel configuration, most of the dispersion occurs as the wave spread out in the direction of shock wave propagation. This fact makes the 1D pressure trace a good, simple metric for understanding how microstructural variations alter the dispersive response between configurations.

With all the microstructures having the same orientation, the easiest way to compare the bulk dissipation of each material is by using the EOS. As the material loads, it follows the Rayleigh line. The area under this curve is the energy deposited into the system. Since the material unloads along the isentrope, the area under that curve represents the energy recovered. For the pressures investigated in this study (< 25 GPa), the Hugoniot and isentrope are essentially the same, as discussed in Section 2.1.1. Representing the isentrope with the Hugoniot, greatly simplifies the determination of the energy dissipated. This means the energy dissipated through shock loading is the area between the Rayleigh line and the Hugoniot. This is shown schematically in Figure 4.20.

Using the Rankine-Hugoniot conditions and the linear EOS approximation described in Section 2.1.1, the conservation of momentum as a function of the compression, $\mu = 1 - \frac{\rho_0}{\rho}$, takes the following form.

$$P = \frac{\rho_0 C_0^2 \mu}{(1 - S_1 \mu)^2} \tag{4.3}$$

Expressing the Hugoniot in P-μ space means that the area under the curve corresponds directly to the energy dissipated. As a result, dividing this area by the initial density provides the specific energy dissipated. For the Rayleigh line, the specific

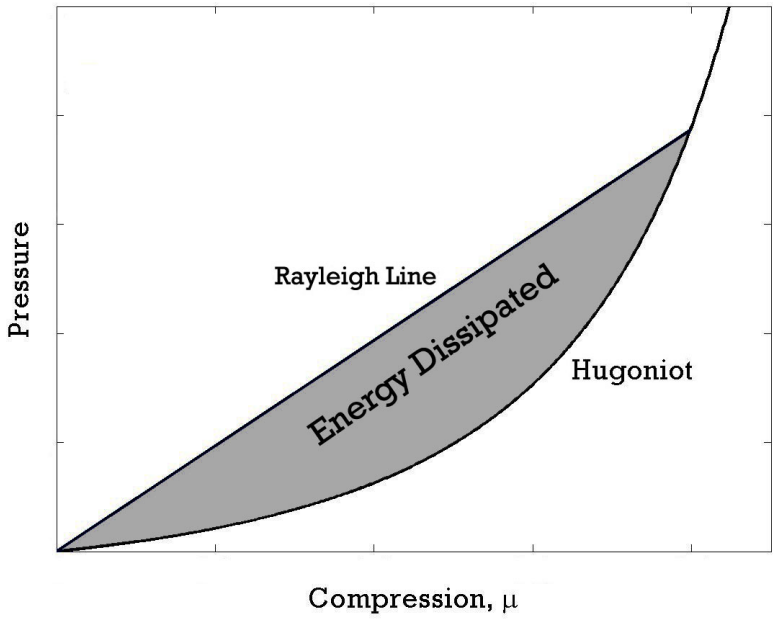

Figure 4.20: Schematic showing the Hugoniot and Rayleigh line along with the energy dissipated in the shock event.

energy deposited is given with the following.

$$e_R = \frac{1}{2}\frac{P\mu}{\rho_0} = \frac{C_0^2\mu^2}{2(1-S_1\mu)^2} \tag{4.4}$$

Additionally, the specific energy recovered is found by integrating the Hugoniot expressed with Equation 4.3.

$$e_H = \int_{\mu=0}^{\mu} \frac{C_0^2\mu}{(1-S_1\mu)^2} \tag{4.5}$$

The energy dissipated is simply the difference between the deposited and recovered energies.

$$e_{Diss} = e_R - e_H \tag{4.6}$$

This procedure enables the specific energy dissipated as a function of pressure to be determined.

This method for determining the bulk specific energy dissipated relies only on the EOS parameters. Insight into how each EOS parameter affects the dissipative response can be obtained by plotting the energy dissipated at a specific pressure for

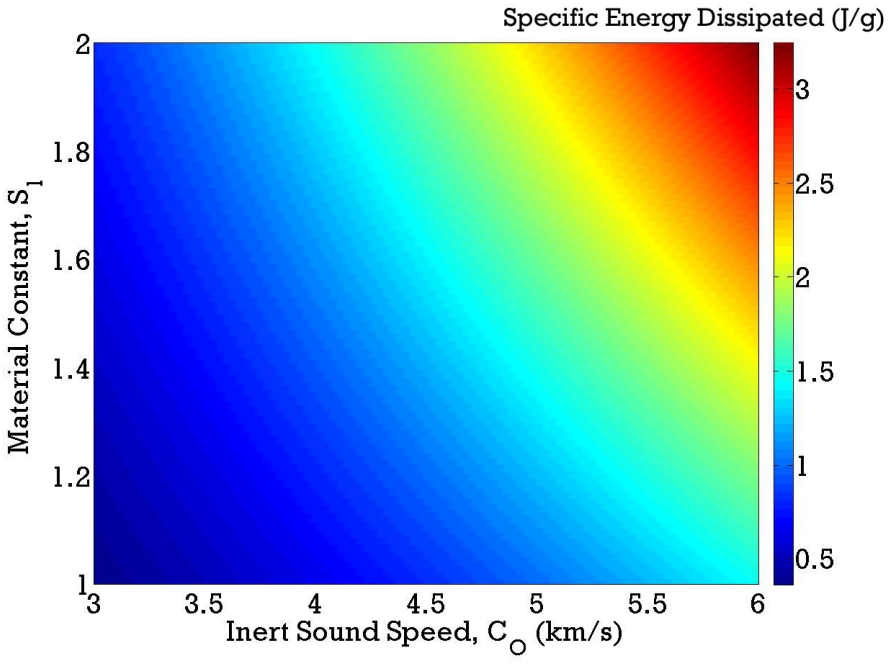

Figure 4.21: Plot showing the change in specific energy dissipated as the inert sound speed, C_0, and the material constant, S_1, change. The results show that increases in dissipation occur with increases in both C_0 and S_1.

various EOS parameters, C_0 and S_1. This is done in Figure 4.21 for a compression of $\mu = 0.0476$ (*i.e.* $\rho = 1.05\rho_0$). It is clearly evident that the energy dissipated by the microstructure increases with both C_0 and S_1. There is a slight curve to the graph, which stems from the quadratic form of the Hugoniot in P-μ space. However, the effects of each parameter are seen to be similar.

The application of this method to Ni, Al, and a homogeneous composite determined through McQueen mixture theory [45] is given in Figure 4.22. As expected, at any given pressure, the more compressive Al is seen to dissipate more energy than the stiffer Ni. In addition, the McQueen mixture response lies between the two curves, since the mixture Hugoniot is found by averaging the properties of Ni and Al. The results clearly show that the individual dissipative behavior of a material can be found with the EOS.

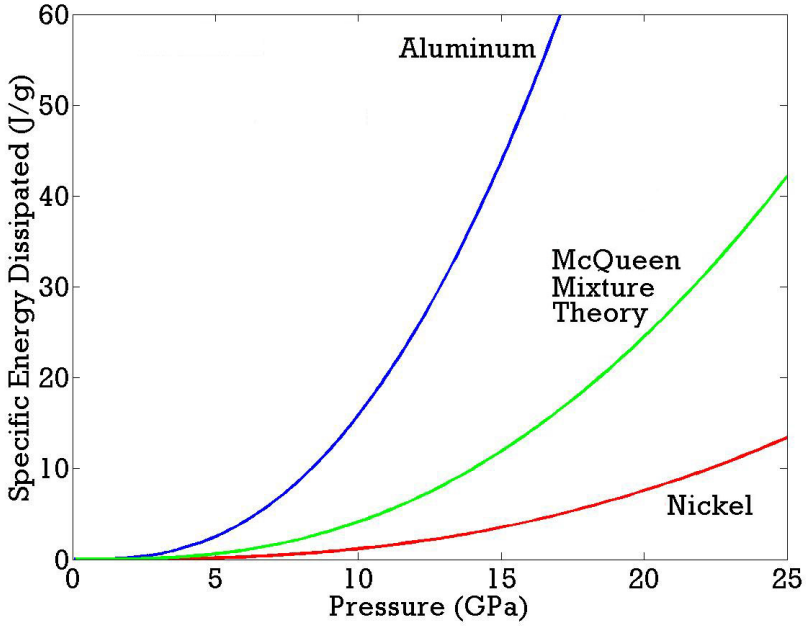

Figure 4.22: Plot showing the change in specific energy dissipated for Al, Ni, and a homogeneous composite determined through McQueen Mixture theory [45]. Al, being the softest phase, is seen to dissipate the most energy, while the homogeneous composite is seen to reside between the Al and Ni response.

The proposed method of bulk dissipation has a few drawbacks that deserve addressing. The use of the EOS response to quantify the bulk dissipation does not fully account for the 2D effects present in the parallel configuration outlined in Section 4.1.4. This comes from the use of the Rankine-Hugoniot conditions for the determination of the energy dissipated. These equations assume a 1D steady wave which loads along the Rayleigh line. This loading is assumed an instantaneous jump from the initial to equilibrium state. This means the smearing of the shock front resulting from the 2D effects is not fully accounted for in the bulk material response.

This can be illustrated by comparing the bulk dissipation response of the various angular orientations presented in Section 4.1. The pressure traces and high resolution microstructural simulations showed that the parallel configuration exhibited more dissipation as a result of interfacial shear, as stated in Section 4.1.4. However, plotting the bulk dissipation for each orientation, which is given in Figure 4.23, shows that

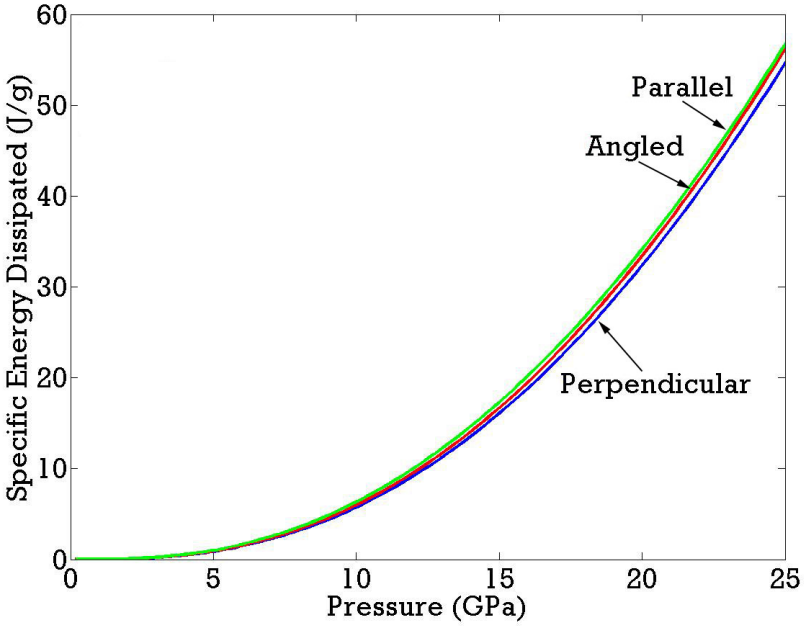

Figure 4.23: Specific energy dissipated as a function of pressure for the perpendicular, angled, and parallel orientations.

only a slight difference between the three orientations is observed. Not accounting for the 2D effects in the shock rise leads to the similar behavior, which was also seen in the P-U_P response given in Figure 4.18. To fully capture the dissipative response, the shock rise times and particle level simulations must be considered. These two metrics help to quantify and explain the dissipation occur during shock loading, and provide a means for identifying the underlying mechanisms responsible for changes in the bulk dissipation, even if they are small.

For the present study on microstructural parameters, each configuration described in this section has an identical orientation. This means all the assumptions inherent in calculating the bulk dissipation are consistent across each configuration. This consistency enables trends to be extracted from the bulk dissipation results, which are further understood and explained using the shock rise times and particle resolved simulations. In addition, the microstructural changes in this section are more pronounced than the change in interfacial orientation presented previously. This causes

Table 4.4: U_W vs. U_P fits for each configuration for $U_P < 1000$ m/s.

Configuration	C_0 (m/s)	S_1
14 micron	4491	1.572
28 micron	4408	2.003
42 micron	4533	1.981
56 micron	4642	1.989
112 micron	5227	1.492
Pure	4753	1.600
Half	4474	1.888
Uniform	4276	1.969
Non-Bonded	5126	1.482

the variations in bulk dissipation to be more severe, more clearly illustrating the dissipative trends. Based on these factors, the bulk dissipation was assumed to be an appropriate metric for determining trends in dissipation between configurations.

4.2.2 EOS Determination for Each Parallel Configuration

Using the same procedure as outlined in Section 4.1.1, the EOS was found for each parallel microstructural variation. The inert sound speeds and material constants corresponding to the U_W-U_P response for each configuration, valid for $U_P < 1000$ m/s, are given in Table 4.4. The results show that there is a marked change in the bulk properties as the bilayer spacing and material properties change. These changes result from alterations in the dispersion and dissipation of the shock wave, which are discussed in the following sections.

An interesting outcome of these results is the validation of the convergence of the mesh used for the orientation study in Section 4.1. To investigate the effects of microstructural changes on the parallel configuration, the mesh resolution was increased by a factor of two, which was justified in Section 4.2.1.2. The EOS parameters for the 28 micron configuration presented in Table 4.4 are within 3% of those reported in Section 4.1.4 ($U_S = 4455 + 1.952U_P$ m/s). This proves the mesh used in Section 4.1 had converged, since the EOS response did not appreciably change when the mesh resolution increased.

4.2.3 Effect of Interfacial Density on Shock Wave Dispersion and Dissipation

For the purpose of comparing the dispersive behavior, the shock fronts for the various bilayer spacings are shown in Figure 4.24. To aid in the comparisons and clearly display the trends, the curves are shifted along the abscissa. The 14 micron configuration is seen to have a shorter rise time compared to the 28 micron response. Additionally, the 42 and 56 micron configuration are seen to have similar rise times to the 28 micron configuration, showing only slight increases with increasing bilayer spacing. However, this trend does not continue for the 112 micron configuration. The rise time decreases drastically compared to the 56 micron configuration, becoming similar to that seen for the 14 micron configuration. These results show how important interfacial density is on the dispersion of the system. In addition, they suggest a maximum in dispersion is observed for a bilayer spacing of around 50 microns. This peak in dispersion can be explained by the differing 2D effects in each configuration.

At higher interfacial densities, like the 14 micron configuration, two dimensional effects become less pronounced. With a high number of layers, the areal change of each is less. In addition, the increased interfacial density and smaller separation of materials causes more wave interactions, leading to faster dispersion of the wave energy and quicker equilibration of the system. Less separation is then generated between the wave front and the equilibrated response, meaning shorter rise times. As interfacial density decreases, longer times are needed to equilibrate the response and the shock front begins to spread out. This separation seems to remain relatively constant between bilayer spacings of 28 to 56 microns, with only slight increases observed in dispersive behavior. As the interfacial density is lowered further to that of the 112 micron configuration, there are now very few wave interactions. With so few wave interactions, the dispersion in the system decreases. In addition, the lower interfacial density decreases the energy dissipated over the rise of the shock

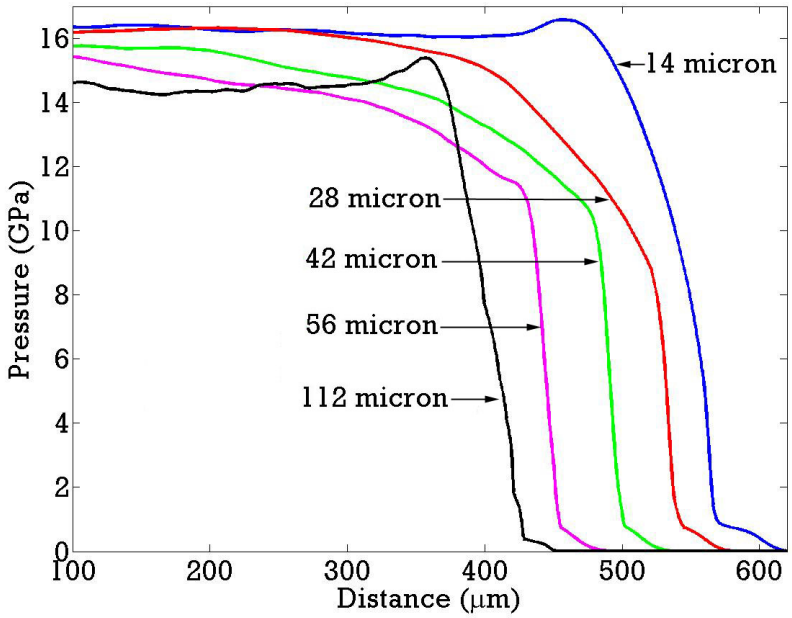

Figure 4.24: Shock fronts for the various bilayer spacings showing an initial increase in dispersion with decreasing interfacial density. Further decreases in interfacial density eventually lead to a decrease in dispersion.

pulse. These factors lead to less smearing of the shock front over the computational domain, which is seen in the shorter rise time. It is possible, that after a long enough propagation distance, the rise time of the 112 micron configuration could be on the same order or larger than the 28, 42, and 56 microns configuration. However, simulations on a 2mm long domain did not show any change in the rise time of the shock pulse over the composite. As a result, the shock front shown in Figure 4.24 was assumed to accurately represent the dispersion in the 112 micron configuration.

The effect of the interfacial density on dissipation is closely related to the dispersive behavior. Figure 4.25 shows the specific energy dissipated at various shock pressures for each bilayer spacing. The dissipation is seen to increase from the 14 to the 28 micron configurations. However, with further increases in bilayer spacing, the dissipation is seen to decrease slightly until the 112 microns configuration when the dissipation drops significantly. As a result, a peak in the dissipative response is

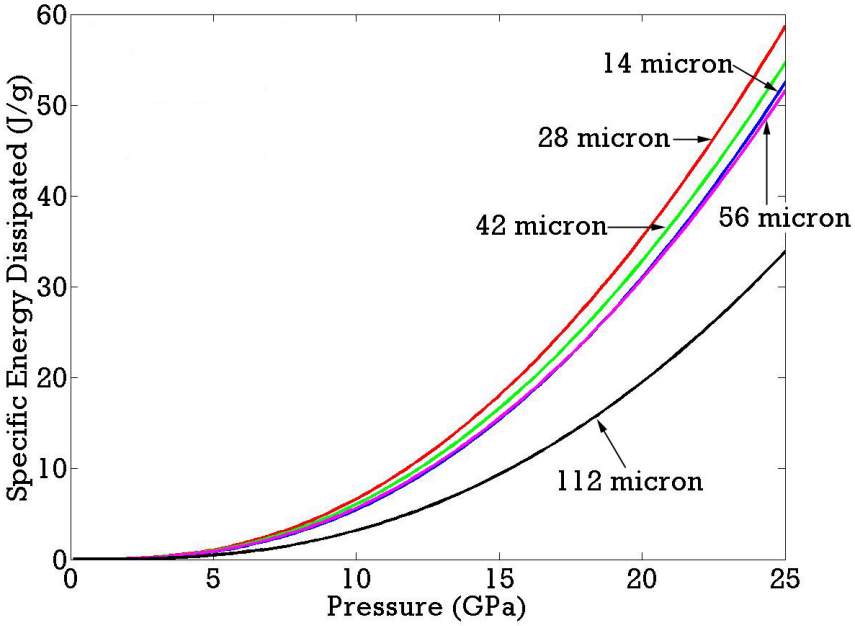

Figure 4.25: Effect of bilayer spacing on the specific energy dissipated as a function of pressure. The dissipation is seen to increase from the 14 to the 28 micron configurations. With further increases in the bilayer spacing, the dissipation is seen to decrease.

seen for a bilayer spacing of around 30 microns in the parallel configuration. While these differences can be observed with the bulk response, the rise times and higher resolution simulations clearly illustrate the mechanisms responsible.

The high-resolution AMR simulations were used to explore the peak in the dispersion and dissipation based on the interfacial responses of each configuration. As shown previously, differing material velocities in the Ni and Al layers lead to elevated temperatures and strain at the material interfaces. Since the temperature and strain responses are closely tied, profiles of either can be used to understand the interfacial behavior in each configuration. For this section, the temperature profiles are used because they are believed to give a more complete picture of the microstructural effects.

The temperature profile generated with the high resolution simulations for the 14 micron configuration is shown in Figure 4.26a. A histogram corresponding to this

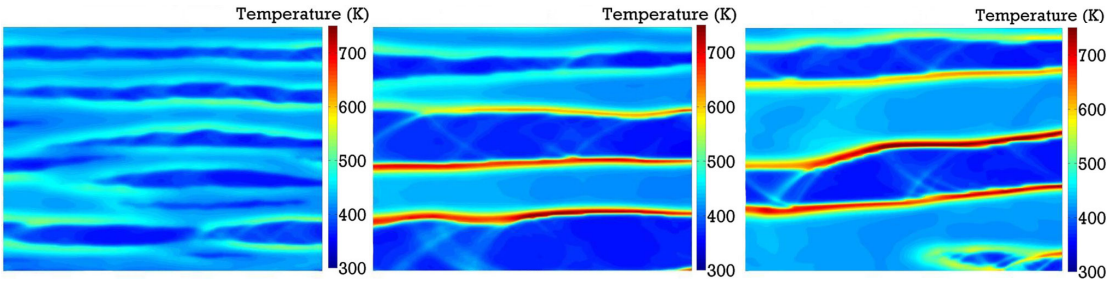

(a) 14 Micron (b) 28 Micron (c) 56 Micron

Figure 4.26: High resolution simulation showing the temperature profiles for the 14 (a), 28 (b), and 56 (c) micron configurations. The 14 micron simulation is seen to have a more uniform temperature response due to the faster equilibration of the system. As the bilayer spacing is increased, the interfacial temperatures are seen to increase due to the prolonging of the disparity between material velocities. Since the increase in interfacial temperature is closely tied to the rise of the shock pulse, the temperature profiles for the 28 and 56 micron configurations are seen to be similar.

temperature profile was also generated and is shown in Figure 4.27a. As was seen in the orientation simulations in Section 4.1, the Al layers exhibit elevated temperatures compared to the Ni layers. The multiple wave interactions and small separation distance of the materials at such a high interfacial density leads to the fast equilibration of the material response. Not only does this cause a shorter rise time, as seen in Figure 4.24, but it also affects the interfacial temperatures.

With fast equilibration of the system, the disparity in material velocities between Ni and Al does not persist long. This effect, coupled with the high interfacial density, means each interface is undergoing less strain, which causes the lack of elevated temperatures at the material interfaces seen in Figure 4.26a. Since the interfaces are not reaching elevated temperatures and high strain values, they dissipate less energy. This result can also be seen in the temperature histogram shown in Figure 4.27a. The histogram shows one large, broad peak and no tail. The broad peak means the multilayer is equilibrating fast. In addition, the lack of a tail means that hot regions are not being developed at the material interfaces.

As the interfacial density decreases for the 28 micron configuration, the dissipation

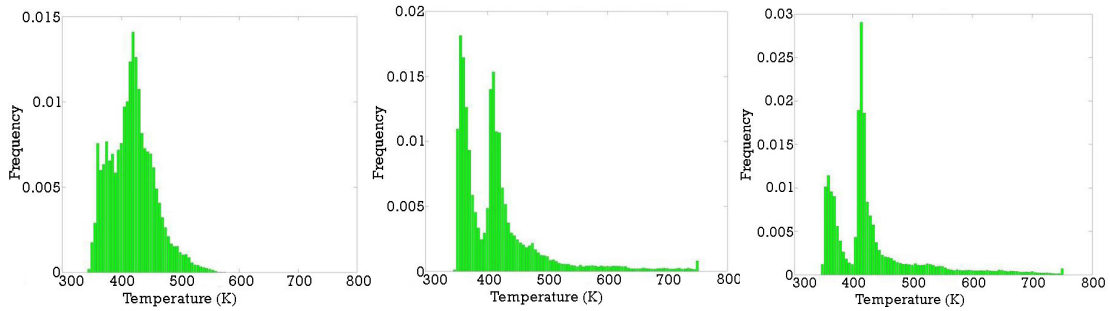

(a) 14 Micron (b) 28 Micron (c) 56 Micron

Figure 4.27: Temperature histograms for the high resolution simulation on the 14 (a), 28 (b), and 56 (c) micron configurations. The 14 micron simulation is seen to have a single large, broad peak with no tail, due to the faster equilibration of the composite. The histograms for the 28 and 56 micron configurations are seen to exhibit two peaks corresponding to the temperatures seen in each material. Additionally, the 28 and 56 micron configurations exhibit extensive tails in the distributions signifying elevated interfacial temperatures. The similarities between the tails of the 28 and 56 micron configurations show that the interfacial temperatures are not significantly increasing between the configurations.

increases, as seen in Figure 4.25. The reasons for this can, once again, be seen in temperature profile and corresponding histogram are presented in Figures 4.26b and 4.27b, respectively. From the temperature profile, it is immediately obvious that the interfacial strain has increased in the 28 micron configuration compared to the 14 micron simulation. The decrease in interfacial density has further separated the materials and reduced the number of wave interactions. This produces longer equilibration times, as indicated by the rise times shown in figure 4.24. As a result, the disparity in material velocities persists longer in the 28 micron configuration than the 14 micron configuration. The longer equilibration time generates more strain at the material interfaces, producing the higher temperatures seen in Figure 4.26b. This effect is also visible in the temperature histogram shown in Figure 4.27b.

The temperature histogram for the 28 micron configuration shown in Figure 4.27b exhibits two distinct peaks, which correspond to each constituent. The first peak represents the cooler Ni layers, while the second the warmer Al layers. With further separation of the materials, the individual layers maintain larger temperature

differences and the dual peak structure develops in the histogram. The temperature histogram shown in Figure 4.27b also contains a long tail, which corresponds to the development of higher temperatures at the material interfaces. In the 28 micron configuration, the longer equilibration times lead to more interfacial shear. This causes the energy dissipated at each interface to increase when compared to the 14 micron configuration. The increase in dissipation at the interfaces is large enough to offset the decrease in interfacial density of the 28 micron configuration relative to the 14 micron configuration. This produces the elevated dissipative response of the 28 micron configuration seen in Figure 4.25. The results show that more interfaces do not necessarily translate into more dissipation, since such changes to the geometry alter the energy dissipated per interface.

As the bilayer spacing is further increased, the dissipation was seen to decrease in Figure 4.25. The behavior can, once again, be explained with the high resolution temperature profile for the 56 micron configuration shown in Figure 4.26c. As was shown in Figure 4.24, the dispersion is seen to remain fairly consistent between the 28, 42, and 56 micron configurations. Only slight increases in rise times were seen to occur. Therefore, the further separation of the materials has not dramatically affected the time scale of the wave interactions. This means the disparity in the material velocities persists on a similar time scale for the 28 and 56 micron configurations. The interfacial strain is then expected to be similar between the two configurations. This is seen in the similar interfacial temperatures observed in Figures 4.26b and 4.26c. There are slight differences between the 28 and 56 micron configurations, which are more clearly distinguished in the temperature histograms shown in Figures 4.27b and 4.27c.

The 56 micron configuration histogram (Figure 4.27c) is seen to have a dual peak structure similar to that of the 28 micron configuration (Figure 4.27b). The peaks

corresponding to the individual materials are more distinct in the 56 micron configuration, due to the further separation of materials. More importantly, the tails of the distributions, which represent the elevated interfacial temperatures, are seen to increase only slightly. This suggests a sort of saturation point for the interfaces or, more appropriately, a point of diminishing marginal returns. As the interfacial density decreases further from the 28 micron configuration to the 56 micron configuration, the interfaces are seen to only accommodate modest increases in strain. This results in only slight increases in dissipation per interface, which are not significant enough to offset the loss of interfacial area. As a result, the bulk dissipation decreases, causing the downturn in dissipation with increasing bilayer spacing after the 28 micron configuration shown in Figure 4.25.

The differing dispersive and dissipative characteristics of each configuration can also be observed in the EOS response. The EOS parameters for each bilayer spacing were provided in Table 4.4 and are shown graphically in Figure 4.28. It is hard to draw strict comparisons between C_0 and S_1 with dispersion or dissipation, since both phenomena alter the value of these parameters. However, using the results discussed above, it becomes apparent that a decrease in dispersion or dissipation produces a shallower slope and increased inert sound speed in the multilayer composites. These effects are evident in the similar slopes of the two extremes (14 and 112 micron configurations) and the three middle configurations (28, 42, and 56 micron configurations). Both the 14 and 112 micron simulations had lower dispersion than the other configurations. The 112 micron simulation also has a much lower bulk dissipation, which would suggest S_1 is closely tied to the dispersion.

An additional observation is seen in the position of each of these curves. As the bilayer spacing is increased, the EOS response is seen to shift upwards to higher wave speeds. This can be thought of as a decrease in the impedance of the composite. With a lower interfacial density, there are fewer obstacles to inhibit wave motion and

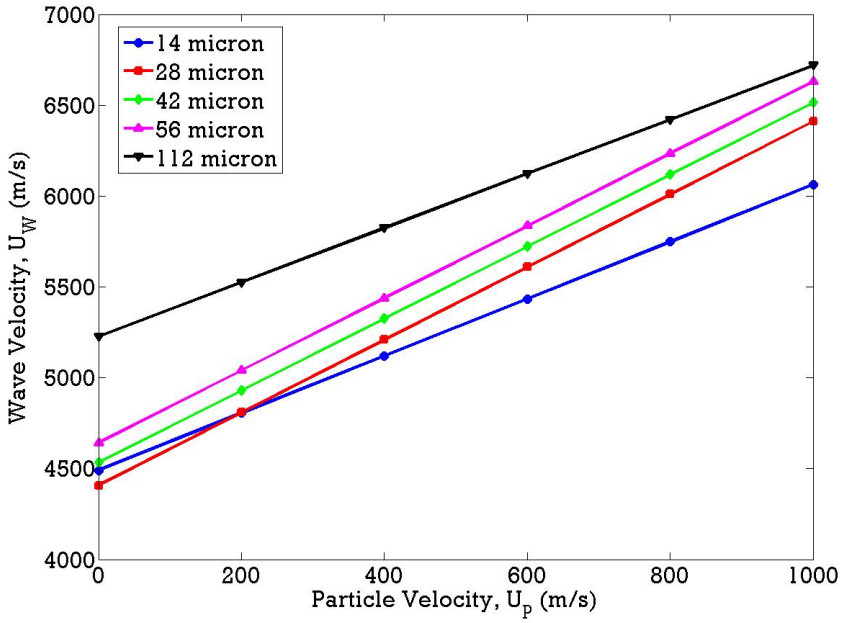

Figure 4.28: U_W vs. U_P relationship for the different bilayer spacings up to $U_P =$ 1000 m/s. Dispersive and dissipative effects are seen to have a large effect on the observed EOS response.

the material appears less stiff.

The differences in the EOS responses seen in Figure 4.28 are not particularly large ($\sim$ 100 m/s) for the three middle configurations. This presents some complexities if the differences are attempted to be distinguished experimentally. If the differences found in this analysis were too small to be distinguished experimentally, it would render this analysis moot. However, the separation of the various bilayer spacings is not too small to prevent experimental validation. Their close proximity would add complexity to the experimental procedure, but nothing that could not be overcome with standard practices. With sufficient sample size and proper preparation, errors in wave speed below 100 m/s can be obtained and these trends can be validated.

4.2.4 Effect of Interfacial Structure and Strength on Dispersion and Dissipation

The nature of the material interfaces also influences the dispersive and dissipative response of the multilayer composites. Both the interfacial structure and strength were varied to understand these effects. Interfacial structure was investigated by comparing the responses of a cold-rolled multilayer, represented by the 28 micron configuration, to that of a uniformly layered composite with the same bilayer spacing, constituent ratio, and material properties. This isolated the effects of the heterogeneities generated through rolling. Bounds were also obtained for the interfacial coherency by comparing the responses of the 28 micron configuration with both perfectly bonded and completely unbonded interfaces. Through these studies, the effects of the interfacial strength and structure on the particle level and bulk material responses were determined.

The shock fronts for these three configurations are presented in Figure 4.29. Once again, the curves are shifted along the abscissa to more clearly present the trends. As was seen previously in Section 4.1.4, the uniform composite has a dual wave structure. The heterogeneities generated during rolling are seen to obscure this dual wave structure, smoothing the wave front without altering the rise time. This shows that rolling only slightly increases the dispersion of the wave, and suggests that the dispersion of the wave is influenced more by the orientation and density of the interfaces than their structure. For the non-bonded composite, the wave dispersion is seen to decrease dramatically. With both materials able to move freely, the interfaces dissipate no energy. Without dissipation at the material interfaces, the waves in each material never significantly separate. The free motion also causes fewer wave interactions. These factors lead to the short rise time and lower pressure observed in the non-bonded composite.

The effects of interfacial strength and structure on the bulk dissipation response

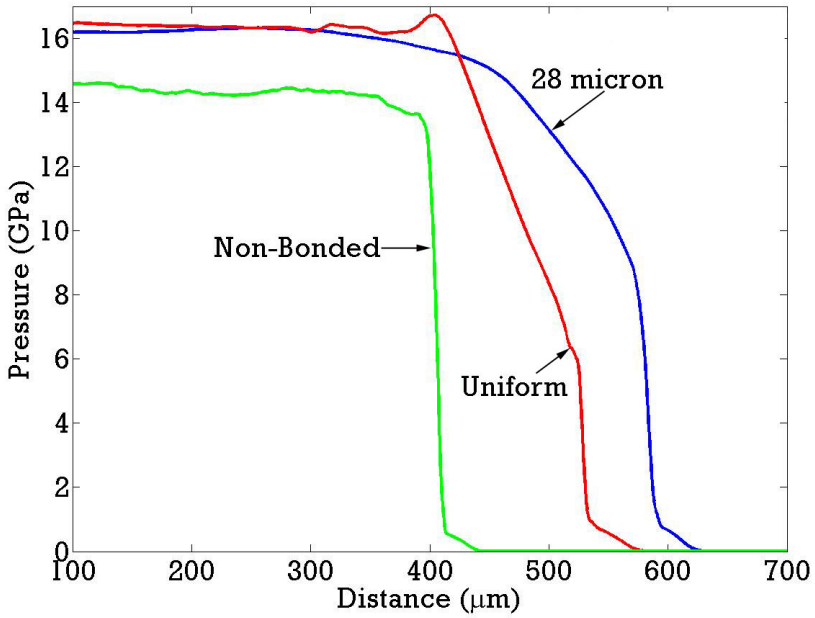

Figure 4.29: Shock fronts for the 28 micron, uniform, and non-bonded composites. Heterogeneities generated through rolling are seen to only slightly increase dispersion, while the interfacial strength is seen to have a dramatic effect.

are presented in Figure 4.30 and highlight the importance of interfacial strain for dissipating energy. Interfacial structure is seen to have a slight effect on the dissipation, with the uniform composite being slightly more dissipative than the cold-rolled composite. This results from the geometry of the uniform composite. With uniform layering, all material interfaces are aligned perfectly parallel to the propagating shock wave. This orients the entire material interface to maximize the interfacial shear generated by the disparity in particle velocities between the layers, leading to the larger amount of energy dissipation seen in Figure 4.30. The increase is only slight though, since the rolled composite is still fairly laminar. In contrast, the effect of interfacial strength has a significant effect on the bulk dissipation. With no interfacial strength, the free motion of each material eliminates interfacial shear as a means of energy dissipation. This makes compression the only mechanism for energy dissipation, and the bulk dissipation drops dramatically from that of the perfectly bonded case, as

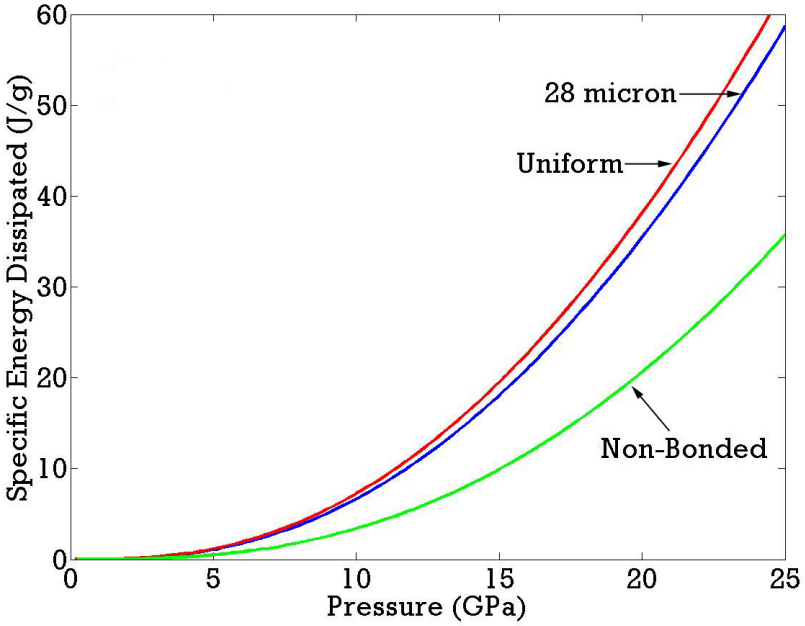

Figure 4.30: Effect of material heterogeneities and bonding on the specific energy dissipated as a function of pressure. The results highlight the importance of interfacial shear in each configuration. With uniform layers, the entire interface is aligned to optimization interfacial shear and leads to a slight increase in dissipation. When the strength of the interfaces is removed, no interfacial shear develops and the dissipation drops drastically.

seen in Figure 4.30.

The dispersive and dissipative characteristics can also be seen in the EOS response for each composite, which is shown in Figure 4.31. The parameters corresponding to each curve can be found in Table 4.4. The lower dispersion and dissipation in the non-bonded configuration decreases the material slope and increases the inert sound speed compared to the 28 micron composite. This is consistent with the observations made for the various bilayer spacings. Of more interest are the responses of the 28 micron and uniform composites. Both are seen to have similar slopes, but varying inert sound speeds. This comes from the somewhat off-setting combination of an increase in dissipation and a decrease in dispersion seen in the uniform configuration. While the increase in dissipation lowers the slope and increases the sound speed, the increase in dispersion acts oppositely. The end result is the slight shifting up of the

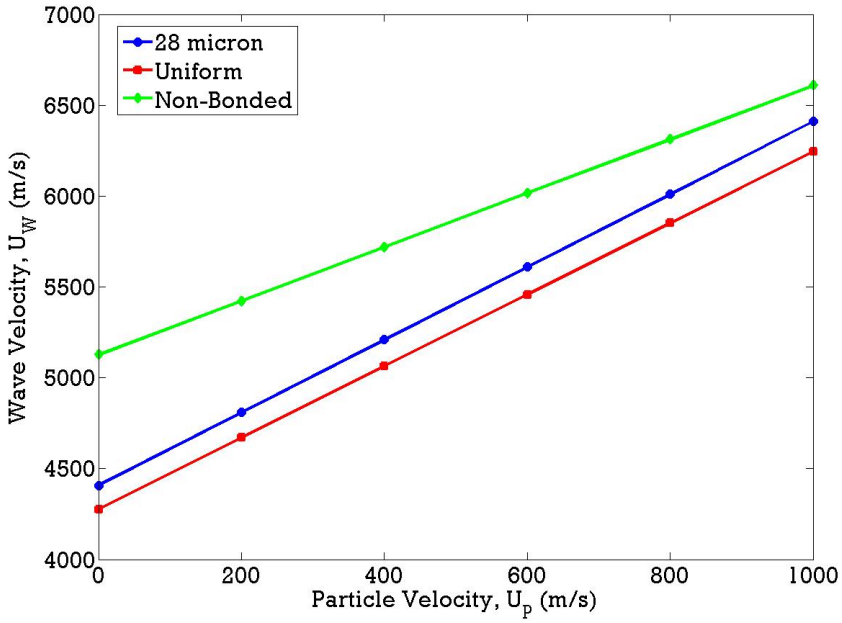

Figure 4.31: U_W vs. U_P graph for the uniform and non-bonded cases compared to that for the 28 micron configuration.

uniform EOS curve to higher wave speeds.

4.2.5 Effect of Strain Hardening on Dispersion and Dissipation

The effect of strain hardening on the dispersion and dissipation response was also investigated. This was accomplished by using the 28 micron configuration as a standard. With this standard microstructure, the yield strength of each composite was changed to mimic varying levels of strain hardening. Simulations were run with the strengths of pure Ni and Al, termed the pure configuration, and values half way between the measured values and those for the pure materials, termed the half configuration. The results were then compared to the 28 micron configuration to fully characterize the effect of strain hardening.

The shock fronts for the three degrees of strain hardening investigated are presented in Figure 4.32. Once again, the curves are shifted along the abscissa. Strain hardening is strictly a material property and does not affect the geometry of the

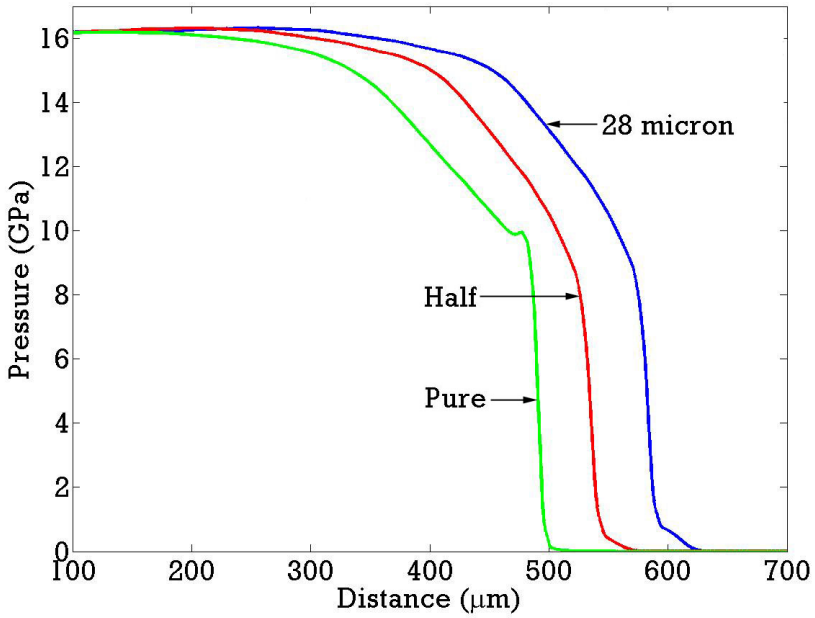

Figure 4.32: Effect of strain hardening on the shock front. Since variations in the strain hardening do not affect the geometry of the system, no significant change in the dispersion of the shock wave is observed.

system. As a result, no significant variations were expect or seen in the dispersive response of each strain hardening configuration. There is some increase in dispersion in the half hardened configuration compared to the pure configuration. However, it is very slight and represents an areal change of the layers. In the pure configuration, the layers are softer and deform more in the rise of the shock pulse. This changes the geometry of the system and causes the slight change in the dispersion of the shock wave.

The dissipative response of each level of strain hardening can be seen in Figure 4.33. The results show a non-linear trend of decreasing dissipation with decreasing strain hardening. The decrease in dissipation between the half and 28 micron configurations is small compared to the decrease between the half and pure configurations. The lower level of dissipation in the softer composite stems from the increased compressibility of the materials. With less strain hardening, the interiors of each layer

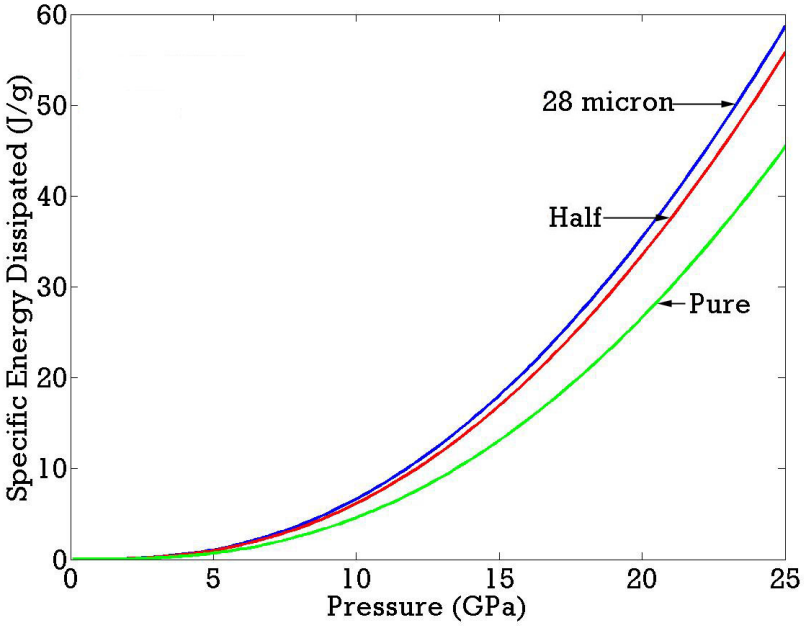

Figure 4.33: Effect of work hardening on the specific energy dissipated as a function of pressure. As the strain hardening decreases, the specific energy dissipated is seen to decrease. This can be attributed to the increased deformation of the layer interiors.

accommodate more deformation. This means the deformation is not being isolated at the interfaces like in the more hardened composites. That lowers the amount of interfacial strain and decreases the bulk dissipation, as seen in Figure 4.33.

This behavior is clearly seen in the high resolution temperature profiles for the pure and half configurations presented in Figure 4.34. The higher compressibility of the layers in the pure configuration reduces the interfacial strains and temperatures generated in the composite. This is seen when comparing the temperature profiles of the pure and 28 micron configurations in Figures 4.34a and 4.26b. However, the decrease in dissipation is not directly proportional to the strain hardening of the material. This observation is evident in the similar interfacial temperatures achieved in the half hardened and 28 micron configurations, shown in Figures 4.34b and 4.26b. Despite being hardened to a much lower degree, the half hardened configuration is seen to have similar interfacial temperatures to the 28 micron composite. These

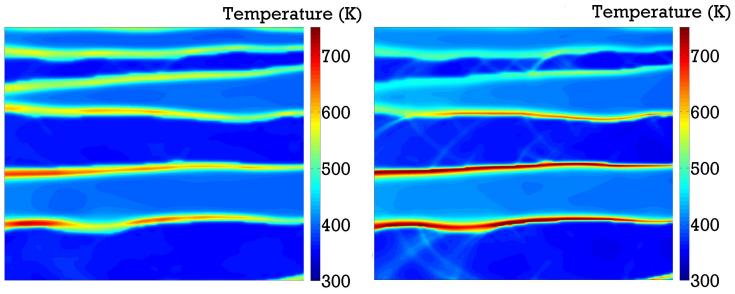

(a) Pure Configuration (b) Half Configuration

Figure 4.34: High resolution simulation showing the temperature profiles for the pure (a) and half (b) configurations. The increased compressibility of the pure configuration leads to more deformation in the material layers, lowering interfacial strain compared to the half and 28 micron (Figure 4.26b) configurations. This loss in interfacial strain causes the decrease in dissipation seen with decreasing strain hardening in Figure 4.33.

results show that the influence of strain hardening on the dissipative response of the multilayers is tied very closely to the level of deformation in the interior of the material layers. As a result, the effects of increased hardening are seen to diminish at a certain point, since most of the deformation is already isolated at the interfaces.

The dissipative characteristics can also be observed in the EOS response of each configuration, as shown in Figure 4.35. The differing strain hardenings have essentially identical dispersive characteristics, due to their identical geometry. This means that the variations in their EOS responses are solely the result of their differing levels of dissipation. As stated previously, decreases in dissipation produce a decrease in the slope of the EOS and an increase in the inert sound speed, which is exactly what is observed in the responses of the various strain hardenings. The 28 micron and half configurations have slight different slopes and inert sound speeds, due to the small difference in their dissipative behavior. The less dissipative pure configuration, on the other hand, has a much larger inert sound speed and a lower slope.

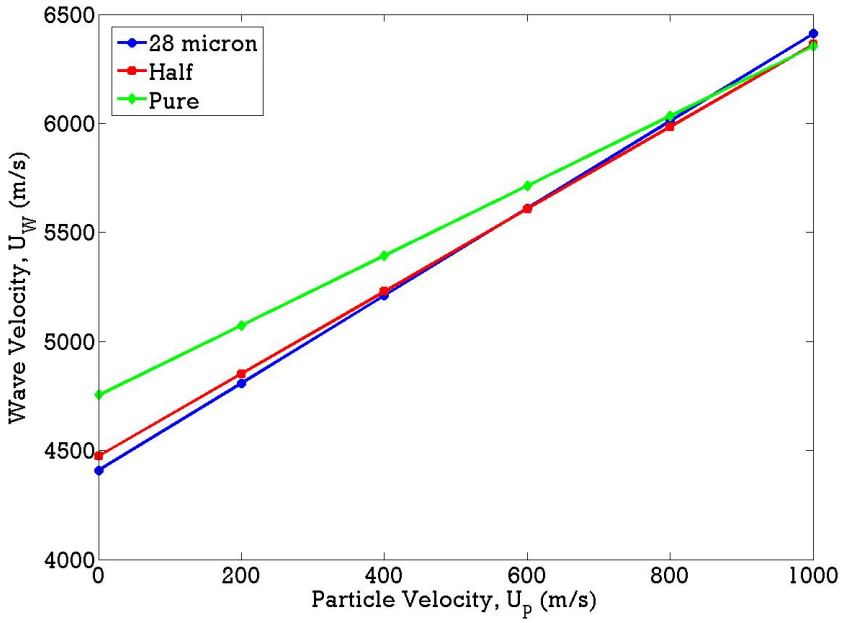

Figure 4.35: U_W vs U_P graph for various degrees of strain hardening investigated for the 28 micron bilayer composite. The decrease in dissipation between these configurations leads to a decrease in the slope and an increase in the inert sound speed.

4.2.6 Microstructural Effects on Shock Wave Attenuation

The above results showed how microstructural variations affect the observed material response. One of the more interesting results was the identification of an optimal bilayer spacing for maximizing both dispersion and dissipation based on the mechanics of the wave interactions. Building on these results, it was desired to see if an optimal configuration could be achieved for the attenuation of a shock wave. The ability to quickly attenuate a shock wave is useful for a variety of applications, such as a spall liner.

For this purpose, the computational domains for each parallel configuration were extended to 2mm to allow for longer tracking of the shock pulse. The composites were then impacted by a thin Cu flier at 1500 m/s to propagate a 50 ns shock pulse through the composite. For constancy, the simulation parameters and method for tracking the shock wave were kept identical to that outlined in Sections 4.1.1 and 4.2.1. In

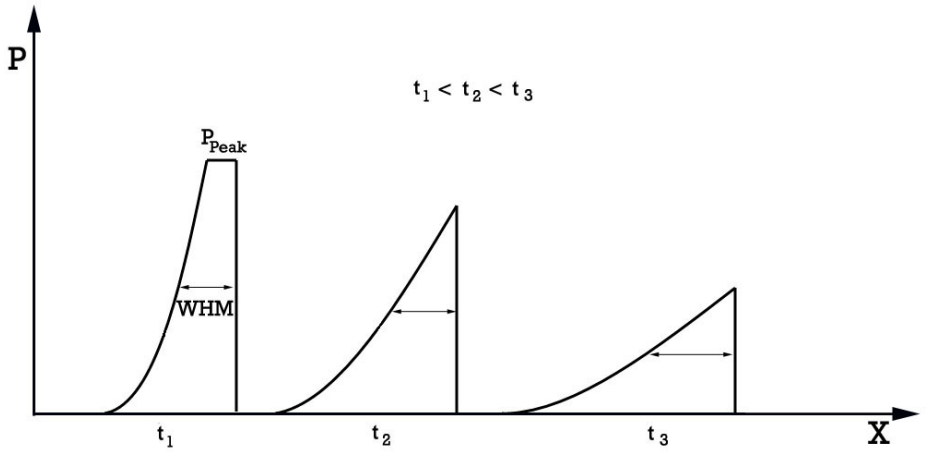

Figure 4.36: Schematic of the attenuation of a shock pulse showing the peak pressure and width-at-half-max.

addition, bounds for the attenuation of the shock wave were found by simulating each constituent and a homogeneous mixture as defined by McQueen mixture theory [45]. This generated the responses for composites containing infinite and zero bilayer spacings, respectively.

To characterize the attenuation of the shock pulse two metrics were employed: the peak pressure, P_{Peak}, and the width-at-half-maximum, WHM. These metrics are shown schematically in Figure 4.36. Both the peak pressure and WHM change with propagation distance and these changes can be used to characterize the attenuation of the shock pulse. The WHM provides an excellent metric of dispersion, since it is directly related to the spreading of the wave energy. The WHM values 280 ns after impact for each configuration are presented in Table 4.5. The more dispersive a system is the larger WHM value it has at 280 ns. Consequently, the WHM allows for a qualitative way to compare the dispersive behavior between each configuration, which is observed in how closely the values presented in Table 4.5 match the dispersive characteristics described in the previous sections. The peak pressure, on the other hand, is affected by both the dispersion and dissipation. As a result, the peak pressure was used to quantitatively describe the attenuation of the shock pulse.

Table 4.5: Critical propagation time and distance for each configuration along with the WHM values 280 ns after impact.

Configuration	t_{cr} (ns)	λ_{cr} (bilayers)	λ_{cr} (mm)	WHM at 280 ns (μm)
14 micron	4694	2044.7	28.6	378.4
28 micron	3712	769.3	21.5	491.6
42 micron	3279	467.7	19.6	564.4
56 micron	3252	353.3	19.8	556.0
112 micron	5118	287.6	32.2	391.6
Pure	3791	794.7	22.2	502.4
Half	3696	767.6	21.5	493.6
Uniform	4189	850.8	23.8	415.2
Non-Bonded	5019	1129.7	31.6	367.6
Al 5052	10662	-	-	324.0
Ni	16690	-	-	271.0
Mixture	14091	-	-	296.0

The peak pressure was tracked every 40 ns for all configurations. Using the decay of the peak pressure with propagation distance, the critical time and distance at which the wave had fully attenuated was determined. This was accomplished by using an exponential fit to describe the change in peak pressure observed at each time interval.

$$M = A_P^x exp(k_x x) \tag{4.7}$$

Here, x corresponds to the variable of interest, either the propagation time or distance. The parameters in each configuration for these exponential fits for both time and distance are presented in Table 4.6. The point at which the wave was assumed to fully attenuate was chosen to be when $P_{Peak} = 0.01$ GPa. This value enables the determination of the resulting critical propagation times (expressed in ns) and distances (expressed in bilayers and mm) for each configuration using the fit obtained from Equation 4.7. The values are listed in Table 4.5. From these results, the effects of interfacial structure, interfacial strength, and strain hardening on wave attenuation can be observed. In addition, it is clearly seen that an optimal bilayer spacing exists for the attenuation of a shock wave.

From the results presented in Table 4.5, it is observed that dispersion is the

Table 4.6: Fit parameters for the peak pressure to the propagation time and length.

Configuration	$A^t_{P_{Peak}}$ (GPa)	k_t (ns^{-1})	$A^\lambda_{P_{Peak}}$ (GPa)	k_λ (μm^{-1})
14 micron	31.09	2.204e-3	31.07	-5.059e-3
28 micron	30.40	2.781e-3	30.47	-1.342e-2
42 micron	30.47	3.149e-3	30.37	-2.207e-2
56 micron	30.36	3.176e-3	30.41	-2.922e-2
108 micron	28.15	2.002e-3	31.07	-3.559e-3
Pure	30.15	2.721e-3	30.17	-1.298e-2
Half	30.42	2.793e-3	30.48	-1.345e-2
Uniform	31.71	2.474e-3	31.92	-1.219e-2
Non-Bonded	27.82	2.039e-3	27.53	-9.049e-3

dominant factor effecting the attenuation of a shock wave. This is clearly illustrated by the influence of strain hardening. As stated previously in Section 4.2.5, strain hardening has very little effect on the dispersion of the shock wave but a noticeable influence on dissipation. From the results presented in Table 4.5, the attenuation of the shock pulse is not significantly altered by strain hardening, suggesting dissipation has a negligible effect. Additional evidence is obtained when comparing the effects of interfacial structure and strength. The heterogeneities due to rolling were seen to slightly increase dispersion and lower dissipation. Despite being more dissipative, the uniform composite takes longer to attenuate the shock wave. Based on these results, shock wave attenuation is seen to be influenced almost exclusively by dispersion.

The results presented in Table 4.5 also suggest an optimal bilayer spacing exits for the attenuation of a shock wave. For this analysis, the response of the homogeneous mixture is set as the lower bound for interfacial density with an assumed bilayer spacing of 0.1 microns. The upper bound for bilayer spacing is then set as the average response between Al and Ni. Since the domain investigated was 1 mm x 1 mm, this upper limit was set at a bilayer spacing of 1000 microns. Since the critical times at both extremes are roughly the same, each was set at 14000 ns, and the critical distance at each bound was assumed to be 100 mm.

Figure 4.37 shows the critical time and distance data for each bilayer spacing. It

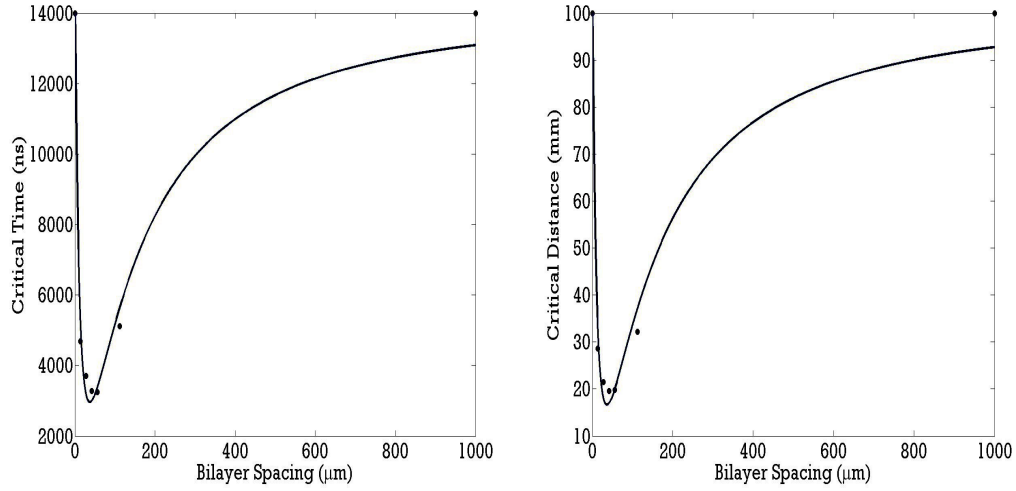

(a) t_{cr} (b) λ_{cr}

Figure 4.37: Attenuation data and corresponding fits for t_{cr} (a) and λ_{cr} (b). Both results suggest the optimal bilayer spacing for the dispersion of a shock wave around 50 μm.

becomes apparent that each data set can be fit with an inverted log-normal distribution of the following form.

$$f(x) = Y_0 - \frac{a}{x\sqrt{b\pi}} exp\left(\frac{-(ln(x) - c)^2}{b}\right) \tag{4.8}$$

Here, x is once again the variable of interest (*i.e.* time or distance) and a, b, and c are fitting parameters. Using this equation, the fits presented in Figure 4.37 for both the critical time and distance were generated. The parameters for these fits can be found in Table 4.7. While this functional form captures the overall trends, its accuracy in the trough is poor. Regardless, both the raw data and computational fits can be used to estimate the optimal bilayer spacing for the attenuation of a shock wave of around 50 microns, which is in agreement with the shock fronts presented in Section 4.2.3. The results show that through a judicious choice of bilayer spacing the attenuation of a shock wave in a layered, binary composite can be lowered to $\sim$ 20% of that for either constituent.

Table 4.7: Fit parameters for t_{cr} and λ_{cr}.

Variable	Y_0	a ($Y\mu m^2$)†	b (μm^2)	c (μm)
t_{cr}	14000 ns	8.219e-7	5.786	4.334
λ_{cr}	100 mm	1.071e-4	5.842	4.493

†Y corresponds to either time or distance

4.3 Shock Compression Response of the Shock Compacted Powder Compact

In addition to the multilayer composites, fully dense powder compacts of Ni and Al generated through shock compaction [163, 164] were also investigated. The shock compacted microstructures present a fully dense composite with a similar volume ratio to the multilayer composites but very different interfacial characteristics. The spherical nature and random distribution of the particles in the shock compacted composite present a microstructure that lacks the periodicity and consistent angular orientation of the material interfaces present in the multilayered composites. This makes the shock compacted microstructure a nice complement to the multilayer composite for understanding the effects of interfacial characteristics on the shock compression response. In addition, the shock compacted composites can provide a bridge for comparison to past work on porous powder composites [27], which is discussed later in Chapter 7.

4.3.1 Microstructure Generation and Computational Method

The differing interfacial characteristics of the shock compacted composite can be seen in the CTH rendering of its micrograph (Figure 3.15), presented in Figure 4.38. The shock compacted microstructure is represented in CTH as Ni particles embedded in an Al matrix. During the dynamic compaction process used to generate these composites, the softer Al flows around the harder Ni generating this matrix. This leaves the Ni particles fairly undeformed, leading to the convex interfaces seen in Figure 4.38.

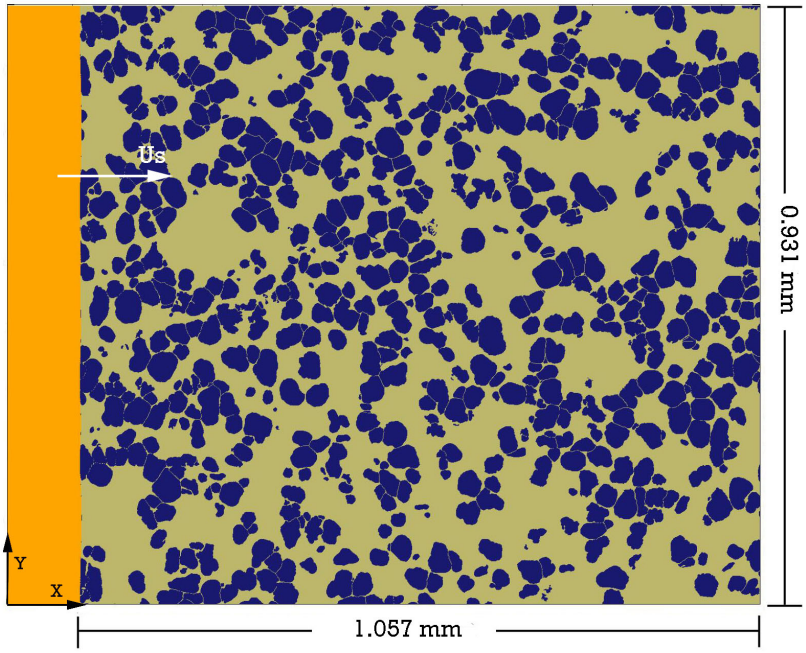

Figure 4.38: CTH rendering of the shock compacted composite. The microstructure is represented as spherical Ni particles in an Al matrix.

The shock compacted microstructure was incorporated into CTH with the same procedure used for the multilayer composites outlined in Section 4.1.1. The CTH rendering, shown in Figure 4.38, accounts for particle pullout during polishing, as discussed in Section 3.5. The CTH rendering has a Ni volume fraction of $\sim 44.7\%$ and a $S_V = 110.9\frac{1}{mm}$. Once again, the CTH rendering is seen to accurately represents the optical micrograph (Figure 3.15) maintaining the volume fractions of the constituents to within an error (*i.e.* $\frac{\sigma_{V_V}}{V_V}$) of 2%. Computationally, the analysis of the shock compacted composite was essentially identical to that of the multilayers given in Section 4.1.1. The only exception was in the mesh resolution. While the simulations were found to converge around the same point, the odd shape of the shock compacted computational domain lead to the choice of ~ 0.75 μm per cell. Since both mesh resolutions were found to converge, the deviation in resolution presents no obstacles for comparison between the results.

4.3.2 Shock Compacted Powder Compact Results

The shock compacted composite presents a more isotropic microstructure than the multilayer composites. However, heterogeneities in the distribution of the Ni particles lead to spikes in the observed pressure response. These spikes tend to be dispersed more than those observed in the perpendicular multilayer composite. This gives a more uniform pressure response, similar to that seen in the angled multilayer composite. This is observed in the small undulations in the average pressure response of the shock compacted composite 120 ns after impact at 1000 m/s seen in Figure 4.39.

The shock compacted composite is seen to behave most closely to the angled configuration, giving in Figure 4.8a. Both responses have similar rise times and fairly uniform pressure responses. The main difference between the two responses stems from the periodicity of the angled configuration. This periodicity leads to more wave interactions and a more uniform response. The periodicity also causes less disparity between the maximum and minimum pressures observed, which is seen by comparing the pressure trace of the shock compacted composite (Figure 4.39) to any of the multilayer orientations (Figures 4.5, 4.8a, and 4.11a). The random nature of the Ni particles in the shock compacted composite leads to areas of lower and higher Ni content compared to the multilayer composite. This leads to more variation in pressure over the shock compacted composite, causing a larger discrepancy between the maximum and minimum pressures.

The interfacial response of the shock compacted composite was also found with higher resolution AMR simulations, identical to those performed on the multilayer composites discussed in Section 4.1.1. The material, temperature, and strain response of the shock compacted composite is shown in Figure 4.40. Some interfacial shear is seen to develop due to material flow around the Ni particles. The shear tends to be located on the top and bottom of the Ni particles and not the sides. This highlights the importance of the interfacial orientation for generating strain. With

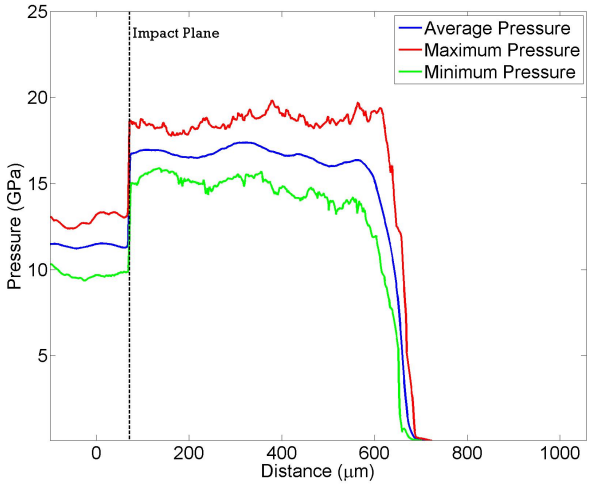

Figure 4.39: Pressure trace for the shock compacted composite showing the maximum, minimum, and average pressures along the composite 100 ns after impact at 1000 m/s. The pressure trace is seen to have a quick rise time and a relatively uniform average pressure response. A larger range in pressures is observed, due to the random distribution of the Ni particles.

the interfaces oriented with or at a slight angle to the propagating shock wave, full advantage can be taken of the disparity in material velocities for generating interfacial strain. This result is in agreement with that observed in the multilayer composites. While the degree of interfacial shear is less in the shock compacted composite than the parallel or angled configurations, similar trends are observed to govern the interfacial response.

The similarities between the shock compacted and angled multilayer composites can also be seen in their bulk responses. The computationally predicted EOS for the shock compacted composite ($U_S = 4483 + 1.606U_P$) compared to the perpendicular, angled and parallel configurations ($U_P \leq 1000$ m/s) is shown in Figure 4.41. Like the perpendicular and angled orientations, the shock and wave front velocities of the shock compacted composite were similar, enabling comparisons to the parallel orientation. The EOS responses of shock compacted, perpendicular, and angled composites are seen to match very closely, with the deviations being small. This supports

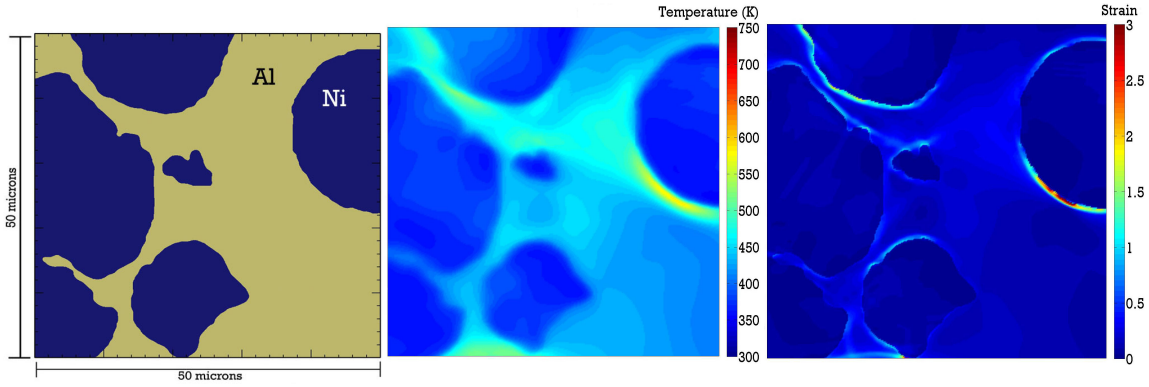

(a) Materials (b) Temperature (c) Strain

Figure 4.40: High resolution simulations showing the material deformation (a), temperature (b) and strain (c) response for the shock compacted composite. The results show elevated heating at the material interfaces, particularly when aligned with the direction of shock propagation.

the conclusions drawn in Section 4.1.5 that the orientation of the material interfaces is not a significant factor on the bulk response as long as extensive 2D effects are not induced. The 2D effects complicate the rise of the shock pulse and alter the wave speed observed, which is seen in the drastically different slope of the parallel configuration.

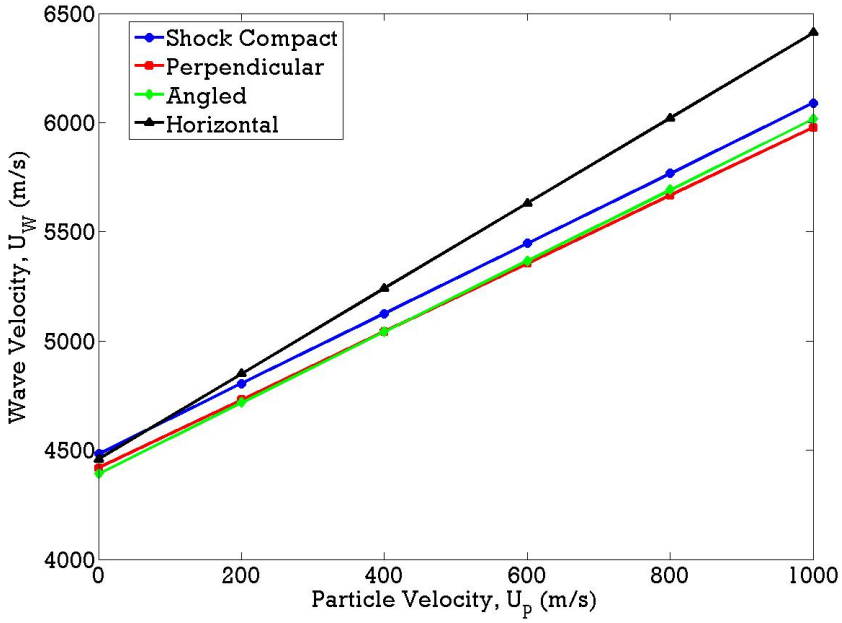

Figure 4.41: Predicted EOS response for the shock compacted composite compared to the three orientations of the multilayer composite. The orientation of the interfaces is seen not to be a significant factor unless extensive 2D effects develop.

CHAPTER V

UNIAXIAL STRAIN PLATE-ON-PLATE IMPACT EXPERIMENTS

Six uniaxial strain plate-on-plate impact experiments were performed on the cold-rolled multilayers using the 80 mm single stage gas gun at Georgia Tech in order to validate the computational results presented in Chapter 4. The experimental results and procedures were complicated by the thin, irregular nature of the multilayer composites. Consequently, the experimental procedure presented below shows a progression of experimental arrangements in an attempt to obtain more accurate measurements. In addition, with such thin samples, only the perpendicular orientation could be experimentally measured. This meant that any validation of the perpendicular configuration would have to be extended to the other configurations. Since the other microstructural configurations were generated through simple rotations and scalings of the original perpendicular microstructure, this was assumed to be an adequate assumption. As a result, the experimental data presented in this section is assumed to validate all of the computational results presented previously.

5.1 Uniaxial Strain Plate-on-Plate Impact Experiment Setup

A representative schematic of the 80 mm single stage gas gun experiments is shown in Figure 5.1. All impact experiments were performed using a projectile consisting of an Al 6061 sabot and OFHC Cu flier and driver plates. The driver and flier plates were lapped until the faces were parallel to within ± 0.0003 and ± 0.001 inches, respectively. Due to the time-scale of the shock transit through the material, all useful data occurs well before the release wave coming from the back surface (side away from impact) of

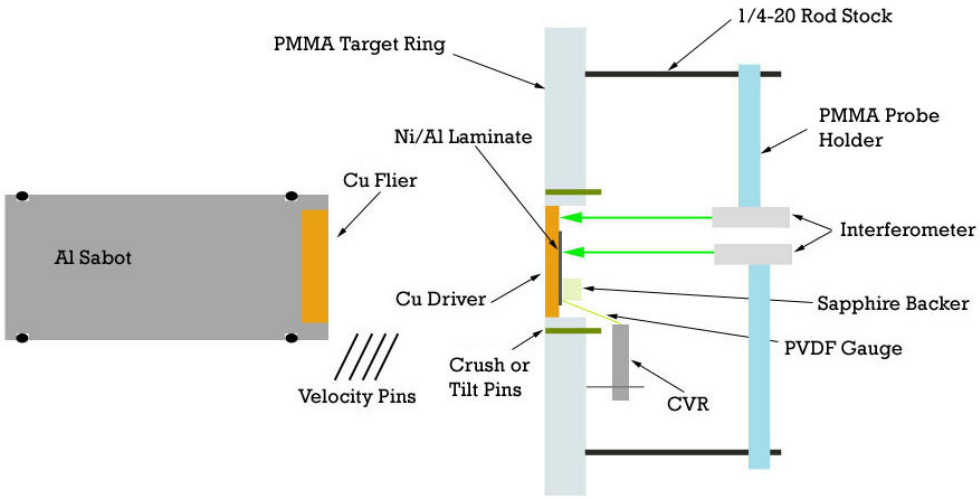

Figure 5.1: Schematic of a representative plate-on-plate uniaxial strain gas gun experiment showing the time-resolved diagnostics.

the flier is observed. As a result, the fliers did not need to be as parallel as the drivers. To ensure a planar, parallel impact, the flier was mounted onto a machined pocket in the Al sabot with Hysol epoxy, and the front face of this projectile/flier assembly was lapped flat. This means that the majority of the experimental tilt comes from the angle at which the projectile exits the barrel relative to the sample mounts, which is around 1.5 to 2 milliradians for the gas gun used.

For all experiments, the impact velocity was measured with a set of 4 shorting pins, giving 3 independent measurements of the impact velocity. In each experiment, the time between pins 1 and 3, 1 and 4, and 2 and 4 were used to obtain the impact velocity and its associated error. These pin combinations provide the largest distances traveled by the projectile, and gives the least amount of error in the measured impact velocity.

The sample and diagnostic setup employed in this study was not constant. The changes highlight a progression of experimental arrangements and diagnostics to obtain more accurate results. Illustrations of each sample and diagnostic configuration

Table 5.1: Experimental configuration measurements in inches.

Shot Number	Flier Thickness	Driver Thickness	Sample Thickness	Input Gauge Thickness	Propagated Gauge † Thickness	Backer† Thickness
0902	0.2425 ± 0.0002	0.0930 ± 0.0001	0.0269 ± 0.0007	0.0032 ± 0.0003	-	-
0912	0.2393 ± 0.0006	0.0936 ± 0.0000	0.0269 ± 0.0007	-	-	-
1003	0.2025 ± 0.0004	0.0921 ± 0.0001	0.0273 ± 0.0008	-	-	-
1038	0.1800 ± 0.0010	0.1229 ± 0.0002	0.0269 ± 0.0006	0.0042 ± 0.0003	0.0030	0.1182
1041	0.1819 ± 0.0008	0.1227 ± 0.0003	0.0294 ± 0.0006	0.0054 ± 0.0004	0.0032	0.1181
1207	0.1824 ± 0.0011	0.0856 ± 0.0003	0.0280 ± 0.0005	-	0.0030	0.1183

†Due to the small diameter of the backer, only one measurement could be made.
Errors listed as zero were below 0.0001 inches and assumed negligible.

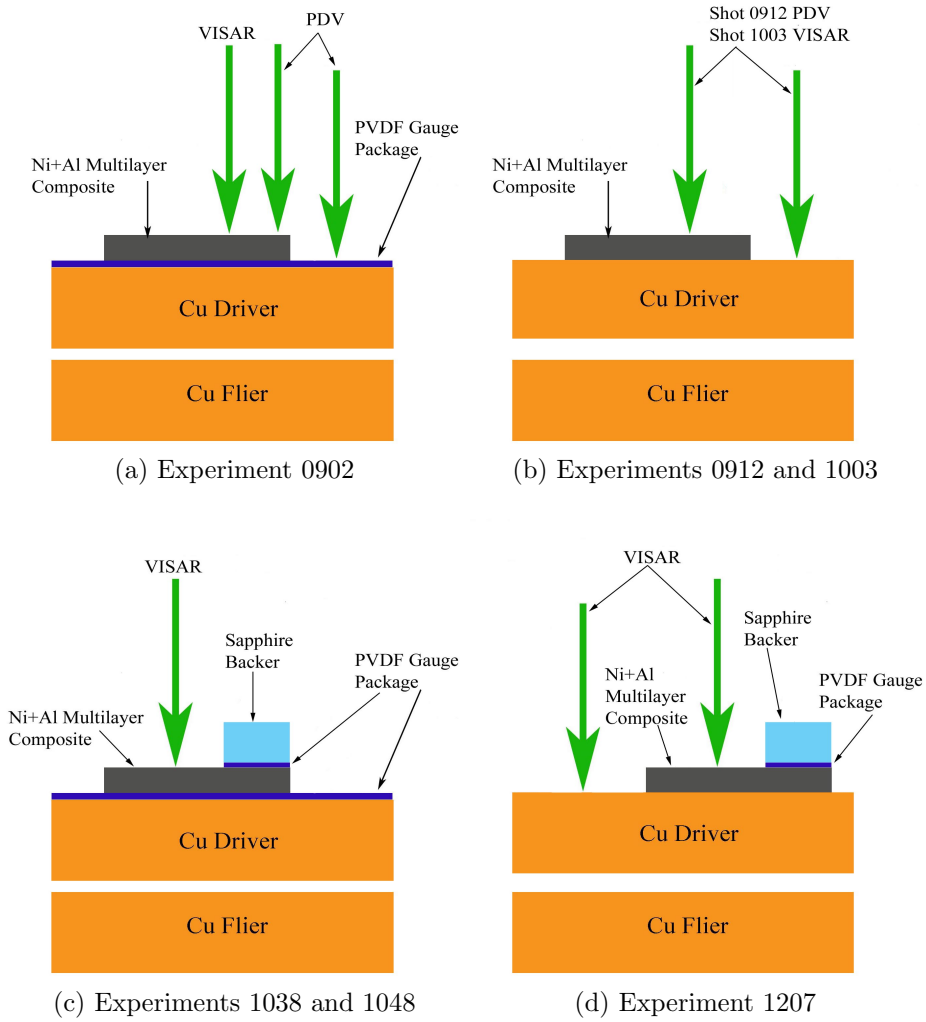

(a) Experiment 0902

(b) Experiments 0912 and 1003

(c) Experiments 1038 and 1048

(d) Experiment 1207

Figure 5.2: Sample and diagnostic configurations used for each plate-on-plate experiment.

are shown in Figure 5.2. The dimensional measurements corresponding to each setup are presented in Table 5.1. Three *in-situ* diagnostics were used through out these experiments: polyvinylidene flouride (PVDF) stress gauges, velocity interferometer system for any reflector (VISAR), and photonic doppler velocimetry (PDV). A brief description of each diagnostics is presented in Section 5.1.1. Each experimental setup was designed to record both the shock and particle velocities. Due to the thin nature of the samples, there are too many wave interactions to accurately determine a steady-state stress for the multilayers. However, for most experiments only one

measurement was reliably recorded. The consequences of this are elaborated on in Section 5.2.

The setup for experiment 0902, shown in Figure 5.2a, utilized a PVDF gauge package to measure the input stress profile into the multilayer. VISAR and PDV probes were used to measure the free surface velocity of the multilayer, while a second PDV probe was used to record the free surface velocity of the driver. This enabled a direct comparison between the velocities recorded by PDV and VISAR. Experiments 0912 and 1003, seen in Figure 5.2b, used two interferometry measurements to obtain the free surface and shock velocities (PDV for experiment 0912 and VISAR for experiment 1003). Experiments 1038 and 1041, shown in Figure 5.2c, used an input and propagated PVDF gauge package to measure the shock velocity along with a VISAR probe to record the free surface velocity. For experiment 1207, shown in Figure 5.2d, two VISAR probes were used to measure the shock speed with tilt pins to ensure more accurate timing. In addition, a PVDF gauge was placed on the back side of the sample in an attempt to record a propagated stress profile. The results for these experiments are described in Section 5.2 after a brief discussion of each of the experimental diagnostics.

One of the main reasons for so many experimental arrangements stem from the thin, irregular nature of the multilayer samples. These factors complicate the experimental determination of U_S, leading to large errors. Measurements of U_S are obtained by dividing the sample thickness by the shock wave transit time. This makes U_S a differential measurement and sensitive to errors in the timing or sample thickness.

As the sample thickness decreases, the transit time of the shock wave also decreases, which shortens the amount of reliable data that can be recorded before multiple wave interactions cloud the results. Naturally, the shorter the transit time, the more sensitive the measurement is to timing errors. For the multilayer composites investigated here, the transit times were ~ 200 ns. Consequently, errors in the transit

time on the order of 10 ns become a significant source of error. Every effort must be made to minimize the error in the transit time to obtain accurate measurements. However, this is more difficult when the diagnostics have a 1-2 ns temporal resolution, like the ones used in this work.

The cold-rolled multilayers also have the added complication of having irregularities in the sample thickness due to the rolling process. The multilayer samples used in this work were lapped to reduce this variation in thickness to $\pm$ 15 μm. However, given the multilayers used have a total thickness of $\sim$ 650 μm, this thickness variation is not insignificant. These considerations highlight the complexities of working with thin, irregular samples, and are a major source of error in the experimental results.

5.1.1 Time-Resolved Experimental Diagnostics

5.1.1.1 PVDF Stress Gauges

Thin films of the ferroelectic polymer PVDF have been used since the late 1980's as a stress gauge in shock experiments. Through a process of biaxial stretching under an applied electric field and cyclic polarization, Bauer was able to develop a PVDF film with consistent piezoelectric properties [167, 168]. This discovery enabled the calibration of PVDF films for shock stress measurements.

The advantage of the PVDF stress gauge is its fast data acquisition without an external power source [169]. Stressing the PVDF gauge generates a potential. This potential is recorded through a low inductance current view resistor (CVR) connected to the electrical leads coming from the active area of the gauge. The voltage is recorded on an oscilloscope and converted into a current density by using the known CVR resistance and active gauge area. The current density represents the rate of change in the stress across the gauge [170]. As a result, the current density can be integrated to yield the charge density, which can be related to the stress experienced by the gauge through a polynomial fit. Unfortunately, this polynomial fit changes depending on the stress regime [171, 170].

The geometry of any PVDF gauge must be chosen carefully. PVDF gauges need a large aspect ratio in their active area. This ensures the gauge is thinner than the rise of the shock and minimizes two-dimensional effects [172]. Having too small an active area can lead to lateral strains and a "thick-mode" response [172]. The piezoelectric strain coefficients in these lateral directions are of opposite sign to those in the direction of compression [173]. As a result, significant lateral strains can alter the dependence of the charge density on the stress, leading to an over prediction of the stress.

There are also reliability concerns with PVDF gauges due to their complex composition. PVDF gauges are known to show some history dependence on the recorded pressure. This is seen in the inability of PVDF gauges to accurately record stepped shock waves [169]. The response may stem from the complexity of the PVDF material and the resulting changes to its composition during shock loading. The crystalline phase of PVDF is responsible for its ferroelctric properties [173]. A poled gauge is composed of around 50% crystalline phase in an amorphous matrix [172]. This amorphous phase is known to undergo softening around 15 GPa [172], which can change the local stress state around the crystalline phase, altering the recorded charge density and invalidating the calibration curve [172].

It is also possible that shock loading changes the crystalline phase in the PVDF gauge. There are two crystalline phases in PVDF: α and β. The β phase is favored at high pressures and conversion of the α phase to the β phase could explain the history dependence of the gauge. This was investigated with diamond anvil cell experiments at room temperature on poled PVDF by Neel [173], but no increase in the percentage of β phase was observed. As a result, changes in the gauge response based solely on pressure are not expected. However, these results did not include the added complexity of elevated temperatures, which are present in shock compression. Neel suggested that this combination of elevated pressures and temperatures during

shock compression could induce a phase change in PVDF, since the glass transition temperature increases with pressure [173]. Based on these considerations, there is an inherent uncertainty in PVDF gauge data.

The PVDF gauges used in this work were all poled with the Bauer process and obtained from Piezotech. The gauges had a thickness of 25 microns, an active area of $\sim$ 9 mm^2, and electrodes of sputtered gold over platinum. The experimental PVDF measurements were taken by creating what is termed a gauge package. The gauge package consists of a PVDF gauge electrically insulated between two 0.001 inch Teflon films. The input gauge package is constructed in two stages. The first involves epoxying the first Teflon sheet on the face of the driver with de-gassed Hysol epoxy. De-gassing the epoxy helps to eliminate air bubbles, which can cause surface irregularities upon curing. The excess epoxy is pushed out by hand with a small roller, and the assembly is allowed to cure under weight to ensure a smooth surface with a thin epoxy layer. In the second step, the PVDF gauge along with two spacers provided with the gauge are placed on the driver/Teflon assembly with de-gassed Hysol epoxy. The spacers ensure the sample rests flat on the gauge package by providing three points at equal height. The second Teflon layer is then placed over the PVDF gauge with more de-gassed Hysol epoxy. Once again, the excess epoxy is pushed out by hand with a roller, and the whole assembly is cured under weight. This procedure was used for each PDVF package created. The generation of the propagated PVDF packages differs from the above description only in that they were built on 0.5 inch diameter sapphire backers. The thicknesses of all the gauge packages used in this work can be found in Table 5.1.

For the experiments preformed here, there are multiple wave interactions and reverberations, due to the thin nature of the samples. This precludes the possibility of determining a steady state pressure from the PVDF gauges. Instead, the PVDF gauges were used either for validation of the simulations or timing to determine the

shock velocity as done by Frendenburg [54]. For all experiments, the PVDF data was analyzed in PlotData v2.3 [174].

5.1.1.2 VISAR Interferometry

The VISAR system was first developed by Barker and Hollenbach [175] to circumvent many of the challenges present in the Sandia laser velocity interferometer. The Sandia interferometer used an air delay to provide an interference pattern with the light reflecting off a specular sample. As the sample motion began, the fringe pattern changes and was correlated to the velocity [175, 176]. Unfortunately, the need for a mirrored sample surface for maintaining spatial coherency of the light was a major restriction, especially since many materials loose reflectivity once shocked [175]. To get around these limitations, Barker and Hollenbach built the VISAR system utilizing the concepts of a wide-angled Michelson interferometer (WAMI) [177, 175]. The main feature of a WAMI is the use of an etalon. The etalon can be positioned such that the length of each leg appears the same. However, since light travels slower in the etalon, the light in that leg is delayed in time. This arrangement, eliminates the need for spatial coherence of the light for maintaining good fringe contrast [175]. As a result, a mirrored surface is no longer necessary [175].

Figure 5.3 shows a schematic of the VISAR system [175]. Here a laser is used to illuminate a diffuse surface. The reflected light is then collected by a lens and sent into the interferometer, where the beam is split in quadrature using a polarizer and a 1/4 wave plate [175]. This splits the beam into S and P components by polarizing at 45° to vertical. The P component is then retarded 90° out of phase with respect to the S component with the 1/4 wave plate [175]. The polarization and phase shift is done for two reasons. First, it allows for the determination of acceleration and deceleration. Second, it reduces error. If one plots the light intensity, I, versus the fringe count, F, it would be a sine wave. At the maxima and minima, dI/dF=0 resulting in poor

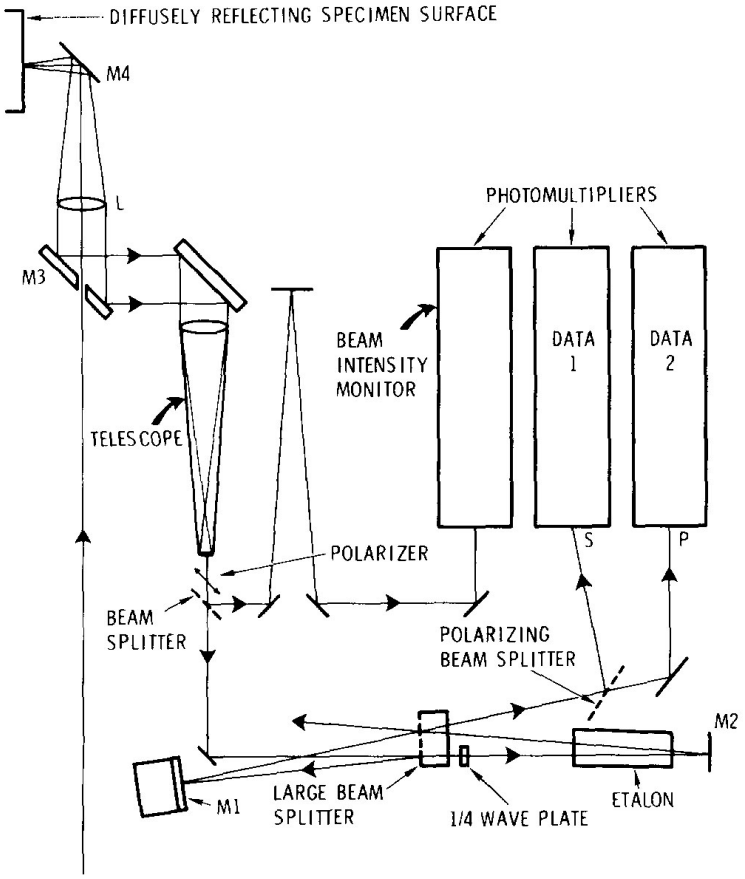

Figure 5.3: Schematic of the VISAR system.

resolution of any changes at these extremes. With the beam split in two out-of-phase components, a signal always exists with good resolution [175].

After the polarizer, some of the beam light is siphoned off for the beam intensity monitor (BIM). The BIM allows for corrections to the data in the event of a loss in signal. The delay in this leg of the system ensures the BIM signal corresponds in time to the recorded signal. The remaining signal is then sent through the two legs of the WAMI using a large beam splitter. One leg contains mirror M1, which can be moved to generate fringes for alignment of the system. The second leg is delayed through the use of various sized etalons, which include the large beam splitter and 1/4 wave plate. The two legs are then recombined before being split into S and P components

and sent to the photomulitplier tubes. The accuracy of the VISAR system depends on many factors (*e.g.* laser intensity, surface tilt, probe depth-of-field, calibration of window material), but, for a typical VISAR system, the error is around 0.2% to 1% of the peak velocity [178]. Larger errors result from uncertainties in the velocity corrections for window materials, which is the most significant source of error [178]. As a result, performing experiments without a window, as done in this work, yields experiments with the former degree of error.

There have been many variations made to the original VISAR system [176]. One of the more significant improvements was the development of the "push-pull" VISAR by Hemsing [179]. In Figure 5.3, some of the light reflected from mirror M2 is wasted. Hemsing recovered this light and recombining it with the signals going into the photomultiplier tubes. This increased the efficiency of the system and improved the signal-to-noise ratio.

For measurements recorded in the current work, a "push-pull" [179], multi-beam [180] VISAR obtained from Valyn International was used. The multi-beam VISAR system at Georgia Tech has the capability of measuring four individual points on the specimen simultaneously. The VISAR measurements were made with probes having a 30 mm focal point obtained from Vayln International.

5.1.1.3 PDV Interferometry

Photonic Doppler velocimetry, or heterodyne velocimetry, is a similar system to the VISAR. The PDV system is essentially a fiber-based Michelson interferometer that takes advantage of recent developments in the telecommunications industry [181, 182]. A schematic of the PDV system is presented in Figure 5.4. The system relies on a 1550 nm laser and a 3-port circulator [182]. Any light that enters port 1 of the circulator exits at port 2, and any light that enters port 2 leaves through port 3. This enables the cirulator to easily separate the incident and reflected light [182]. Since there is

very little light entering port 1 that transmits through port 3 ($< 50dB$), another mechanism must be used to combine the incident and reflected signals to generate a fringe pattern. This can be done using the back reflection from the probe itself [182] or a reference signal [183]. Often, both of these methods are used, with the reference signal being slowly added until the desired contrast is reached. The recorded beat frequencies can then be analyzed with a sliding Fourier transform to generate a power spectra of velocity vs. time [182].

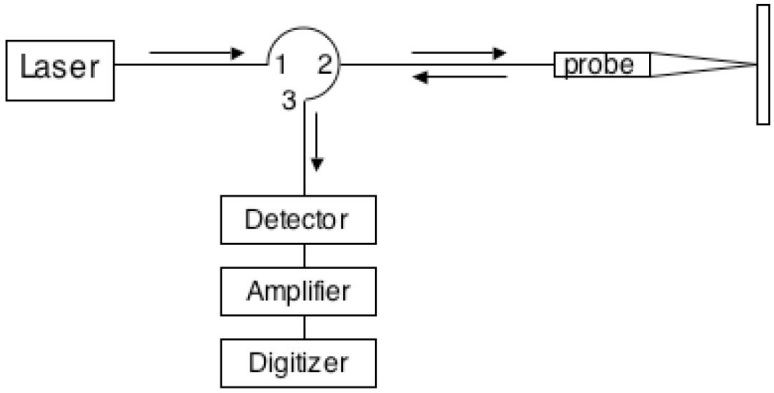

Figure 5.4: Schematic of the PDV system [182].

The PDV has some advantages over VISAR. The total encasement of the laser light makes PDV safer for the user [182]. In addition, the system is simpler and easy to assemble, since it uses commercial off the shelf components [181]. PDV can also record multiple velocities simultaneously with a single probe, which is useful to catch ejecta in powder systems. The main disadvantage of PDV compared to VISAR is the poor resolution of rapid, low velocity changes [184]. For measuring steady-state free surface velocities, PDV has an accuracy of around 0.1% [184]. In the lower frequency region ($<$ 1 GHz or 775 m/s), both accuracy and precision of the PDV system are poor with accuracies around 0.1 GHz ($\sim$ 78 m/s) [181]. This causes poor resolution of low velocity changes with PDV when compared to VISAR. This is seen in the poor resolution of the elastic precursor with PDV in Figure 5.5. Above 2 GHz (1550

m/s), the accuracy of PDV improves dramatically and rivals that of VISAR [181]. For this reason, measurements for velocities under 1 km/s are often performed on an "up-shifted" PDV system, in which the recorded frequency has been shifted by 1 GHz or more [181]. The down side to "up-shifting" is that it lowers the maximum velocity the system is capable of measuring.

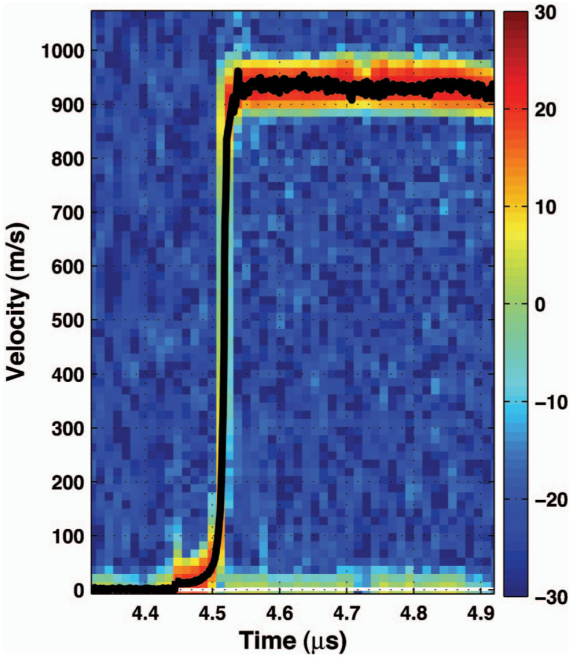

Figure 5.5: Power spectra obtained using PDV compared to the corresponding VISAR trace (black line). The VISAR trace is seen to resolve the elastic precursor much more accurately than PDV [184].

For all experiments in this study, the velocities recorded were all below 1 km/s. Unfortunately, the PDV system used was not "up-shifted", meaning the minutia of the shock wave could not be captured. However, the free surface velocity measured does have high accuracy and could be used. For all measurements, bare-fiber PDV probes positioned a few millimeters from the recorded surface were used and the data was analyzed in pTool v1.4.6 [185].

5.2 Uniaxial Strain Plate-on-Plate Impact Experiment Results

In each experiment, every diagnostic signal was recorded, but not every measurement was useful. While all of the experimental records can be found in Appendix A, Table 5.2 shows what quantities were reliably measured from each experiment. Despite the use of multiple diagnostics, often only one reliable measurement was obtained in each experiment. With only one parameter recorded, it was necessary to use impedance matching to obtain the Hugoniot point. Impedance matching leverages the known Hugoniots of the flier and driver to determine the Hugoniot point of the sample by substituting the impact velocity as the second need experimentally measured quantity. The impedance matching technique is described in detail in Section 5.3. The failure of so many measurements stems from a variety of reasons, which are discussed below.

Table 5.2: Quantities reliably measured in each experiment.

Shot Number	Impact Velocity	Particle Velocity	Shock Velocity
0902	✓	✓	×
0912	✓	✓	×
1003	✓	✓	×
1038	✓	✓	×
1041	✓	×	✓
1207	✓	✓	✓

Despite experiments 0902, 0912, and 1003 having dual interferometry probes, accurate measurements of the shock transit times were not obtained. This is the result of a lack of an accurate tilt measurement and limitations in the diagnostics. As discussed previously, with thin samples, the transit time of the shock wave must be known within nanoseconds to keep from large errors. Any tilt during impact leads to large uncertainties in the transit time. As a result, the shock velocity can not be determined with any confidence without a direct tilt measurement. Experiments 0902 and 0912 also have the drawback of using PDV for timing the shock wave. As stated in Section 5.1.1.3, PDV is inherently poor at resolving small changes in velocity. This

makes determining the rise of the shock pulse to within nanoseconds impractical. This is why VISAR was used in experiment 1003, but, without a tilt measurement, no significant advantage was gained. Regardless, all three experiments yield reliable free surface velocities for impedance matching. While particle velocity is not the ideal variable for impedance matching due to the slope of the Hugoniot in P-U_P space, it does provide a way to obtain information from these experiments.

Experiment 0902 deserves additional discussion due to its use of PDV, VISAR, and a PVDF gauge. If the PVDF gauge was aligned with the VISAR probe, a measurement of the transit time could have been obtained. However, this was not done and a measure of the shock velocity could not be accurately determined this way. The only comparison that could be made between diagnostics was the free surface velocities recorded by PDV and VISAR. These were found to match quite well, as seen in Figure 5.6.

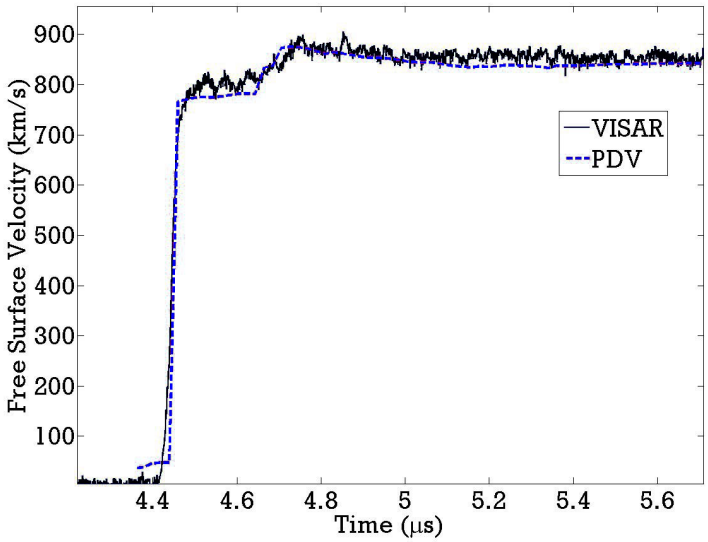

Figure 5.6: Comparison of the free surface velocity record of PDV and VISAR for experiment 0902.

The VISAR and PDV traces in Figure 5.6 show a hump in the free surface velocity record. The hump signifies the end of the signal that is attributed solely to the

multilayer. As the release wave from the back surface of the multilayer interacts with the lower impedance gauge package, a shock wave is propagated back into the multilayer. The release of this shock wave on the back surface of the multilayer leads to the increase in free surface velocity observed. This trace clearly shows the short duration of reliable data ($\sim$ 150 to 300 ns) that can be obtained with such thin samples. As a result, the free surface velocities measured in this work were all obtained from only the first $\sim$ 200 ns of the pulse. The length of reliable data was conservatively estimated from the impact velocity and was always terminated before clear signs of wave interactions, like the hump shown in Figure 5.6, were observed.

Experiments 1038 and 1041 utilized two PVDF gauges to obtain the shock velocity based on the integration time of each gauge following the method of Frendenburg [54]. A VISAR probe was also incorporated to record the free surface velocity. The appeal of this configuration over the ones used for experiments 0902, 0912, and 1003 is that, since the two gauges are aligned, tilt now becomes a nominal issue for measuring the shock speed. For experiment 1038, the propagated pressure gauge failed. While a potential was recorded, it was not characteristic of a PVDF gauge and could not be used. Without a measurement of the shock speed, the free surface velocity had to be used to determine the Hugoniot point through impedance matching. For experiment 1041, both PVDF gauges recorded a signal, enabling the determination of a shock speed. However, the VISAR record had significant electrical noise from a bad coaxial cable used to record the input PVDF gauge. As a result, the Hugoniot point for experiment 1041 was found using the shock speed for impedance matching.

To determine the shock speed for experiment 1041, the transit time of the shock wave through each gauge package must be known. This transit time depends on the pressure, which is unknown. To solve this, the impedance matching technique can be used in an iterative process [54]. Here, the input gauge is assumed to have a pressure equal to that of the driver. The pressure in the propagated gauge is then

estimated to determine the transit time through that gauge package. Subtracting the time in each gauge package from the measured transit time enables the shock speed to be calculated. The new shock speed can be used for impedance matching to obtain a more accurate estimate of the pressure in the propagated gauge. This then provides a more accurate measure of the wave transit time through the gauge package for calculating the shock velocity. The process is repeated until the value of U_S converges to within 0.1 m/s. For this procedure, the Hugoniot behavior of the gauge package was estimated using McQueen mixture theory [45] for a mixture of 66% Teflon and 34% PVDF. This yielded an EOS of $U_S = 1977 + 1.7207U_P$ m/s and an initial density of $\rho_0 = 2.204\frac{g}{cm^3}$.

There is an inherent assumption in experiments 1038 and 1041 that needs to be addressed. In past experiments with PVDF gauges on porous samples [27, 54], the gauge package is assumed to be small compared to the sample thickness and to not affect the resulting shock wave. This assumption is adequate in the thicker powder samples, but is less justified for the multilayer composites. The gauge packages used in this work can be on the order of 100 microns, as seen from Table 5.1. This is over 15% of the thickness of the multilayer composite. While computer simulations suggest the presence of the gauge does not appreciably alter the shock wave in these experiments, it is still not an ideal experimental arrangement.

To account for the short comings of the past experiments, Experimental 1207 utilized two VISAR probes and tilt pins to measure the shock and particle velocities. A PVDF gauge was then added to the back surface of the multilayer in an attempt to record a reliable propagated stress trace. All of the diagnostics for experiment 1207 were recorded reliably, enabling the shock and particle velocities to be accurately measured. In addition, the pressure profile through the propagated gauge enabled some validation of the CTH simulation results, which is presented in Section 5.5.

The experimental results obtained for the multilayer composites are plotted in

Table 5.3: Experimental results within 95% confidence.

Shot Number	Impact Vel. (m/s)	Particle Vel. (m/s)	Shock Vel. (m/s)	Pressure (GPa)	Relative Volume $\frac{V}{V_0}$	Specific Volume (cm^3/g)
0902	677.5 ± 0.6	388.1 ± 11.4	5.2437 ± 522.9	11.211 ± 1.238	0.9288 ± 0.0078	0.1752 ± 0.0022
0912	931.6 ± 1.2	548.1 ± 13.9	5288.1 ± 466.4	15.362 ± 1.525	0.8964 ± 0.0102	0.1691 ± 0.0025
1003	399.0 ± 0.8	230.8 ± 5.7	5096.0 ± 461.7	6.234 ± 0.673	0.9547 ± 0.0049	0.1801 ± 0.0019
1038	1057.9 ± 3.1	664.7 ± 37.8	4895.2 ± 927.6	16.726 ± 3.427	0.8683 ± 0.0270	0.1638 ± 0.0053
1041	614.1 ± 2.0	360.8 ± 7.1	5064.5 ± 98.4	9.686 ± 0.322	0.9288 ± 0.0020	0.1752 ± 0.0017
1207	290.3 ± 0.3	162.9 ± 3.5	4582 ± 606	3.956 ± 0.531	0.9644 ± 0.0048	0.1820 ± 0.0018

U_s-U_P, P-U_P, and P-$\frac{V}{V_0}$ space in Figures 5.8, 5.9, and 5.10, respectively. The data corresponding to these experiments and the accompanying error are shown in Table 5.3. The error associated with the particle velocities includes the error in the VISAR/PDV traces for the first $\sim$ 200 ns of the measurement along with a 2% error in assuming $\frac{U_R}{U_P} = 1$. This was determined to be an appropriate percentage based on the method developed by Walsh and Christian [37] discussed in Section 2.1. The bounds in $\frac{U_R}{U_P}$ computed for Al and Ni are shown in Figure 5.7.

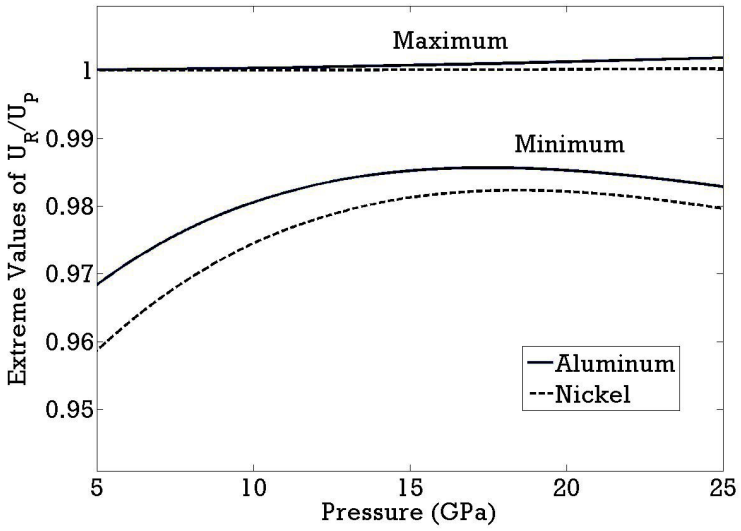

Figure 5.7: Maximum and minimum values of $\frac{U_P}{U_R}$ for Al and Ni based on the derivations of Walsh and Christian [37].

In Figures 5.8, 5.9, and 5.10, the solid line corresponds to the Hugoniot predicted by the 2D perpendicular CTH simulations described in Section 4.1.5. The simulated Hugoniot curve is seen to be within the error of each experimental point. Unfortunately, the large error associated with each point prohibits a strong validation of the computational results. Further validation is obtained through simulations of each experiment using the computed EOS. These results are presented later in Section 5.5. The close correlation of those computational results and the uniaxial strain data presented here showed that the computed EOS is representative, validating the trends extracted from the simulations.

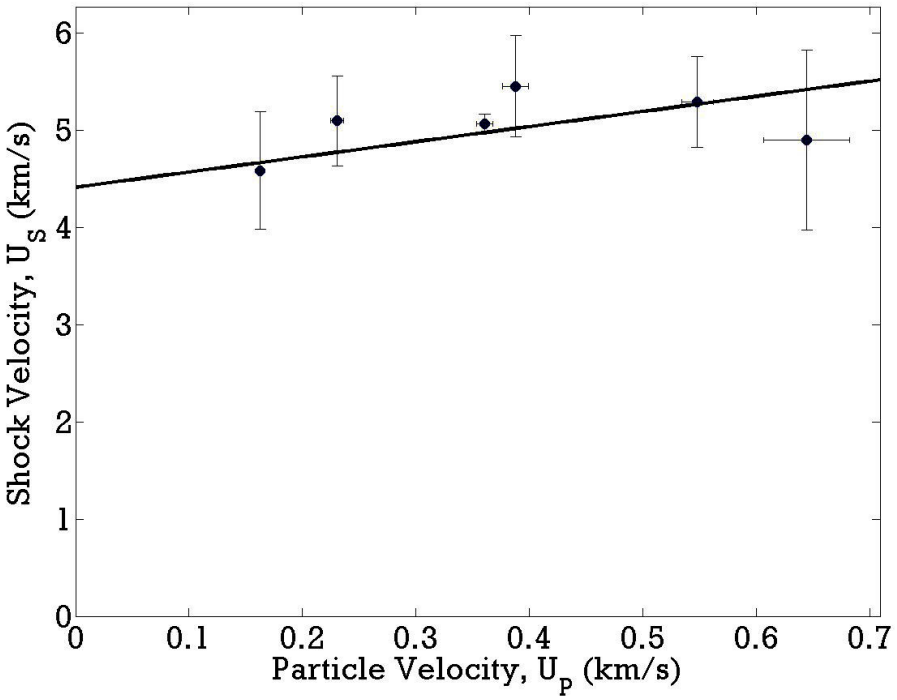

Figure 5.8: Experimentally determined Hugoniot points and corresponding error presented in U_S vs. U_P space along with computed equation of state as determined with CTH simulations (solid black line).

5.3 Impedance Matching Technique

While the shock compression response of an unknown material can be obtained experimentally by the direct measurement of two variables in the Rankine-Hugoniot equations (usually either U_S, U_P, or P), this can often be prohibitive. An alternative approach relies on impedance matching. Impedance matching is built on the assumption that, under steady state conditions, all material interfaces initially achieve continuity in stress and particle velocity. This continuity can be broken with further wave interactions, but, for the initial shock wave, it holds true. This enables the known response of a material to be leveraged to determine the response of an unknown material, by substituting the impact velocity as one of the necessary measured variables. As a result, only one material variable needs to measured for the sample. The following section follows very closely to that of Frendenburg [54] and outlines

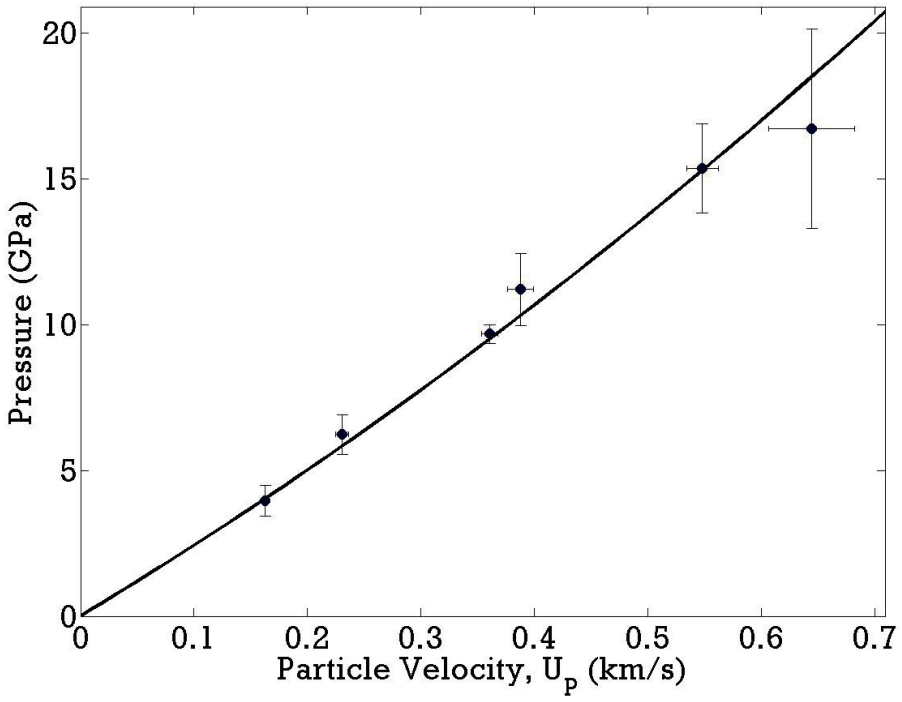

Figure 5.9: Experimentally determined Hugoniot points and corresponding error presented in P vs. U_P space along with computed equation of state as determined with CTH simulations (solid black line).

the impedance match procedure for impact event involving three materials: a flier, a driver, and a sample.

Recall that the conservation of mass, momentum and energy across a shock front can be expressed through the Rankine-Hugoniot equations [31, 30] given in Section 2.1.1. Given the impact velocity, v_i, the conservation of momentum enables the determination of the steady state conditions at the driver and flier interface using the known material EOS, which in this analysis is assumed linear (Equation 2.4).

$$P_D = \rho_D(C_{O_D} + S_D U_{P_D})U_{P_D} \tag{5.1}$$

$$P_F = \rho_F(C_{O_F} + S_F(v_i - U_{P_F})(v_i - U_{P_D}) \tag{5.2}$$

Here, the subscript D and F refer to the values of the driver and flier, respectively. In this work, the flier and driver were both composed of Cu and their densities were

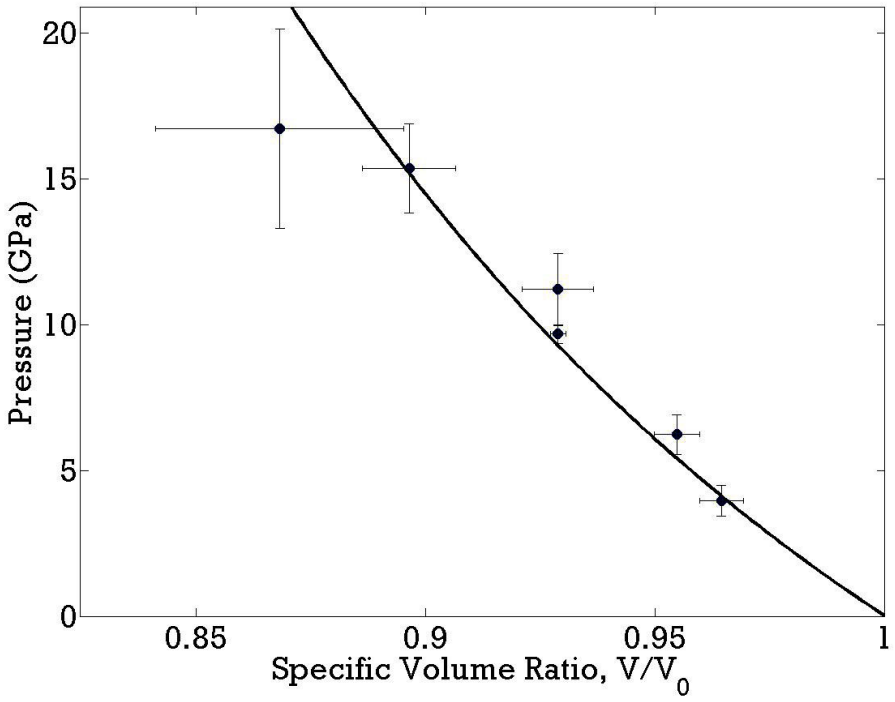

Figure 5.10: Experimentally determined Hugoniot points and corresponding error presented in P vs. $\frac{V}{V_0}$ space along with computed equation of state as determined with CTH simulations (solid black line).

taken from Marsh [56] to be $\rho_{Cu} = 8.924 \pm 0.021 \frac{g}{cm^3}$. Since the materials obtain continuity in P and U_P, the above equations can be equated to determine the particle velocity at the flier/driver interface. For a symmetric impact, it can be shown that the resulting particle velocity is half of the impact velocity

$$U_{P_D} = U_{P_F} = \frac{1}{2} v_i$$

These equations enable the complete characterization of the flier/driver interface.

To determine the conditions at the driver/sample interface, the impedance difference between the sample and driver must be known. Recall, that impedance is the product of the material density and shock speed. The impedance of the driver relative to the sample determines which of two possible scenarios occur. These scenarios are shown in Figure 5.11, and correspond to the reflection of a shock or release wave into the driver.

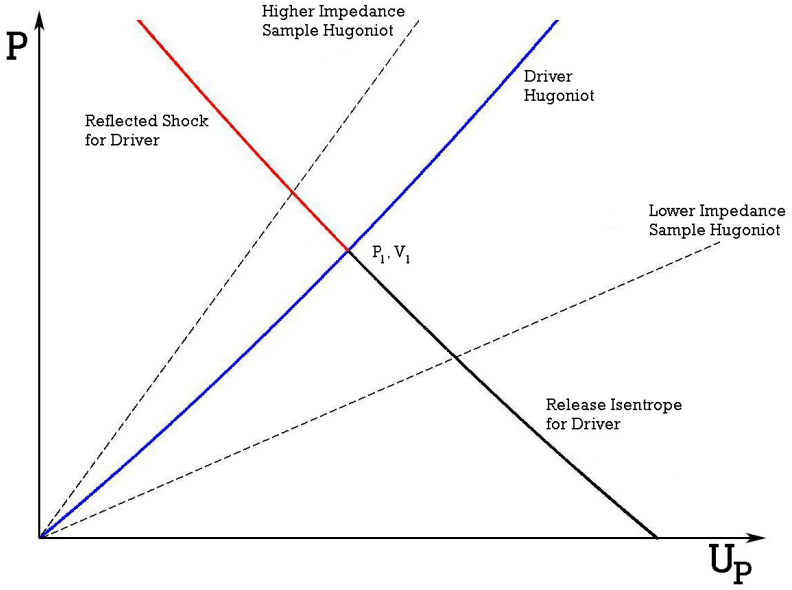

Figure 5.11: Illustration showing the possible scenarios at the driver/sample interface. If the sample has a larger impedance than the driver, the steady state condition of the interface lies on the reflect shock Hugoniot for the driver (solid red). If the sample has a lower impedance than the driver, the steady state condition of that interface lies on the release isentrope for the driver (solid black).

If the sample has a larger impedance than the driver, a shock wave reflects back into the driver. The intersection between the sample Hugoniot and the reflect shock Hugoniot of the driver must then be found. Using the Mie-Grüneisen EOS and the conservation of energy (Equation 2.3), McQueen *et al.* developed a functional form of the reflected shock Hugoniot [45].

$$P_2 = \frac{P_H - \frac{1}{2}\left(\frac{\gamma}{V}\right)_2 [(P_H - P_1)(V_o - V_2)]}{1 - \frac{1}{2}\left(\frac{\gamma}{V}\right)_2 (V_1 - V_2)} \tag{5.3}$$

In the above, P_H refers to the pressure on the original material Hugoniot at specific volume V_2. The subscript 1 refers to the state on the original Hugoniot centered at $P = 0$ and $V = V_0$, as shown in Figure 5.11.

If the sample has a lower impedance than the driver, the intersection of the sample Hugoniot and the driver release isentrope must be found. This is the case for the experiments performed in this work. The calculation of the release isentrope makes

this scenario more computationally intensive. For simplicity, it is common to assume the driver releases along its Hugoniot. As discussed in Section 2.1.1, the isentrope and Hugoniot are similar at moderate pressures. For the analysis performed here, the release isentrope was calculated following Davison [36] for increased accuracy.

To begin, consider an isentrope that intersects the Hugoniot at a point P^* and V^*, as shown in Figure 5.12. Using the first law of thermodynamics, the isentrope can be expressed as the following [36].

$$E_S(V, S^*) = E_S^* - \int_{V^*}^{V} P_S(V', S^*) dV' \tag{5.4}$$

The Mie-Grüneisen EOS can then be used to relate the isentrope to the Hugoniot curve passing through P^* and V^*. Utilizing the conservation of energy along this Hugoniot (Equation 2.3), Equation 5.4 can be expressed with the following [36].

$$P_S(V, S^*) - P_H(V) = \frac{\gamma(V)}{V} \left[E_S^* - \int_{V^*}^{V} P_S(V', S^*) dV' - \frac{1}{2} P_H(V)(V_0 - V) \right] \tag{5.5}$$

Here, the subscript H refers to states along the Hugoniot, which is the reference curve.

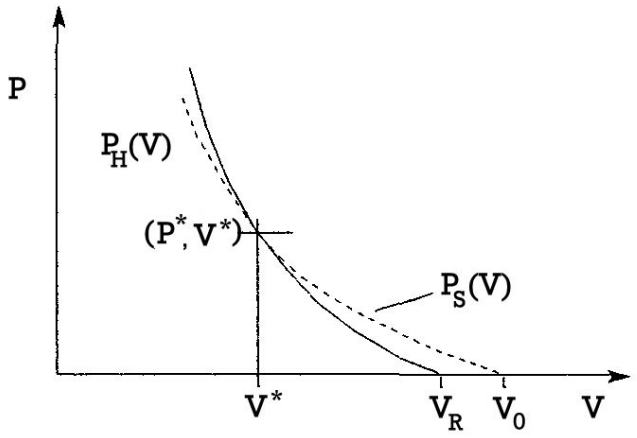

Figure 5.12: Illustration adapted from Davison [36] showing the isentrope that intersects a Hugoniot centered at $P = 0$ and V_0 at points P^* and V^*.

Realizing that the energy of the isentrope and the Hugoniot are equal at the

intersection point (P^*, V^*), E_S^* can be expressed with the conservation of energy.

$$E_S^* = E_H^* = \frac{1}{2}P^*(V_0 - V^*) \tag{5.6}$$

The isentrope can now be written in the following form.

$$\begin{aligned} P_S(V, S^*) =& \frac{\gamma(V}{V}\left[\frac{1}{2}P^*(V_0 - V^*) - \int_{V^*}^{V} P_S(V', S^*)dV'\right] + \\ & P_H(V)\left[1 - \frac{\gamma(V)}{V}(V_0 - V)\right] \end{aligned} \tag{5.7}$$

Assuming that the ratio $\frac{\gamma(V)}{V}$ is a constant and equal to $\frac{\gamma_0}{V_0}$, Equation 5.7 becomes an ordinary differential equation for the isentrope in P-V space [36].

$$\frac{dP_S(V, S^*)}{dV} + \frac{\gamma_0}{V_0}P_S(V, S^*) = \frac{\gamma_0}{2V_0}P_H(V) + \frac{dP_H(V)}{dV}\left[1 - \frac{\gamma_0}{2V_0}(V_0 - V)\right] \tag{5.8}$$

Here, P_H and $\frac{dP_H}{dV}$ are given by Equations 2.22 and 2.23. For this analysis, the Grüneisen coefficient of Cu was taken to be $\gamma_0 = 1.99$.

In an isentropic flow, the particle velocity changes slowly, meaning that the Rankine-Hugoniot equations can not be applied [42]. To obtain the particle velocity behind an isentropic release wave, the differential forms of the conservation of mass and momentum must be used [42].

$$\frac{\partial \rho}{\partial t} + u\frac{\partial \rho}{\partial x} + \rho\frac{\partial u}{\partial x} = 0 \tag{5.9}$$

$$\frac{\rho}{c}\left(\frac{\partial u}{\partial t} + u\frac{\partial u}{\partial x}\right) + c\frac{\partial \rho}{\partial x} = 0 \tag{5.10}$$

Taking the difference of the conservation of mass and momentum and noting that in an isentropic flow $\frac{\partial x}{\partial t} = u - c$, the following is obtained [42].

$$\frac{D\rho}{Dt} - \frac{\rho}{c}\frac{Du}{Dt} = 0 \tag{5.11}$$

Since the material time derivative is defined in the following manner,

$$\frac{D}{Dt} = \frac{\partial}{\partial t} + u\frac{\partial}{\partial x}$$

the integration of Equation 5.11 yields the particle velocity behind an isentropic flow [42].

$$U_R = \int_{\rho_0}^{\rho} \frac{c}{\rho} d\rho \tag{5.12}$$

This result can be put into a more useful form by using the thermodynamic definition of the wave speed.

$$c^2 = -\frac{1}{V}\left(\frac{\partial P}{\partial V}\right)_S$$

The particle velocity behind an isentropic flow can then be expressed with the following [42].

$$U_R = \int_{P_0}^{P} \left(-\frac{\partial V}{\partial P}\right)_S^{\frac{1}{2}} \tag{5.13}$$

This result can then be used to define a more rigorous definition of the measured free surface velocity [42].

$$U_{FS} = U_P + U_R = \sqrt{(P - P_0)(V_0 - V)} + \int_{P_0}^{P} \left(-\frac{\partial V}{\partial P}\right)_S^{\frac{1}{2}} \tag{5.14}$$

The P-U_P response of the driver/sample interface is now completely defined for a lower impedance sample. Equation 5.14 can be difficult to solve, so for most applications the assumption $U_{FS} = \frac{1}{2}U_P$ is used.

The above procedure can be used to determine the Hugoniot point of the sample with any experimentally measured quantity. If the shock speed is measured, the Rayleigh line for the sample is defined and its intersection can be found with the reflected shock or release isentrope. Due to the continuity of P and U_P at the driver/sample interface, either of these quantities defines an identical point on the sample Hugoniot and reflected shock or release isentrope for the driver.

There are two important considerations that need to be addressed about the use of impedance matching for the experiments in this work. First, the impedance matching technique relies on the Rankine-Hugoniot equations, which only apply to steady

waves. This leads to some uncertainly in the legitimacy of using the impedance matching technique to determine Hugoniot points for heterogeneous systems, such as the multilayer composites. It has been previously shown that the Rankine-Hugoniot equations hold for highly heterogeneous porous composites [32]. In addition, computer simulations of these experiments show the shock wave is quasi-steady through the perpendicular orientation of the composite, as discussed in Section 4.1.2. For these reasons, it was determined that the use of impedance matching for the multilayer composites was justified. The other consideration is the presence of the gauge package in experiments 0902, 1038, and 1041. As stated previously, the gauge package thickness is not negligible compared to the sample thickness. Simulations performed in CTH, suggested that the gauge package has a minimal effect on the initial shock wave through the multilayer. Since this initial wave is used for impedance matching, the gauge package was ignored in the impedance matching calculations for experiments 0902, 1038, and 1041.

For most of the experiments performed in this work, the free surface velocity, U_{FS}, was measured. Given the slope of the Hugoniot in P-U_P space, it is more desirable to measure the pressure or shock velocity. The Hugoniot rises very steeply in P-U_P space, meaning that small errors in the particle velocity lead to large errors in the pressure and shock velocity. These error considerations are elaborated on in Section 5.4.

A MATLAB code was written to calculate the Hugoniot points for the experiments in this work and their corresponding error. The accuracy of the routine was checked by reproducing the results reported by Frendenburg [54]. The code was designed to perform the impedance matching with either the U_S, U_P, or P for a sample with lower impedance than the driver. The MATLAB routine can be found in Appendix D and follows very closely to that done by Frendenburg [54].

5.4 Error Analysis

5.4.1 Error in the Impedance Matching Calculations

The error analysis in this section follows very closely to that performed by Mitchell and Nellis [186] and Frendenburg [54]. The error analysis presented by Mitchell and Nellis [186] was for a single interface (flier/sample) and was extended by Frendenburg [54] to include two interfaces (flier/driver/sample). In both cases, the shock velocity in the sample was recorded and used for the impedance matching calculations. For most of the experiments performed in this work, the particle velocity was measured and used for the impedance matching calculations.

The error in any measurement can be divided into two categories: systematic and experimental [187]. Systematic errors are those that propagate through the results. Experimental errors come directly from measurement. In the impedance matching technique, the only systematic error comes from the imperfect calibration of the driver and flier equations of state. Any errors associated with the Hugoniot response of the standard material propagates through the analysis, and must be accounted for. In the present work, OFHC Cu was used for the driver and flier. Thus, only the error associated with the EOS of Cu was determined. However, this analysis can easily be extended to a system with different flier and driver materials.

To determine the error in the Cu EOS, all of the data up to a particle velocity of 1 km/s was taken from Marsh [56]. A linear EOS for the Cu was assumed in this analysis and the best linear fit was found for the measured U_S and U_P data [56]. If the error associated with each individual U_S - U_P point is assumed similar, then they can be treated as exact points. This allows the error associated with each U_S point to be defined as the following [187].

$$\delta U_{S_m} = U_{S_m} - (C_0 + SU_{P_m}) \tag{5.15}$$

Here, the subscript m refers to the measured quantities. Setting the derivative of the

summation of U_{S_m} over all points with respect to C_0 and S equal to zero, the best fit for each coefficient can be found [187].

$$C_0 = \frac{\sum U_{P_m}^2 \sum U_{S_m} - \sum U_{P_m} \sum (U_{P_m} U_{S_m})}{N \sum U_{P_m}^2 - (\sum U_{P_m})^{\frac{1}{2}}} \tag{5.16}$$

$$S = \frac{N \sum (U_{P_m} U_{S_m}) - \sum U_{P_m} \sum U_{S_m}}{N \sum U_{P_m}^2 - (\sum U_{P_m})^{\frac{1}{2}}} \tag{5.17}$$

In the above, N is the number of data points and all summations are over the entire set.

In order to determine the error of this linear fit, the standard deviation of the experimental U_S values compared to the computed best fit are determined [187].

$$\sigma_{U_{S_m}} = \sqrt{\frac{\sum \delta U_{S_m}}{N-1}} \tag{5.18}$$

With the standard deviation between the predicted U_S and actual values know, the error in the coefficients of the fit can then be calculated [187].

$$\sigma_{C_0} = \sigma_{U_{S_m}} \sqrt{\frac{N \sum U_{P_m}^2}{(N-1)\left[N \sum U_{P_m}^2 - (\sum U_{P_m})^{\frac{1}{2}}\right]}} \tag{5.19}$$

$$\sigma_S = \sigma_{U_{S_m}} \sqrt{\frac{N^2}{(N-1)\left[N \sum U_{P_m}^2 - (\sum U_{P_m})^{\frac{1}{2}}\right]}} \tag{5.20}$$

These standard deviations are doubled to obtain the 95% confidence bounds for each coefficient. The coefficients and associated 95% confidence interval determined for Cu are given in Table 5.4.

Table 5.4: Coefficients for the linear EOS for Cu and corresponding 95% confidence intervals.

$C_0(km/s)$	3.8925 ± 0.0368
S	1.5358 ± 0.0558

Recall, the linear fit to the U_S - U_P data was found by assuming each point was exact. In reality, each point has an error associated with it. This allows each point to be treated as a rectangle in U_S-U_P space. For a fit to correspond to an

experimental point, it has to pass through this rectangle defined by the error. Using this fact, a smaller deviation for the linear fit can be defined that accounts for the expected error of each data point. The standard deviation of the linear best fit from an experimentally measured U_S value can then be found at each particle velocity, U_P, through the following [187].

$$\sigma_{U_{S_0}} = \sigma_{U_{S_m}} \sqrt{\frac{N(\sum U_{P_m}^2 - 2U_P \sum U_{P_m} + NU_P^2)}{(N-1)\left[N\sum U_{P_m}^2 - (\sum U_{P_m})^{\frac{1}{2}}\right]}} \tag{5.21}$$

From the above procedure, $\sigma_{U_{S_0}}$ can be expressed as a function of particle velocity U_P, allowing for the 95% confidence interval for the Cu EOS fit to be represented as $U_S \pm 2\sigma_{U_{S_0}}$. The deviation in this new fit increases at the extremes of the data, since linear fits weight the values at the extremes more heavily [186].

As done by Mitchell and Nellis [186] and Frendenburg [54], the deviation, $2\sigma_{U_{S_0}}$, can be expressed as a polynomial to a high degree of accuracy. For the analysis presented here, $2\sigma_{U_{S_0}}$ was represented as a 5^{th} degree polynomial.

$$2\sigma_{U_{S_0}} = A_5 U_P^5 + A_4 U_P^4 + A_3 U_P^3 + A_2 U_P^2 + A_1 U_P + A_0 \tag{5.22}$$

The resulting coefficients found for the Cu fit are given in Table 5.5.

Table 5.5: Coefficients for the polynomial fit for the error in the Cu EOS.

A_5	A_4	A_3	A_2	A_1	A_0
-0.175197	0.357249	-0.185138	0.046119	-0.055285	0.036845

With the error associated with the flier and driver equation of state determined, the systematic error in the impedance matching calculations can be found. Given the impact velocity, the intersection of the driver and flier Hugoniots can be found, and its associated error can be calculated by using $C_0 \pm 2\sigma_{U_{S_0}}$ in place of C_0 in Equations 5.1 and 5.2. This then defines the upper and lower bounds for the Hugoniot states of the driver and flier for each experiment, which is shown graphically in Figure 5.13. The 95% confidence bounds for the flier/driver interface pressure (P_{DF}^+, P_{DF}^-), particle

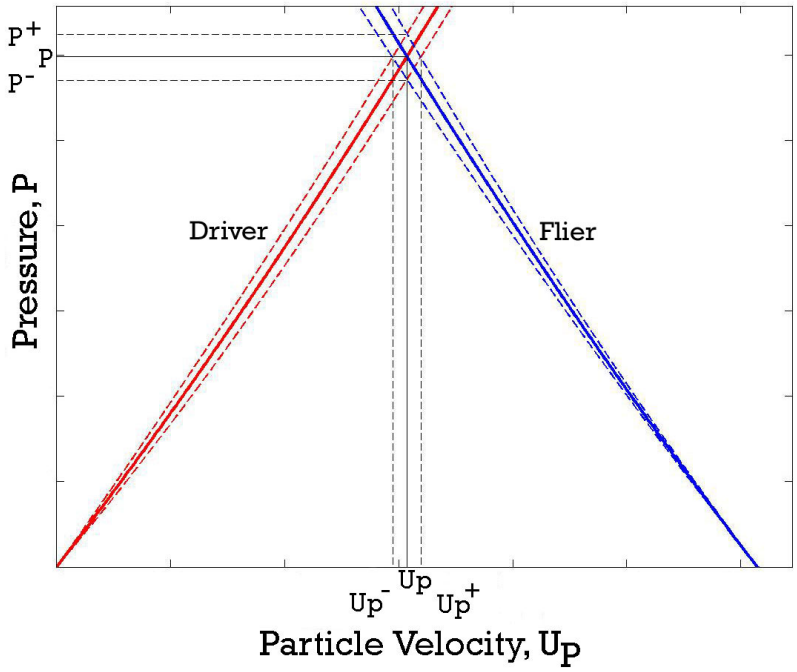

Figure 5.13: Intersection of flier (blue) and driver (red) Hugoniot showing the error resulting from deviation in the EOS of each.

velocity ($U^+_{P_{DF}}, U^-_{P_{DF}}$), and specific volume ($V^+_{DF}, V^-_{DF}$) are defined with the following.

$$U^+_{P_{DF}} \Rightarrow P^-_D = P^+_F \tag{5.23}$$

$$U^-_{P_{DF}} \Rightarrow P^+_D = P^-_F \tag{5.24}$$

$$P^+_{DF} \Rightarrow \rho_D[C_{0_D} + S_D U^+_{P_{DF}}]U^+_{P_{DF}} \tag{5.25}$$

$$P^-_{DF} \Rightarrow \rho_D[C_{0_D} + S_D U^-_{P_{DF}}]U^-_{P_{DF}} \tag{5.26}$$

$$V^+_D \Rightarrow \frac{1}{\rho_D} - \frac{U^{+^2}_{P_{DF}}}{P^+_{DF}} \tag{5.27}$$

$$V^-_D \Rightarrow \frac{1}{\rho_D} - \frac{U^{-^2}_{P_{DF}}}{P^-_{DF}} \tag{5.28}$$

$$V^+_F \Rightarrow \frac{1}{\rho_F} - \frac{U^{+^2}_{P_{DF}}}{P^+_{DF}} \tag{5.29}$$

$$V^-_F \Rightarrow \frac{1}{\rho_F} - \frac{U^{-^2}_{P_{DF}}}{P^-_{DF}} \tag{5.30}$$

The multilayer composites investigated here, have a lower impedance than the Cu driver. This means the release isentrope for Cu must be calculated using Equation

5.8. Substituting $C_0 \pm 2\sigma_{U_{S_{0_D}}}$ into Equation 2.22 and 2.23 for C_0, enables the error associated with calculating the isentrope in P-V space to be found. For a left going release isentrope, the following P-Up relation holds (Equation 5.14).

$$U_{P_{DS}} = U_{P_{DF}} + \int_{P_0}^{P} \left(-\frac{\partial V}{\partial P}\right)_S^{\frac{1}{2}} \tag{5.31}$$

Here, the subscript DS refers to the state at the driver/sample interface. To solve Equation 5.31, the isentrope can be represented in V-P space with a polynomial fit similar to Equation 5.22. The polynomial can then be numerically integrated to various pressures to determine the isentrope in P-U_P space. The procedure is then repeated for the upper and lower bounds of the isentrope to fully characterize the error at the driver/sample interface.

With the bounds of the isentrope determined in P-U_P space, the systematic error for the experimental point is known. The mean of the upper and lower bound values on the isentrope at the measured quantity (either P, U_P, or U_S) defines the systematic error in the two other quantities. This is shown schematically in Figure 5.14. For most of the work presented here, the intersection of the upper and lower bounds of the driver isentrope with half of the measured free surface velocity was used to determine the pressure. This pressure was then used to determine the shock speed, which is related to the slope of the Rayleigh line. However, this procedure is easily adjusted for any parameter.

For most of this work, the particle velocity was used in the impedance matching calculations to determine the shock velocity. To obtain the total error in the shock speed, the experimental error must be found and added to the systematic error [186].

$$\delta U_S = \delta U_S^e + \delta U_S^s \tag{5.32}$$

Here, the superscripts e and s refer to the experimental and systematic errors respectively. The experimental error in the shock velocity can be found by taking the

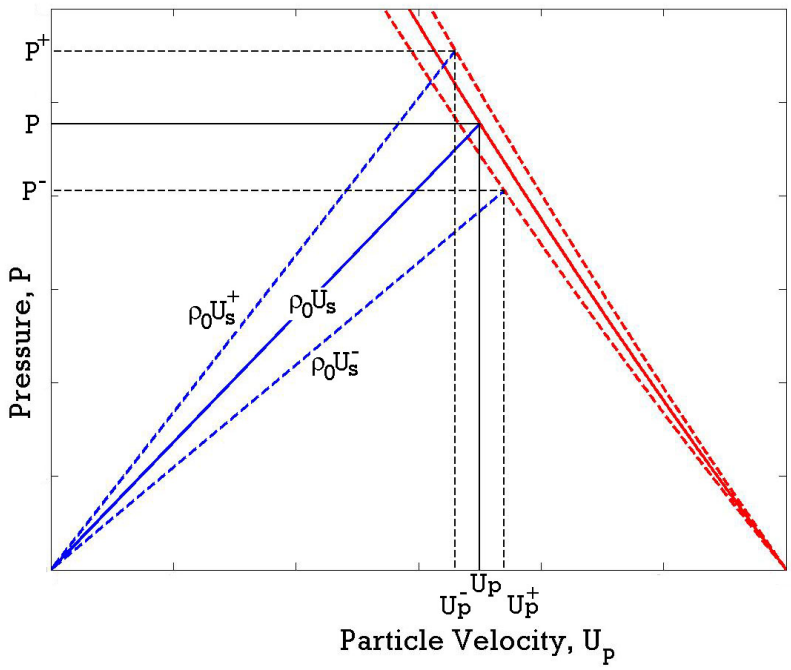

Figure 5.14: Schematic showing the release isentrope of the driver (red) and the Rayleigh line of the sample (blue) along with their upper and lower bounds (dashed). Using the intersections of these bounds, the variations in P, U_S, and U_P (black) can be found regardless of which parameter was measured.

square root of the summation of the squares of the errors in the shock speed associated with each measured variable. For the present analysis, these errors come from the measured impact velocity, v_i, the Cu density, ρ_{0_D}, the sample density, ρ_{0_S}, and the particle velocity, U_P.

$$\delta U_S^e = \sqrt{\delta U_S(U_P)^2 + \delta U_S(\rho_{0_D})^2 + \delta U_S(\rho_{0_S})^2 + \delta U_S(v_i)^2} \tag{5.33}$$

Following the procedure of Mitchell and Nellis [186], the measured upper and lower bounds of each variable can be used in the impedance calculation to determine the experimental error in U_S with respect to each variable. This error is simply the average deviation obtained using these upper and lower bounds. It should be noted that in Equation 5.33, there is no error associated with the density of the flier. This results from the fact that the experiments were done with the same flier and driver material. If the flier material was different than the driver, there would be a $\delta U_S(\rho_{0_F})$

term in Equation 5.33.

The procedure outlined above to obtain the experimental error in U_S from a measured U_P can easily be adapted for obtaining the error in P or U_P from a measured U_S. However, this procedure can not be used to find the experimental error in P from a measured U_P or visa versa. This comes from the relationship between P and U_P generated with the conservation of momentum and the linear EOS assumption. The formulation directly links P and U_P through the initial density ρ_0. This means that for a measured U_P, any errors in the corresponding pressure resulting from uncertainties in the initial density, ρ_0, are not accounted for (*i.e.* $\delta P(\rho_0)$). This uncertainty in ρ_0 is compensated for by changes in U_S, yielding no change in P. Similar arguments can be made if P is measured and the error in U_P is desired.

The above considerations force the errors in P and V for these experiments to be found by relating them to the errors already obtained for U_S and U_P. This can be done using the relation for independent errors [187].

$$\delta Y = \sqrt{\sum \left(\frac{\partial Y}{\partial x_i}\delta x_i\right)^2} \tag{5.34}$$

Here, the summation is over all dependent variables. The resulting errors in P, V, and $\frac{V}{V_0}$ can then be expressed as the following.

$$\frac{\delta P}{P} = \sqrt{\left(\frac{\delta\rho_0}{\rho_0}\right)^2 + \left(\frac{\delta U_S}{U_S}\right)^2 + \left(\frac{\delta U_P}{U_P}\right)^2} \tag{5.35}$$

$$\frac{\delta V}{V} = \sqrt{\left(\frac{\delta\rho_0}{\rho_0}\right)^2 + \left(\frac{U_P\delta U_S}{U_S(U_S-U_P)}\right)^2 + \left(\frac{\delta U_P}{(U_S-U_P)}\right)^2} \tag{5.36}$$

$$\delta\left(\frac{V}{V_0}\right) = \sqrt{\left(\frac{U_P\delta U_S}{U_S^2}\right)^2 + \left(\frac{\delta U_P}{U_S}\right)^2} \tag{5.37}$$

5.4.2 Error in Tilt Measurements

For experiment 1207, tilt pins were used to adjust the time delay between the VISAR record of the driver and sample due to the inclination of impact. The resulting error in this calculation is presented here to illustrate the process used.

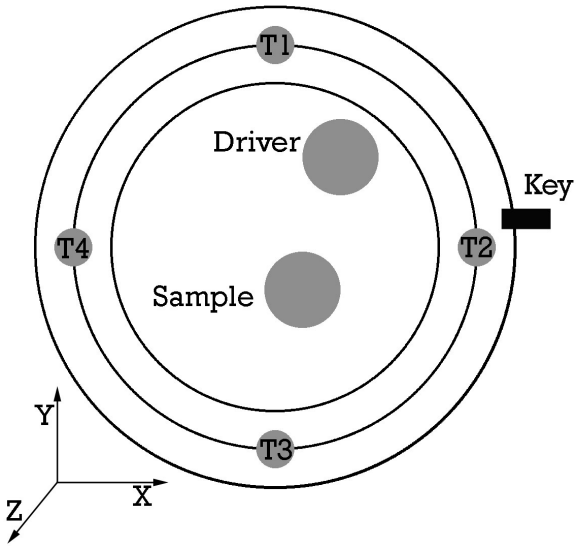

Figure 5.15: Schematic illustrating the location of the tilt pins and driver and sample VISAR measurements.

The tilt pins were used to define a coordinate system with the positive z axis oriented away from the gun breach, as shown by Figure 5.15. The location of each tilt pin and VISAR measurement was known to within a certain error, and the radii of circles defining the 95% confidence intervals of these locations are listed in Table 5.6. Since the target assembly was lapped flat and mounted perpendicular to the barrel axis, each location is assumed to have the same z location. The recorded grounding times of each pin are listed in Table 5.7 along with the times normalized with respect to tilt pin 1, which was the last pin to be grounded. These times can be converted into a height using the measured impact velocity of 290.3 m/s, as shown in Table 5.7. Since all the times are negative relative to pin 1, these heights define the distance the shock wave has traveled into the target at each location when pin 1 is grounded. The average impact velocity is used here, since its corresponding error is accounted for later.

Pin 3 hit a screw hole in the projectile and may not have grounded properly. With doubts about the timing of Pin 3, only Pins 1, 2 and 4 were used for the tilt measurement. Since the flier face was lapped flat, it can be described as a plane using

Table 5.6: Location of tilt pins and VISAR measurements along with the radii defining their 95% confidence intervals.

Feature	X Position (mm)	Y Position (mm)	Radius of Location (mm)
Key	38.22	4.66	-
Tilt Pin 1	0.0	34.0	1
Tilt Pin 2	34.0	0.0	1
Tilt Pin 3	0.0	-34.0	1
Tilt Pin 4	-34.0	0.0	1
Driver	11.79	14.62	2
Sample	5.47	-7.08	2

Table 5.7: Timing measurements for the tilt pins and the corresponding relative distances.

	Time (absolute) (μs)	Time (relative) (μs)	Distance (mm)
Tilt Pin 1	-7.997	0.0	0.0
Tilt Pin 2	-8.262	-0.265	0.077
Tilt Pin 3	-8.259	-0.262	0.076
Tilt Pin 4	-8.601	-0.035†	0.010

†The time was adjusted to account for the pin being proud.

the pin locations and the distances given in Table 5.7. Recall the equation of a plane.

$$Ax + By + Cz + D = 0 \tag{5.38}$$

These coefficients can be defined using the location of the tilt pins as the following.

$$A = det\begin{vmatrix} 1 & y_1 & z_1 \\ 1 & y_2 & z_2 \\ 1 & y_3 & z_3 \end{vmatrix} = det\begin{vmatrix} 1 & 34+\delta y & 0 \\ 1 & \delta y & 0.077 \\ 1 & \delta y & 0.010 \end{vmatrix} \tag{5.39}$$

$$B = det\begin{vmatrix} x_1 & 1 & z_1 \\ x_2 & 1 & z_2 \\ x_3 & 1 & z_3 \end{vmatrix} = det\begin{vmatrix} \delta x & 1 & 0 \\ 34+\delta x & 1 & 0.077 \\ -34+\delta x & 1 & 0.010 \end{vmatrix} \tag{5.40}$$

$$C = det\begin{vmatrix} x_1 & y_1 & 1 \\ x_2 & y_2 & 1 \\ x_3 & y_3 & 1 \end{vmatrix} = det\begin{vmatrix} \delta x & 34+\delta y & 1 \\ 34+\delta x & \delta y & 1 \\ -34+\delta x & \delta y & 1 \end{vmatrix} \tag{5.41}$$

$$D = -det\begin{vmatrix} x_1 & y_1 & z_1 \\ x_2 & y_2 & z_2 \\ x_3 & y_3 & z_3 \end{vmatrix} = -det\begin{vmatrix} \delta x & 34+\delta y & 0 \\ 34+\delta x & \delta y & 0.077 \\ -34+\delta x & \delta y & 0.01 \end{vmatrix} \tag{5.42}$$

In the above equation, the error in the location of each tilt pin is expressed as $\delta x = Rcos(\phi)$ and $\delta y = Rsin(\phi)$, where R is the 95% confidence radius and $\phi = [0, 2\pi)$. Solving the above equations gives the plane of the impacting projectile.

$$-2.278x + (2.958 + 0.154\delta x)y + (2312 + 68\delta y)z = 100.572 - 2.278\delta x + 2.958\delta y \tag{5.43}$$

With the normal vector of this plane defined as the following,

$$\hat{N} = \begin{vmatrix} A \\ B \\ C \end{vmatrix} = \begin{vmatrix} -2.278 \\ 2.958 + 0.154\delta x \\ 2312 + 68\delta y \end{vmatrix} \tag{5.44}$$

the angle between this normal vector and the axis of the barrel, e_3, is then determined.

$$cos\theta = \frac{2312 + 68\delta y}{\sqrt{2.278^2 + (2.958 + 0.154\delta x)^2 + (2312 + 68\delta y)^2}} \tag{5.45}$$

The above equation can be solved through an iterative technique. The range of angles defined by ϕ is divided into increments. This gives a set of δx and δy values that can be used in Equation 5.45. The process effectively moves the three tilt pins iteratively around the edge of their suspected location ranges, which yields the maximum and minimum possible angles between the impact plane normal vector and the axis of the barrel. The range can then be used to define the tilt angle and its associated error. For experiment 1207, this was found to be $\theta = 1.62 \pm 0.07$ milliradians.

The angle between the barrel axis and the normal vector is not enough to fully characterize the orientation of the impact plane. Using the barrel key as a reference point, the angle between the key and the projection of the normal vector on the muzzle plane can be found.

$$cos\phi = \frac{-2.278 * 38.22 + (2.958 + 0.154\delta x) * 4.66}{\sqrt{38.22^2 + 4.66^2}\sqrt{2.278^2 + (2.958 + 0.154\delta x)^2}} \tag{5.46}$$

This equation is solved with the iterative method outlined above, as $\phi = 1.6198 \pm 0.0005$ radians.

To determine the time delay between measurements, Equation 5.43 is used to determine the relative height difference between the driver and sample measurement on the impact plane. As discussed above, these heights are related to the distance the shock has traveled into the sample when pin 1 was grounded. Using the driver and sample locations given in Table 5.6, the height of the driver and sample measurements on the impact plane were found to be $Z = 0.0364 \pm 0.0039$ and $Z = 0.02579 \pm 0.0013$ mm, respectively. The error in these measurements was incorporated in the same manner as the tilt pins. The sample height is larger than the driver, with the difference being $\Delta Z = 0.02179 \pm 0.0059$ mm. This distance represents how much further the shock has traveled into driver at the sample measurement location when impact occurs at the driver measurement location. Using the impact velocity, $V_i = 0.2903 \pm 0.0003$ $mm/\mu s$, the delay can be found as $\Delta t = 0.0751 \pm 0.0203$ μs. This time delay was added to the sample record, shifting it to later times, enabling the true transit time of the shock wave through the multilayer to be obtained.

5.5 Computational Prediction of the Uniaxial Strain Plate-on-Plate Experimental Records

The experimental Hugoniot points were seen to have large errors. While all the data points match the computed EOS predicted in Section 4.1.5, it was desired to try and obtain further validation of the simulations. This was accomplished by altering the meso-scale simulations to reproduce the experimental records. If the simulations can accurately predict the experimental records, it would further support that the computational method is accurate and the microstructure is representative of the multilayers. This result, combined with the measured Hugoniot points, can then be used to provide strong validation for the correlations developed in Chapter 4.

5.5.1 2D Simulations of the Uniaxial Strain Experiments

5.5.1.1 Computational Method

The computational reproduction of the experimental records focused on experiment 1207, since it provided the best experimental data with no obvious irregularities in the PVDF or VISAR trace. Experiment 1207 was simulated in 2D using the real, heterogeneous microstructure for the perpendicular configuration presented in Section 4.1.1. In order to obtain a computational equivalent of the PVDF and VISAR records, two distinct simulations were needed. The only difference between the two simulations is the lack of a propagated gauge package and sapphire backer in the VISAR simulation. Both CTH renderings for the PVDF and VISAR simulations are given in Figure 5.16. The computational domain was extended past the defined materials in both simulations, to accurately capture the release wave from the free surfaces.

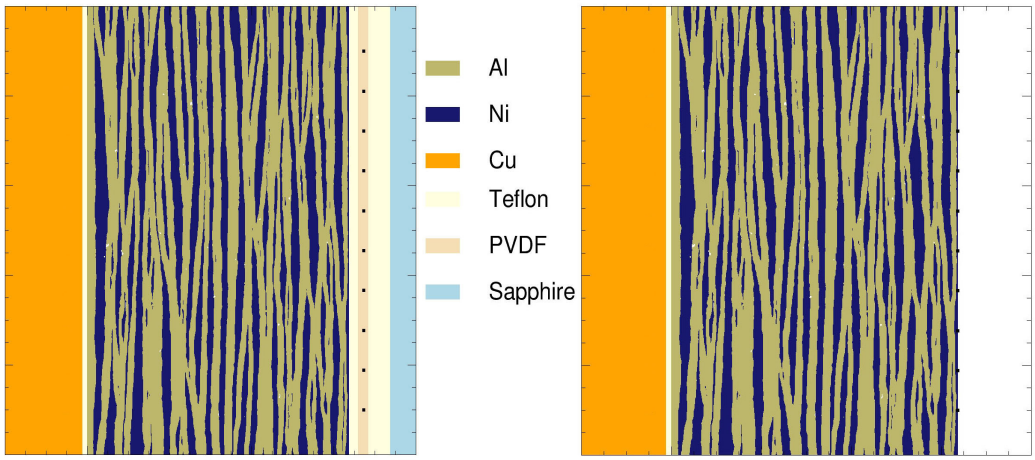

(a) PVDF Simulation (b) VISAR Simulation

Figure 5.16: Configuration of the PVDF (a) and VISAR (b) simulations for experiment 1207.

The experimentally measured thicknesses were used to define the dimension of each material, except for the Cu driver and flier. Modeling the whole thickness of the driver and flier was not necessary, since the release from the back surface of the

Cu does not reach the sample over the timespan of the simulations. Through the proper choice of boundary conditions, only a small portion of the driver and flier need to be simulated, greatly simplifying the computation. This is accomplished by using a transmitting boundary condition in the negative x-direction, which models the flier as semi-infinite. The boundary in the positive x-direction was an extrapolated pressure condition to allow the problem to flow out of the mesh. In the y-direction, the boundary conditions were periodic. An additional simplification was made by assuming the gauge package was a layer of PVDF between two layers of Teflon. This was done since the behavior of the Hysol epoxy was not expected to differ significantly from Teflon.

All the materials were modeled with the Mie-Grüneisen EOS. The properties of Teflon were taken from the CTH database [88]. The ρ_0, C_0, and S_1 values for PVDF were taken to be 1.676 $\frac{g}{cm^3}$, 2600 m/s, and 1.507, respectively [56]. The Grüneisen coefficient was estimated to be 0.7107 [188] and a constant volume specific heat of $1.466e11\frac{erg}{geV}$ was assumed [189]. The ρ_0, C_0, and S_1 values for sapphire were taken to be 3.986 $\frac{g}{cm^3}$, 11140 m/s, and 1.304, respectively [190]. The Grüneisen coefficient was estimated from the relation $\gamma_0 \sim 2S_1 - 1$ and the constant volume specific heat was estimated to be $8.66e10\frac{erg}{geV}$ [191]. The estimations of γ_0 and C_V may not be the most accurate. However, these parameters mostly influence the temperature response, which is not a quantity of interest for these simulations. Consequently, there was no need to obtain better estimates.

The Al, Ni, and Cu were modeled with the Steinberg-Guinan-Lund rate-independent constitutive model [95, 96]. Strain hardening due to rolling was accounted for in the Al and Ni as done previously in Section 4.1.1. The strengths of PVDF and Teflon were modeled with a visco-elastic-plastic model for PMMA, which was assumed to be representative for the materials. The parameters for these model were taken from the CTH database [88]. The sapphire was modeled with a simple elastic perfectly plastic

model with a yield strength equal to the experimentally determined HEL of 15 GPa [190] and an assumed Poisson's ratio of 0.25. This simple model is justified, since the response of sapphire in the simulations is elastic. A simple spall fracture model was also incorporated for every material except sapphire. To save on computational resources, an AMR mesh was used. The multilayer and gauge packages were resolved to 0.89 μm/cell, the sapphire and Cu were resolved to a resolution of 3.57 μm/cell, and the void space was resolved to only 14 μm/cell.

The simulated analog to the experimental PVDF trace was obtained by averaging the σ_{xx} value recorded by 10 Lagrangian tracers located in the center of the PVDF layer. In a similar fashion, the computational analog of the VISAR record was obtained from the average x component of velocity obtained from 10 Lagrangian tracers located 1 micron from the multilayer free surface. These tracers were put 1 micron into the multilayer to ensure they would not advect away from the material and yield nonsensical results. The tracer points corresponding to both of these measurements are marked with black squares in Figure 5.16.

5.5.1.2 Computational Prediction of the Experimental Records

The 2D simulation results are seen to closely match the experimental records in Figures 5.17. The PVDF trace shows two humps. The first hump corresponds to the initial shock wave moving through the gauge package and the reflected shock that comes from the sapphire backer. The second peak is caused by the initial reflected release wave from the gauge package, which reflects off the Cu driver as a shock. The second peak is then relieved by the release wave coming from the back surface of the sapphire backer. Not only are the computational results able to accurately capture all the features of the PVDF record, but they also provide further insight into the complex wave interactions seen in the experimental record.

The VISAR trace is also seen to match the experimental record quite well. At the

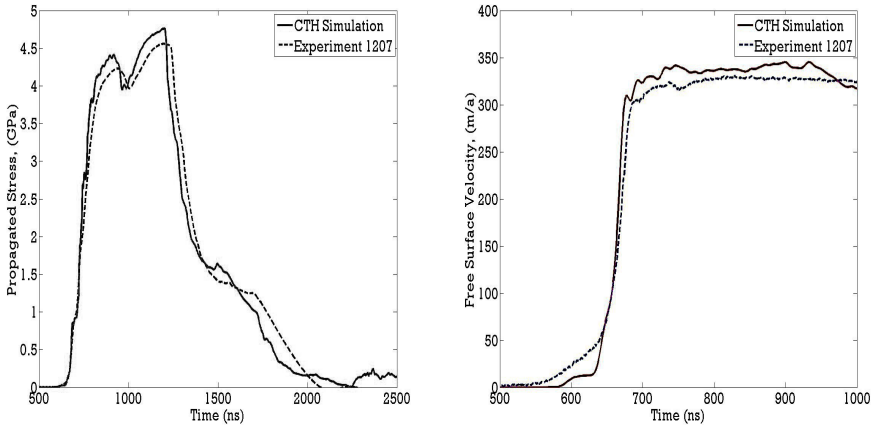

(a) PVDF Simulation (b) VISAR Simulation

Figure 5.17: Comparison the PVDF (a) and VISAR (b) 2D simulation response to the recorded traces for experiment 1207.

end of the computational VISAR trace, the free surface velocity is seen to decrease. This decrease corresponds to an oscillatory response in the computational record due to spallation at the epoxy layer. There is no clear way to tell if the epoxy layer spalls from the experimental record. Most likely, the oscillations due to spall are dispersed by the heterogeneous nature of the composite, but it is also possible that the VISAR record is no longer accurate when the oscillations begin. Regardless, the computational free surface velocity is seen to closely match the portion of the experimental record that was used for the determination of the Hugoniot points.

The accurate prediction of the experimental record computationally provides further validation that the meso-scale simulations are accurately representing the material response. The simulations are able to capture the complex wave interactions in these samples and provide more insight into the experimental results. While the experimental results are seen to have large errors, the ability to reproduce these experimental records computationally shows that the simulated rendering of the multilayer is representative. This provides stronger validation of the conclusions presented in Chapter 4, since the results focus on either rotations or scalings of the original

microstructure. While neither the Hugoniot measurements nor computational prediction alone are enough to justify the computational results, it is believed that, in combination, they provide sufficient validation of the trends reported in Chapter 4.

5.5.1.3 1D Simulations of the Uniaxial Strain Experiments

The microstructure in the 2D experimental simulations was the one used for obtaining the EOS response presented in Section 4.1.5. This fact should allow for the further simplification to 1D. If the computational method in Section 4.1.1 accurately characterized the behavior of the multilayer under uniaxial loading, the determined bulk properties should be able to reproduce the experimental records with a simple 1D computation.

For the 1D simulations, a homogeneous material was defined with a ρ_0 equal to the experimentally determined value for the multilayers defined in Section 3.3.3 and the EOS determined for the perpendicular configuration given in Section 4.1.5. The γ_0 and C_V, where then obtained from volume averaging the values for pure Ni and Al. The strength of the multilayer was modeled with the Steinberg-Guinan-Lund rate-independent model for Al, since it was the majority component. The initial yield strength was set to a volume average of those for each constituent given in Section 3.3.6. A volume average was also used to set the maximum possible strain hardening for the approximated bulk material.

The 1D results are seen to match the experimental records nearly as well as the 2D results using significantly less resources. The PVDF trace is seen to exhibit noise in the response between the two stress peaks, but otherwise matches well. The VISAR trace is seen to rise much faster due to the homogeneous material assumption, which does not capture the dispersive characteristics of the material fully. However, the free surface velocity is accurately reproduced. While the 2D simulations are more accurate, the 1D simulations still capture much of the trends in the experimental

record. This shows that the method of EOS generation presented in Section 4.1.1 is appropriate for determining the bulk material response of these multilayers.

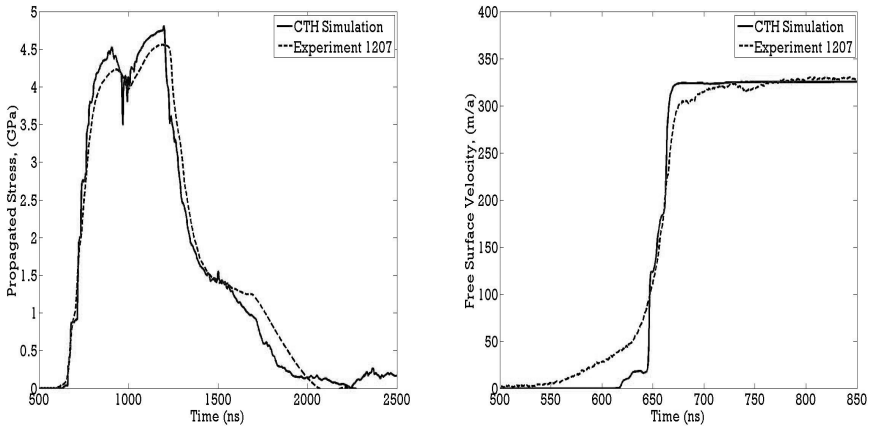

(a) PVDF Simulation (b) VISAR Simulation

Figure 5.18: Comparison the PVDF (a) and VISAR (b) 1D simulation response to the recorded traces for experiment 1207.

CHAPTER VI

UNIAXIAL STRESS MODIFIED ROD-ON-ANVIL EXPERIMENTS

Uniaxial stress experiments were performed to investigate the mechanical initiation of reaction in the Ni/Al multilayered composites. The uniaxial stress condition provides a more likely scenario for reaction initiation than the uniaxial strain experiments, due to the increased sample deformation. To identify the presence of reaction in these experiments, high speed photography was used to capture any visible light emission during compression. For the multilayered samples, light emission was only present for the experiments performed in air, suggesting reaction initiates with the oxidation of Al. Due to the thin, fully dense nature of the multilayers, substantial portions of the samples could be recovered for analysis. A variety of post-mortem analysis methods, including optical and scanning electron (SEM) microscopy, energy-dispersive X-ray spectroscopy (EDS), and XRD, were then used to identify the nature of the observed reaction. The post-mortem analysis provided strong evidence that the oxidation of Al induces localized intermetallic reactions.

6.1 Uniaxial Stress Modified Rod-on-Anvil Experimental Setup

The uniaxial stress experiments performed on the multilayer composites utilized a modified rod-on-anvil, or Taylor, impact geometry [192, 193, 194]. The experiments were done using the 7.62 mm light gas gun at Georgia Tech. A schematic of the gun operation is presented in Figure 6.1. In the experiments, two laser beams are used to measure the projectile velocity and time all diagnostics with an up-down counter (UDC). When the projectile breaks the first laser beam, the UDC begins to count in

time until the second laser beam is broken. Using the known distance between lasers, the UDC estimates the projectile velocity. Assuming the projectile has reached its terminal velocity, the UDC estimates the time of impact for triggering any diagnostics based on the known distance between the second laser and the target.

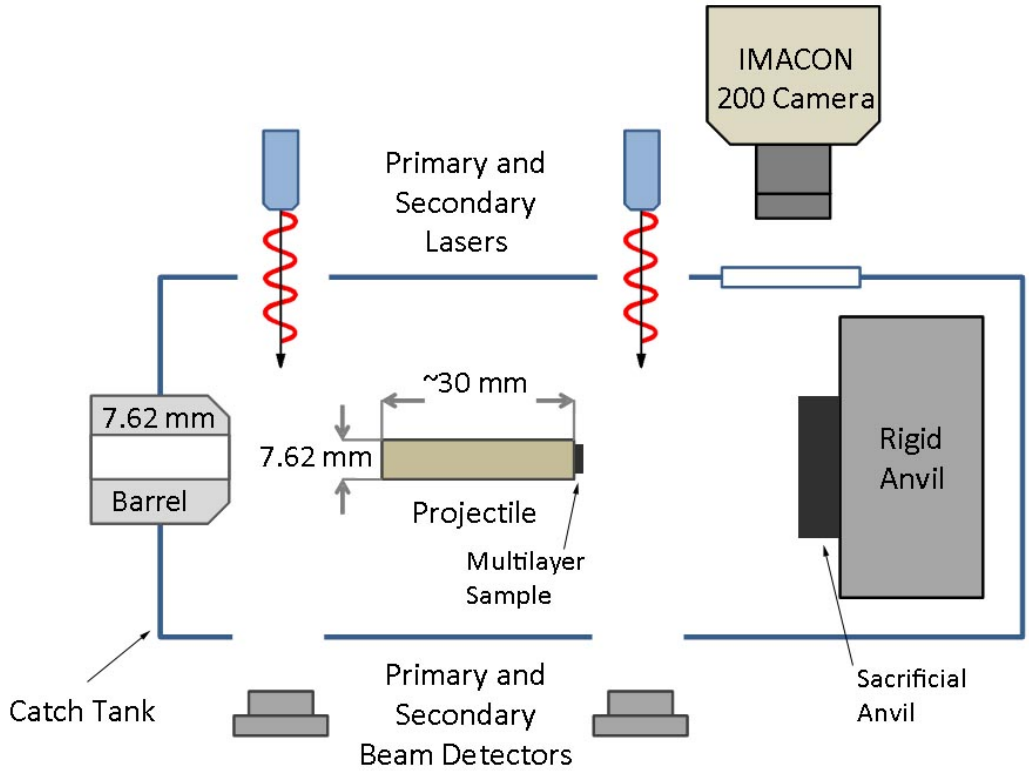

Figure 6.1: Schematic showing the operation of the 7.62 mm light gas gun at Georgia Tech (modified from [160]).

The accuracy of this triggering system is tied to the uncertainty in each of the measured distances. Errors in these measurements lead to a typical uncertainty in the impact time of around 1 μs. Through some algebraic manipulations, a relationship for the maximum possible error in timing of the impact event can be determined based on the uncertainty in each measurement, $\frac{\delta m_1}{m_1}$ and $\frac{\delta m_2}{m_2}$.

$$\frac{\delta t_{imp}}{t_{imp}} = \frac{\frac{\delta m_1}{m_1} + \frac{\delta m_2}{m_2}}{1 - \frac{\delta m_1}{m_1}} \tag{6.1}$$

Here, m_1 represents the distance between the two lasers, while m_2 represents the distance between the second laser and the target. Given the typical dimensions of the

gun, at an impact velocity of 300 m/s, an error in the measurement of each distance of only 0.1% yields a maximum possible uncertainty in the impact time of ~ 0.7 μs. As a result, care must be taken when determining the camera timings so useful data can be obtained.

The sample preparation for these experiments consists of mounting a small section of the multilayer on the end of a Cu projectile. Top and side views of a typical sample/projectile assembly are shown in Figure 6.2. The Cu projectiles are lapped before sample mounting to remove any turning marks on the projectile faces. These machining marks can act as stress concentrators and change the observed response of the sample. Additionally, lapping helps to ensure a flat impact face that is perpendicular to the projectile axis. Ideally, the experiments should consist of a perfectly flat projectile impacting perpendicular to the anvil face. As a result, it is important to minimize surface roughnesses and inclinations in the impact. This helps to strength any correlations between an experiment and an idealized simulated response.

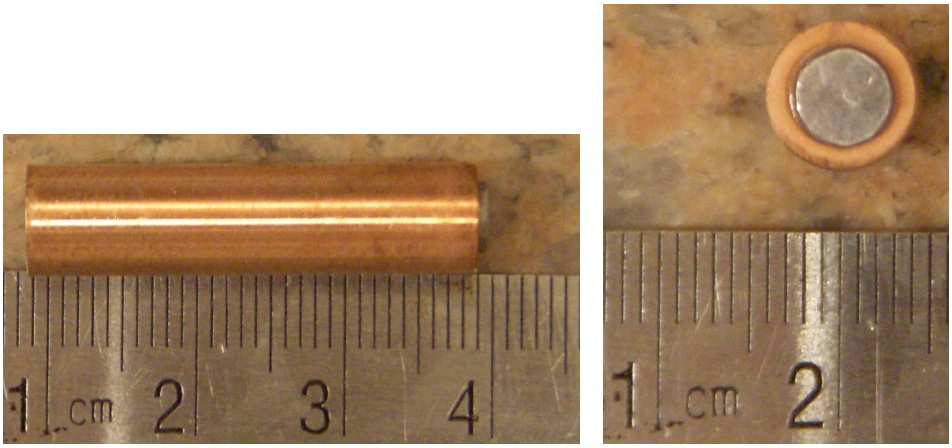

(a) Side View (b) Top View

Figure 6.2: Image of a typical modified Taylor experiment sample/projectile assembly.

The multilayer samples were punched out of a larger sheet with a $3/8^{\text{ths}}$ inch punch. The edges of the round samples were then sanded by hand to remove any lips as a result of shearing during the punching process. This ensured the multilayers

rested flat on the face of the Cu projectiles and eliminated any deformation or mixing generated by the punching process. The use of $3/8^{\text{ths}}$ inch samples was done to eliminate edge effects in the experiment. With larger sample diameters, the sample flow during deformation can exceed the projectile diameter. The Cu projectile then acts as a punch, shearing through the sample and disrupting the uniaxial stress state. The samples are mounted on the Cu projectile face with a small amount of de-gassed Hysol epoxy. The sample/projectile assembly was then cured under weight, to help the epoxy spread out into a thin film.

The projectile/sample assemblies were fired at small 1.25 inch diameter hardened S7 steel sacrificial anvils (measured as HV $= 666 \pm 43$). The S7 anvils were precision ground to ensure the surfaces were parallel to within 0.0001 inches. The sacrificial anvils were then mounted on a larger precision ground anvil with Loctite® 401 epoxy. Following adhesion, a measurement was taken to ensure the surface of the sacrificial anvil was parallel within 0.0002 inches with the back side of the larger anvil. The assembly was then placed in the experiment chamber on a fixture that has been aligned perpendicular to the barrel axis. All of this was done to minimize errors caused by inclination in the impact, ensuring the only significant source of tilt results from perturbations in the projectile flight path.

The use of the smaller sacrificial anvils was done in an effort to gain conclusive proof of an intermetallic reaction in the experiments. The 1.25 inch diameter anvils are small enough to fit into an XRD machine. Additionally, the small geometry and high density of the sample enabled easy recovery of $\sim$80% of the original mass. While this aids in the post-mortem analysis, it also presents a limitation on the amount of material deformation induced, which affects the extent of reaction.

The uniaxial stress experiments performed on the multilayer composites ranged in impact velocity from 350 to 500 m/s. The details of each experiment are presented in Table 6.1. Table 6.1 shows that the uniaxial stress experiments were done in both air

and vacuum to investigate if an Al oxidation reaction could trigger an intermetallic reaction to propagate into the sample bulk through an SHS mechanism.

For all experiments, an IMACON 200 high speed camera was used to obtain 16 still frame images of the impact event. While the timings and exposure times varied, typically the images were spaced around 0.25 to 1 μs apart and had an exposure time of 150 ns. The camera was oriented essentially perpendicular to the impact and a flash was used to provide back lighting. This produced silhouettes of the projectile impact for visualizing the transient deformation of the sample and capturing any light emission during impact.

6.2 Uniaxial Stress Modified Rod-on-Anvil Experimental Results

In the past, the presence of an intermetallic reaction was identified in Al-based intermetallic powder mixtures during uniaxial stress loading through the presence of visible light emission during impact [195]. This light emission was observed through high speed photography and was used to develop a reaction threshold [195]. However, the presence of light emission provides no information of the nature or the kinetics of the reaction.

For Al-based reactive mixtures, there is always the potential for the reaction to correspond to the oxidation of Al and not an intermetallic reaction. While it is possible for an oxidation reaction to trigger an intermetallic reaction or visa versa, the presence of light provides no means to determine the reaction type. Even under vacuum, there could be enough residual oxygen present to initiate an oxidation reaction. There is also the possibility that early light emission represents an ionization event. Experiments performed in air and under vacuum on the impact of Cu projectiles on steel anvils have shown low level light emission. This light most likely corresponds to the ionization of air between the projectile and anvil. There is also the potentially

Table 6.1: Measurements for the modified rod-on-anvil Taylor experiments.

Experiment Number	Projectile Mass (g)	Multilayer Mass (g)	Multilayer Thickness (in)	Final Sample Mass (g)	Impact Velocity (m/s)	Vacuum Level (mtorr)	Visible Light
11458	12.1085	0.0697	0.03100	12.1795	447.39	74	No
11459	12.0753	0.0681	0.02935	12.1451	404.11	67	No
11460	12.1033	0.0699	0.02895	12.1738	479.52	83	No
11461	12.0942	0.0665	0.02970	12.1648	422.54	74	No
11462	12.1000	0.0639	0.02835	12.1660	354.86	71	No
11513	12.0931	0.0673	0.02850	12.1616	471.06	Ambient	Yes
11514	12.1405	0.0702	0.02900	12.2113	407.55	Ambient	Yes
11517	12.1299	0.0658	0.02900	12.1965	354.01	Ambient	Yes
11518	12.1107	0.0646	0.02840	12.1756	379.63	Ambient	No

Only one measurement was made for all quantities, so no errors can be given.

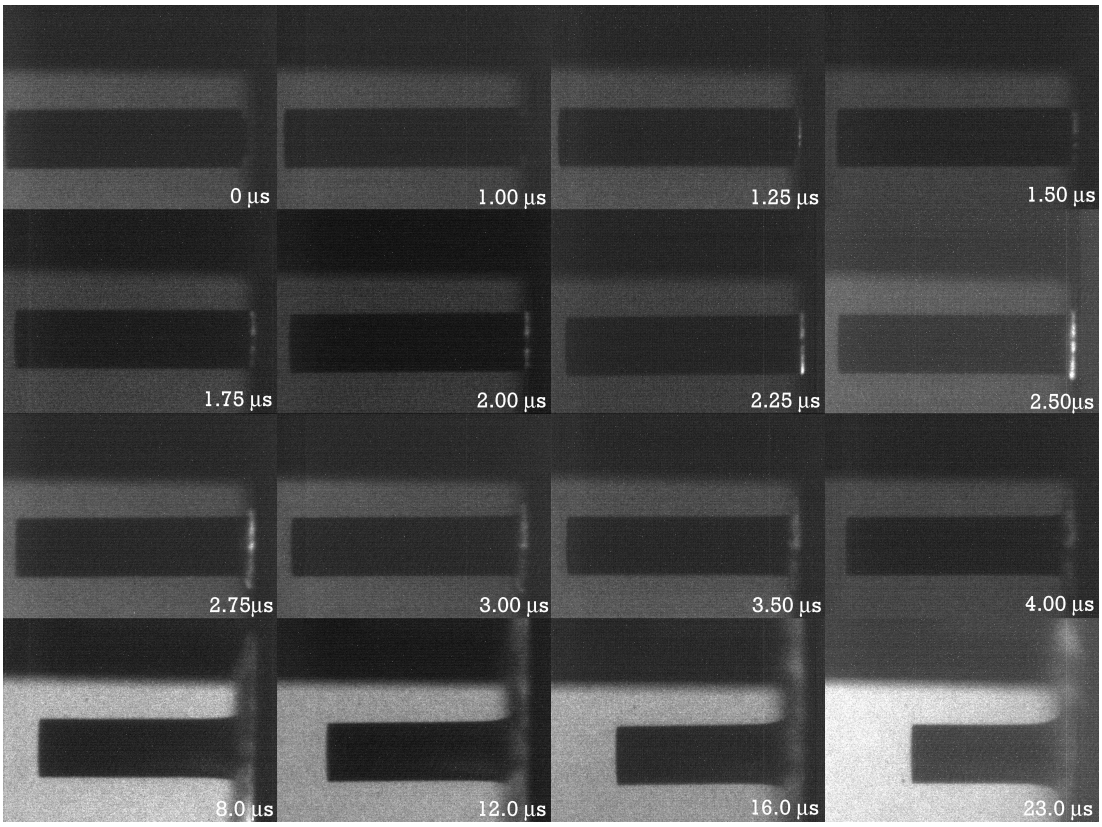

Figure 6.3: High speed images from experiment 11513 showing light emission during the impact event.

that the Cu is ionizing and emitting light, which has been observed during hypervelocity impacts [196]. However, this is unlikely at the impact velocities investigated. As a result, light emission is only an indication that a reaction has occurred. Without some diagnostic to probe the nature of this light emission, such as time-resolved spectroscopy, no conclusive determination of intermetallic formation can be obtained and other methods must be employed. In this work, post-mortem analysis was used for this purpose.

As seen in Table 6.1, visible light emission was only observed from the multilayered composites for the experiments performed in air. Figure 6.3 shows the light emission observed in the cold-rolled multilayer composites with the high speed photography for experiment 11513. The times given in Figure 6.3 are all referenced from first image, which is assigned $t = 0$. The light is seen to originate at the impact face

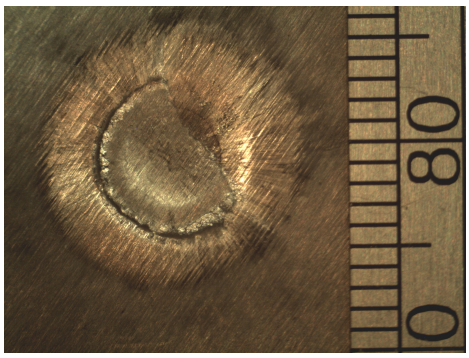

(a) Anvil

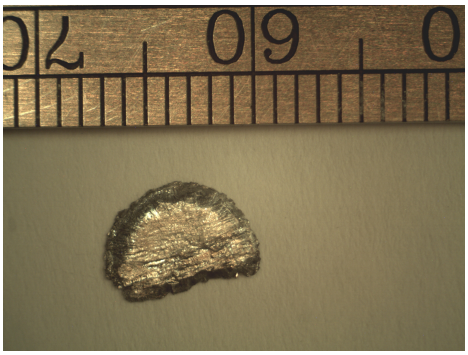

(b) Impact Face

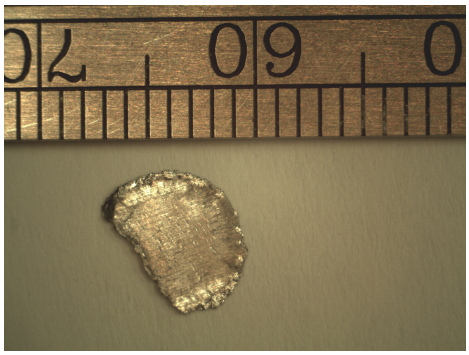

(c) Back Face

Figure 6.4: Images of the impacted anvil (a) and both the impact (b) and back surface (c) of the recovered multilayer for experiment 11513.

before complete compaction of the multilayer and continue in the debris cloud at later times. This persistence of the light emission to later times indicates a reaction, and not an ionization event, is taking place. In addition, the observation of light emission for only the experiments performed in air indicates that the reaction is initiated with the oxidation of the Al. The question now becomes whether or not this oxidation reaction can trigger an intermetallic reaction. If an intermetallic reaction is initiated in the multilayers, the reaction could propagate into the bulk of the sample through an SHS mechanism.

To conclusively determine if an intermetallic reaction had taken place during impact of the multilayers, post mortem analysis (*i.e.* optical and SEM microscopy, EDS, and XRD analysis) was employed. In past experiments on porous powder compacts, recovery of the sample after impact was not feasible [195]. Due to the violent nature

of the experiments, the sample fractures and disperses into the chamber during impact. The fully dense, thin nature of the multilayer composites allows for easy recover due to the flow of the Cu projectile, which encapsulates and preserves the sample. This containment, while allowing for recovery, also imposes a severe limitation on the amount of deformation the multilayer experiences. The flow of the multilayer and the impacting edge of the Cu rod creates a pinch point in the experiment. This generates intense deformations at the sample periphery and welds the multilayer to the sacrificial anvil. This process limits the deformation experienced by the sample interior and ejects the highly deformed sample periphery into the experiment chamber, generating the debris cloud.

An example of the recovered portion of the sample from experiment 11513 is shown in Figure 6.4a. The sample is clearly seen to be adhered to the anvil surface, facilitating easy recovery. The impact and rear surfaces of the sample after removal from the anvil are shown in Figures 6.4b and 6.4c, respectively. In Figures 6.4, a large section of the sample is seen to have fractured during impact and was lost. This is not uncommon, since the strain hardening due to rolling embrittles the multilayers.

For all recovered samples, XRD analysis was performed in an effort to identify the presence of a bulk intermetallic reaction. Since the multilayers can undergo SHS reactions, the heat generated from an oxidation reaction could trigger an intermetallic reaction that propagates into the sample bulk. XRD traces were obtained on the multilayers while still adhered to the sacrificial anvil and on both sides of the sample once removed. For every experiment, no signs of a bulk intermetallic reaction were observed. Figure 6.5a shows the XRD results for the impact surface of the recovered sample for experiment 11460, which is characteristic of all the experiments. All of the XRD traces showed no peaks corresponding to any known intermetallics of Ni and Al. The only peaks found in any of the XRD results not corresponding to either Ni or Al were for the rear sample surface in experiment 11460. These extra peaks are

seen in Figure 6.5b and correspond to an Al and Cu alloy.

This lack of an observed bulk intermetallic reaction is tied to the thin nature of the multilayer samples. The encapsulation of the multilayer by the projectile, while aiding in recovery, limits the material deformation to the periphery of the sample. These hot, highly deformed edges, which are reacting, as indicated by the high speed photography, are ejected into the chamber. This ejection happens to quickly for the heat generated by the oxidation reaction to initiate and propagate an intermetallic reaction back into the sample bulk. Consequently, the portion of the sample most likely to have reacted is lost into the chamber. Attempts to catch these particles with water soluble soap and identify if an intermetallic phase had formed proved to be messy and impractical. As a result, there could be no determination of the presence of an intermetallic reaction in these ejected fragments. Even though these fragments do not have enough time to trigger a bulk reaction, it is possible that they were able to trigger localized areas of reaction that quickly quenched, which can be observed through microscopy.

The recovered samples were examined in an SEM to identify areas of material flow and reaction initiation along the highly deformed edges. The deformation observed at the sample periphery was found to be heavily dependent on the chamber atmosphere, as observed in Figure 6.6. Since Figure 6.6 is a SEM backscatter image, Ni is the brighter phase, due to its larger atomic number. In vacuum, the sample fractures and flakes apart, as observed in Figure 6.6a. In fact, no significant signs of material flow were observed in any of the recovered samples performed in vacuum. For the experiments performed in air, signs of material flow were observed at every impact velocity as seen in Figure 6.6b, which corresponds to the recovered sample for the lowest impact velocity experiment in air (experiment 11517). This result leads to two conclusions: there is not enough residual oxygen under vacuum to trigger an oxidation reaction and an oxidation reaction provides the heat necessary to induce

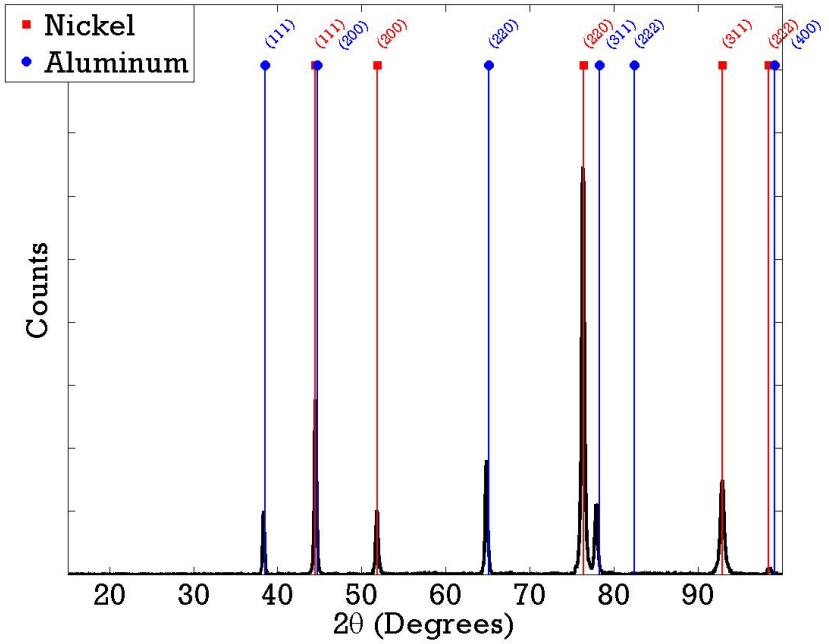

(a) Impact Surface

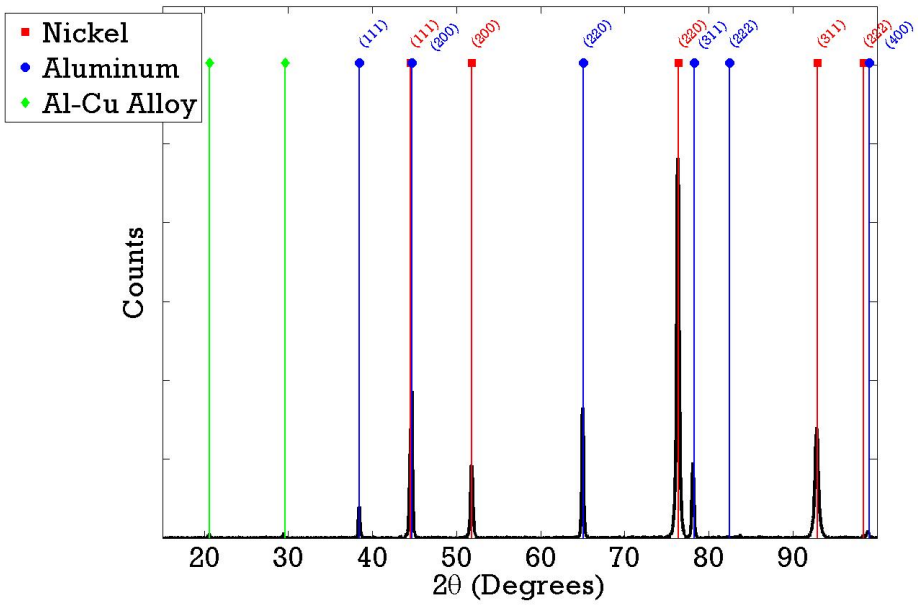

(b) Back Surface

Figure 6.5: XRD traces for the impact (a) and back (b) surfaces for experiment 11460. The impact surface trace (a) is characteristic of all experiments. In all cases, no evidence of a bulk intermetallic reaction was observed in either air or vacuum. The only peaks not corresponding to Ni and Al belong to an Al-Cu alloy, which was observed only for the back surface of the sample in experiment 11460 (b).

material flow and mixing. As a result, the oxidation reaction, and consequently the presence of air in the experiment, is critical for initiating an intermetallic reaction.

The experiments performed in air were further investigated in an effort to identify areas of localized intermetallic reaction. Figure 6.7 shows the SEM backscatter image for a section of the recovered multilayer in experiment 11513, which was performed at the highest impact velocity. In Figure 6.7, an area of differing contrast can be observed as indicated by the blue box. The differing contrast suggests that portion of the sample is neither pure Al or pure Ni. The composition of this section was investigated with EDS, as indicated in Figure 6.7, and found to be in the range for AlNi. Unfortunately, EDS only provides compositional information and not structural information, so there is no way to conclusively prove that this section is indeed AlNi. While this was the only sample to exhibit signs of a possible intermetallic reaction, the results provide strong evidence that the oxidation of Al is triggering isolated regions of localized intermetallic reaction in the multilayer composites.

After analyzing the recovered sample periphery in the SEM, the meso-scale deformation and possible reaction response of the sample interior was also investigated. The recovered samples were mounted in epoxy, cross-sectioned, polished, and then imaged with an optical microscope. The cross-sections of some of the recovered samples can be seen in Figure 6.8. The interior of the recovered samples exhibited clear signs of shear banding regardless of chamber atmosphere. The irrelevance of the chamber atmosphere on the interior deformation of the samples is not surprising, since the interior is, by its nature, shielded from the chamber atmosphere. The shear banding can be seen in both air (Figure 6.8a), vacuum (Figure 6.8a), and at every impact velocity investigated (Figures 6.8a and 6.8c). Shear banding has been observed in the past to initiate reaction in porous powder reactive mixtures [79, 17, 15], but, for the multilayers investigated, no reaction occurred along the shear bands.

Figure 6.8c also shows cracking in the multilayer during the experiment. The

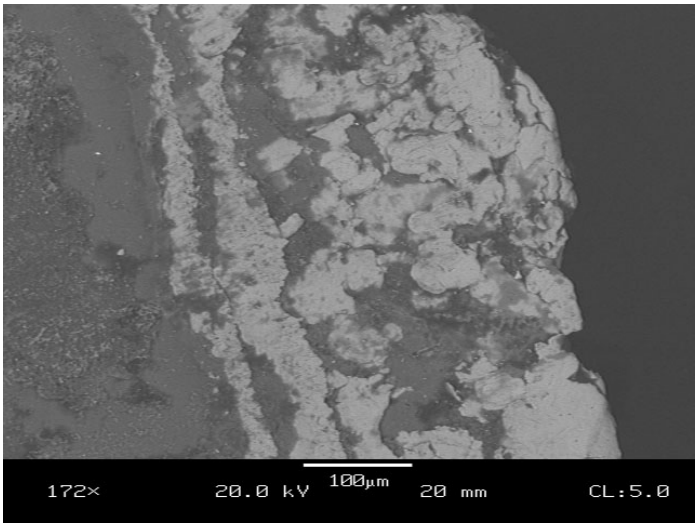

(a) Experiment 11460

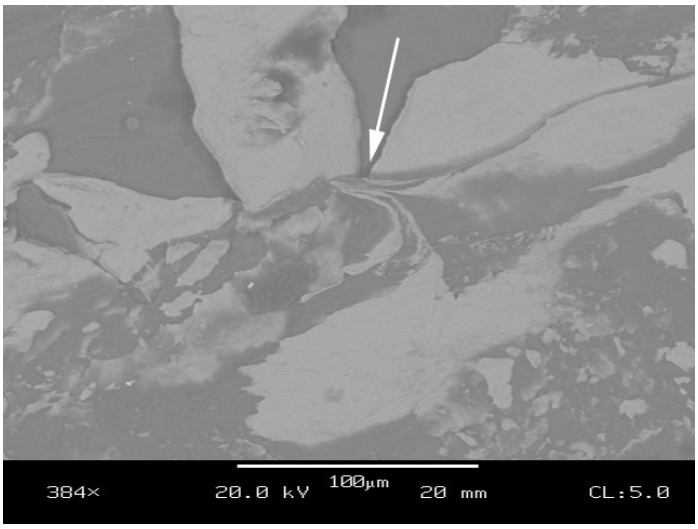

(b) Experiment 11517

Figure 6.6: SEM backscatter images for experiments 11460 (a) and 11517 (b) showing the differing deformation behavior observed at the periphery of the recovered multilayer composites as a result of chamber atmosphere. For experiment 11460, which was done in air, the periphery of the sample is seen to fracture and flake apart, showing no significant signs of material flow. In contrast, experiment 11517 was performed in air and the heat generated from the Al oxidation reaction is seen to induce material flow and mixing, which promotes intermetallic reaction initiation.

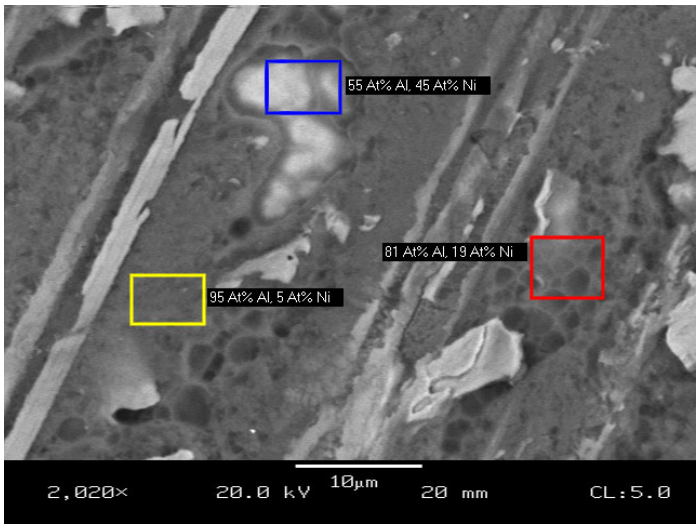

Figure 6.7: SEM backscatter images for the recovered multilayer for experiment 11513 along with EDS results for portions of the microstructure. An area of potential reaction initiation was observed (blue box) in the sample through EDS. Since EDS provides no structural information, the results provide strong evidence of an intermetallic reaction, but not conclusive proof.

cracking is not unexpected, due to the rolling process, which embrittles the multilayer. More interestingly, this cracking occurs in the Al phase and not the interface. The propagation of the crack through the Al indicates that the multilayer composites have relatively high interfacial strength [197], supporting the choice of perfectly bonded interfaces for most of the simulations performed in Chapter 4.

The uniaxial stress rod-on-anvil impact experiments suggest that any intermetallic reaction that occurs in these multilayers is initiated by an oxidation reaction. Unfortunately, the vast majority of any portion of the sample undergoing an oxidation, or potential intermetallic, reaction occurs along the periphery of the sample and is ejected into the experiment chamber. This prohibits propagation of the reaction into the bulk of the sample, making conclusive confirmation of reaction difficult. However, the post-mortem analysis on the recovered sample provided strong evidence of isolated regions of localized intermetallic reaction, suggesting that intermetallic reaction occurs in the debris cloud and, under the right conditions, could propagate back into the bulk in and SHS manner.

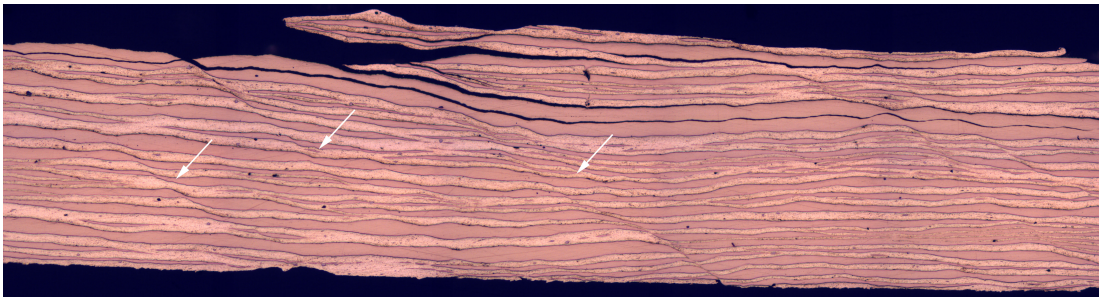

(a) Experiment 11513 - $\sim$ 480 m/s in Air

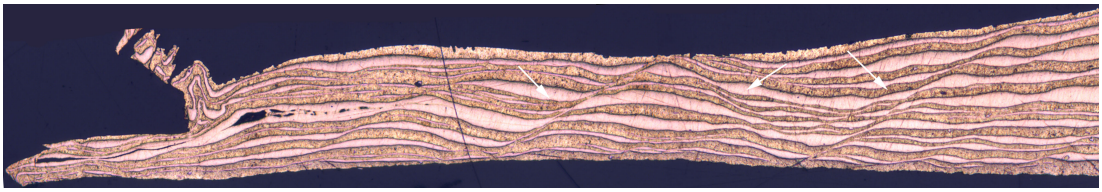

(b) Experiment 11460 - $\sim$ 480 m/s in Vacuum

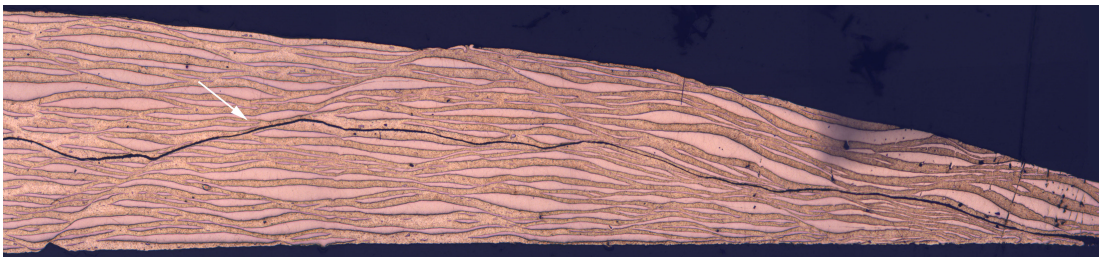

(c) Experiment 11517 - $\sim$ 350 m/s in Air

Figure 6.8: Optimal micrographs of the interior shear banding observed in experiments 11513 (a), 11460 (b), and 11517 (c). The shear banding (arrows) is observed to occur in both air (a) and vacuum (b) and at every impact velocity (a and c). Additionally, cracking can be observed in some of the recovery samples (c). This cracking is seen to occur in the Al and not the phase boundary and follows the shear bands (c).

CHAPTER VII

COMPARISON OF SHOCK WAVE PROPAGATION IN FULLY DENSE AND POROUS Ni/Al COMPOSITES

As mentioned in Chapter 2, the shock compression response of Ni and Al porous powder compacts was previously investigated experimentally and computationally by Eakins [27]. Eakins focused on the effects of the initial composite density and morphology on the shock-induced reaction response. In particular, he used the computationally predicted particle level deformation to explain the observed reaction response in each composite [27]. In this section, the computational results generated by Eakins are utilized for comparison to the fully dense Ni/Al composites investigated in this work. This includes the various multilayer configurations and the shock compacted Ni/Al powder composite. These comparisons help in understanding how material interfaces influence the shock compression response of such highly heterogeneous systems.

7.1 Porous Powder Compact Properties

The powder compacts used by Eakins [27] were composed of -325 mesh Ni and Al powders mixed in an equivolumetric ratio [27]. Four compact densities were investigated: 45%, 52%, 60%, and 80% TMD. For the 45% TMD compacts, two different morphologies of Ni particles were used: spherical and flake. This allowed for the effects of particle morphology to be investigated, similar to the work of Dunbar *et al.* [2]. Eakins simulated a 1620 μm x 261 μm area of each pressed powder compact in CTH using real, heterogeneous microstructures obtained from SEM images.

Both the shock compacted and porous powder compacts have an equivolumetric

ratio of constituents, while the multilayers have a stoichiometric ratio. This means that the volume fractions of each phase in the multilayer composite are slightly different than the porous and fully dense powder compacts (60% Al compared to 50%, respectively). While this variation in volume fraction does slightly alter the bulk shock compression response, it does not appreciably affect the interfacial and particle level responses. The paricle interactions are influenced more by the morphology and arrangement of the materials. Since the interfacial interactions are of interest in the current work, the variation in volume fractions was not felt to prohibit comparisons between the composites.

Using Eakins' binary SEM images, measurements of V_V and S_V for each phase were determined in this work to aid in the comparison between composites. These values are presented in Table 7.1. The volume fractions were obtained from the pixel ratio of each phase. The surface areas per unit volume were found using Equation 4.1, with L_A found by summing the perimeters of the particles and dividing by the image area. The values in Table 7.1 immediately show that there are large variations in the parameters due to the small domain size.

Table 7.1: Stereological measurements for each powder compact.

Composite	$V_{V_{Al}}$	$V_{V_{Ni}}$	$V_{V_{por}}$	$S_{V_{Al}}$ (mm^{-1})	$S_{V_{Ni}}$ (mm^{-1})	$\bar{\lambda}$ (mm)
80 Spherical	0.3803	0.3684	0.2513	157.42	113.89	0.0037
60 Spherical	0.2698	0.3444	0.3858	108.81	119.16	0.0068
52 Spherical	0.2348	0.2817	0.4835	92.99	106.34	0.0097
45 Spherical	0.2390	0.2241	0.5369	95.06	93.89	0.0114
45 Flake	0.1455	0.3088	0.5457	88.78	1756.99	0.0012

7.2 Bulk Response of the Composites

For the porous powder compacts, Eakins generated the EOS response by simulating a rigid Cu piston impacting at 3 different velocities: 0.5, 0.75, and 1 km/s [27]. The transit time of the shock wave was then determined from the arrival of the wave at

locations 1 and 1.5 mm into the composite. The EOS responses of each composite investigated by Eakins are presented in Table 7.2 [27]. For these simulations, Eakins assumed that the specified Cu piston velocity was constant. This is not an entirely accurate assumption, since the velocity is actually determined by the impedance mismatch between the sample and driver. This means the particle velocities reported by Eakins are slightly higher than those in the simulation, but, given the low impedance of the powder compacts, this deviation should be small and not appreciably alter the results.

Table 7.2: EOS parameters for the various Ni/Al powder compacts investigated by Eakins [27].

Composite	C_0 (km/s)	S_1
80 Spherical	0.5667	2.1853
60 Spherical	0.2242	1.8630
52 Spherical	0.1363	1.6978
45 Spherical	0.0727	1.5848
45 Flake	0.0931	1.5387

The porosity of the powder compacts lowers their density and inert sound speed, causing their low impedance. The C_0 values for the porous powder compacts listed in Table 7.2 are all under 1 km/s, which is substantially lower than the 4 to 5 km/s seen in the fully dense composites. With porosity in the system, transmission of the shock wave becomes more difficult, since the shock wave can not propagate across the pores. Consequently, the voids must collapse to transmit the wave, which occurs on a time scale controlled by the particle velocity. This leads to slower transmission of the wave energy and lower wave speeds, as seen in Table 7.2. In the fully dense composites, constant contact between the phases enables the quick transmission of the wave, leading to the higher wave velocities.

The bulk response is also influenced by the nature of the wave interactions in the composite. The slopes of the EOS for each composite are listed in Table 7.2 and range between ~ 1.5 for the 45% TMD composites and ~ 2 for the 80% TMD composite.

This range is similar to that observed for decreasing angles of interfacial inclination in the multilayer composites (90 to 0 degrees). The perpendicular configuration exhibited the lowest S_1 value of around 1.5, while the parallel configuration had the largest at around 2. This result suggests that the wave interactions from the material interfaces in the multilayer composites and porosity in the powder compacts have similar characteristics. Most likely, these interactions are tied to the nature and number of the wave interactions. With increased porosity, the probability of an interaction at a particle/void interface increases. Interactions of this type generate a reflected wave opposing the propagating shock pulse. This is similar in nature to the reflections in the perpendicular multilayer composite. As porosity decreases, transmission of the wave across the powder compact becomes easier and strong release waves from the particle/void interfaces become less prominent. This provides less hindrance to the propagating wave, and is analogous to when the orientation of the multilayer layers is parallel to the propagating shock wave. This result highlights the complexity of the wave interactions in these highly heterogeneous systems, and suggests that the interactions generated by the porosity in the powder compacts have similar characteristics to those resulting from the periodicity in the multilayers.

The results from the porous powder compacts also show that particle morphology has a negligible effect on the EOS, which is observed by comparing the responses of both 45% TMD composites. This result is not surprising, since the EOS is a bulk measurement averaged over many particles. Consequently, the EOS is determined more by the ratio of constituents and the porosity, rather than their shape or orientation. However, particle shape has a much larger influence on the particle level deformation, which is discussed later in Section 7.4.

7.3 Shock Front Structure in the Composites

Due to the presence of void space, the structure of the shock wave in the porous powder compacts is vastly different from those in the fully dense composites. The shock fronts for the various porous powder compacts investigated by Eakins are shown in Figure 7.1 [27], and are seen to have very jagged profiles. The fluctuations in the pressure response of the powder compacts generated by their porosity are similar in structure, but larger in magnitude, than those observed in the shock compacted composite (Figure 4.39) or the perpendicular multilayer orientation (Figure 4.5). This can be related to the impedance mismatch across the interfaces. Zhuang *et al.* have shown that the oscillations in the pressure response of a multilayered system increase in magnitude as the impedance mismatch across the interface increases [125]. The wave interactions with the void space, which has negligible impedance, generate strong release waves, which produce the very jagged pressure profile. With a lower impedance difference across the interface, these perturbations become smaller as seen in the fully dense composites. In the perpendicular multilayer, not only are the pressure oscillations smaller in amplitude, they are also more frequent and dampen out more quickly due to the periodicity of the system. With periodic layering, more wave interactions are generated creating more fluctuations and more dispersion, which leads to quicker attenuation of these oscillations. This shows that the nature of the material interfaces affects the magnitude, frequency, and attenuation of these perturbations.

The rise times of the shock front also depends heavily on the composite microstructure. The rise times of the wave fronts in Figure 7.1 decrease with decreasing porosity, due to the quicker transmission of the shock wave, as discussed in Section 7.2. However, with flake Ni particles, the rise time decreases drastically compared to the corresponding spherical compact. In addition, the pressure response becomes more uniform. This is a consequence of increased contact between particles during compaction and the smaller void spaces in the green compact due to the flake geometry.

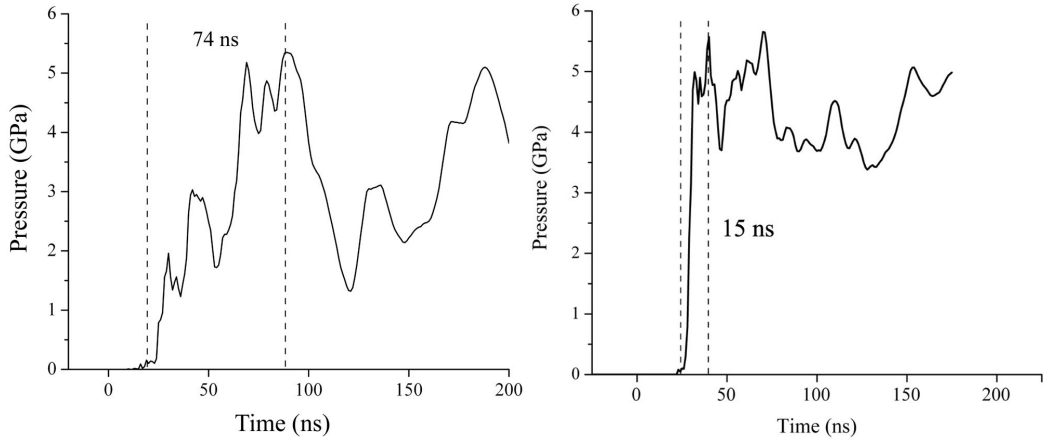

(a) 45% TMD Spherical

(b) 45% TMD Flake

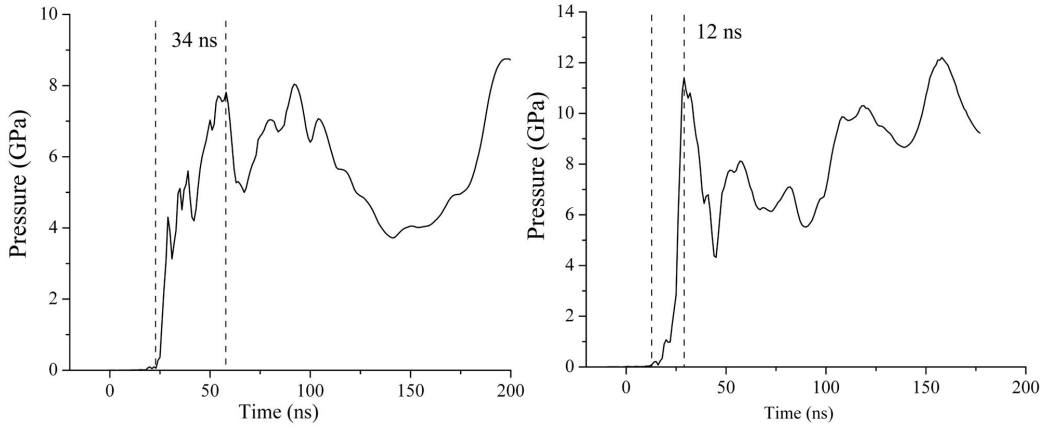

(c) 60% TMD Spherical

(d) 80% TMD Spherical

Figure 7.1: Pressure traces for various porous powder compacts of Ni and Al investigated by Eakins: 45% TMD spherical (a), 45% TMD flake (b), 60% TMD spherical (c), and 80% TMD spherical (d) [27]. The shock profiles are jagged, due to the porosity in each system. In addition, a general trend of decreasing rise time with decreasing porosity is seen. However, this trend does not hold for the 45% TMD flake mixture (b), suggesting that $\bar{\lambda}$ is an important parameter affecting the shock rise.

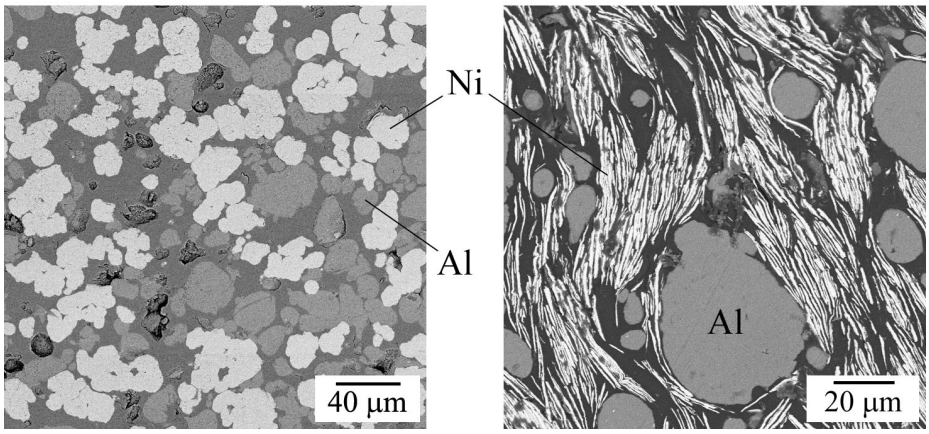

Figure 7.2: SEM image showing the distribution of particles in the 60% TMD spherical and 45% TMD flake powder compacts [27]. The flake geometry of the Ni particles is seen to increase the number of Ni particles necessary to achieve the desired volume fraction. With so many Ni particles, the average distance between particles decreases, leading to the quicker rise times for the composite. The flatter shape of the Ni particles in the 45% TMD flake compact also produces a more uniform compaction between constituents, as indicated by the more steady pressure response observed in Figure 7.1.

As the flake composite is compacted, the Al begins to flatten between the Ni flakes, as discussed with Figure 2.29. This leads to longer, more periodic interfaces, as opposed to the point contacts in the spherical mixtures. In addition, the average size of the void space in the flake mixture is smaller than any other composite. This is seen in Figure 7.2, which compares the initial microstructures of the 60% TMD spherical and 45% TMD flake composites [27]. The average dimension of the void space in each composite can be described with the mean free path, $\bar{\lambda}$, which represents the average distance between particles on a randomly oriented test line [155].

$$\bar{\lambda} = \frac{4(1 - V_V)}{S_V} \tag{7.1}$$

The mean free paths for each composite are listed in Table 7.1. The flake composite has the smallest $\bar{\lambda}$, due to the geometry of the flake Ni particles. With such a thin, elongated shape more particles are necessary to achieve the desired volume fraction, as seen in Figure 7.2. This more evenly disperses the Ni particles between the Al

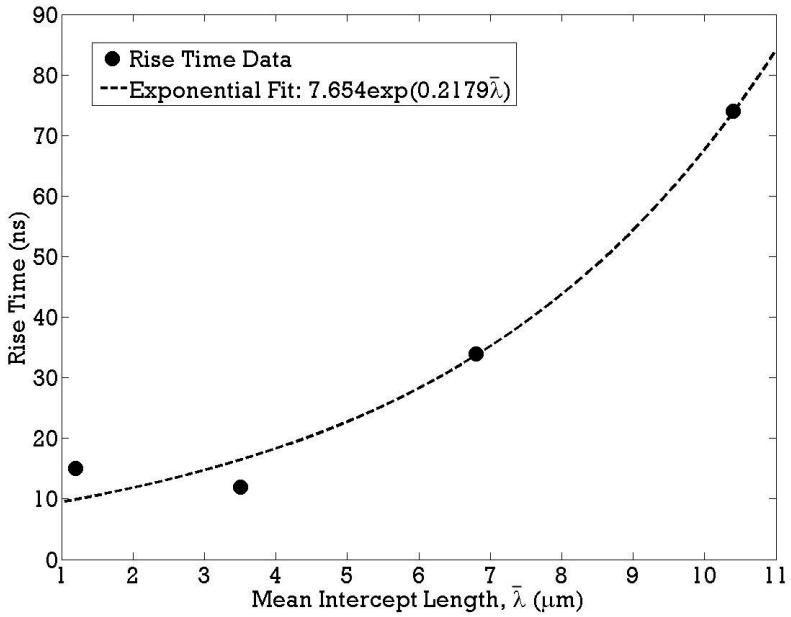

Figure 7.3: Dependence of the rise time on the mean free path $\bar{\lambda}$. The rise time can be approximated from $\bar{\lambda}$ using a simple exponential fit.

particles and decreases $\bar{\lambda}$. With shorter distance between particles, the voids collapse much more quickly, leading to shorter rise times. In addition, the flat nature of the Ni particles leads to much more uniform compaction and material deformations as discussed with Figure 2.29. Both of these factors produce a smoother shock pulse with a sharp rise, as seen in Figure 7.1b. This behavior is analogous to the multilayer composites, which also have a uniform response due to their long, continuous material interfaces.

Since $\bar{\lambda}$ represents the average dimension of each void, the timescale of void collapse can be used to estimate the rise time for a porous powder compact loaded above its crush strength. As $\bar{\lambda}$ decreases, the void space becomes smaller and collapses more quickly, leading to shorter rise times. This relationship can be expressed with a simple exponential fit as shown in Figure 7.3.

There is an important consideration that must be addressed about the rise times reported for the powder compacts. The shock profiles were generated at a random

location across the thickness of the computational domain, which was only 261μm. With such a small domain thickness, it is not possible to obtain a statistically representative response. This means that the rise times can vary depending on where the measurement is taken. While the profiles may not be statistically accurate, they are still believed to capture the general trends in rise time between each Ni/Al composite.

7.4 Particle Level Deformation in the Composites

When compared to the fully dense composites, the porous powder composites undergo extensive particle level deformation during void collapse, which generates increased material mixing and elevated interfacial strains and temperatures [2, 69]. This process is critical for inducing reaction. Hence, the particle level deformation is an important phenomenon for understanding the shock compression and reaction response of any porous powder composite. The particle temperatures at each impact velocity for the various spherical powder composite investigated by Eakins are presented in Figure 7.4 [27]. From these images, it is clearly evident that particle deformations and, consequently, interfacial temperatures increase with increasing porosity and impact velocity. The extensive particle level deformation and high temperatures seen in Figure 7.4 are not observed in the multilayer composites. The lower level of deformation in the multilayer composite controls the extent and nature of the energy dissipated and can be used to explain their higher reaction thresholds when compared to the porous powder compacts.

Without the presence of void space, the fully dense composites do not dissipate as much energy as the porous powder compacts. Even structuring the material interfaces to maximize dissipation can not match the energy dissipated by void collapse. This is illustrated in Figure 7.5, which shows the specific energy dissipated as a function of pressure for a 60% TMD porous powder compact and the 28 micron parallel multilayer composite. The porous curve in Figure 7.5 is only 10% of the actual value and is still

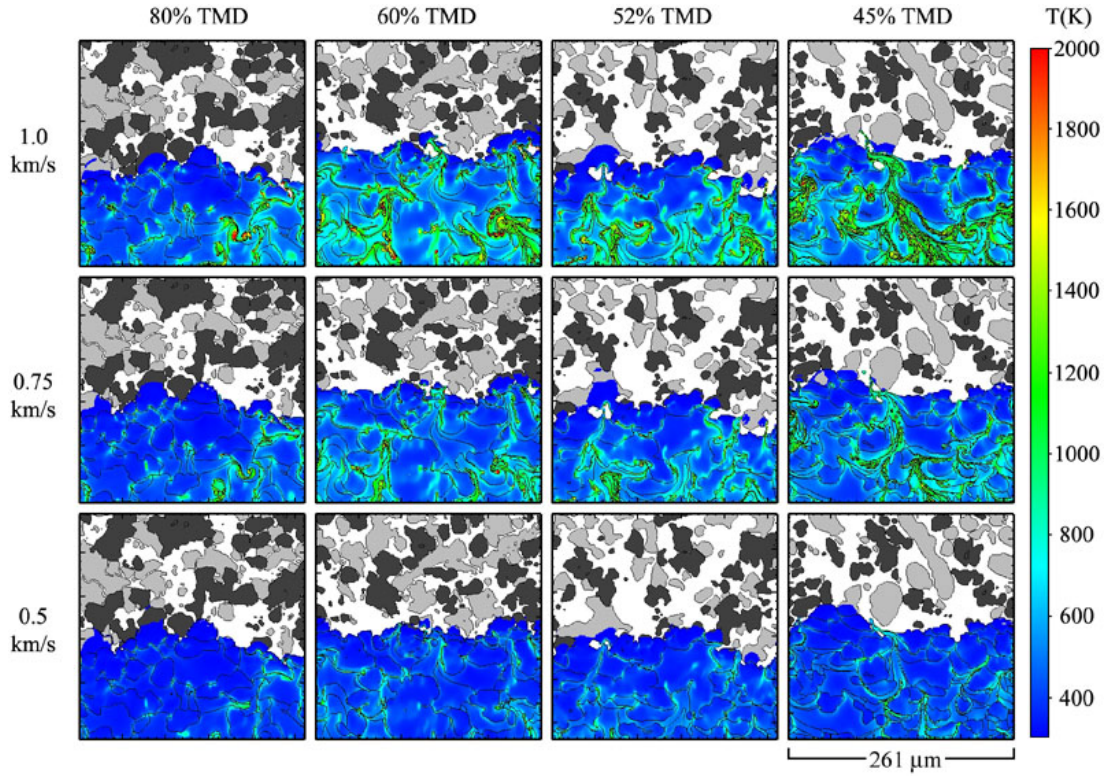

Figure 7.4: CTH prediction of the particle temperatures for various initial densities of spherical Ni/Al powder compacts impacted at 0.5, 0.75 and 1.0 km/s [27]. The results show that the predicted temperatures increase with increasing porosity and impact velocity. In addition to the higher temperatures, the materials are seen to undergo extensive deformation which is not seen in the fully dense multilayer composites.

around twice that of the multilayer composite. While this calculation is simplified by the assumption of no crush strength, it still illustrates the extremely dissipative nature of a porous system, due to the large particle deformations present.

Even though the multilayers dissipate less energy, they concentrate that energy at the material interfaces, which is ideal for initiation of reaction. In addition, the close proximity of the phases in the multilayers increases the likelihood that a reaction will propagate once initiated. In porous systems, the energy is distributed over all particle interactions, including the ones that do not lead to reaction (*i.e.* Al/Al and Ni/Ni). Despite the distribution of some of the energy to inert locations, more energy is deposited at interfaces capable of initiating reaction (*i.e.* Ni/Al) than in the multilayers. This makes the porous systems more likely to initiate reaction. However, the spherical particle shapes also make the powder compacts more likely to have the reaction quench than in the multilayers, which is why typical reaction yields are $\sim$ 10% to 30% [13].

Energy deposition in the powder systems is stochastic in nature. While the nature of the particle deformation is the dominant factor influencing the reaction response, it is also related to the nearest reactive neighbor distance (NRND) and the surface area per unit volume of the microstructure. The NRND describes the proximity between Ni and Al in the powders composites [27]. This metric is analogous to the bilayer spacing used to characterize the multilayers. Eakins investigated the NRND in both the spherical and flake powder compacts and found that particle morphology affected the NRND [27]. Eakins used the increased flow of Al due to the flake geometry of the Ni particles [27] to explain the lower NRND observed for the Al in the 45% TMD flake composite. However, it is also possible that much of this change can be tied to the larger volume fraction of Ni in the 45% TMD flake mixture, seen in Table 7.1. Dunbar *et al.* showed that increasing the Ni content leads to increased material mixing and higher reaction yeilds [2]. The high Ni content can also help to explain

the decrease in separation between Al and Ni and the increased flow in the Al, both of which increase the likelihood of reaction.

The increased reaction response of the 45% TMD flake composite can also be further explained with S_V, which relates to the area available for reaction. As S_V increases, the probability of reaction initiation also increases, since more area is available for contact between constituents. Table 7.1 clearly shows that the porous powder compacts have significantly more surface area then the multilayer or shock compacted composites. This is particularly true for the 45% TMD flake composite. The flake morphology of the Ni particles produces an almost order of magnitude increase in the S_V while still containing a high level of porosity. Consequently, the flake geometry of the Ni particles increases not only the particle deformation in the system, as seen in Figure 2.29c, but also the likelihood of a favorable particle interactions for inducing reaction. These reasons factor into the increased reactivity observed in the 45% flake mixture [27], and highlight the importance of material interfaces for reaction initiation.

It is important to note that the deformation response predicted computationally by Eakins [27] in Figure 7.4 is more extensive than what is experimentally observed. This stems from the limitations of the constitutive model and the 2D approximation, which were discussed in Section 2.3.1. Regardless, the simulations provide valuable insight into the particle level phenomena of the experiments which can help to understand the bulk reaction response.

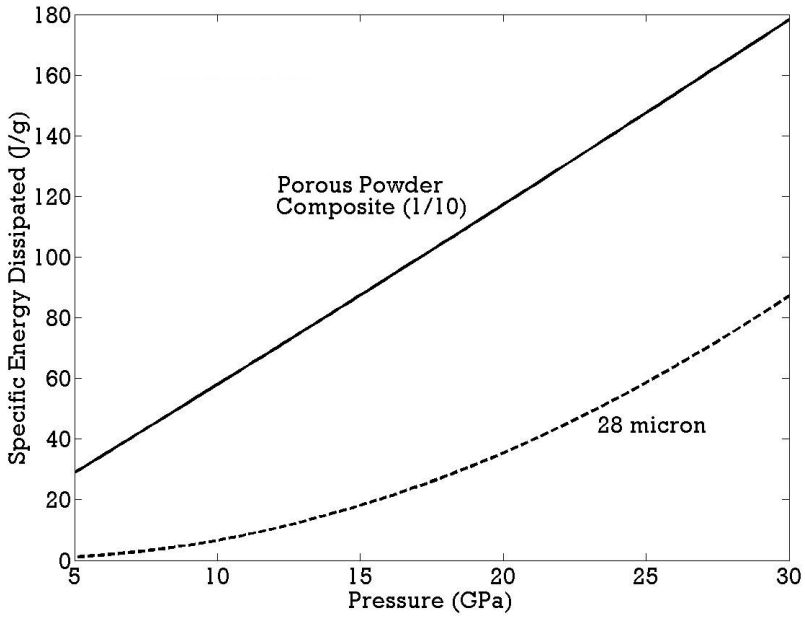

Figure 7.5: Comparison of the specific energy dissipated by a 60% TMD powder composite compared to a 28 micron parallel multilayer composite. The powder composite curve plotted is 10% of the actual amount dissipated for clarity. Even scaled to 10% of its value, the specific energy dissipated by the powder compact far exceeds that of the multilayer composite.

CHAPTER VIII

DESIGN SPACE FOR THE MULTILAYER COMPOSITE RESPONSE

The computational analysis presented in Chapter 4 showed how various microstructural parameters influence the dispersion and dissipation of a shock wave in multilayer composites, by focusing on the effect of each parameter individually. While this approach makes it easier to understand the effects of each variation, it makes the determination of the relative dissipative characteristics of composites with vastly different microstructures more difficult. To facilitate rough comparisons between differing multilayer configurations, it was desired to develop a parameter encapsulating the bulk dissipation characteristics of the various microstructural properties investigated in this work. Such a parameter can then be used to define a design space for multilayered composites for informing decisions during fabrication to increase or decrease the propensity of mechanical reaction initation.

8.1 Formulation of the Design Space

Assuming that the likelihood for reaction initiation is tied to the degree of bulk energy dissipation in the composite (*i.e.* the energy irreversible deposited into the microstructure by the passage of the shock wave), the dissipative behavior for each configuration obtained computationally in Chapter 4 can be used to develop a design space. The computational analysis focused on the effect of both interfacial and material properties on the bulk energy dissipation. Consequently, both of these considerations must factor into the formulation of the design space. However, this necessitates the consideration of four interfacial parameters (*i.e.* the inclination angle of the interfaces,

θ, the surface area per unit volume, S_V, the bilayer spacing, λ, and the interfacial strength, σ_{int}), as well as three material properties (*i.e.* the volume fraction ratio of the constituents, ΔV_V, the impedance difference between constituents, ΔZ, and the average strength of the constituents, $\bar{\sigma_Y}$). This presents a system with 7 unknowns, excluding the EOS parameters for each constituent, making the formulation of a comprehensive design space non-trivial.

In order to simplify this process, the design space was formulated around the concept of a dissipation coefficient. The formulation assumes that the dissipation of each configuration can be related to the dissipation of a known standard, regardless of the pressure, through a constant scaling factor. This allows for easy characterization of each configuration at every pressure. If the standard is assumed to be that of a homogeneous mixture as defined by McQueen mixture theory [45], the effects of both the ΔV_V and ΔZ are then accounted for in the formulation of the standard. This reduces the number of variables needed to be consider for the dissipation coefficient to five.

For this formulation to accurately describe the various composite responses, the relative dissipations of each configuration (*i.e.* the percentage difference between their bulk dissipation compared to that of the homogeneous mixture) must remain roughly constant with pressure. The relative dissipations, expressed as a percentage change, for each configuration investigated in Chapter 4 are presented in Figure 8.1. The relative dissipations of each bilayer spacing are presented in Figure 8.1a, while those for interfacial structure, strength, and strain hardening are seen in Figure 8.1b. Recall that the uniform composite is one with uniform layering of the constituents, which isolates the effects of interfacial structure. The half and pure configurations represent various levels of material strain hardening. The pure configuration has the strength properties of nascent Ni and Al, representing no strain hardening. The half configuration corresponds to half the strain hardening measured and each constituent has

a yield strength half way between those measured for the multilayers and those for the pure materials. Lastly, the non-bonded composite represents a multilayer with no interfacial strength.

Many of the relative dissipations seen in Figure 8.1 have a significant pressure dependence. As a result, the accuracy of this method depends on the pressure at which the dissipation parameter is defined. However, this dependence should not affect the ability of this formulation to predict which configurations are more dissipative over the pressure range investigated. It just lowers the precision to which the differences can be determined. Since the objective of the design space is to facilitate rough comparisons between configurations, it was felt the simplification of a dissipation coefficient was adequate.

The design space can then be defined as the following.

$$E_{diss} = F_{diss} E_{diss_H} \tag{8.1}$$

In this formulation, F_{diss} represents the dissipation coefficient and E_{diss_H} the specific energy dissipated by a homogeneous mixture of the constituents as defined by McQueen mixture theory [45], which was given in Section 4.2.1.3 as the area between the Rayleigh line and Hugoniot.

$$E_{diss_H} = \frac{C_{0_H}^2 \mu^2}{2(1 - S_{1_H}\mu)^2} - \int_{\mu=0}^{\mu} \frac{C_{0_H}^2 \mu}{(1 - S_{1_H}\mu)^2} \tag{8.2}$$

Here, the curves are defined in terms of the compression, μ so they are directly related to the specific energy dissipated, and the subscript H indicates that the values correspond to the homegeneous mixture.

8.2 Formulation of the Dissipation Coefficient

There are five remaining microstructural variables that need to be incorporated into the dissipation coefficient. To aid in the formulation, each microstructural variable is assumed universal, meaning its effect is assumed to have the same functional form

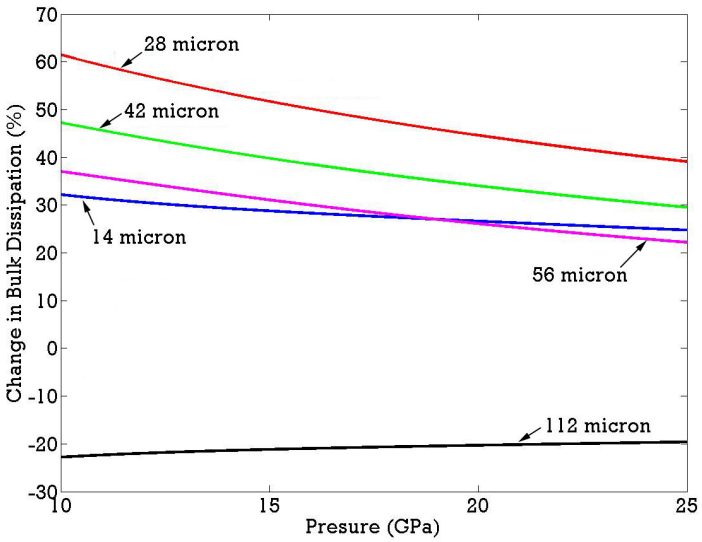

(a) Relative Dissipations for Various Bilayer Spacing

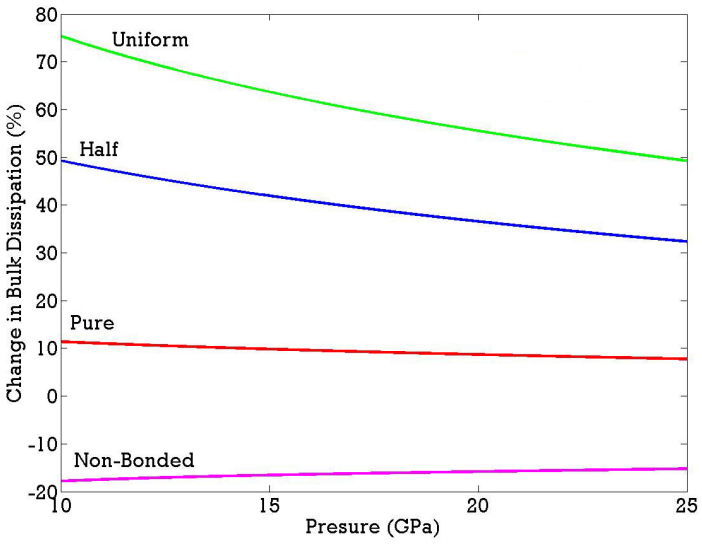

(b) Relative Dissipations for the Other Configurations

Figure 8.1: Relative differences in dissipation between the various configurations with respect to a homogeneous composite. The relative changes for various bilayer spacings (a) along with those for the uniform, half, pure, and non-bonded composites (b) are presented for the generation of a comprehensive design space. Many of the configurations show a strong pressure dependence in their relative dissipations. While this casts doubt on the use of a dissipation coefficient to characterizing their responses, the variation was not large enough to prohibit such a formulation.

regardless of variations in the other parameters. This allows the computational data, which isolates individual parameters, to be used to define the dissipation coefficient.

The first parameter investigated was the angle of interfacial inclination, θ, which varies between 0 and $\frac{\pi}{2}$ in the multilayer composites. In Section 4.1, the dissipation was found to decrease with increasing angle of inclination. Based on these considerations, the effect of inclination angle can be represented with the following equation.

$$f(\theta) = a_1 + a_2(1 - sin\theta) \tag{8.3}$$

Here, a_1 and a_2 are fitting parameters that can be determined from the computational results for the perpendicular, angled, and parallel (*i.e.* 28 micron) configurations. In this form, the parallel configuration (*i.e.* $\theta = 0$) yields the maximum value of $f(\theta)$. This enables the effect of the interfacial inclination to be incorporated as a percentage decrease from the more dissipative parallel configuration.

The next consideration is the influence of bilayer spacing on the dissipation, which was investigated for the parallel configuration in Section 4.2.3. The simulations showed that an optimum bilayer spacing exists for maximizing dissipation, but these effects were not investigated in any other inclination. The experimental work of Zhuang *et al.* [125] has shown that dissipation increases with decreasing bilayer spacing in the perpendicular configuration. However, only a few bilayer spacings were investigated in their work, so no functional form was given for this dependence. Given that the bulk dissipation responses for the parallel and perpendicular 28 micron configurations were fairly similar, as seen in Figure 4.23, it is assumed that the effect of λ remains the same regardless of orientation. In addition, this peak in dissipation was assumed to mirror the peak in dispersion presented in Section 4.2.6, meaning the effect of bilayer spacing on the dissipative response can also be represented with a log-normal distribution.

$$f(\lambda) = \frac{b_1}{\lambda\sqrt{b_2\pi}} exp\left(\frac{-(ln(\lambda) - b_3)^2}{b_2}\right) \tag{8.4}$$

In this equation, the parameters b_1, b_2, and b_3 are fitting parameters that can be determined from the computational results for the various bilayer spacings investigated in the parallel configuration.

The influence of material strength is also incorporated into the dissipation coefficient. The computational results in Section 4.2.5 showed that dissipation decreases as the layers become softer. This stems from the increased compression of the layer interiors, which limits interfacial shear. These results suggest that the ratio of strengths is not as important as the average strength for determining the dissipative response. Regardless of how hard one phase is, if the other phase is soft, deformation in the softer phase layers will decrease the interfacial shear and corresponding dissipation. As a result, the average yield strength is the best parameter to incorporate the effects of strain hardening. From the computational results, the decrease in dissipation with decreasing strain hardening is known to occur in a non-linear fashion. As the materials harden, the resulting increase in dissipation becomes smaller. This sort of functional relationship can be captured with the following.

$$f(\bar{\sigma_Y}) = c_1 + c_2 \bar{\sigma_Y}^{c_3} \tag{8.5}$$

Here, the fitting parameters c_1, c_2, and c_3 are used to match the computational results for the 28 micron, half, and pure configurations.

To account for the effects of interfacial structure, the simulations on the uniform and 28 micron configurations can be used. With uniform layering, an increase in dissipation was observed. This stems from the perfect alignment of the entire interfacial area with the propagating shock wave, which increases the interfacial shear. Since a uniformly layered composite has the lowest possible interfacial area, the effects of interfacial structure can be described through the increase in surface area that results from interfacial heterogeneity. This means a non-dimensionalized surface area per unit volume parameter, S_V^*, that describes the percentage increase in surface area due to interfacial heterogeneity can be used to characterize the structure of the

interfaces.

$$S_V^* = \frac{S_V \lambda}{2} \tag{8.6}$$

From Figure 8.1b, it can be seen that the influence of interfacial structure on the relative dissipation of the multilayer composite remains fairly constant and is directly related to S_V^* for the parallel configuration. However, in the perpendicular orientation, the influence of interfacial structure is expected to be minimal due to the low interfacial shear generated. As a result, the effect of interfacial structure on the dissipation coefficient must include an orientation term.

$$f(S_V^*) = \frac{1}{S_V^* + (1 - S_V^*) sin\theta} \tag{8.7}$$

Since S_V^* increases with increasing heterogeneity, the inverse is taken to account for the corresponding decrease in dissipation. The parameter $f(S_V^*)$ varies from S_V^* to 1 as the angle changes from 0 to $\frac{\pi}{2}$, eliminating the effect of interfacial heterogeneity in the perpendicular configuration.

The last parameter to consider is the interfacial strength, which can be incorporated in a similar fashion as interfacial structure. As interfacial strength decreases, the dissipation drops, due to the removal of the interfacial shear. However, in the perpendicular orientation, interfacial shear is minimal and the interfacial strength should have a negligible influence. Consequently, the effects of interfacial strength can be described in a similar functional form as interfacial heterogeneity, using a non-dimensionalized interfacial strength coefficient, σ_{int}.

$$f(\sigma_{int}) = \frac{1}{1 + (f_i - 1) cos\theta (1 - \sigma_{int})} \tag{8.8}$$

Here, the factor, f_i is a coefficient to fit the drop in dissipation seen in the 28 micron and non-bonded simulations. For perfectly bonded interfaces, σ_{int} equals unity making $f(\sigma_{int}) = 1$ regardless of the orientation. When the interfaces are not bonded, σ_{int} equals zero and $f(\sigma_{int})$ ranges from $\frac{1}{f_i}$ in the parallel orientation to one in the perpendicular orientation.

With all the variables considered, the functional form of the dissipation coefficient can now be represented as the following.

$$F_{diss} = \frac{(a_1 + a_2(1 - sin\theta)) \left(\frac{b_1}{\lambda\sqrt{b_2\pi}} exp\left(\frac{-(ln(\lambda) - b_3)^2}{b_2} \right) \right) (c_1 + c_2 \bar{\sigma_Y}^{c_3})}{(S_V^* + (1 - S_V^*)sin\theta)\,(1 + (f_i - 1)cos\theta(1 - \sigma_{int}))} \tag{8.9}$$

It can be seen that there are now nine fitting parameters that must be determined to completely represent this design space, all of which can be found using the computational results presented in Chapter 4.

8.3 Calibration of the Dissipation Coefficient

To determine the fitting parameters of the dissipation coefficient for the Ni/Al multilayered system, the relative differences of each configuration must be defined. Since these differences vary with pressure, as seen in Figure 8.1, a common point must be used to approximate the fit over the entire domain. For this analysis, 25 GPa was chosen and the relative dissipations of each configuration at that pressure, expressed as a percentage, are listed in Table 8.1. At higher pressure, the dissipation becomes larger, meaning errors in the predicted relative dissipation cause larger absolute differences between the estimated and actual responses. As a result, it was assumed that, by fitting to the upper end, better overall results could be achieved. However, this procedure can be applied at any pressure.

The process to determine the fitting parameters that best represent the computational results presented in Table 8.1 involves numerous steps. Since the most data points correspond to changes in bilayer spacing, these parameters are determined first. The relative dissipations for each bilayer spacing correspond to the cold-rolled condition, meaning the layers are not uniform. As a result, the computationally determined coefficients must be multiplied by $\frac{1}{f(S_V^*)}$ to eliminate the effect of interface heterogeneity. Since all the layers are parallel, the inclination term in $f(S_V^*)$ does not need to be considered, and the relative dissipations can be multiplied by S_V^* directly.

Table 8.1: Relative dissipation of each configuration at 25 GPa when compared to that of a homogeneous mixture.

Configuration	Relative Dissipation (%)	Dissipation Coefficent (%)
14 micron	1.248	1.222
28 micron	1.391	1.353
42 micron	1.295	1.297
56 micron	1.222	1.121
112 micron	0.804	0.935
Half	1.324	1.287
Pure	1.078	1.048
Uniform	1.493	1.500
Angled	1.335	1.293
Perpendicular	1.299	1.265
Non-Bonded	0.848	0.821

This product can then be fit to the bilayer spacings, expressed in mm, through Equation 8.4 to determine the appropriate values for b_1, b_2, and b_3, which are listed in Table 8.2.

The effects of average yield strength can then be determined using the computational results for the 28 micron, half, and pure configurations. To ensure that this fit does not invalidate the values determined for b_1, b_2, and b_3, the relative dissipations are converted into a percentage with respect to the 28 micron configuration (*i.e.* the ratio of its relative dissipation to that of the 28 micron configuration). This ensures that $f(\bar{\sigma_Y}) = 1$ for the 28 micron configuration and decreases with decreasing hardening, as was observed computationally. The parameters a_1, a_2, and a_3, which are presented in Table 8.2, are then found by fitting the average yield strength of each composite, expressed in MPa, to the adjusted relative dissipations using Equation 8.5.

To determine the fitting parameters for $f(\theta)$, the computational results for the perpendicular, angled, and 28 micron (*i.e.* parallel) configurations are used. This result must also account for the effect of interfacial heterogeneity in the analysis without altering the fitting parameters already defined. This is done in a similar

Table 8.2: Fitting parameters for the dissipation coefficient.

a_1	a_2	b_1	b_2	b_3	c_1	c_2	c_3	f_i
0.8441	0.1568	0.3598	3.824	-1.714	1.218	-2.195	-0.3557	1.647

fashion as $f(\bar{\sigma_Y})$. The percentage dissipated by each orientation relative to the 28 micron configuration is determined and its product with $\frac{1}{f(S_V^*)}$ is then fit to Equation 8.7. Once again, the fitting parameters for $f(\theta)$ are presented in Table 8.2, when θ is expressed in radians.

This leaves only the determination of f_i, which represents the drop in dissipation as a result of lower interfacial strength. The parameter is simply the percentage drop in dissipation between the non-bonded and 28 micron composites; its value is also listed in Table 8.2.

8.4 Application of the Dissipation Coefficient

With the fitting parameters determined, the dissipation coefficient for each configuration can now be estimated. These values are given in Table 8.1 and show that the dissipation coefficient is fairly close to the value obtained computationally for all configurations. However, the accuracy of the fit is best examined graphically, since it enables a comparison of the responses over the entire pressure range.

The predicted bulk dissipations for a selection of the configurations investigated are presented in Figure 8.2. Figure 8.2a compares the computationally determined specific energy dissipated (solid line) to that predicted using the dissipation coefficient (dashed line) for the 14, 28, and 112 micron configurations up to 25 GPa. The fits are fairly accurate, with the only configuration with a significant deviation being the 112 micron composite. Figure 8.2b shows the comparisons for the uniform, perpendicular, pure, and non-bonded configurations. The accuracy of these fits are seen to be very good over the entire pressure range. The results from Figure 8.2 illustrate that the dissipation coefficient is able to capture the general trends in dissipation between

configurations, and, as a result, can be used to define a comprehensive design space.

The results in Figure 8.2 represent only individual configurations. In fact, Equation 8.9 can easily be solved for any combination of variables given the fitting parameters in Table 8.2. To present a more useful illustration of the design space, it was desired to plot the change in dissipation as each parameter varies. The effect of interfacial structure and strength are linear and tied to the interfacial orientation. This makes the most influential variables on the dissipative response the bilayer spacing, average yield strength, and angle of inclination. In order to graphically show the variation in dissipation with these microstructural parameters, two of the variables were changed while the third parameter was held constant. In this way, the relationship between each of the main variables can be visualized and understood.

The design space for variations in bilayer spacing and average yield strength, assuming $\theta = 0$ rad, $S_V^* = 1.1$, and $\sigma_{int} = 1$, is presented in Figure 8.3. The dissipation is seen to peak at bilayers of around 30 microns, with this difference increasing with higher average material strength. These results match those previously outlined in Chapter 4. Figure 8.4 shows the variation in dissipation coefficient as bilayer spacing and orientation vary, assuming $\bar{\sigma_Y} = 663$ MPa, $S_V^* = 1.1$, and $\sigma_{int} = 1$. The results still show the characteristic peak in dissipation with bilayer spacing, but also illustrate that the dissipation increases with lower angles of inclination for all bilayer spacings. Lastly, the effects of both average yield strength and orientation on the dissipation coefficient are presented in Figure 8.5, assuming $\lambda = 28$ microns, $S_V^* = 1.1$, and $\sigma_{int} = 1$. The results show that dissipation increases as the average yield strength increases and the angle of inclination decreases. These results suggest that bilayer spacing is the dominant factor in determining the dissipative response of a multilayered composite, followed by the average yield strength and then the angle of inclination.

The results in Figures 8.3 through 8.5 are not unexpected, since they match how the dissipation coefficient was formulated. However, the main function of these figures,

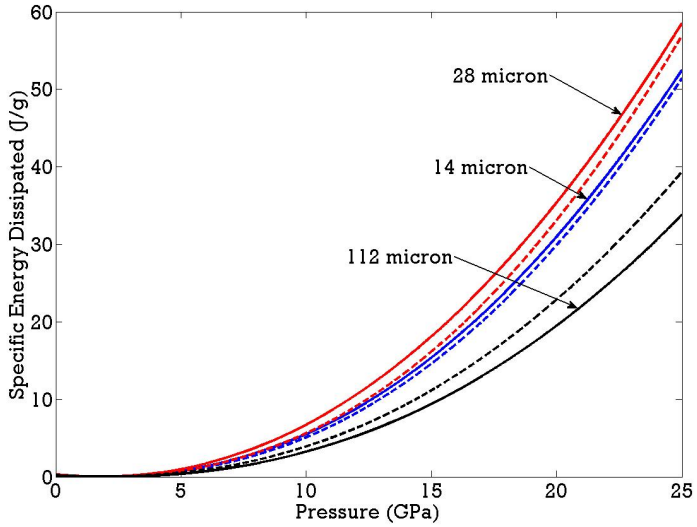

(a) Bilayer Spacing

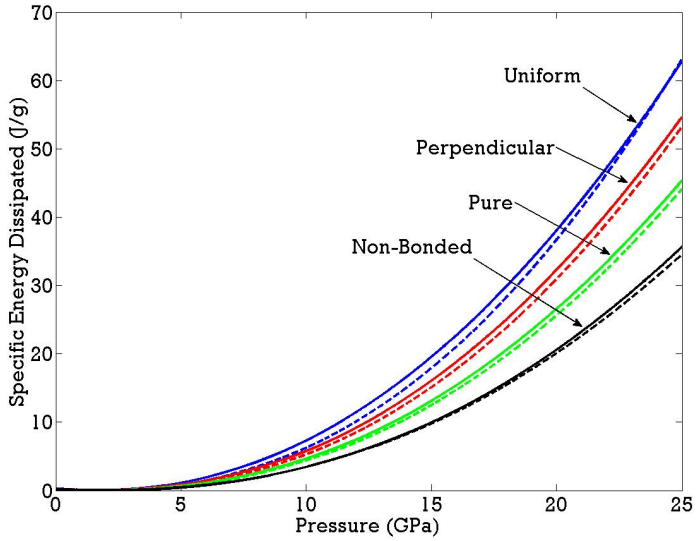

(b) Rolling, Bonding, Orientation, and Hardening

Figure 8.2: Comparisons between the computationally predicted specific energy dissipated to that found with the dissipation coefficient for various bilayer spacings (a) and microstructural variations (b). The solid lines correspond to the dissipation found computationally, while the dashed lines represent those approximated with the dissipation coefficient. The results using the dissipation coefficient show relatively good agreement with the computational results.

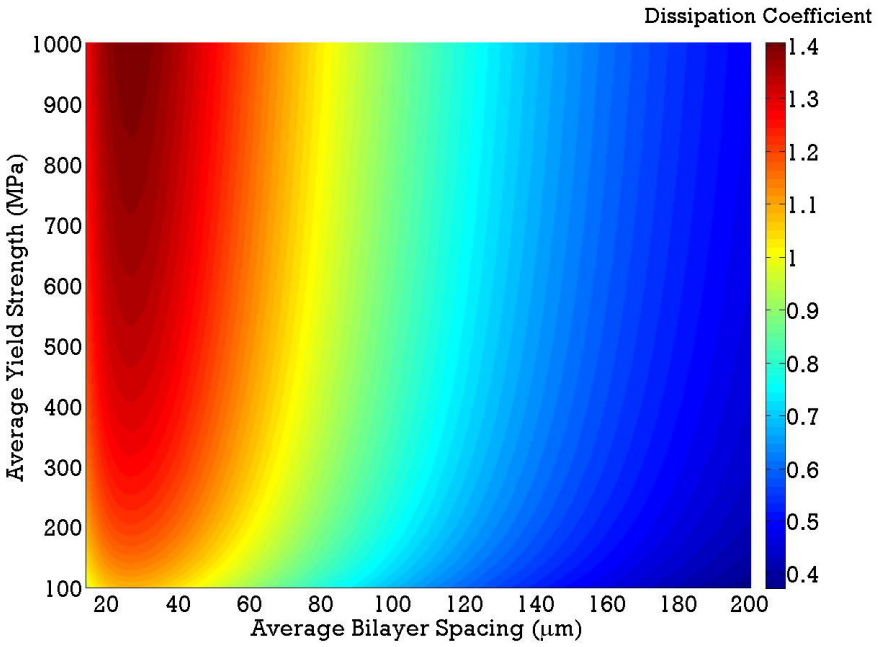

Figure 8.3: Design space showing the variation in the dissipation coefficient as the bilayer spacing and average yield strength change, assuming $\theta = 0$ rad, $S_V^* = 1.1$, and $\sigma_{int} = 1$. The results show that the dissipation coefficient peaks around 30 microns and increases with increasing average hardness, which is in agreement with the results presented in Chapter 4.

and the dissipation coefficient in general, is to facilitate rough comparisons between configurations. With so many important microstructural variables, it is difficult to easily determine which composite may be more dissipative and have a potentially lower reaction threshold. The ability to predict and compare the dissipation response of various multilayered configurations easily through the dissipation coefficient can aid in determining which systems are most appropriate for a given application.

8.4.1 Effect of Porosity and Particle Morphology

The above development of the dissipation coefficient focused only on multilayer systems. However, it is desirable to extend this formulation to other composites, such as the shock compacted and porous powder compacts. In order to do that, provisions must be made in the formulation of the dissipation coefficient to handle spherical (equiaxed) particles and porosity.

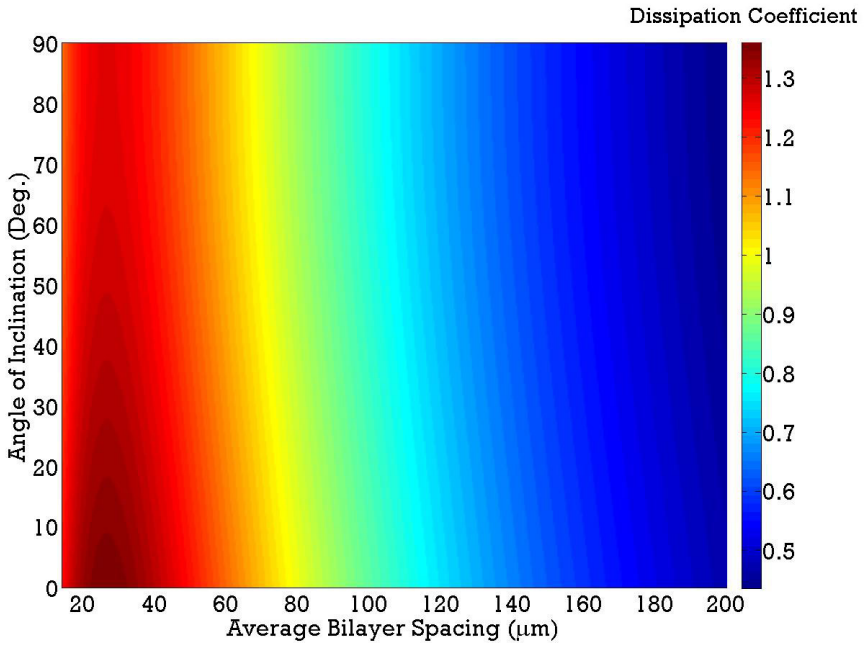

Figure 8.4: Design space showing the variation in the dissipation coefficient as the bilayer spacing and angle of inclination change, assuming $\bar{\sigma_Y} = 633$ MPa, $S_V^* = 1.1$, and $\sigma_{int} = 1$. The results show that the dissipation coefficient decreases for each bilayer spacing as the inclination angle decreases.

Spherical particles, or any shape particles for that matter, can be accounted for by redistributing the materials into a layered geometry. Drumheller and Sutherland developed a non-dissipative lattice model for wave propagation that assumed the dispersive character of a composite to be redistributed into a laminar structure [130]. In this manner, the shock compacted composite can be considered as a periodic structure of Ni and Al, with thicknesses estimated from two stereological measurements: V_V and S_V.

Taking the shock compacted microstructure as Ni particles in an Al matrix, the average dimension of the Ni particles can be defined by the mean intercept length, $\bar{d}$ [155].

$$\bar{d} = 4\frac{V_V}{S_V} \tag{8.10}$$

This represents the average length segment on a randomly oriented test line that lies in a Ni particle. The mean free path, $\bar{\lambda}$, between the Ni particles can then be used

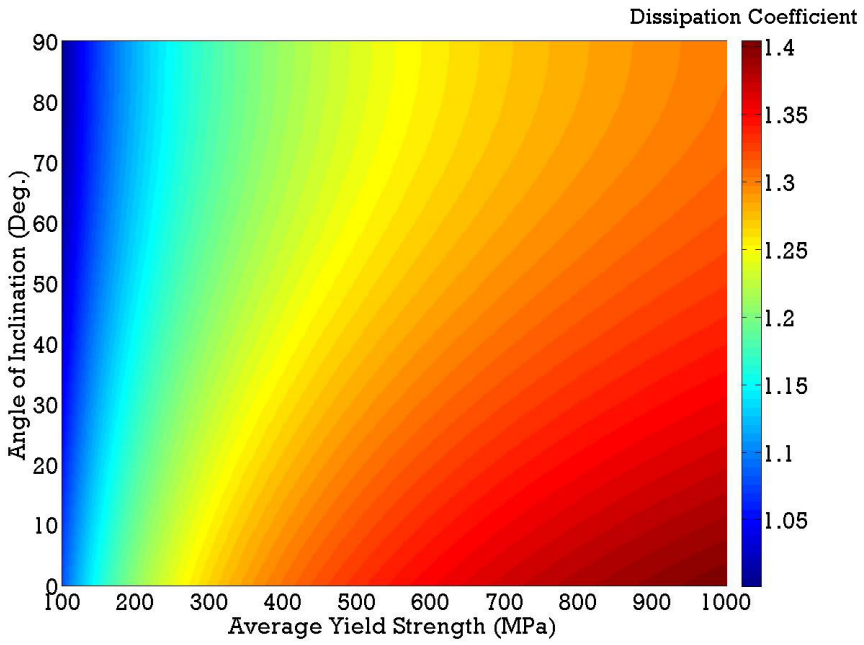

Figure 8.5: Design space showing the variation in the dissipation coefficient as average yield strength and angle of inclination change, assuming $\lambda = 0.028$ mm, $S_V^* = 1.1$, and $\sigma_{int} = 1$. The dissipation coefficient is seen to increases as the average yield strength increases and the angle of inclination decreases.

to determine the Al layer thickness [155].

$$\bar{\lambda} = \bar{d}\left(\frac{1 - V_V}{V_V}\right) = \frac{4(1 - V_V)}{S_V} \tag{8.11}$$

The summation of $\bar{d}$ and $\bar{\lambda}$ now defines the bilayer spacing of the laminated representation of the shock compacted composite, which was found to be 36 microns.

The other parameters for the dissipation coefficient can now be determined. The spherical particles contain every angle between 0 and $\frac{\pi}{2}$, so their angle of inclination is assumed to be $\frac{\pi}{4}$. Since the shock compacted composite has been redistributed into a uniformly layered composite, $S_V^* = 1$. The average yield strength can also be determined from the values given in Section 3.5 as 485 MPa. Lastly, the interfaces are assumed perfectly bonded, $\sigma_{int} = 1$. Using these parameters, the dissipation coefficient can be estimated from Equation 8.9 as 1.270. This value matches very closely to that determined from the computations, which was 1.279. The predicted

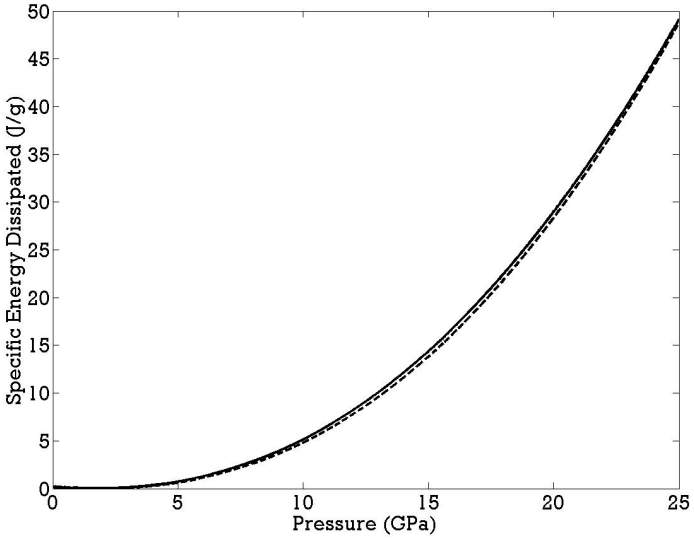

Figure 8.6: Comparisons between the computationally predicted specific energy dissipated (solid) in the shock compacted composite to that found with the dissipation coefficient (dashed). Despite representing the shock compacted composite as a laminated structure, the dissipation coefficient is seen to match the computational results.

and computationally obtained dissipations are presented graphically in Figure 8.6. Even though the shock compacted composite was represented as a laminated material, the dissipation coefficient is seen to predict its dissipative response. It is important to note that, for this calculation, E_{diss_H} was changed from that used for the multilayers to match the differing volume fraction ratio of the shock compacted composite given in Section 3.5.

The porosity, α, can be considered as adding a third material into the composite that has no impedance. As was shown in Figure 7.5, porosity increases the energy dissipation enormously. Even at very small porosities (*i.e.* 1%) the porosity term is much larger than the dissipation coefficient term. As a result, the porosity becomes the only real microstructural parameter that needs to be considered. For a porous system, the energy dissipated can be determined with the following modification to

E_{diss_H}, which assumes the dissipation coefficient is immaterial and equal to unity.

$$E_{diss_H} = \frac{C_{0_H}^2 \mu^2}{2(1 - S_{1_H}\mu)^2} - \int_{\mu=0}^{\mu} \frac{C_{0_H}^2 \mu}{(1 - S_{1_H}\mu)^2} + \frac{C_{0_H}^2 \mu}{2(1 - S_{1_H}\mu)^2} \frac{\alpha}{1 - \alpha} \tag{8.12}$$

8.4.2 Limitations of the Design Space

It is important to remember that the dissipation coefficient is designed only for rough, first-order comparisons. In addition, the above development of the dissipation coefficient was built heavily on the assumptions inherent in the computational analysis. Thus, the fitting parameter is only as accurate as the simulations used to generate it. However, given the experimental validation obtained for the simulations, it is felt that the parameter is representative for the Ni/Al system. Extension of the dissipation coefficient to other material systems may require the determination of new fitting parameters, since this its formulation was completely empirical. Nonetheless, the functional forms of each portion of the dissipation coefficient should hold for any multilayer system. This means that the above method can be used for the determination of a design space for any multilayered system.

It is important to also remember that the above analysis focuses only on the wave mechanics observed in the multilayers. There has been no attempt in this work to account for reaction. The wave mechanics considerations can give the conditions best suited for initiation of reaction based on the energy dissipated. They provide no information about the propagation of reaction. When the reaction kinetics are taken into account, it may be found that different microstructural characteristics are advantageous. This would be particularly true for bilayer spacing. As bilayer spacing increases, the materials are separated further, which can increase the likelihood of burn-out after ignition. As a result, it may be found that smaller bilayer spacings, while harder to initiate, are better for the propagation of reaction in cold-rolled composites. However, without appropriate reaction models, there is no way to fully incorporate these effects into the simulations.

CHAPTER IX

CONCLUSIONS AND PROPOSED FUTURE WORK

9.1 Summary of Results and Conclusions

Cold-rolled Ni/Al multilayer composites were used to understand the influence of material interfaces on the shock compression response of highly heterogeneous systems. This was done computationally through the parametric variation of numerous interfacial properties in the multilayer composites. In particular, the work focused on interfacial and material properties controllable through fabrication. The microstructural variations were seen to manifest themselves as changes in the observed dispersive and dissipative characteristics of the composite. The computational results were validated with uniaxial strain impact experiments, justifying the trends extracted. From the trends identified, a design space for guiding the fabrication of these multilayer composites for a particular application was developed.

Interfacial orientation was computationally investigated and found to influence the propagating shock wave through the development of multiple wave interactions and 2D effects. In the perpendicular orientation, oscillatory behavior was observed in the stress response, in agreement with past experimental investigations [123, 125, 124, 128]. These oscillations resulted from the reverberations of the shock wave between the material layers. Due to the heterogeneities generated during rolling, these oscillations were not periodic and attenuated rapidly. While the nature of these interfaces produced numerous wave interactions, their orientation normal to the shock wave generated very little interfacial shear. Without interfacial shear, no substantial increase in temperature occurred at the material interfaces, decreasing the likelihood of reaction initiation. When the orientation of the interfaces was changed to that

of the angled and parallel configurations, 2D effects began to dominate the material response. The 2D response stemmed from the areal changes in the individual layers as the shock wave traversed the composite. This was particularly true for the parallel orientation. With the layers aligned with the shock wave, the disparity in material velocities generated substantial interfacial shear and, as a result, increased interfacial temperatures. This made the parallel orientation the most dissipative, giving it the highest probability of reaction initiation.

Since the parallel configuration exhibited the most dispersion and dissipation of the shock wave, it was chosen for a parametric study of various microstructural properties. Both interfacial and material properties were altered to develop a comprehensive understanding of how various microstructural features affect the shock compression response in multilayered composites. The most extensively investigated microstructural parameter was the interfacial density. This parameter relates directly to thicknesses of the layers and was found to have the largest influence on the dispersive and dissipative behavior of the composite. In particular, optimum bilayer spacings were identified for maximizing dispersion and dissipation, respectively.

For dissipation, this optimum bilayer spacing was found to be around 30 μm. The existence of an optimal bilayer spacing results from the interplay between the equilibration time in the system and the amount of interfacial shear generated. With higher interfacial densities, the composite equilibrated quickly. This limited the interfacial shear, since the disparity in the material velocities in each layer did not persist for a very long time. As the interfacial density decreased, the system took longer to equilibrate, producing more interfacial strain. This increased the energy dissipated at each interface. Initially, the increase in dissipation at each interface was enough to offset the loss of interfacial area, causing a net increase in dissipation. However, with further decreases in interfacial density, the increase in energy dissipated per interface was not sufficient to offset the loss of interfacial area. As a result, the total energy

dissipated by the composites decreased, producing an optimum bilayer spacing for dissipation.

For dispersion, the optimum bilayer spacing was found through the shape and attenuation of the shock pulse. Using these metrics, the optimum bilayer spacing for maximizing dispersion was found to be around 50 μm. This result depended on the number and nature of the wave interactions in the composite. Maximizing the dispersive behavior in the parallel orientation, it was found that a shock wave propagating along the layers can be attenuated in around 20% of the time as a corresponding wave in either constituent.

The effect of both dispersion and dissipation were also seen to influence the EOS response. With higher interfacial densities, the EOS response shifted to lower wave speeds in the multilayers. Since increased interfacial density inhibits wave motion, this can be viewed as causing an increase in the impedance of the composite.

In addition to interfacial density, the effects of interfacial structure and strength were also investigated in the parallel configuration. The interfacial structure was found to slightly influence both the dispersion and dissipation of the shock wave. In a uniformly layered composite, the heterogeneities due to rolling are removed and all of the material interfaces are aligned perfectly with the propagating shock wave. This maximizes the shear strain experienced at the interfaces, leading to increased dissipation. Additionally, the removal of those heterogeneities reduced the number of wave interactions, thereby lowering the dispersion of the composite. To understand the influence of interfacial strength, bounds were generated using perfectly bonded and completely unbonded composites. Without interfacial strength, no interfacial strains developed and the dissipation drastically decreased. The free motion of each layer also reduced the number of wave interactions decreasing the dispersion as well.

The final microstructural parameter investigated was the strain hardening of each constituent. Since this parameter does not alter the geometry of the system, it had

a negligible effect on wave dispersion. However, strain hardening did have a significant influence on the dissipation of the composite. The variation in dissipation due to strain hardening was related to the degree of deformation induced in the layer interiors. As strain hardening decreased, the material layers became softer and accommodated more deformation. This meant less deformation was concentrated at the material interfaces, reducing interfacial shear and the energy dissipated by the system.

The trends developed through this computational analysis highlight the importance of the nature and number of material interfaces on determining the shock compression response of a composite system. In order to validate these trends, uniaxial strain impact experiments were performed. The experimental investigation was limited to the perpendicular orientation, due to the thin nature of the samples. Since each microstructure was generated through simple scalings and rotations of that perpendicular microstructure, validation of this orientation was sufficient for all of the computational trends developed. While a variety of experimental arrangements were employed, one that provided reliable and accurate data on such thin, irregular samples was eventually developed.

The Hugoniot measurements obtained on the multilayer composites were generated through a combination of direct measurement and the impedance matching technique. The Hugoniot points had large error bars, due to the thin, irregular nature of the samples. While all of the experimental points matched the computationally predicted EOS, the large error bars for each point prohibited a robust validation of the computational results. In order to obtain further validation, the computational method was used to reproduce the experimental VISAR and PVDF records. This was done using both the 2D multilayer microstructure and the bulk properties determined from the computational investigation. Strong agreement was found in both

cases. Using the agreement in both the predicted EOS and experimental records, sufficient validation of the computational trends developed in this work was obtained.

An investigation of the reaction response of these multilayers during uniaxial stress loading was also undertaken. The experiments showed that the multilayer response was influenced heavily by the sample geometry and chamber atmosphere. With such thin samples, the Cu projectile flowed around and encapsulated the multilayer. While this made sample recovery easy, it limited the material deformation to the periphery of the sample, ejecting fragments into the experiment chamber. In the presence of oxygen, these hot, highly deformed fragments reacted, as observed via light emission recorded with the high-speed photography. Post-mortem analysis on the recovered samples was able to provide evidence that the oxidation reaction induced isolated regions of intermetallic reaction in the sample periphery. In contrast, the interior of the sample was found to show no signs of reaction and deformed through shear banding regardless of the chamber atmosphere or impact velocity.

The responses of the various multilayered composites were then contrasted with the results of past work on porous Ni/Al powder composites [27]. Due to their porosity, the powder compacts have a vastly different shock compression response than the fully dense multilayer composites. In particular, porosity leads to wave interactions at the particle boundaries instead of material interfaces, like in the multilayers. The nature of the wave interactions at the pores generates vastly different bulk responses, shock profiles, and particle level deformations than observed in the fully dense composites. Despite these differing responses, similarities were found between the wave interactions in the porous and fully dense composites. In addition, the elevated particle deformation, surface area, and energy deposited in the porous powder compact were used to further explain the increased reactivity of these systems when compared to the fully dense composites.

Lastly, the effects of these microstructural changes were shown in relative terms

to completely define a design space through the formulation of a dissipation coefficient. This dissipation coefficient encompassed the effects of both the interfacial and material parameters investigated, enabling the determination of a comprehensive design space to facilitate comparisons between multilayer configurations. Such a design space can aid in the careful and informed fabrication of a multilayer composite for a particular application. However, the dissipation coefficient is a completely empirical parameter, and the fitting parameters determined for it in this work are only appropriate for the Ni/Al systems. In addition, its formulation was based solely on the mechanics of the wave interactions, since no reaction kinetics were included in this analysis. Even with these limitations, the dissipation coefficient offers a valuable tool for understanding and comparing the dissipative, and corresponding reaction response, of various multilayered composites.

9.1.1 Major Contributions

The main contributions resulting from this work are listed below:

- The mechanisms responsible for alterations in the shock compression response of cold-rolled Ni/Al multilayer composites due to microstructural variations were characterized and explained. These microstructural parameters included the interfacial orientation, density, structure, and strength, in addition to the strain hardening of the layers.

- The computational results were validated through the use of uniaxial strain impact experiments. These experiments provide the first Hugoniot measurements on cold-rolled Ni/Al multilayer composites.

- Intermetallic reaction initiation in the multilayered composites under uniaxial stress loading was shown to initiate with the oxidation of Al under the conditions investigated.

- A comparison of the multilayer composites to previous work on powder compacts was used to explain the role material interfaces, particularly around pores where strong release waves are generated, play in the shock compression and reaction response of Ni/Al based composites.

- The relative effects of each variation were identified and used to generate a dissipation coefficient to completely define a design space for the informed fabrication of multilayer composites for various applications.

9.2 Proposed Future Work

This work focused mostly on variations in the computational response of cold-rolled Ni/Al multilayers under shock compression due to changes in the underlying microstructure. The simulations were validated through uniaxial strain impact experiments. While the experimental work proved the computational renderings representative and the analysis methods accurate, its extent was limited, focusing on one orientation and bilayer spacing. Consequently, there is room for further experimental investigation on these multilayered composites.

As stated previously, multilayer composites can be made through a variety of fabrication techniques. This provides significant flexibility in the underlying microstructure. This flexibility can be exploited for further experimental efforts on microstructures with various bilayer spacings, uniform or irregular interfacial characteristics, and material properties under shock compression. Not only would these experimental investigations potentially provide further validation of the conclusion drawn in this work, they could also yield new insights into the behavior of layered materials. It would also be of interest to look a samples with bilayer spacings in the nanometer range, so that the microstructural features would be on the same times scale as the shock rise. Given the interesting mechanical properties of nanofilms, such as high flow strengths, a study at high strain rates could provide some interesting results.

These efforts would be greatly aided by the development of thicker multilayer samples. Thicker samples would not only reduce the error in the experiments, but would also enable experimental investigations on different orientations. This would be especially valuable, since much of the interesting behavior was found with the layers parallel to the propagating shock wave.

Future experimental investigations would also benefit from extension to higher impact velocities. The work presented here was limited by the velocities obtainable on our single stage, light gas gun (< 1100 m/s). Increasing the impact velocity, would increase the likelihood of a phase change, whether it be melting or a shock-induced intermetallic reaction. These phenomena could easily be viewed through changes in the measured wave speed of the composite. Experimental identification of a phase change can then be combined with computational analysis to help in understanding the nature of the transformation and identifying the mechanisms responsible.

There are no models capable of accurately handling the shock initiation of a reaction in highly heterogeneous reactive systems, such as Ni/Al. If experimental identification of a shock-induced reaction can be obtained with multilayer systems, it would provide useful additional information about the mechanisms responsible. This information can then be used to help develop new reaction models for reactive mixtures. However, substantial progress on both the understanding of the mechanisms of reaction and the numerical implementation of such a process would need to be done first. If such a model was developed, then the reaction kinetics could be implemented in future computational analysis to understand its effect on the shock compression response

The above suggestions for future work have focused on extensions to the presented work on the Ni/Al system. However, multilayer systems can be made from a variety of reactive (*e.g.* Al/Teflon, Al/Ta, and Ti/B) and inert (*e.g.* Cu/Ni, and Cu/Nb) multilayer systems, each one presenting a unique combination of inherent material

properties useful for various applications. The most natural extension of this work is an investigation on multilayers with various intrinsic material property differences. Varying the multilayer materials would allow for the influence of numerous factors (*e.g.* density ratio, material strength ratio, crystal structure, and heat of reaction) on the mechanical or chemical response under shock compression to be understood. Not only would this further our understanding of the role material interfaces play in the high strain rate mechanical behavior of such composites, but it would also extend the design space generated in this work.

APPENDIX A

UNIAXIAL STRAIN EXPERIMENT RECORDS

A.1 Experiment 0902

A.1.1 Velocity Data

The target velocity was 650 m/s. Four shorting pins were used, with all recording data. The results are given in Table A.1.

Table A.1: Velocity pin measurements for experiment 0902.

Pin Number	Position in inches	Time in μs
1	0.1615	-0.002
2	0.4820	12.025
3	0.7375	21.603
4	1.0150	31.998

A.1.2 PVDF Gauge Record

A PVDF gauge was used on the impact face of the sample. The active gauge area was 0.0905 cm^2 and the CVR termination resistance was 0.0977 Ohms. The integration time was 4.288 μs. The relevant section of the current and resulting stress profile are given in Figure A.1.

A.1.3 VISAR Record

The fringe constant was 543 m/s/fringe. The phase angle was not measured and assumed to be 90 degrees. No fringes were added or subtracted and no smoothing points were used. The raw VISAR data and resulting velocity profile are shown in Figure A.2. A hump in the free surface velocity trace is observed due to interference of the gauge package with the shock wave. The portion of the VISAR trace preceding this hump is what can be used for mesurement, which is shown in Figure A.2c.

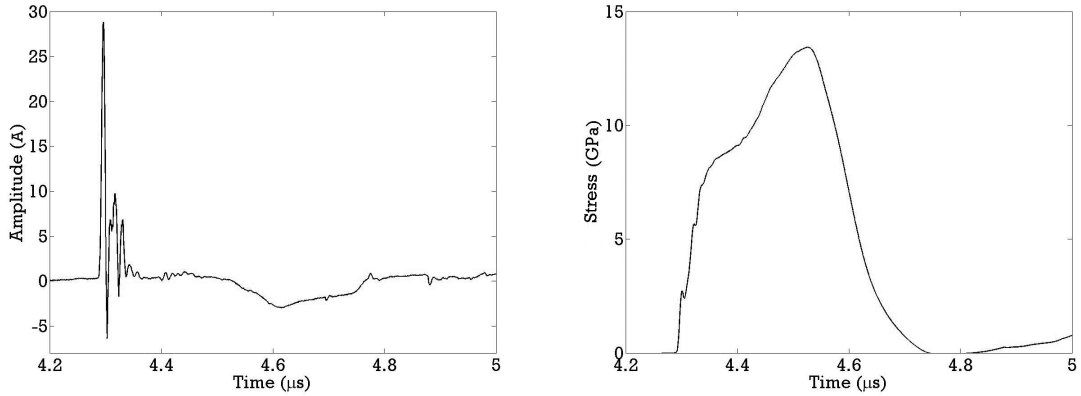

(a) Current (b) Stress

Figure A.1: PVDF trace for experiment 0902.

A.1.4 PDV Record

A.1.4.1 Driver

The PDV signal was recorded at a sampling rate of 25 Gs/s. The fast Fourier transform was performed with a Hamming window of 4000 points and a shift of 512 points. The signal was divided into a high and low resolution trace. The power spectra and extracted velocity profile for the high resolution signal are given in Figure A.3. They are identical to those obtained with the low resolution signal. Numerous harmonics are seen in the driver power spectra.

A.1.4.2 Sample

The PDV signal was recorded at a sampling rate of 25 Gs/s. The fast Fourier transform was performed with a Hamming window of 4000 points and a shift of 512 points. The signal was divided into a high and low resolution trace. The power spectra and extracted velocity profile for the high resolution signal are given in Figure A.4. They are identical to those obtained with the low resolution signal. Similar to the VISAR record, Figure A.2, a hump in the free surface velocity is observed due to interference from the gauge package. The portion of the PDV trace preceding this hump is what can be used for measurement, which is shown in Figure A.4c.

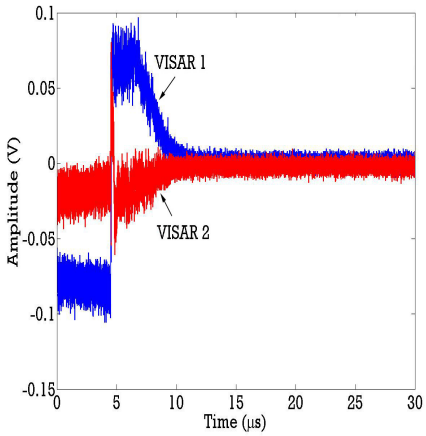

(a) VISAR Raw Data

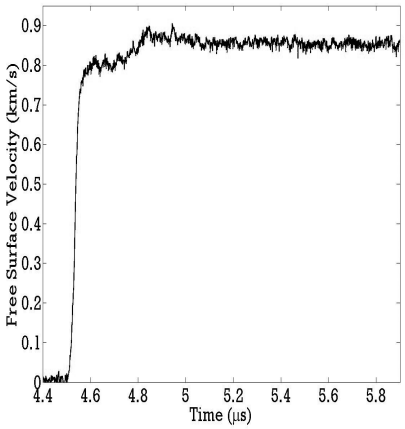

(b) Free Surface Velocity - All

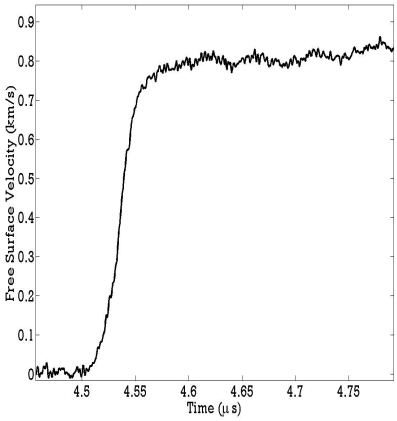

(c) Free Surface Velocity - Zoomed

Figure A.2: VISAR trace for experiment 0902.

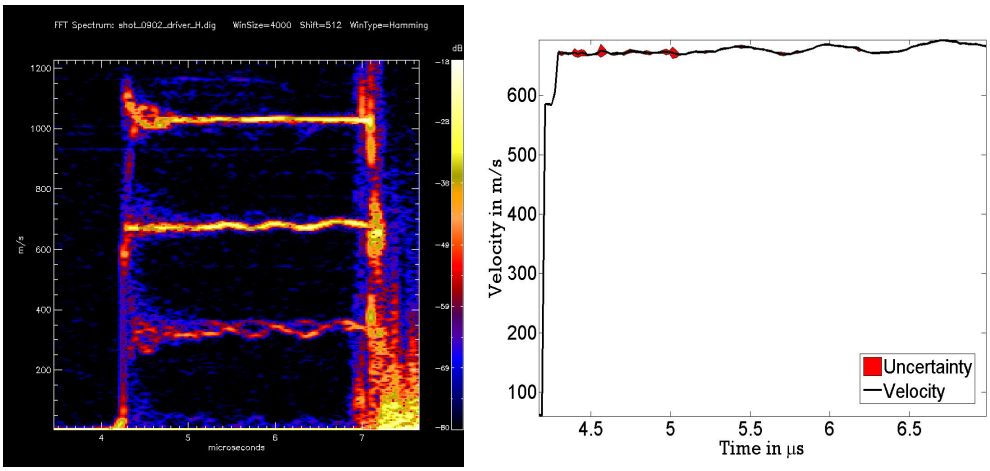

(a) High Resolution Power Spectra (b) High Resolution Velocity Profile

Figure A.3: Driver PDV trace for experiment 0902.

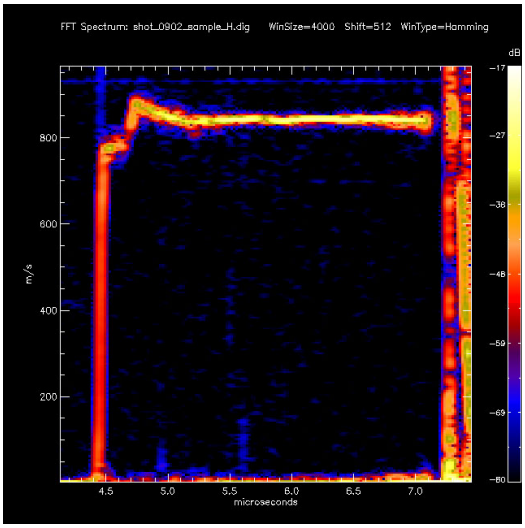

(a) High Resolution Power Spectra

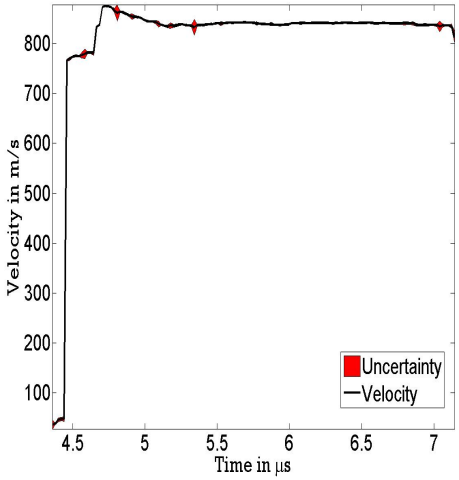

(b) High Resolution Velocity Profile - All

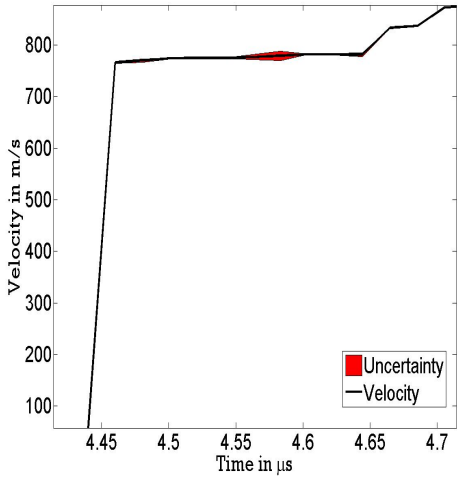

(c) High Resolution Velocity Profile - Zoomed

Figure A.4: Sample PDV trace for experiment 0902.

A.2 Experiment 0912

A.2.1 Velocity Data

The target velocity was 1000 m/s. Four shorting pins were used, with all recording data. The results are given in Table A.2.

Table A.2: Velocity pin measurements for experiment 0912.

Pin Number	Position in inches	Time in μs
1	0.162	0.001
2	0.421	7.064
3	0.752	16.100
4	0.981	22.325

A.2.2 PDV Record

A.2.2.1 Driver

The PDV signal was recorded at a sampling rate of 25 Gs/s. The fast Fourier transform was performed with a Hamming window of 4000 points and a shift of 512 points. The signal was divided into a high and low resolution trace. The power spectra and extracted velocity profile for the high resolution signal are given in Figure A.5. They are identical to those obtained with the low resolution signal.

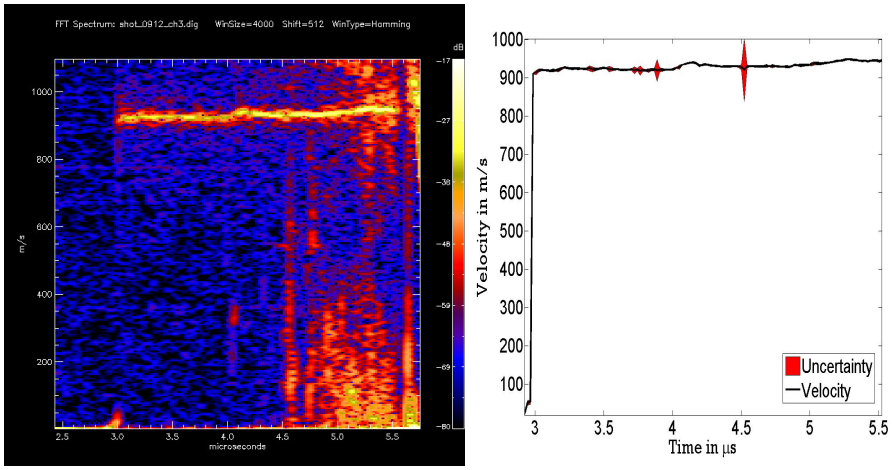

(a) High Resolution Power Spectra (b) High Resolution Velocity Profile

Figure A.5: Driver PDV trace for experiment 0912.

A.2.2.2 Sample

The PDV signal was recorded at a sampling rate of 25 Gs/s. The fast Fourier transform was performed with a Hamming window of 4000 points and a shift of 512 points. The signal was divided into a high and low resolution trace. The power spectra and extracted velocity profile for the high resolution signal are given in Figure A.6. They are identical to those obtained with the low resolution signal. The portion of the PDV trace used for measurement is shown in Figure A.6c.

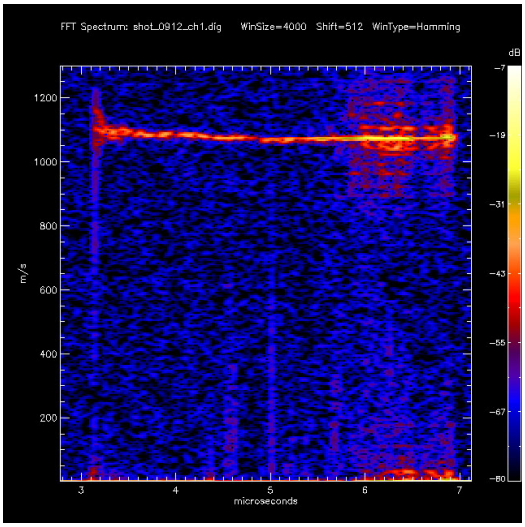

(a) High Resolution Power Spectra

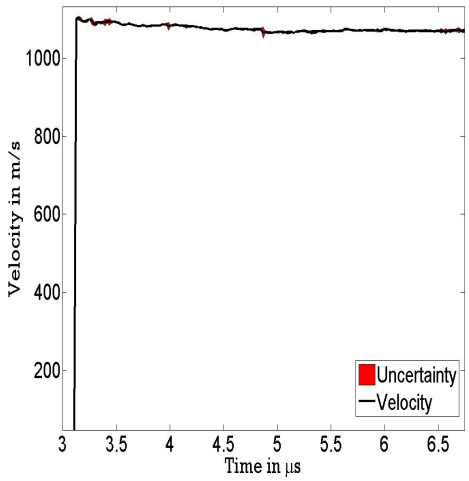

(b) High Resolution Velocity Profile - All

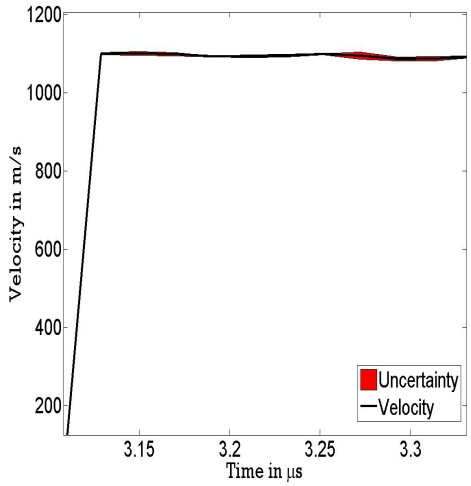

(c) High Resolution Velocity Profile - Zoomed

Figure A.6: Sample PDV trace for experiment 0912.

A.3 Experiment 1003

A.3.1 Velocity Data

The target velocity was 400 m/s. Four shorting pins were used, with all recording data. The results are given in Table A.3.

Table A.3: Velocity pin measurements for experiment 1003.

Pin Number	Position in inches	Time in μs
1	0.120	-0.001
2	0.389	17.178
3	0.739	39.438
4	1.001	56.098

A.3.2 VISAR Record

The fringe constant was 230.3 m/s/fringe. The phase angle was not measured and assumed to be 90 degrees for both the driver and sample. No fringes were added or subtracted and no smoothing points were used on either signal.

A.3.2.1 Driver

The raw VISAR data and resulting velocity profile for the driver are shown in Figure A.7.

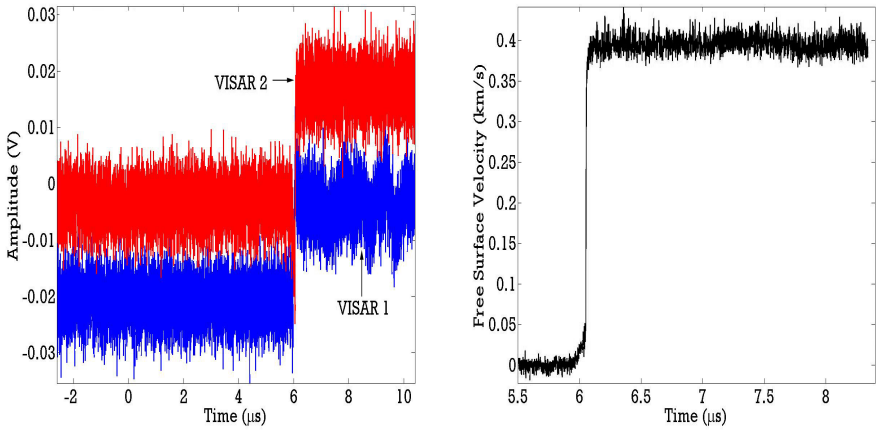

(a) VISAR Raw Data (b) Free Surface Velocity

Figure A.7: VISAR trace for the driver in experiment 1003.

A.3.2.2 Sample

The raw VISAR data and resulting velocity profile for the sample are shown in Figure A.8. The portion of the VISAR trace used for measurement is shown in Figure A.8c.

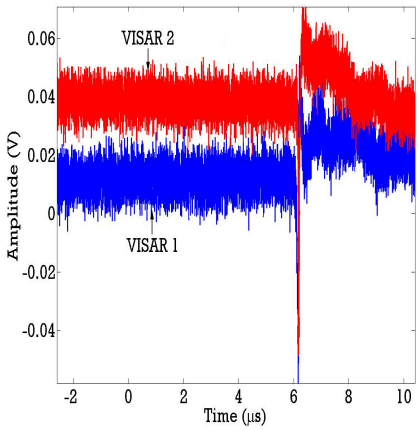

(a) VISAR Raw Data

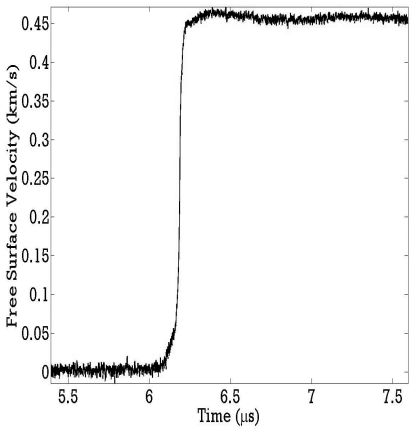

(b) Free Surface Velocity - All

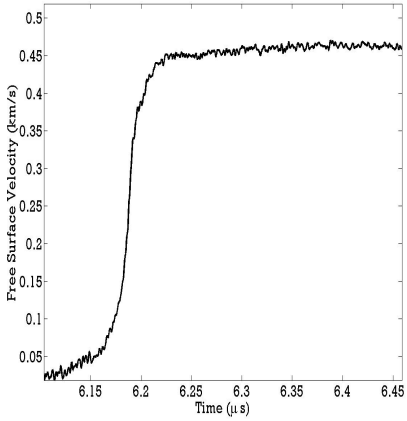

(c) Free Surface Velocity - Zoomed

Figure A.8: VISAR trace for the sample in experiment 1003.

A.4 Experiment 1038

A.4.1 Velocity Data

The target velocity was 1000 m/s. Four shorting pins were used, with all recording data. The results are given in Table A.4.

Table A.4: Velocity pin measurements for experiment 1038.

Pin Number	Position in inches	Time in μs
1	0.1675	-0.002
2	0.3735	4.919
3	0.6170	10.778
4	0.8220	15.705

A.4.2 PVDF Gauge Record

A PVDF gauge was used on the impact face and rear surface of the sample. For the input gauge, the active gauge area was 0.0900 cm^2, the CVR termination resistance was 0.05136 Ohms, and the integration time was 3.016 μs. For the propagated gauge, the active gauge area was 0.0900 cm^2, the CVR termination resistance was 0.05005 Ohms, and the integration time was 3.211 μs. The current and resulting stress profiles for each are given in Figure A.9. The propagated signal failed, yielding a current trace atypical for a PVDF gauge.

A.4.3 VISAR Record

The fringe constant was 543 m/s/fringe. The phase angle was not measured and assumed to be 90 degrees. No fringes were added or subtracted and no smoothing points were used. The raw VISAR data and resulting velocity profile are shown in Figure A.10. The portion of the VISAR trace used for measurement is shown in Figure A.10c. Not all of the rise is shown since it was elongated by the addition of a fringe. This elongation does not affect the steady state velocity measured.

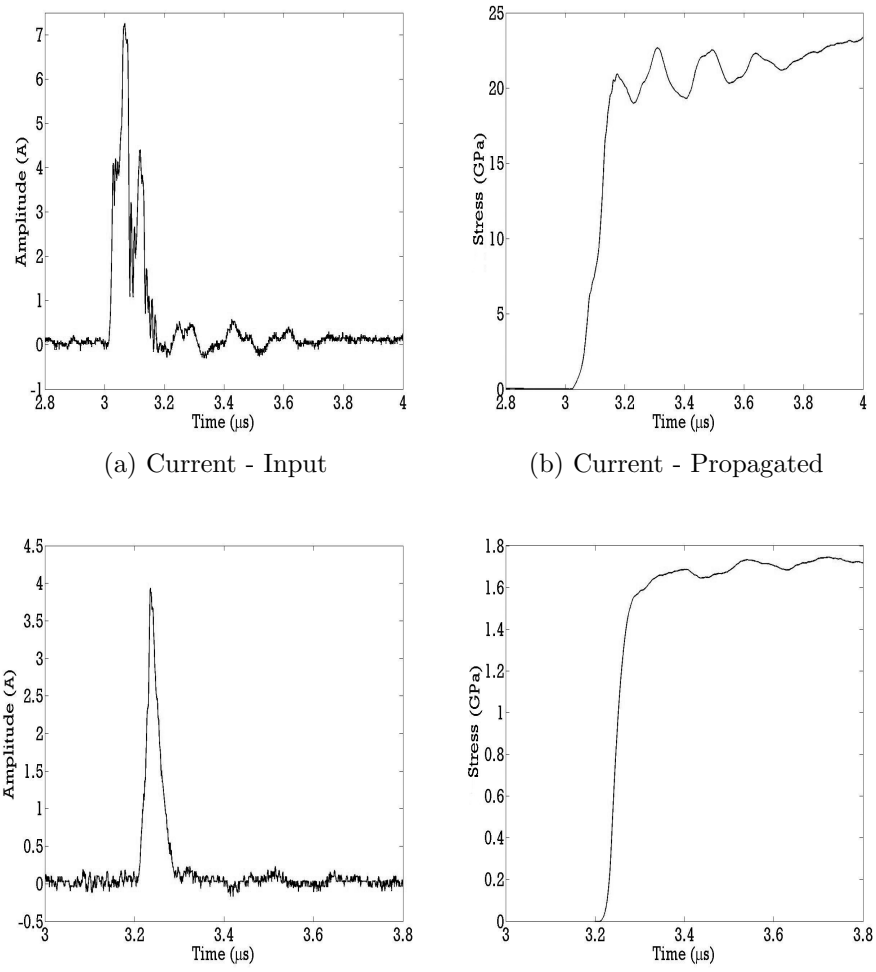

(a) Current - Input

(b) Current - Propagated

(c) Stress - Input

(d) Stress - Propagated

Figure A.9: PVDF traces for experiment 1038.

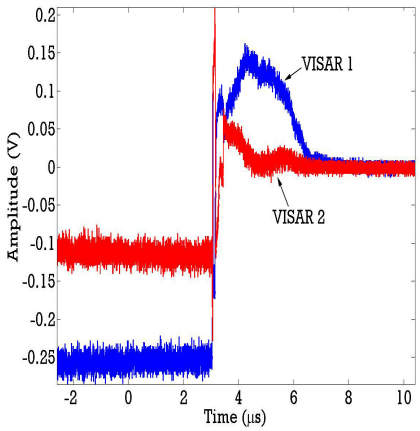

(a) VISAR Raw Data

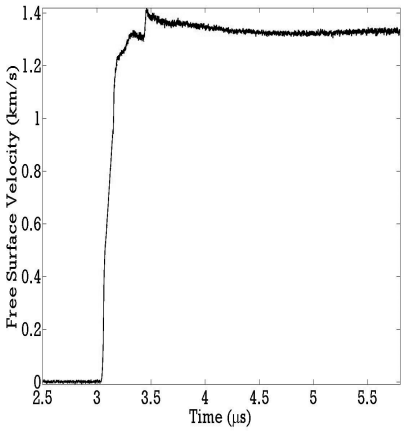

(b) Free Surface Velocity - All

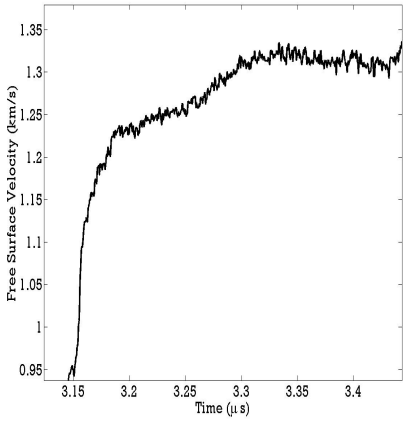

(c) Free Surface Velocity - Zoomed

Figure A.10: VISAR trace for experiment 1038.

A.5 Experiment 1041

A.5.1 Velocity Data

The target velocity was 600 m/s. Four shorting pins were used, with all recording data. The results are given in Table A.5.

Table A.5: Velocity pin measurements for experiment 1041.

Pin Number	Position in inches	Time in μs
1	0.1915	-0.002
2	0.3940	8.327
3	0.6040	17.038
4	0.8220	24.480

A.5.2 PVDF Gauge Record

A PVDF gauge was used on the impact face and rear surface of the sample. For the input gauge, the active gauge area was 0.0900 cm^2, the CVR termination resistance was 0.0996 Ohms, and the integration time was 3.863 μs. For the propagated gauge, the active gauge area was 0.0900 cm^2, the CVR termination resistance was 0.0970 Ohms, and the integration time was 4.042 μs. The current and resulting stress profile are given in Figure A.11.

A.5.3 VISAR Record

The fringe constant was 330.9 m/s/fringe. The phase angle was not measured and assumed to be 90 degrees. A positive fringe was added between 4.086 and 4.087 μs. No smoothing points were used. The raw VISAR data and resulting velocity profile are shown in Figure A.12. The VISAR 1 record has substantial electrical noise from the input PVDF gauge. As a result, no free surface velocity record was obtained.

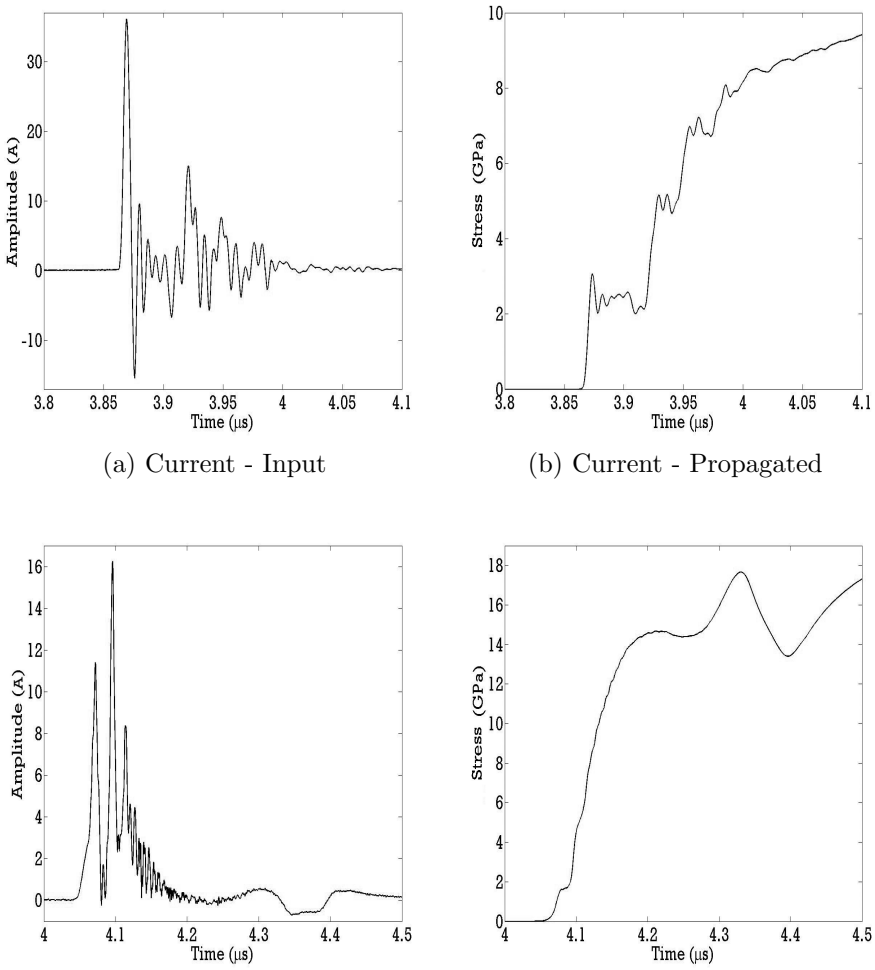

(a) Current - Input

(b) Current - Propagated

(c) Stress - Input

(d) Stress - Propagated

Figure A.11: PVDF traces for experiment 1041.

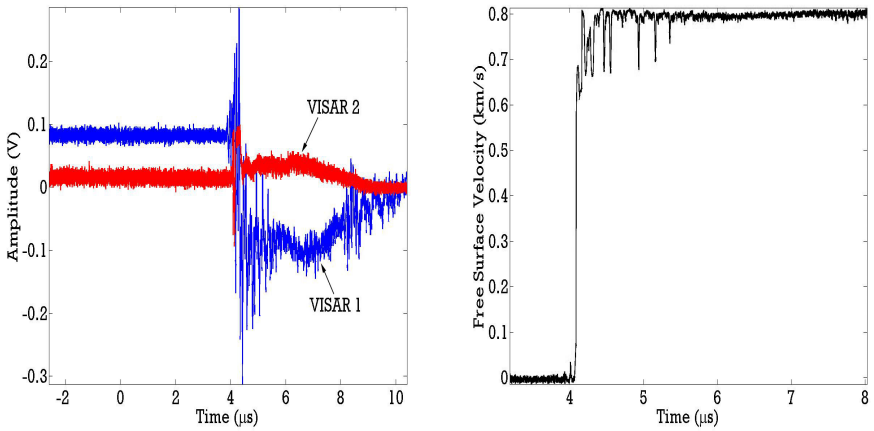

(a) VISAR Raw Data (b) Free Surface Velocity

Figure A.12: VISAR trace for experiment 1041.

A.6 Experiment 1207

A.6.1 Velocity Data

The target velocity was 300 m/s. Four shorting pins were used, with all recording data. The results are given in Table A.6.

Table A.6: Velocity pin measurements for experiment 1207.

Pin Number	Position in inches	Time in μs
1	0.0797	39.996
2	0.3473	63.400
3	0.6403	89.051
4	0.8940	111.251

A.6.2 PVDF Gauge Record

An PVDF gauge was used on the back surface of the sample. The active gauge area was 0.0900 cm^2, the CVR termination resistance was 0.50068 Ohms, and the integration time was -7.472 μs. The current and resulting stress profile are given in Figure A.13.

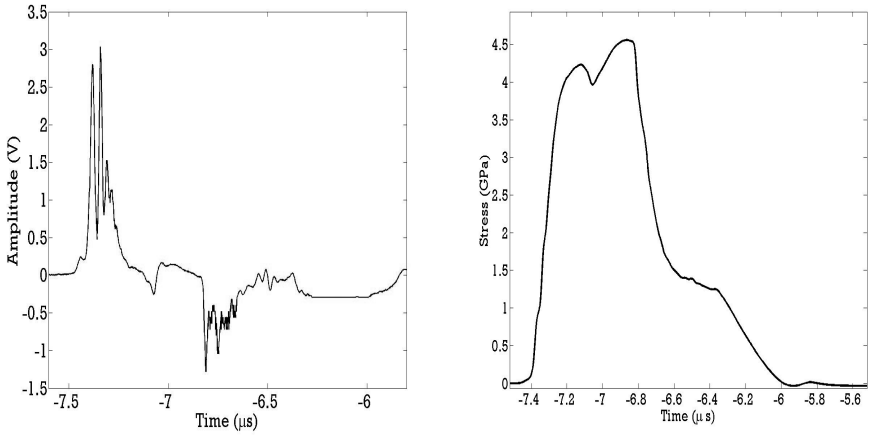

(a) Current (b) Stress

Figure A.13: PVDF trace for experiment 1207.

A.6.3 VISAR Record

The fringe constant was 106.4 m/s/fringe. The records were done on different scopes. A reference pulse was used for cross timing between the two oscilloscopes. They were found to have a negligible (< 1 ns) delay.

A.6.3.1 Driver

The phase angle was measured to be 59.4 degrees. A positive fringe was added between -7.479 and -7.477 μs. No smoothing points were used. The raw VISAR data and resulting velocity profile are shown in Figure A.14.

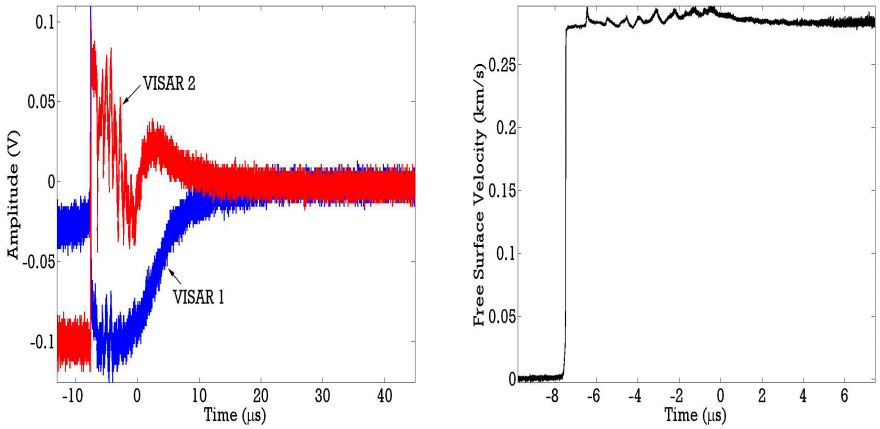

(a) VISAR Raw Data (b) Free Surface Velocity

Figure A.14: VISAR trace for the driver in experiment 1207.

A.6.3.2 Sample

The phase angle was measured to be 100.67 degrees. No fringes were added and no smoothing points were used. The raw VISAR data and resulting velocity profile is shown in Figure A.15. The portion of the VISAR trace used for measurement is shown in Figure A.15c.

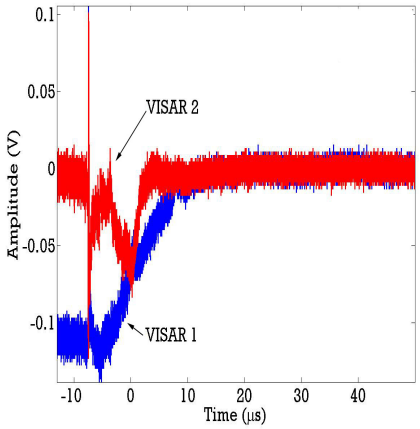

(a) VISAR Raw Data

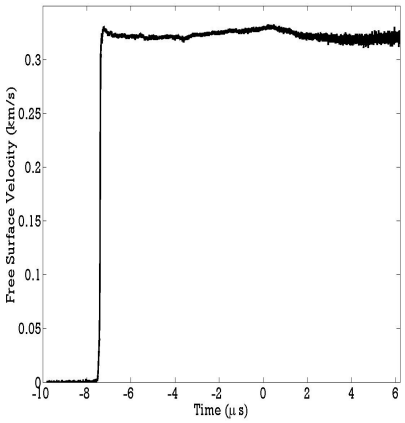

(b) Free Surface Velocity - All

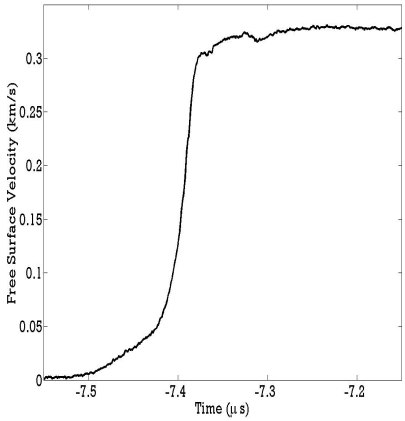

(c) Free Surface Velocity - Zoomed

Figure A.15: VISAR trace for the sample in experiment 1207.

A.6.4 Tilt Record

The tilt was measured with a series of 4 tilt pins. Pin 3 hit a small hole in the projectile and was not used. The tilt record is presented in Figure A.16

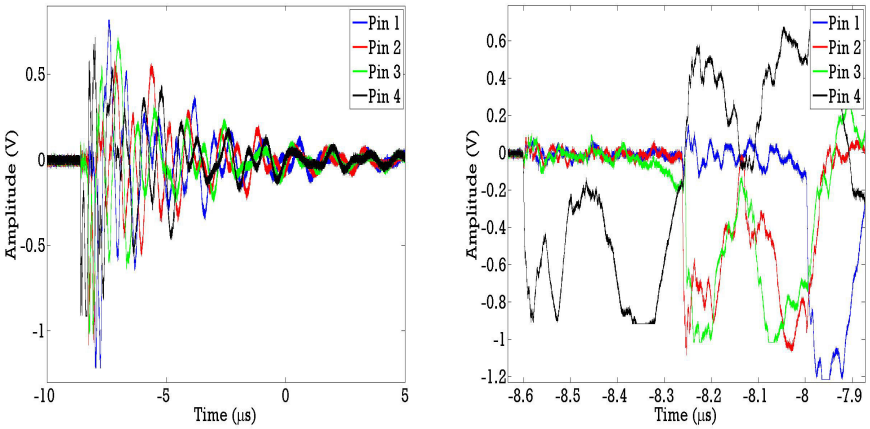

(a) Tilt Signals

(b) Tilt Signals - Zoomed

Figure A.16: Tilt pin record for experiment 1207.

APPENDIX B

IMAGE TO DIATOM ALGORITHM (IDA)

To aid in the incorporation of real, heterogeneous microstructures, an image to diatom algorithm (IDA) was written in MATLAB. The IDA routine provides a graphical user interface (GUI) for the generation of CTH microstructures. The IDA code works as a basic raster to vector converter for binary microstructural images (*i.e.* white particles in a black matrix) capable of handling complex geometries and internal voids. If the image(s) loaded are not in binary format, the IDA routine can run a simple thresholding algorithm to ensure proper operation of the code. This process can be run on the whole image or a specified section as desired by the user. Upon calling the IDA routine, the dialog box shown in Figure B.1 appears presenting the two run modes possible: 2D and 3D.

The main window for the 2D run mode is presented in Figure B.2. The IDA routine has several options for the generation of a variety of microstructures. The code can insert a matrix material around the particles in the loaded image, or define the image particles as voids in a matrix. The code also has options for plotting the results and obtaining stereological measurements (*i.e.* volume fraction, V_V, and length per unit area, L_A) of the particles. In addition, the code can separate out material definitions. This option helps to eliminate material coalescence in the CTH simulation. There are two separation algorithms programmed into the IDA code that can be changed by launching the advanced dialog box shown in Figure B.4a.

The 3D run mode is very similar to the 2D run mode, and its main window is presented in Figure B.3. The main difference in the 3D run mode is the importation of multiple images to define the 3D microstructure. Since multiple images are used,

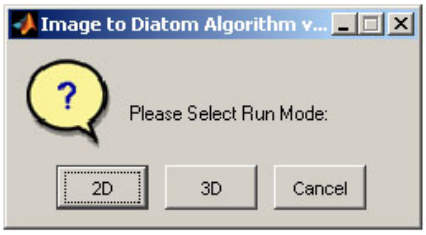

Figure B.1: Initial dialog box for the IDA code allowing for selection of the run mode.

a text file containing the thicknesses of each image must also be loaded into the code. This text file should have no headers. If the file has headers or does not contain enough values to represent all the images an error is generated by the code to alert the user. The 3D run mode has two additional features over the 2D run mode. The first is the ability to interpolate layers between images. This option can be used to smooth out the particles in the microstructure. The second is the ability to group particle slices together to define single particles in 3D. The number of interpolated layers and the amount of overlap necessary to group particles can be changes with the advanced dialog box, which is shown in Figure B.4b.

More detailed information of the code options and operation is presented in the beginning comments of the IDA GUI function in Section B.1. If the IDA routine is added to the MATLAB path these instructions are displayed in the command window by typing *help IDA*. The actual diatom generation code is presented in Section B.2.

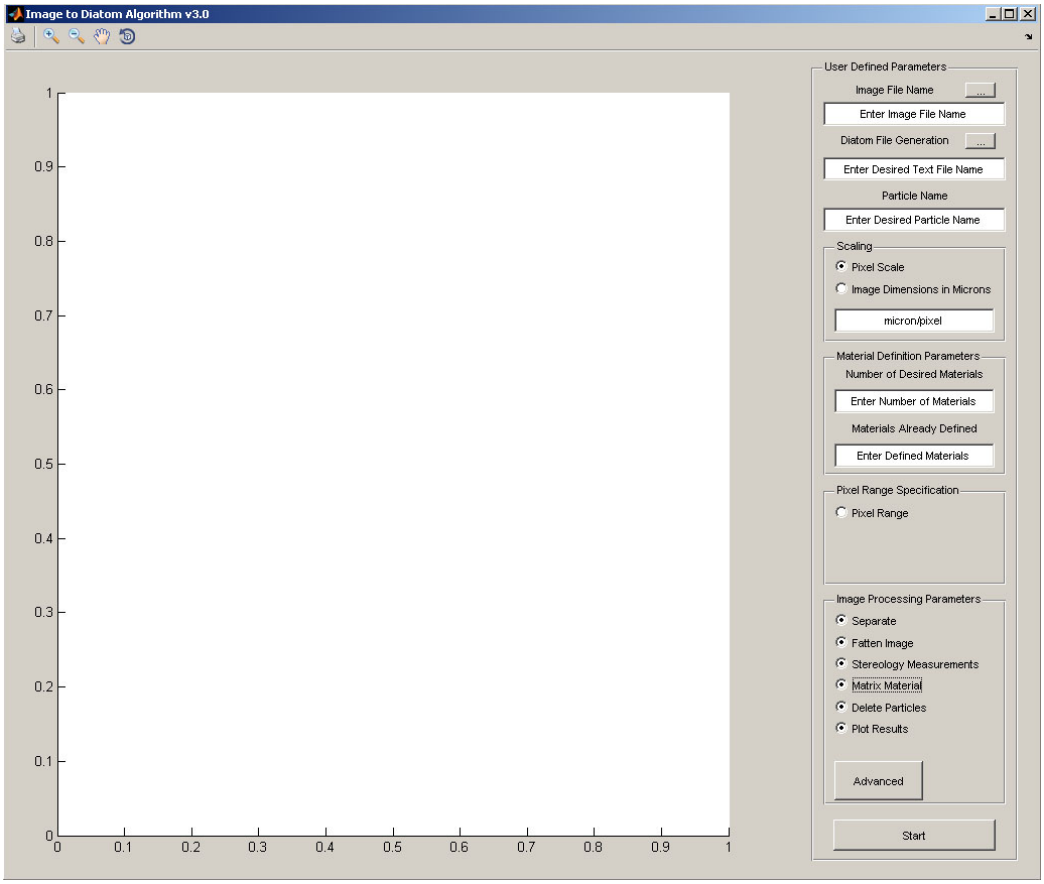

Figure B.2: 2D IDA main window showing the various options for the code.

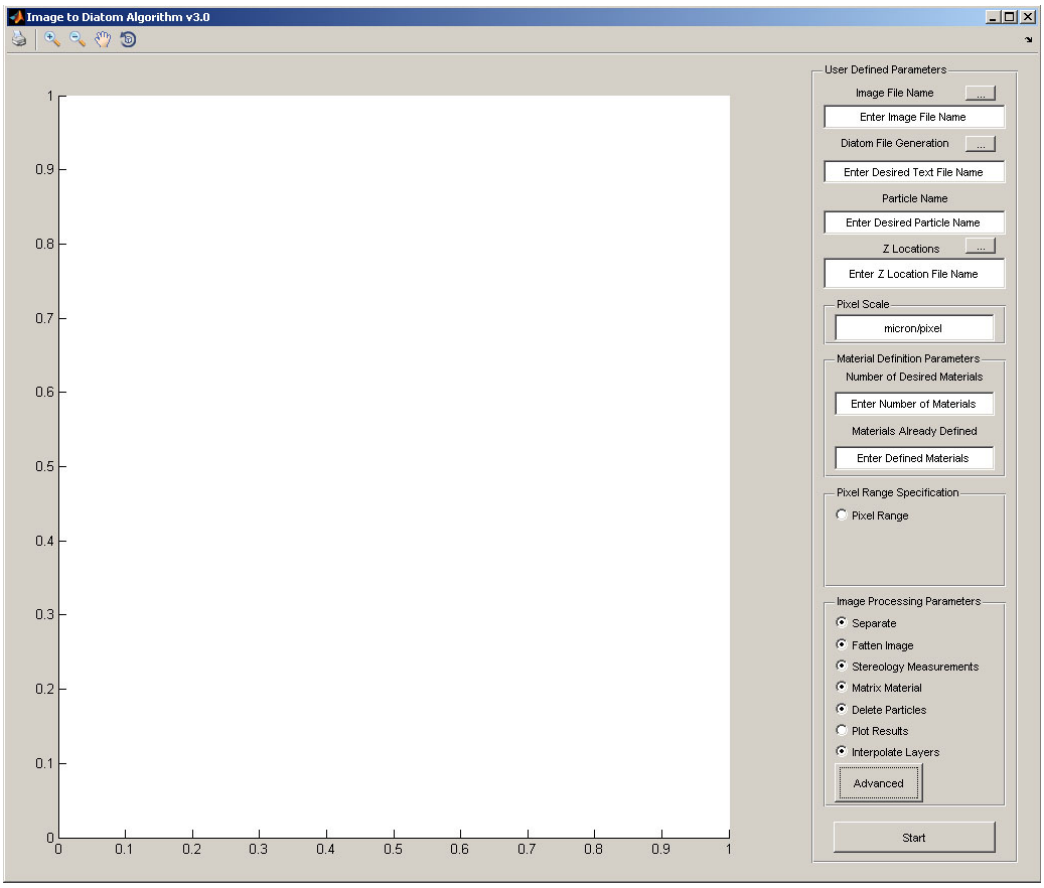

Figure B.3: 3D IDA main window showing the various options for the code.

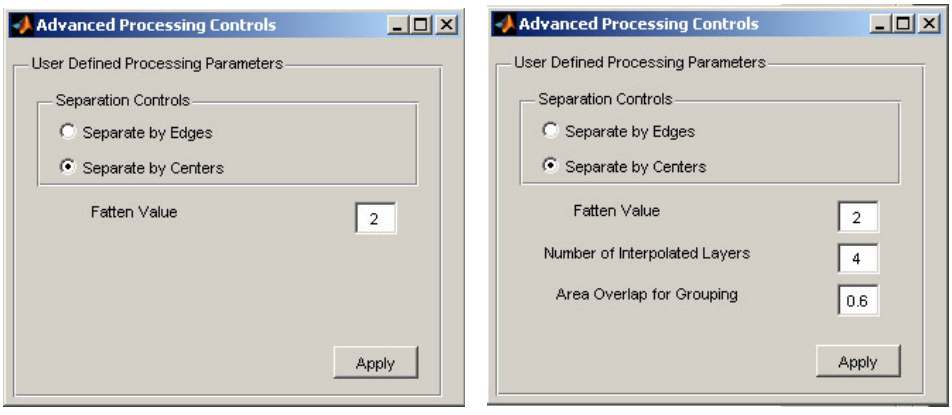

(a) 2D Run Mode (b) 3D Run Mode

Figure B.4: Advance properties dialog box for the 2D (a) and 3D (b) IDA routines.

B.1 IDA GUI Code

```
function IDA

% Image to Diatom Alogrithm v3.0
%
% This help section outlines the capabilities of the IDA code.  The IDA
% code is designed to take in a binary image (white particles, black matrix)
% into CTH.  The code can handle 2D and 3D microstructures.  Upon
% launching IDA, a dialog box appears.  The dialog box provides 3
% options:  2D, 3D, and cancel.  The 2D button launchs the 2D version,
% and the 3D button launcheds the 3D version.  The cancel option
% exits the code.  Below is a list of all the capabilities.  Each capability
% is flagged to signify if it is an option in 2D, [2D], 3D [3D], or both
% [2-3D].
%
% The code has 5 main input sections, which are outlined below.
% 1.   Image Parameters
%
% Image File Name  [2-3D]  The name of the image file(s) desired for the
% code is(are) entered into this text box.  The button to the
% upper right (marked '...') launchs a file browser allowing the desired
% file(s) to be picked.  The browser starts in the current directory.
% For both versions, the code checks to ensure each image is in binary
% format.  If they are not, a warning message appears and allows for the
% option of performing a simple thresholding operation.  This thresholding
% permanently alters the file and should be used with caution. For the 3D
% version, all the desired files to be imported into the code are
% selected.  The code checks to see if all the images are the same size.
% If they are not, an error message appears specifying that the pixel
% range option must be used.  The option to give the image dimensions
% is then removed.  Limits are also set for the maximum pixel range that can be
% selected to ensure each image is large enough.
%
% Diatom File Generation  [2-3D]  The name of the desired output text
% file for the code is entered into this text box.  The button to the upper
% right (marked '...') launchs a file browser allowing a file to be chosen
% The browser starts in the directory chosen for the image file(s).  If no
% file is chosen, the output is placed into a file titled Diatom.txt in the
% current directory.
%
% Particle Name  [2-3D]  The label desired to be put into the text file
% for each particle is entered here.  For example, for Ni
% particles, enter Ni to have package Ni particle.X in the
% diatom section, where X is a number signifying the particular particle.
% The default label is particle.
%
% Z Locations  [3D] - The name of the text file containing the thicknesses
% of each image in (microns).  The button to the upper right (marked '...')
% launchs a file browser allowing the desired file to be chosen.
% The browser start in the directory chosen for the image files.
% The file must have no header lines.  If the text files has more entries
% than images loaded, the code starts at the top of the list and take
% only enough values to represent all the images.  If there are not enough
% entries in the file a warning is generated and the code assumes a
% thickness of 1 mircon per image.
%
% 2. Scaling
%
% Pixel Scale  [2-3D]  In 2D, there is a radio button that is selected
% when this option is desired.  In 3D, it is the only option available.
% The scale, or width, of each pixel in the image is entered in the text
% box of this section.  The default assumed is 1 micron/pixel.
%
% Image Dimension in Microns  [2D]  When this radio button is selected,
% the width and height of the image in microns can be entered.  The code
% then automatically determines the scale, or width, of each pixel.  To use
% this option, the entire image must be used.  The pixel range option
% is deactivated if this option is selected.
%
% 3. Material Definition Parameters
%
% Number of Desired Materials  [2-3D]  The number of materials to be
% assigned to the particles is entered into this dialog box.  The maximum
% number of total materials in CTH is 20.  The values of this box can not
% be set above the limit to which the summation of the materials desired
% and the materials already defined equals 20.
%
% Number of Predefined Materials  [2-3D]  The number of materials
% already assigned is entered in this dialog box.  This option is to
% be used if you already have materials assigned (such as the matrix).  The
% material number assigned to the particles start from one
% integer higher then this number.  So, if a value of 3 is entered, the
% materials assigned to the particles start at 4.  The values of this box
% can not be set above the limit to which the summation of the materials
% desired and the materials already defined equals 20.
%
% 4. Pixel Range Specification
%
% Pixel Range  [2-3D]  This radio button runs the code on the pixel range
% specified.  This is done by giving a starting and finishing row and
% column.  This option can only be run if a pixel scale has been
```

```
% defined.  The dimensions are limited to those of the smallest image
% loaded.
%
% 5. Image processing Parameters
%
% Separate  [2-3D]  When this option is selected, the code runs a
% simple algorithm to spread out the material definitions to prevent
% coalescence in CTH.  The algorithm provides a better result than
% random material definitions, but it takes longer to run.
%
% Fatten  [2-3D]  When this option is selected, the code increases
% the size of the image.  This helps ensure that the particles are
% accurately represented.  It is suggested that this always be selected.
% If it is not selected, the code may produce unrealistic representations
% of the particles
%
% Stereology Measurements - [2-3D] - This option performs measurements of
% the volume fractions of the particles in both 2D and 3D.  In 2D, this
% option also calculates the length per unit area of the particles.
% The sterological measurements include internal voids in the
% calculations.
%
% Matrix Material - [2-3D] - This option allows for the insertion of a
% matrix material.  The selection of this option launchs a input dialog
% box.  In this dialog box the name of the matrix material is entered and
% the material number corresponding to it.  If the particles are in the
% matrix, then the material number assigned to the matrix must be either
% one of the materials already assigned or one not accounted for.
% Errors ensure that this criteria is met.  This option also launches
% the delete particles option.
%
% Delete Particles - [2-3D] - This option allows for the particles defined
% by the image to be subtracted from the matrix material.  This allows for
% porous structrues to be rendered.  If the material assigned to the matrix
% is the same as the particles, this option is assumed.
%
% Plot Results - [2-3D] - This option plots the results generated in MATLAB
% so the user can enure everything is working properly.  This option is
% very useful in 2D, but not so much in 3D.  As a result, the option must
% be selected in 3D.  In 3D, the code only outputs 2D polygons for the
% loaded images.  It does not plot the interpolated layers.
%
% Interpolate Layers  [3D]  When this option is selected, the code
% interpolates layers in between the images.  This algorithm works very
% well, but is time consuming.
%
% Advanced  [2-3D]  This button allows a variety of options
% for each of the image processing parameters to be changed.
%
% Separation Controls  [2-3D]  This allows the method to be specified
% for the separation algorithm.  Separation by centers is the
% default and uses the distance between particle centers as the
% criterion for assigning material definitions.  This option is recommended
% and seems to give the best results.  Separation by edges uses the
% minimum distance between the particles in each direction as the
% separation criterion.  The code essentially puts a box around the
% particle and then determine the distance between each particle based on
% the minimum x, y, and z distance between each box.
%
% Fatten Value  [2-3D]  This text box allows the degree of image resizing
% to be changed.  The default is 2 and is preferred.  If memory
% issues arise, the value can be set as low as 1.5.  Any value lower
% than 1.5  roduces an error message and could lead to unexpected
% results.  The large the value specified here, the more accurate the CTH
% rendering is.  However, this results in more memory use and
% slower running of the code.
%
% Number of Interpolated Layers  [3D]  This text box allows the number of
% interpolated layers to be specified.  The default is one.  The more
% layers interpolated, the slower the code runs, but the smoother the
% particles look.  This option should be used with care.  To large a
% number results in excessive run times and output files that are
% extremely large and unwieldy.
%
% Area Overlap for Grouping - [3D] - This option allows for the
% specification of the area overlap necessary to define two sections as the
% same particle.  The default is set at 0.6.
%
% Apply  [2-3D]  This button gives the user a sense that the
% values are set.  In actuality, the values are changed as soon as they are
% entered.  The apply button, really only closed the Advanced Parameters
% dialog box.
%


% Determine if running in 2D or 3D
choice = questdlg('Please Select Run Mode:', ...
'Image to Diatom Algorithm v3.0', ...
'2D','3D','Cancel','2D');
% Handle response
switch choice
    case '2D'
```

```
        TwoD=1;
    case '3D'
        TwoD=0;
    case 'Cancel'
        return
end

%get the screensize
scrnsize=get(0,'ScreenSize');
%  Create and then hide the GUI as it is being constructed.
f = figure('Visible','off','NumberTitle','off','Menubar','none','Toolbar','figure',...
    'Name','Image to Diatom Algorithm v3.0','Color', ...
    get(0, 'defaultuicontrolbackgroundcolor'),'Position',...
    [scrnsize(1)+0.2*scrnsize(3) scrnsize(2)+0.2*scrnsize(4) .8*scrnsize(3) 0.8*scrnsize(4)]);

%remove toolbar options that are of no use
tbh=findall(f,'Type','uiToolBar');
kids=allchild(tbh);
delete(kids(length(kids)-2:length(kids)));
delete(kids(1:7));
delete(kids(12));


%Generate the Panel for the User defined parameters
controls = uipanel('Parent',f,'Title','User Defined Parameters',...
    'Position',[.78 .02 .2 .97]);

uicontrol(controls,'Style','text','String','Image File Name',...
    'Units','normalized','Position',[0.05 0.95 0.7 0.04]);

Imgname = uicontrol(controls,'Style','edit','String','Enter Image File Name',...
    'BackgroundColor',[1 1 1],'Units','normalized','Position',[0.05 0.935 0.9 0.03],...
    'Callback',{@Imgname_Callback});

uicontrol('Parent',controls,'Units','normalized',...
    'Callback',{@ImgFileButtonCallback},...
    'Position',[0.75 0.97 0.15 0.02],...
    'String','...','TooltipString','Import Image File');

uicontrol(controls,'Style','text','String','Diatom File Generation',...
    'Units','normalized','Position',[0.05 0.885 .7 .04]);

Textname = uicontrol(controls,'Style','edit','String','Enter Desired Text File Name',...
    'BackgroundColor',[1 1 1],'Units','normalized','Position',[0.05 0.865 0.9 0.03],...
    'Callback',{@Textname_Callback});

uicontrol('Parent',controls,'Units','normalized',...
    'Callback',{@TextFileButtonCallback},...
    'Position',[0.75 0.905 0.15 0.02],...
    'String','...','TooltipString','Save Text File');

uicontrol(controls,'Style','text','String','Particle Name',...
    'Units','normalized','Position',[0.05 0.815 0.9 0.04]);

uicontrol(controls,'Style','edit','String','Enter Desired Particle Name',...
    'BackgroundColor',[1 1 1],'Units','normalized','Position',[0.05 0.8 0.9 0.03],...
    'Callback',{@Name_Callback});

if TwoD == 1
    Scale_control = uibuttongroup('Parent',controls,'Title','Scaling',...
        'Position',[0.05 0.66 0.9 0.13],'SelectionChangeFcn',...
        {@Scale_control_SelectionChangeFcn});

    Scale_button = uicontrol(Scale_control,'Style','radiobutton',...
        'String','Pixel Scale','Tag','Scale','Units','normalized',...
        'Value',1,'Position',[0.05 0.75 0.9 0.2]);

    Scaleval = uicontrol(Scale_control,'Style','edit','String','micron/pixel',...
        'Units','normalized','BackgroundColor',[1 1 1],'Position',[0.05 0.08 0.9 0.28],...
        'CallBack',{@Scaleval_Callback});

    Dimval_button = uicontrol(Scale_control,'Style','radiobutton',...
        'String','Image Dimensions in Microns','Tag','Dimensions','Units','normalized',...
        'Value',0,'Position',[0.05 0.5 0.9 0.2]);

    Dimval1 = uicontrol(Scale_control,'Style','edit','String','Height',...
        'Units','normalized','BackgroundColor',[1 1 1],'Position',[0.05 0.08 0.4 0.28],...
        'Visible','off','CallBack',{@Dimval1_Callback});

    Dimval2 = uicontrol(Scale_control,'Style','edit','String','Width',...
        'Units','normalized','BackgroundColor',[1 1 1],'Position',[0.5 0.08 0.4 0.28],...
        'Visible','off','CallBack',{@Dimval2_Callback});
else
    Scale_control = uipanel('Parent',controls,'Title','Pixel Scale',...
        'Position',[0.05 0.66 0.9 0.06]);

    Scaleval = uicontrol(Scale_control,'Style','edit','String','micron/pixel',...
        'BackgroundColor',[1 1 1],'Units','normalized','Position',[0.05 0.05 0.9 0.9],...
        'Callback',{@Scaleval_Callback});

    uicontrol(controls,'Style','text','String','Z Locations',...
        'Units','normalized','Position',[0.13 0.75 0.7 0.04]);
```

```
    Zname = uicontrol(controls,'Style','edit','String','Enter Z Location File Name',...
        'BackgroundColor',[1 1 1],'Units','normalized','Position',[0.05 0.73 0.9 0.04],...
        'Callback',{@Zname_Callback});

    uicontrol('Parent',controls,'Units','normalized',...
        'Callback',{@ZFileButtonCallback},...
        'Position',[0.75 0.775 0.15 0.02],...
        'String','...','TooltipString','Import Image File');
end

Mat_controls = uipanel('Parent',controls,'Title','Material Definition Parameters',...
    'Position',[0.05 0.49 0.9 0.16]);

uicontrol(Mat_controls,'Style','text','String','Number of Desired Materials',...
    'Units','normalized','Position',[0.05 0.75 0.9 0.22]);

Mat_number = uicontrol(Mat_controls,'Style','edit','String',...
    'Enter Number of Materials','Units','normalized',...
    'BackgroundColor',[1 1 1],'Position',[0.05 0.55 0.9 0.22],...
    'Callback',{@Materials_Callback});

uicontrol(Mat_controls,'Style','text','String','Materials Already Defined',...
    'Units','normalized','Position',[0.01 0.25 0.98 0.22]);

Mat_defined = uicontrol(Mat_controls,'Style','edit','String','Enter Defined Materials',...
    'BackgroundColor',[1 1 1],'Units','normalized','Position',[0.05 0.05 0.9 0.22],...
    'Callback',{@MaterialStart_Callback});

Pixel_controls = uipanel('Parent',controls,'Title','Pixel Range Specification',...
    'Position',[0.05 0.35 0.9 0.13]);

Pixel_button=uicontrol(Pixel_controls,'Style','radiobutton',...
    'String','Pixel Range','Units','normalized',...
    'Value',0,'Position',[0.05 0.7 0.9 0.25],...
    'Callback',{@Pixel_Range_Callback});

Pixel_row_S = uicontrol(Pixel_controls,'Style','edit','String','Start',...
    'Units','normalized','BackgroundColor',[1 1 1],'Position',[0.4 0.4 0.25 0.25],...
    'Visible','off','CallBack',{@Pixel_row_S_Callback});

Pixel_row_F = uicontrol(Pixel_controls,'Style','edit','String','Finish',...
    'Units','normalized','BackgroundColor',[1 1 1],'Position',[0.7 0.4 0.25 0.25],...
    'Visible','off','CallBack',{@Pixel_row_F_Callback});

Pixel_column_S = uicontrol(Pixel_controls,'Style','edit','String','Start',...
    'Units','normalized','BackgroundColor',[1 1 1],'Position',[0.4 0.03 0.25 0.25],...
    'Visible','off','CallBack',{@Pixel_column_S_Callback});

Pixel_column_F = uicontrol(Pixel_controls,'Style','edit','String','Finish',...
    'Units','normalized','BackgroundColor',[1 1 1],'Position',[0.7 0.03 0.25 0.25],...
    'Visible','off','CallBack',{@Pixel_column_F_Callback});

RowsDirect = uicontrol(Pixel_controls,'Style','text','String','Rows',...
    'Visible','off','Units','normalized','Position',[0.05 0.39 0.25 0.25]);

ColumnsDirect = uicontrol(Pixel_controls,'Style','text','String','Columns',...
    'Visible','off','Units','normalized','Position',[0.05 0.02 0.25 0.25]);

Process_controls = uipanel('Parent',controls,'Title','Image Processing Parameters',...
    'Position',[0.05 0.07 0.9 0.27]);

uicontrol(Process_controls,'Style','radiobutton',...
    'String','Separate','Units','normalized',...
    'Value',1,'Position',[0.05 0.88 0.9 0.1],...
    'Callback',{@separate_Callback});

uicontrol(Process_controls,'Style','radiobutton',...
    'String','Fatten Image','Units','normalized',...
    'Value',1,'Position',[0.05 0.77 0.9 0.1],...
    'Callback',{@Fatten_Callback});

uicontrol(Process_controls,'Style','radiobutton',...
    'String','Stereology Measurements','Units','normalized',...
    'Value',1,'Position',[0.05 0.66 0.9 0.1],...
    'Callback',{@Stereo_Callback});

Matrix_button = uicontrol(Process_controls,'Style','radiobutton',...
    'String','Matrix Material','Units','normalized',...
    'Value',0,'Position',[0.05 0.55 0.9 0.1],...
    'Callback',{@Matrix_Callback});

Void_button = uicontrol(Process_controls,'Style','radiobutton',...
    'String','Delete Particles','Units','normalized',...
    'Value',0,'Visible','off','Position',[0.05 0.44 0.9 0.1],...
    'Callback',{@Void_Callback});

Plot_button = uicontrol(Process_controls,'Style','radiobutton',...
    'String','Plot Results','Units','normalized',...
    'Value',1,'Position',[0.05 0.33 0.9 0.1],...
    'Callback',{@Plot_Callback});
```

```
if TwoD == 0

    set(Plot_button,'Value',0)

    uicontrol(Process_controls,'Style','radiobutton',...
        'String','Interpolate Layers','Units','normalized',...
        'Value',1,'Position',[0.05 0.22 0.9 0.1],...
        'Callback',{@Interpolate_Callback});
end

uicontrol(Process_controls,'Style','pushbutton',...
    'String','Advanced','Units','normalized',...
    'Position',[0.05 0.01 0.5 0.2],...
    'Interruptible','off','Callback',{@Advanced_Callback});

uicontrol(controls,'Style','pushbutton','String','Start',...
    'Units','normalized','Position',[0.1 0.01 0.8 0.04],...
    'Interruptible','off','Callback',{@Run_Callback});

axes('Parent',f,'Units','Pixels','Units','normalized',...
    'Position',[0.05 0.05 0.65 0.9]);

%Advanced Dialog Box
fa = figure('Visible','off','NumberTitle','off','Menubar','none','Toolbar','none',...
    'Name','Advanced Processing Controls','Color',...
    get(0, 'defaultuicontrolbackgroundcolor'),'Position',...
    [scrnsize(1)+0.5*scrnsize(3) scrnsize(2)+0.5*scrnsize(4) .25*scrnsize(3) 0.25*scrnsize(4)]);

acontrols = uipanel('Parent',fa,'Title','User Defined Processing Parameters',...
    'Position',[.01 .01 .95 .95]);

Separate_acontrol = uibuttongroup('Parent',acontrols,'Title','Separation Controls',...
    'Position',[0.05 0.65 0.9 0.3],'SelectionChangeFcn',...
    {@Separate_acontrol_SelectionChangeFcn});

uicontrol(Separate_acontrol,'Style','radiobutton',...
    'String','Separate by Edges','Tag','Edges','Units','normalized',...
    'Value',0,'Position',[0.05 0.5 0.9 0.45]);

uicontrol(Separate_acontrol,'Style','radiobutton',...
    'String','Separate by Centers','Tag','Centers','Units','normalized',...
    'Value',1,'Position',[0.05 0.01 0.9 0.45]);

uicontrol(acontrols,'Style','text','String','Fatten Value',...
    'Units','normalized','Position',[0.03 0.53 0.5 0.07]);

fattenval = uicontrol(acontrols,'Style','edit','String','2',...
    'BackgroundColor',[1 1 1],'Units','normalized','Position',[0.8 0.50 0.1 0.1],...
    'Callback',{@fattenval_Callback});

if TwoD == 0
    uicontrol(acontrols,'Style','text','String','Number of Interpolated Layers',...
        'Units','normalized','Position',[0.1 0.40 0.5 0.07]);

   imagineval = uicontrol(acontrols,'Style','edit','String','4',...
        'BackgroundColor',[1 1 1],'Units','normalized','Position',[0.8 0.37 0.1 0.1],...
        'Callback',{@imagineval_Callback});

    uicontrol(acontrols,'Style','text','String','Area Overlap for Grouping',...
        'Units','normalized','Position',[0.1 0.27 0.5 0.07]);

   groupval = uicontrol(acontrols,'Style','edit','String','0.6',...
        'BackgroundColor',[1 1 1],'Units','normalized','Position',[0.8 0.24 0.1 0.1],...
        'Callback',{@groupval_Callback});
end

uicontrol(acontrols,'Style','pushbutton','String','Apply',...
    'Units','normalized','Position',[0.75 0.05 0.2 0.1],...
    'Interruptible','off','Callback',{@apply_Callback});
%
%%%%%%%%%%%%%%%%%%%%%%%%%%%%%%%%%%%%%%%%%%%%%%%%%%%%%%%%%%%%%%%%%%%%%%%%%%%%%%%
% Move the GUI to the center of the screen.
movegui(f,'center')
% Make the GUI visible.
set(f,'Visible','on');
%%%%%%%%%%%%%%%%%%%%%%%%%%%%%%%%%%%%%%%%%%%%%%%%%%%%%%%%%%%%%%%%%%%%%%%%%%%%%%%
%Set the initial parameters to be passed by the code.
maxmat=20;
Diatom_String='Diatom.txt';
Image_String='Something';
Zfile_String='Z';
Name_String='Particle';
MS=0;
NF=1;
H=0;
Hdefault=0;
Wdefault=0;
h=1000;
w=1000;
W=0;
M=1;
F=2;
```

```
I=1;
G=0.6;
pixelrange=0;
Rowstart=1;
Rowfinish=1;
Columnstart=1;
Columnfinish=1;
fatten_val=1;
separate_val=1;
stereo_val=1;
matrix_val=0;
Matrix_String='Matrix';
Matrix_mat=1;
void_val=0;
interpolate_val=1;
plot_val=1;
scale_factor=1;
S_temp=1;
usecenter=1;
Equal=0;
%set the starting directory
imgFile=fullfile(cd);
textFile=fullfile(cd);
%%%%%%%%%%%%%%%%%%%%%%%%%%%%%%%%%%%%%%%%%%%%%%%%%%%%%%%%%%%%%%%%%%%%%%%%%%%%
%set up the call back function for each option
    function Textname_Callback(source,eventdata)
        Diatom_String = get(source,'String');
    end

    function ImgFileButtonCallback(source, eventdata)
        filespec = {'*.*', 'All files (*.*)';...
            '*.bmp', 'BMP files (*.bmp)'; ...
            '*.jpg', 'JPEG files (*.jpg)';...
            '*.tif', 'TIFF files (*.tif)';
            '*.gif', 'GIF files (*.gif)';...
            '*.pnp', 'PNP files (*.pnp)'};
        if TwoD == 1
            [filename, pathname] = uigetfile(filespec, 'Pick an image file', imgFile);
        else
            [filename, pathname] = uigetfile(filespec,'MultiSelect','on',...
                'Pick image files', imgFile);
            filename=sort(filename);
        end
        if ~isequal(filename,0)
            if TwoD == 1
                imgFile=fullfile(pathname, filename);
                textFile=fullfile(pathname,'\');
                set(Imgname, 'String',imgFile);
                Image_String=get(Imgname,'String');
                A=imread(imgFile);
                A=A(:,:,1);
                dimA=size(A);
                Hdefault=dimA(1);
                H=Hdefault;
                Wdefault=dimA(2);
                W=Wdefault;
                lowA=sum(sum(A == min(min(A))));
                highA=sum(sum(A == max(max(A))));
                if lowA+highA ~= dimA(1)*dimA(2)
                    choicet = questdlg('Images are not binary.  Convert to binary?', ...
                        'Image to Diatom Algorithm v3.0', ...
                        'Yes','No','Yes');
                    % Handle response
                    waitfor(choicet);
                    switch choicet
                        case 'Yes'
                            A=double(A)/double(max(max(A)));
                            [a b]=size(A);
                            for k=1:a
                                for n=1:b
                                    if A(k,n) > 0.5
                                        A(k,n)=1;
                                    else
                                        A(k,n)=0;
                                    end
                                end
                            end
                            imwrite(A,imgFile);
                        case 'No'
                            close
                    end
                end
                clear A dimA lowA highA
            else
                clear imgFile
                if iscell(filename) == 0
                    m20=errordlg('Use 2D Version for single image',...
                        'Bad Input','modal');
                    uiwait(m20);
                    close
                else
                    NF=length(filename);
```

```
                imgdim=ones(NF,2);
                threshold = 0;
                ending=0;
                for k=1:NF
                    tempfile=filename{k};
                    imgFile{k}=fullfile(pathname, tempfile);
                    A=imread(imgFile{k});
                    A=A(:,:,1);
                    imgdim(k,1:2)=size(A);
                    lowA=sum(sum(A == min(min(A))));
                    highA=sum(sum(A == max(max(A))));
                    if threshold == 0
                        if lowA+highA ~= imgdim(k,1)*imgdim(k,2)
                            choicet = questdlg('Images are not binary.  Convert to binary?', ...
                                'Image to Diatom Algorithm v3.0', ...
                                'Yes','No','Yes');
                            % Handle response
                            switch choicet
                                case 'Yes'
                                    threshold = 1;
                                case 'No'
                                    ending=1;
                            end
                        end
                    end
                    if threshold == 1
                        A=double(A)/double(max(max(A)));
                        [a b]=size(A);
                        for m=1:a
                            for n=1:b
                                if A(m,n) > 0.5
                                    A(m,n)=1;
                                else
                                    A(m,n)=0;
                                end
                            end
                        end
                        imwrite(A,imgFile{k});
                    end
                end
                clear A
                Hdefault=min(imgdim(:,1));
                H=Hdefault;
                Wdefault=min(imgdim(:,2));
                W=Wdefault;
                Equal=sum(imgdim(:,1)~=imgdim(1,1))+sum(imgdim(:,2)~=imgdim(1,2));
                if Equal > 0
                    m16=errordlg('Image sizes not equal.  Must specify Pixel Range.',...
                        'Bad Input','modal');
                    uiwait(m16);
                    set(Pixel_button,'Visible','off')
                    set(Pixel_row_S,'Visible','on');
                    set(Pixel_row_F,'Visible','on');
                    set(Pixel_column_S,'Visible','on');
                    set(Pixel_column_F,'Visible','on');
                    set(RowsDirect,'Visible','on');
                    set(ColumnsDirect,'Visible','on');
                    return
                end
                textFile=fullfile(pathname,'\');
                set(Imgname, 'String',imgFile{1});
                Image_String=imgFile;
                if ending == 1
                    close
                end
            end
        end
        clear imgdim Equal tempfile
    end
end

function TextFileButtonCallback(source, eventdata)
    filespec = {'*.txt', 'Text files (*.*)'};
    [filename, pathname] = uiputfile(filespec, 'Pick a directory', textFile);
    textFile =fullfile(pathname, filename);
    set(Textname, 'String',textFile);
    Diatom_String = get(Textname,'String');
end

function ZFileButtonCallback(source, eventdata)
    filespec = {'*.txt', 'Text files (*.*)'};
    [filename, pathname] = uigetfile(filespec, 'Pick an image file', textFile);
    ZFile =fullfile(pathname, filename);
    set(Zname, 'String',ZFile);
    Zfile_String = get(Zname,'String');
    hp1=helpdlg('Z locations file should list the thicknesses of each image in microns with no header lines.',...
        'Entering Z Locations');
    uiwait(hp1);
    Z=load(ZFile);
    if length(Z) < NF
        m001=errordlg('Not enough Z locations.  Defaulting to 1 micron per image.',...
            'Bad Input','modal');
```

```
        uiwait(m001);
        Zdefault=ones(NF,1);
        csvwrite('ZFile_Defaulted.txt',Zdefault);
        ZFile =fullfile(pathname, 'Zfile_Defaulted.txt');
        set(Zname, 'String',ZFile);
        Zfile_String = get(Zname,'String');
        return
    end
    if length(Z) > NF
        m002=errordlg(sprintf('Extra thicknesses in File. Taking first %g values.',NF),...
            'Bad Input','modal');
        uiwait(m002);
        return
    end
end

function Zname_Callback(source,eventdata)
    Zfile_String = get(source,'String');
end

function Imgname_Callback(source,eventdata)
    Image_String = get(source,'String');
end

function Name_Callback(source,eventdata)
    Name_String = get(source,'String');
end

function Scaleval_Callback(source,eventdata)
    Scale_String = get(source,'String');
    S_temp=str2double(Scale_String);
    if isnan(S_temp)
        m1=errordlg('You must enter a numeric value','Bad Input','modal');
        uiwait(m1);
        set(Scaleval,'String','micron/pixel');
        S_temp=1;
        return
    end
end

function Dimval1_Callback(source,eventdata)
    Dimval1_String = get(source,'String');
    h=str2double(Dimval1_String);
    if isnan(h)
        m2=errordlg('You must enter a numeric value','Bad Input','modal');
        uiwait(m2)
        set(Dimval1,'String',num2str(1000));
        h=1000;
        return
    end
end

function Dimval2_Callback(source,eventdata)
    Dimval2_String = get(source,'String');
    w=str2double(Dimval2_String);
    if isnan(w)
        m3=errordlg('You must enter a numeric value','Bad Input','modal');
        uiwait(m3)
        set(Dimval2,'String',num2str(1000));
        w=1000;
        return
    end
end

function Scale_control_SelectionChangeFcn(source,eventdata)
    switch get(eventdata.NewValue,'Tag')
        case 'Scale'
            scale_factor=1;
            set(Scaleval,'Visible','on')
            set(Dimval1,'Visible','off')
            set(Dimval2,'Visible','off')
        case 'Dimensions'
            scale_factor=2;
            set(Scaleval,'Visible','off')
            set(Dimval1,'Visible','on')
            set(Dimval2,'Visible','on')
            if pixelrange == 1
                m8b=helpdlg('Use Pixel Scale with this option instead of image dimensions');
                uiwait(m8b)
                set(Scaleval,'Visible','on')
                set(Dimval1,'Visible','off')
                set(Dimval2,'Visible','off')
                set(Scale_button,'Value',1)
                set(Dimval_button,'Value',0)
                set(Pixel_button,'Value',0)
                set(Pixel_row_S,'Visible','off');
                set(Pixel_row_F,'Visible','off');
                set(Pixel_column_S,'Visible','off');
                set(Pixel_column_F,'Visible','off');
                set(RowsDirect,'Visible','off');
                set(ColumnsDirect,'Visible','off');
                scale_factor=1;
```

```
                pixelrange=0;
            end
    end
end

function Materials_Callback(source,eventdata)
    Materials_Num = get(source,'String');
    M=str2double(Materials_Num);
    if isnan(M)
        m4=errordlg('You must enter a numeric value.','Bad Input','modal');
        uiwait(m4)
        set(Mat_number,'String',num2str(1))
        M=1;
        return
    end
    if M < 1
        m4b=errordlg('You must enter a positive value.','Bad Input','modal');
        uiwait(m4b)
        set(Mat_number,'String',num2str(1))
        M=1;
        return
    end
    if M+MS > maxmat
        m5=errordlg(sprintf('You can only have %g materials in CTH.',maxmat),...
            'Bad Input','modal');
        uiwait(m5)
        M=maxmat-MS;
        set(Mat_number,'String',num2str(M));
        return
    end
end

function MaterialStart_Callback(source,eventdata)
    MatStart_Num = get(source,'String');
    MS=str2double(MatStart_Num);
    if isnan(MS)
        m6=errordlg('You must enter a numeric value.','Bad Input','modal');
        uiwait(m6)
        set(Mat_defined,'String',num2str(0))
        MS=0;
        return
    end
    if MS < 0
        m6b=errordlg('You must enter a positive value.','Bad Input','modal');
        uiwait(m6b)
        set(Mat_defined,'String',num2str(0))
        MS=0;
        return
    end
    if MS+M > maxmat
        m7=errordlg(sprintf('You can only have %g materials in CTH.',maxmat),...
            'Bad Input','modal');
        uiwait(m7)
        MS=maxmat-M;
        set(Mat_defined,'String',num2str(MS))
        return
    end
end

function Pixel_Range_Callback(source,eventdata)
    if (get(source,'Value') == get(source,'Max'))
        pixelrange=1;
        if scale_factor == 2
            m8=helpdlg('Use Pixel Scale with this option instead of image dimensions');
            uiwait(m8)
            set(Pixel_button,'Value',0)
            pixelrange=0;
        else
            set(Pixel_row_S,'Visible','on');
            set(Pixel_row_F,'Visible','on');
            set(Pixel_column_S,'Visible','on');
            set(Pixel_column_F,'Visible','on');
            set(RowsDirect,'Visible','on');
            set(ColumnsDirect,'Visible','on');
        end
    else
        pixelrange=0;
        set(Pixel_row_S,'Visible','off');
        set(Pixel_row_F,'Visible','off');
        set(Pixel_column_S,'Visible','off');
        set(Pixel_column_F,'Visible','off');
        set(RowsDirect,'Visible','off');
        set(ColumnsDirect,'Visible','off');
    end
end

function Pixel_row_S_Callback(source,eventdata)
    Rows_S = get(source,'string');
    Rowstart=str2double(Rows_S);
    if isnan(Rowstart)
        m9=errordlg('You must enter a numeric value','Bad Input','modal');
        uiwait(m9)
```

```
        set(Pixel_row_S,'String',num2str(1))
        Rowstart=1;
        return
    end
    if Rowstart < 1
        m9b=errordlg('You must enter a postive value greater than 1',...
            'Bad Input','modal');
        uiwait(m9b)
        set(Pixel_row_S,'String',num2str(1))
        Rowstart=1;
        return
    end
    if Rowstart >= Hdefault
        m9c=errordlg('Image is not that Large.','Bad Input','modal');
        uiwait(m9c)
        set(Pixel_row_S,'String',num2str(1))
        Rowstart=1;
        return
    end
end

function Pixel_column_S_Callback(source,eventdata)
    Columns_S = get(source,'string');
    Columnstart=str2double(Columns_S);
    if isnan(Columnstart)
        m10=errordlg('You must enter a numeric value','Bad Input','modal');
        uiwait(m10)
        set(Pixel_column_S,'String',num2str(1))
        Columnstart=1;
        return
    end
    if Columnstart < 1
        m10b=errordlg('You must enter a postive value greater than 1',...
            'Bad Input','modal');
        uiwait(m10b)
        set(Pixel_column_S,'String',num2str(1))
        Columnstart=1;
        return
    end
    if Columnstart >= Wdefault
        m10c=errordlg('Image is not that Large.','Bad Input','modal');
        uiwait(m10c)
        set(Pixel_column_S,'String',num2str(1))
        Columnstart=1;
        return
    end
end

function Pixel_row_F_Callback(source,eventdata)
    Rows_F = get(source,'string');
    Rowfinish=str2double(Rows_F);
    if isnan(Rowfinish)
        m11=errordlg('You must enter a numeric value','Bad Input','modal');
        uiwait(m11)
        set(Pixel_row_F,'String',num2str(Hdefault))
        Rowfinish=Hdefault;
        return
    end
    if Rowfinish < 1
        m11b=errordlg('You must enter a postive value greater than 1',...
            'Bad Input','modal');
        uiwait(m11b)
        set(Pixel_row_F,'String',num2str(Hdefault))
        Rowfinish=Hdefault;
        return
    end
    if Rowfinish <= Rowstart
        m11c=errordlg('The ending row must be larger than the starting row',...
            'Bad Input','modal');
        uiwait(m11c)
        set(Pixel_row_F,'String',num2str(Hdefault))
        Rowfinish=Hdefault;
        return
    end
    if Rowfinish > Hdefault
        m11d=errordlg('Image is Not That Large.','Bad Input','modal');
        uiwait(m11d)
        set(Pixel_row_F,'String',num2str(Hdefault))
        Rowfinish=Hdefault;
        return
    end
end

function Pixel_column_F_Callback(source,eventdata)
    Columns_F = get(source,'string');
    Columnfinish=str2double(Columns_F);
    if isnan(Columnfinish)
        m12=errordlg('You must enter a numeric value','Bad Input','modal');
        uiwait(m12)
        set(Pixel_column_F,'String',num2str(Wdefault))
        Columnfinish=Wdefault;
        return
```

```
    end
    if Columnfinish < 1
        m12b=errordlg('You must enter a postive value greater than 1',...
            'Bad Input','modal');
        uiwait(m12b)
        set(Pixel_column_F,'String',num2str(Wdefault))
        Columnfinish=Wdefault;
        return
    end
    if Columnfinish < Columnstart
        m12c=errordlg('The ending row must be larger than the starting row',...
            'Bad Input','modal');
        uiwait(m12c)
        set(Pixel_column_F,'String',num2str(Wdefault))
        Columnfinish=Wdefault;
        return
    end
    if Columnfinish > Wdefault
        m12d=errordlg('Image is Not That Large','Bad Input','modal');
        uiwait(m12d)
        set(Pixel_column_F,'String',num2str(Wdefault))
        Columnfinish=Wdefault;
        return
    end
end

function Fatten_Callback(source,eventdata)
    if (get(source,'Value') == get(source,'Max'))
        fatten_val=1;
    else
        fatten_val=0;
    end
end

function separate_Callback(source,eventdata)
    if (get(source,'Value') == get(source,'Max'))
        separate_val=1;
    else
        separate_val=0;
    end
end

function Stereo_Callback(source,eventdata)
    if (get(source,'Value') == get(source,'Max'))
        stereo_val=1;
    else
        stereo_val=0;
    end
end

function Matrix_Callback(source,eventdata)
    if (get(source,'Value') == get(source,'Max'))
        matrix_val=1;
        set(Void_button,'Visible','on');
        if M == maxmat
            m27=errordlg('No more materials available for a matrix',...
                'Bad Input','modal');
            uiwait(m27)
            set(Matrix_button,'Value',0);
            set(Void_button,'Visible','off');
            matrix_val=0;
            void_val=0;
            return
        else
            prompt = {'Enter matrix Material','Enter Matrix Material Number'};
            dlg_title = 'Input for peaks function';
            num_lines = 1;
            def = {'Matrix','1'};
            answer = inputdlg(prompt,dlg_title,num_lines,def);
            if isempty(answer) == 1
                set(Matrix_button,'Value',0);
                matrix_val=0;
                set(Void_button,'Visible','off');
                void_val=0;
            else
                Matrix_String=answer{1};
                Matrix_mat=str2double(answer{2});
                if isnan(Matrix_mat)
                    m28=errordlg('You must enter a numeric value',...
                        'Bad Input','modal');
                    uiwait(m28)
                    set(Matrix_button,'Value',0);
                    matrix_val=0;
                    set(Void_button,'Visible','off');
                    void_val=0;
                end
                if Matrix_mat < 1
                    m29=errordlg('You must enter a positive numeric value',...
                        'Bad Input','modal');
                    uiwait(m29)
                    set(Matrix_button,'Value',0);
                    matrix_val=0;
```

```
                    set(Void_button,'Visible','off');
                    void_val=0;
                end
                if Matrix_mat > MS
                    if Matrix_mat <= M+MS
                        m28=errordlg('Matrix is defined as one of the materials.  Must be deleting particles',...
                            'Bad Input','modal');
                        uiwait(m28)
                        set(Void_button,'Value',1)
                        void_val=1;
                    end
                end
                if Matrix_mat > maxmat
                    m29=errordlg(sprintf('CTH only has %g materials.',maxmat),...
                        'Bad Input','modal');
                    uiwait(m29)
                    set(Matrix_button,'Value',0);
                    matrix_val=0;
                    set(Void_button,'Visible','off');
                    void_val=0;
                    Matrix_mat=1;
                    Matrix_String='Matrix';
                end
            end
        end
    else
        matrix_val=0;
        set(Void_button,'Visible','off');
        void_val=0;
    end
end

function Void_Callback(source,eventdata)
    if (get(source,'Value') == get(source,'Max'))
        void_val=1;
    else
        void_val=0;
    end
end

function Interpolate_Callback(source,eventdata)
    if (get(source,'Value') == get(source,'Max'))
        interpolate_val=1;
    else
        interpolate_val=0;
    end
end

function Plot_Callback(source,eventdata)
    if (get(source,'Value') == get(source,'Max'))
        plot_val=1;
    else
        plot_val=0;
    end
end

function Advanced_Callback(source,eventdata)
   set(fa,'Visible','on')
end

function Separate_acontrol_SelectionChangeFcn(source,eventdata)
    switch get(eventdata.NewValue,'Tag')
        case 'Edges'
            usecenter=0;
        case 'Centers'
            usecenter=1;
    end
end

function fattenval_Callback(source,eventdata)
    Fatten_Num = get(source,'string');
    F=str2double(Fatten_Num);
    if isnan(F)
        m13=errordlg('You must enter a numeric value','Bad Input','modal');
        uiwait(m13)
        set(fattenval,'String',num2str(2));
        F=2;
        return
    end
    if F < 1.5
        m13b=errordlg('You must enter an number of 1.5 or more.','Bad Input','modal');
        uiwait(m13b)
        set(fattenval,'String',num2str(1.5));
        F=1.5;
        return
    end
end

function imagineval_Callback(source,eventdata)
    Imagine_Num = get(source,'string');
    I=str2double(Imagine_Num);
    if isnan(I)
```

```
            m13O=errordlg('You must enter a numeric value','Bad Input','modal');
            uiwait(m13O)
            set(imagineval,'String',num2str(4));
            I=4;
            return
        end
        if I < 0
            m13Ob=errordlg('You must enter a positive interger','Bad Input','modal');
            uiwait(m13Ob)
            set(imagineval,'String',num2str(4));
            I=4;
            return
        end
        if I > 6
            m13Oc=errordlg('Number of interpolated layers is high.  Text file will be very large.',...
                'Bad Input','modal');
            uiwait(m13Oc)
            return
        end
    end

    function groupval_Callback(source,eventdata)
        Group_Num = get(source,'string');
        G=str2double(Group_Num);
        if isnan(G)
            m14O=errordlg('You must enter a numeric value','Bad Input','modal');
            uiwait(m14O)
            set(groupval,'String',num2str(0.6));
            G=0.6;
            return
        end
        if G < 0
            m14Ob=errordlg('You must enter a decimal between 0 and 1.','Bad Input','modal');
            uiwait(m14Ob)
            set(groupval,'String',num2str(0.6));
            G=0.6;
            return
        end
        if G > 1
            m14Oc=errordlg('You must enter a decimal between 0 and 1.','Bad Input','modal');
            uiwait(m14Oc)
            set(groupval,'String',num2str(0.6));
            G=0.6;
            return
        end
    end


    function apply_Callback(source,eventdata)
        set(fa,'Visible','off');
    end

    function Run_Callback(source,eventdata)
        if scale_factor == 1
            S=S_temp;
        else
            S=mean([h/H w/W])*10^-4;
        end
        GUI_borders(Image_String,Diatom_String,Name_String,S,M,MS,pixelrange,...
            Rowstart,Rowfinish,Columnstart,Columnfinish,...
            separate_val,fatten_val,usecenter,F,interpolate_val,...
            I,NF,Zfile_String,TwoD,G,stereo_val,matrix_val,...
            Matrix_String,Matrix_mat,void_val,plot_val,H,W);
        if stereo_val == 1
            if TwoD == 1
                m15=helpdlg(sprintf('The Volume Fraction of this Material is %5g. \n The Length per Unit Area is %5g cm^-1.',...
                    [ans(1) ans(2)]),'Diatom Length Per Unit Area');
                uiwait(m15)
            else
                m15=helpdlg(sprintf('The Volume Fraction of this Material is %5g',ans(1)),'Diatom Volume Fraction');
                uiwait(m15)
            end
        end
    end
end
```

B.2 IDA Source Code

```
% Paul Specht
% High Strain Rate Laboratory
% Georgia Tech School of Material Science and Engineering
% Created July 24 2007
% Last Modified 10/2012

%Function will output the points necessary to define particles in a
%picture. Takes pictures with black background and white particles.

function stereo=GUI_borders(Image,Diatom,Name,scale,nummat,moffset,pixelrange,Rowstart,Rowfinish,Columnstart,Columnfinish,...
           seperate,fatten_val,usecenter,fatten,interpolate_val,num,slices,Zfile,TwoD,groupval,stereo_val,matrix_val,...
           Matrix_String,Matrix_mat,void_val,plot_val,HH,WW)
tic
%Opens a text file for the output points
file=fopen(Diatom,'w+');
divider=2;  %counter to divide the number of particles and voids from each picture
VOID(1)=0;  %voids per picture (sort of)
PART(1)=0;  %particles per picture (sort of)
V=0;        %will be an array defining what particle each void belongs to
part=1;     %defines the initial particle number
void=1;     %defines the inital void number
counter=0;  %set variables for movement here incase first cell moved to is a corner cell
C1=0;
C2=0;
mat=1;         %material number
blob=1;        %3d particle number (particles is 2D)
if stereo_val == 1
    volfrac=0;
    surfacearea=0;
end

if slices > 1
    Ztemp=load(Zfile);                      %Loads the z locations (in column format) for each picture form a text file in microns
    Ztemp=Ztemp.*10^-4;                         %puts Z into cm
    if length(Zfile) > slices
        Ztemp=Ztemp(1:slices);
    end
    Z=zeros(length(Ztemp)+1);
    for dd=2:length(Z)
        Z(dd)=sum(Ztemp(1:(dd-1)));
    end
end

if matrix_val == 1
    if void_val == 1
        fprintf(file,['package ''',Matrix_String,''' \n']);
        fprintf(file,['   material ',num2str(Matrix_mat),' \n']);
        fprintf(file,['   insert Box',' \n']);
        if TwoD == 1
            fprintf(file,['       p1 = ',num2str(0),', ',num2str(-HH*scale*10^-4),' \n']);
            fprintf(file,['       p2 = ',num2str(WW*scale*10^-4),', ',num2str(0),' \n']);
        else
            fprintf(file,['       p1 = ',num2str(0),', ',num2str(-HH*scale*10^-4),', ',num2str(0),' \n']);
            fprintf(file,['       p2 = ',num2str(WW*scale*10^-4),', ',num2str(0),', ',num2str(Z(end)),' \n']);
        end
        fprintf(file,['   endi',' \n']);
        fprintf(file,['*',' \n']);
    end
end
```

```
for k=1:slices;                                     %For loop to go through each picture
    fprintf('Processing Image Number %g \n',k);
    if TwoD == 1
        A=imread(Image);                    %Reads in the picture file
    else
        A=imread(Image{k});
    end
    if length(size(A)) > 2
        A=A(:,:,1);
    end
    if pixelrange == 1
        A=A(Rowstart:Rowfinish,Columnstart:Columnfinish)/double(max(max(A)));
    else
        A=A(:,:)/double(max(max(A)));
    end
    if fatten_val == 1
        A=imresize(A,fatten,'nearest');
        if k == 1
            scale=(scale*10^-4)/fatten;
            dim=size(A);
        end
    else
        scale=scale*10^-4;
        dim=size(A);
    end
    B=ones(dim(1)+4,dim(2)+4)*.25; %Adds black border cells to the picture.
    B(2:dim(1)+3,2:dim(2)+3)=0;
    B(3:dim(1)+2,3:dim(2)+2)=A;
    clear A
    for l=3:dim(1)+2                                %For loop to go through the picture pixel by pixel.(right to left, top to bottom)
        for m=3:dim(2)+2
            number=1;                               %set up dummy variables here so reset after each particle
            guard=0;
            inside=1;
            value=0;
            back=B(l,m-1);                          %looks at the cell previous
            if back == 1                            %If the previous cell is not black then want to look for voids (black pixels)
                value=1;                            %makes you look for white neighbors
                inside=0;                           %makes you look for black center cell
            end
            if B(l,m)== inside                                          %Flags the right color pixel
                border=sum([B(l,m-1),B(l+1,m),B(l,m+1),B(l-1,m)]==value);  %uses neighboring cells to determine if the cell is an edge
                if border > 1                                           %Selects the cells that are on the edge of a particle
                    B(l,m)=0.5;                                         %changes the color of the edge cells so they disapear
                    if inside == 1                                      %enter if outlining a particle
                        particles{part,1}=['particle ',num2str(part)];  %stores particle number
                        points=0;                                       %resets points
                        points(number,1:2)=[m-2,-(l-2)];                   %saves points of this egde cell (subtract due to boundary cell)
                        part=part+1;                                    %gets ready for new part
                    else                                                %same as above but for voids
                        voids{void,1}=['void ',num2str(void)];
                        points=0;
                        points(number,1:2)=[m-2,-(l-2)];
                        void=void+1;
                    end
                    number=number+1;                                    %gets ready for the next cell point to be stored
                    n=l;                                                %Changes the variables of the cell index
                    o=m;
                    while guard == 0;                                   %This while loop will run until the whole particle is outlined
                        guard=0;                                        %resets up some variables to keep track of things
```

```
stopper=0;
p=0;
neighbors=[B(n,o+1),B(n+1,o),B(n,o-1),...          %looks at all the neighboring cells(R,B,L,T,BL,BR,TR,TL)
    B(n-1,o),B(n+1,o-1),B(n+1,o+1),...
    B(n-1,o+1),B(n-1,o-1)];
place(1:2,:)=[n n+1 n n-1 n+1 n+1 n-1 n-1;...      %stores the location of those neighboring cells
    o+1 o o-1 o o-1 o+1 o+1 o-1];
while stopper == 0                                 %this loop runs until it finds a similar neighbor
    p=p+1;                                         %indexes which cell is being searched first
    if p == 9                                       %enters if none of the neighboring cells are borders or inside corners
        stopper=1;                                 %stops both while loops, since the particle is outlined
        guard=1;
        p=8;                                       %resets p for one more go through
    end
    if neighbors(p) == inside                      %Flags right color neighboring cells
        b1=sum([B(place(1,p),place(2,p)-1),...     %calculates if T and B edge cells are different
            B(place(1,p),place(2,p)+1)]==value);
        b2=sum([B(place(1,p)+1,place(2,p)),...     %calculates if L and R edge cells are different
            B(place(1,p)-1,place(2,p))]==value);
        border2=sum([b1 b2]);                      %Calculates how many border cells are different
        c1=sum([B(place(1,p)-1,place(2,p)-1),...   %Same with corner cells
            B(place(1,p)+1,place(2,p)+1)]==value);
        c2=sum([B(place(1,p)+1,place(2,p)-1),...
            B(place(1,p)-1,place(2,p)+1)]==value);
        corner2=sum([c1 c2]);
        if b1 ~= 2 && b2 ~= 2                          %these 2 for loops keep from moving to a cutoff cell
            if sum(sqrt([c1 c2])) ~= sqrt(2)
                if border2 > 0                          %Enters if atleast one cell is different
                    B(place(1,p),place(2,p))=0.25;      %changes the color of the cell so it is invisible to the code
                    counter=0;
                    if border2 == 2                     %enters if it is an edge cell
                        B(place(1,p),place(2,p))=0.5;   %changes cell value so it is invisible to the code
                        points(number,1:2)=[place(2,p)-2,... %stores the pixel location
                            -(place(1,p)-2)];
                        number=number+1;                %gets ready for the next point
                    end
                    n=place(1,p);                       %resets the center pixel
                    o=place(2,p);
                    stopper=1;                          %exits the second while loop
                elseif corner2 > 0                      %enters if the cell is an inside corner
                    if p > 4                             %no primary moves corner to corner get cutoff
                        counter=0;
                    end
                    if C1 ~= c1 && C2 ~= c2             %allows primary move from corner to corner to pass two pixel wide bridges
                        counter=0;
                    end
                    if counter == 0
                        B(place(1,p),place(2,p))=0.5;
                        points(number,1:2)=[place(2,p)-2,...
                            -(place(1,p)-2)];
                        number=number+1;
                        n=place(1,p);
                        o=place(2,p);
                        stopper=1;
                        counter=1;
                    end
                end
            else
                B(place(1,p),place(2,p))=(value==1);        %converts cut off cell so won't go to it
                stopper=1;
            end
```

```
                            else
                                B(place(1,p),place(2,p))=(value==1);        %converts cut off cell so won't go to it
                                stopper=1;
                            end
                            C1=c1;                                  %stores corner of last cell for comparison purposes
                            C2=c2;
                        end
                    end
                end
                if inside == 1                          %Enters the points necessary to outline the particle or void into a cell array
                    if length(points) > 3               %Deletes particles or voids that are too small
                        particles{part-1,2}=points.*scale;
                    else
                        part=part-1;
                    end
                else
                    if length(points) > 3
                        voids{void-1,2}=points.*scale;
                    else
                        void=void-1;
                    end
                end
            end
        end
    end
    clear points
    clear neighbors
    clear B
    VOID(divider)=void-1;                           %stores the void and particle number for the picture
    PART(divider)=part-1;
    divider=divider+1;
    %determines which particle the void belongs.  This only searches the
    %current picture to speed up the process.  Will not enter if no void
    %was found
    if VOID(divider-2) < (void-1)                                           %keeps from entering for loop if no particle is found
        for q=(VOID(divider-2)+1):void-1                                    %Goes through each void found
            local1=voids{q,2}(1,1);                                         %gets X of first point used to outline void
            local2=voids{q,2}(1,2);                                         %gets Y of first point used to outline void
            finder=PART(divider-2)+1;                                         %generic counter
            while finder <= part-1                                           %Goes until particle containing void is found
                ring1=particles{finder,2}(:,1);                             %gets the x values of points used to outline each particle
                ring2=particles{finder,2}(:,2);                             %gets the Y values of points used to outline each particle
                if inpolygon(local1,local2,ring1,ring2) == 1                %true if void point is in the polygon outlined by the X, and Y values
                    voids{q,3}=finder;                                      %stores the particle number
                    V=[voids{:,3}];                                         %lists particles with voids in array
                    finder=part;                                            %exits the loop
                end
                finder=finder+1;                                            %cycles through each particle
            end
        end
    end
end
%This will assign different material numbers to the particles as they
%grow in 3D.
%$$$$$$$$$$$$$$$$$$$$$$$$$$$$$$$$$$$$$$$$$$$$$$$$$$$$$$$$$$$$$$$$$$$$$$$$
for L=1:slices
    Icount=0;
    for Q=(PART(L)+1):PART(L+1)   %This will assign different material numbers to the particles as they grow in 3D
        if L == 1                       %for first picture just goes through since no overlap
            particles{Q,3}=mat;         %puts material number into cell array
```

```
    particles{Q,4}=blob;       %puts blob number into cell array (this is for finding odd shapes)
    mat=mat+1;
    blob=blob+1;
    if mat == nummat+1                      %resets the material number
        mat=1;
    end
else
    outline1=particles{Q,2}(:,1);                                   %x points of polygon
    outline2=particles{Q,2}(:,2);                                   %y points of polygon
    match=0;                                 %used to signify if found a lower section match (resets here)
    holder=1;                                %used to count how many lower section matches there are (resets here)
    others=0;                                %resets others
    Icount=Icount+1;                         %resets Icount
    matched(holder)=Q;                       %stores the overlaping part
    for R=(PART(L-1)+1):PART(L)                     %goes through polygons of previous picture
        outline3=particles{R,2}(:,1);                               %x points of lower polygon R
        outline4=particles{R,2}(:,2);                               %y points of lower polygon R
        overlap1=sum(polyxpoly(outline1,outline2,outline3,outline4));%will give points of intersection between the two polygons Q and R
        if overlap1 > 0;
            [o1cw o2cw]=poly2cw(outline1,outline2);                 %reverses the order of vertices to clockwise so polybool can understand it
            [o3cw o4cw]=poly2cw(outline3,outline4);
            [polyx polyy]=polybool('intersection',o1cw,o2cw,o3cw,o4cw);     %gets area of overlap
            if polyarea(polyx,polyy) < (groupval*polyarea(outline1,outline2))    %finds out if overlap is too small to be same part
                if polyarea(polyx,polyy) < (groupval*polyarea(outline3,outline4))
                    overlap1=0;                                     %unflags small overlaps
                end
            end
        end
        if inpolygon(outline1,outline2,outline3,outline4) == 1  %will be true if inside the lower section
            overlap2=1;
        else
            overlap2=0;
        end
        if inpolygon(outline3,outline4,outline1,outline2) == 1  %will be true if inside section is inside this particle
            overlap3=1;
        else
            overlap3=0;
        end
        Overlap=overlap1+overlap2+overlap3;                %sums this up
        if Overlap ~= 0                                        %if not zero then there was a match
            if match == 0                                      %enters if it is the first match
                particles{Q,3}=particles{R,3};                 %gives it the same material number as match
                particles{Q,4}=particles{R,4};                 %gives it the same blob number as match
                others(holder)=particles{R,4};                 %stores the blob number
                matched(holder+1)=R;                           %stores the particles that overlaps with upper
                Material=particles{R,3};                       %stores the material number
                holder=holder+1;                               %indexes the number of matches found
                match=1;                                       %closes this if loop off
            else                                          %enters if this is a second or higher match
                others(holder)=particles{R,4};            %stores the blob number
                matched(holder+1)=R;                      %stores the particles that overlap
                holder=holder+1;                          %indexes for next match
            end
        end
        if R == PART(L)             %enters when done searching all particles of previous picture
            if match == 0                   %enters if no match was found.  means new particles so same as first picture
                particles{Q,3}=mat;
                particles{Q,4}=blob;
                mat=mat+1;
                blob=blob+1;
                if mat == nummat+1
```

```
                        mat=1;
                    end
                elseif length(others) > 1      %enters if there were multiple matches
                    for S=1:Q                   %serches all the previous particles
                        if sum(particles{S,4}==others) >0       %enters if previous particles has the same blob number
                            particles{S,3}=Material;            %gives anything with the matching blob number the same material
                            particles{S,4}=others(1);           %gives anything with the matching blob numbers a common blob number
                        end
                    end
                end
            end
            if match ~= 0                                   %enters if an overlap has been found
                imagine{L,Icount}=matched;         %stores all overlaping particles between two layers (rows are layer, columns the intersection)
                matched=0;
            end
        end
    end
end
%$$$$$$$$$$$$$$$$$$$$$$$$$$$$$$$$$$$$$$$$$$$$$$$$$$$$$$$$$$$$$$$$$$$$$$$$$$$
clear others
clear matched
%filter to ensure particles are as far apart as possible
%Begin by establishing the maximum and minmum x,y and z coordinates of the
%blob
index=1;        %counter to identify the nubmer of blobs, may not be equal to blob-1, since we erase many that combine together
for W=1:blob-1
    halt=0;         %used for identifying the min z
    for X=1:part-1                  %go through all particles
        if particles{X,4} == W      %gets particles that match the blob number
            if halt == 0            %enters if first particle found this will be zmin by default
                BLOB(index,1)=particles{X,4};       %stores the blob number in cell array of this particle for future reference
                BLOB(index,2)=particles{X,3};       %stores the material in cell array for future reference
                Zmin=sum(X <= PART);                 %gets Zmin
                Xmax=max(particles{X,2}(:,1));          %gets initial max and min values of this particle in x and y direction
                Xmin=min(particles{X,2}(:,1));
                Ymax=max(particles{X,2}(:,2));
                Ymin=min(particles{X,2}(:,2));
                halt=1;                             %ensure don't re-enter this loop
            end
            Zmax=sum(X <= PART);                                %sets Z max, will be default last time though this loop
            xmax=max(particles{X,2}(:,1));          %gets max and min values of this particle in x and y direction
            xmin=min(particles{X,2}(:,1));
            ymax=max(particles{X,2}(:,2));
            ymin=min(particles{X,2}(:,2));
            if xmax > Xmax                          %These compare max and min X and Y values will replace the values if more extreme
                Xmax=xmax;
            end
            if ymax > Ymax
                Ymax=ymax;
            end
            if xmin < Xmin
                Xmin=xmin;
            end
            if ymin < Ymin
                Ymin=ymin;
            end
        end
    end
    %%%%
    BLOB(index,3:8)=[Xmax Xmin Ymax Ymin Zmax Zmin];
```

```
    Center(index,1:3)=[(Xmax+Xmin)/2,(Ymax+Ymin)/2,(Zmax+Zmin)/2];
    %%%%%
    %BLOB(index,3:5)=[(Xmax+Xmin)/2,(Ymax+Ymin)/2,(Zmax+Zmin)/2];  %stores the rough center point of the particle
    index=index+1;                                          %counts up index for next blob
end
if seperate == 1
    if nummat > 1
        partsper=floor((index-1)/nummat);       %determine number of particles for each material definition
        numlast=(index-1)-partsper*(nummat);    %determine the number of materials that will have 1 more particle
        matstart=1;
        MATS=ones(1,index-1);
        done=0;
        while done == 0                             %builds up an array with mats listed 1:nummat and repeats
            if (index-matstart) >= nummat
                MATS(matstart:(matstart+nummat-1))=1:nummat;
                matstart=matstart+nummat;
            else
                if numlast > 0
                    MATS(matstart:index-1)=1:numlast;   %adds the extra materials on the end
                    done=1;
                else
                    done=1;
                end
            end
        end
        %%%%%%
        [val ind]=min(sqrt((((0.5*dim(1)*scale)-Center(:,1)).^2)+(((0.5*dim(2)*scale)-Center(:,2)).^2)+((0.5*slices-Center(:,3)).^2))); %finds center most particle
        clear val
        Xdist=min(BLOB(:,3)-BLOB(ind,3), BLOB(:,4)-BLOB(ind,4));      %gets the minimum x distance between the first particle and the rest
        Ydist=min(BLOB(:,5)-BLOB(ind,5), BLOB(:,6)-BLOB(ind,6));
        Zdist=min(BLOB(:,7)-BLOB(ind,7), BLOB(:,8)-BLOB(ind,8));
        if usecenter == 0                                       %get distanced based on centers or edges
            Dist(1:(index-1),1:3)=[BLOB(:,1) BLOB(:,2)  sqrt((Xdist.^2)+(Ydist.^2)+(Zdist.^2))];
        else
            Dist(1:(index-1),1:3)=[BLOB(:,1) BLOB(:,2)  sqrt(((Center(:,1)-Center(ind,1)).^2)+((Center(:,2)-Center(ind,2)).^2)+((Center(:,3)-Center(ind,3)).^2))];
        end
        Distance(1:(index-1),1:3)=sortrows(Dist,3);     %sort based on the distance
        clear Dist
        clear Center
        clear Xdist
        clear Ydist
        clear Zdist
        Distance(:,2)=MATS;             %set the materials to match the distance
        Distance=sortrows(Distance,1);
        clear MATS
        for mm=1:part-1                                  %go through every part
            blobnum=particles{mm,4};
            particles{mm,3}=Distance(blobnum,2);       %replaces the material number for this particle
        end
    end
end
clear Distance
clear BLOB
%$$$
```

```
for SI=2:length(imagine{QI,RI})     %will go through multiple intersections per part
    Ipart1=imagine{QI,RI}(SI);       %gets the points of the lower polygon
    Ipart2=imagine{QI,RI}(1);      %gets the points of the upper polygon
    Ix1=particles{Ipart1,2}(:,1);   %stores the x values of upper polygon
    Ix1(length(Ix1)+1,:)=Ix1(1);    %closes the polygon
    Iy1=particles{Ipart1,2}(:,2);
    Iy1(length(Iy1)+1,:)=Iy1(1);
    Ix2=particles{Ipart2,2}(:,1);
    Ix2(length(Ix2)+1,:)=Ix2(1);
    Iy2=particles{Ipart2,2}(:,2);
    Iy2(length(Iy2)+1,:)=Iy2(1);
    sections=99;                    %number of radial lines from point
    pivot=(2*pi)/sections;          %angle for those lines
    delta=((min(Ix2)+(max(Ix2)-min(Ix2))/2)-(min(Ix1)+(max(Ix1)-min(Ix1))/2))/10; %difference in x value of center points
    %slope of line between center points
    slope=((min(Iy2)+(max(Iy2)-min(Iy2))/2)-(min(Iy1)+(max(Iy1)-min(Iy1))/2))/(eps+((min(Ix2)+(max(Ix2)-min(Ix2))/2)-(min(Ix1)+(max(Ix1)-min(Ix1))/2)));
    Ipoint=[min(Ix2)+(max(Ix2)-min(Ix2))/2 min(Iy2)+(max(Iy2)-min(Iy2))/2];    %start at polygon two center
    locate=0;       %used to find a point within each polygon
    enter=1;        %Used to see if point in polygons found
    run=1;          %determines how many times it has looked for the a point in polygons
    Ivoid=0;        %resets the number of voids found
    while locate == 0       %enters if point in polygons is not found
        [in on]=inpolygon(Ipoint(1),Ipoint(2),Ix1,Iy1); %sees if it is in or on the polygon
        if in == 1          %enters if in
            if on ~= 1      %enters if not on
                if inpolygon(Ipoint(1),Ipoint(2),Ix2,Iy2) == 1  %enters if in the lower polygon
                    locate=1;                                   %kick out of while loop
                    Icenter=[Ipoint(1) Ipoint(2)];   %if in both polygons this is reference point
                end
            end
        end
        Ipoint=[Ipoint(1)-delta Ipoint(2)-delta*slope];    %moves toward center of polygon 1 until finds point in both
        run=run+1;                                         %stores the total times through while loop
        if run == 11                %enters if have made too many runs of while loop
            locate=1;               %kicks out of while loop
            enter=0;                %ensures will not make imaginary parts since no ref point was found
        end
    end
    if enter == 1
        for HI=1:num     % goes for number of imaginary polygons
            mid1=cell(20,2);       %generates variables to be used latter in storing voids
            AI=0;
            CI=0;
            for KI=1:sections    %generates the lines
                line=[Icenter(1) Icenter(2); Icenter(1)+30*cos(KI*pivot) Icenter(2)+30*sin(KI*pivot)]; %line
                [m1 m2]=polyxpoly(line(:,1),line(:,2),Ix1,Iy1); %intersection with polygon 1
                [m3 m4]=polyxpoly(line(:,1),line(:,2),Ix2,Iy2); %intersection with polygon 2
                M1=sortrows([m1 m2],-cos(KI*pivot)/abs(cos(KI*pivot)));     %orders the points from out to in
                M2=sortrows([m3 m4],-cos(KI*pivot)/abs(cos(KI*pivot)));
                mark1=M1(:,1);                                              %sets the x and y values
                mark2=M1(:,2);
                mark3=M2(:,1);
                mark4=M2(:,2);
                d=length(mark1);            %determines if more than one intersection with single polygon meaning there are voids
                d2=length(mark3);
                if length(mark1) > 1        %enters if found a void
                    for LI=d:-2:2           %goes through all the intersections in order
                        [AI BI]=size(mid1{(((d-LI)/2)+1),1});       %used to build up the cell array
                        %will generate points that are spaced equally from each intersection point determined from the number of imaginary layers desired
                        mid1{(((d-LI)/2)+1),1}(AI+1,:)=[mark1(LI)-HI*((mark1(LI)-mark1(LI-1))/(2*(num+1))) mark2(LI)-HI*((mark2(LI)-mark2(LI-1))/(2*(num+1)))];
                        mid2{(((d-LI)/2)+1),1}(AI+1,:)=[mark1(LI-1)-HI*((mark1(LI-1)-mark1(LI))/(2*(num+1))) mark2(LI-1)-HI*((mark2(LI-1)-mark2(LI))/(2*(num+1)))];
```

```
                end
                middle(KI,:)=[mark1(1)-HI*((mark1(1)-mark3(1))/(num+1)) mark2(1)-HI*((mark2(1)-mark4(1))/(num+1))];  %point between polygons
            elseif length(mark3) > 1            %same as above but for other polygon
                for MI=d2:-2:2
                    [CI DI]=size(mid1{(((d2-MI)/2)+1),2});
                    Ivalue=[(mark3(MI)-mark3(MI-1))/2 (mark4(MI)-mark4(MI-1))/2];
                    mid1{(((d2-MI)/2)+1),2}(CI+1,:)=[Ivalue(1)-HI*((mark3(MI)-mark3(MI-1))/(2*(num+1))) Ivalue(1)-HI*((mark4(MI)-mark4(MI-1))/(2*(num+1)))];
                    mid2{(((d2-MI)/2)+1),2}(CI+1,:)=[Ivalue(1)+HI*((mark3(MI-1)-mark3(MI))/(2*(num+1))) Ivalue(2)-HI*((mark4(MI-1)-mark4(MI))/(2*(num+1)))];
                end
                middle(KI,:)=[mark1(1)-HI*((mark1(1)-mark3(1))/(num+1)) mark2(1)-HI*((mark2(1)-mark4(1))/(num+1))];
            else
                middle(KI,:)=[mark1-HI*((mark1-mark3)/(num+1)) mark2-HI*((mark2-mark4)/(num+1))];  %point between polygons if no voids
            end
        end
        if AI ~= 0 || CI ~= 0  %enters if there was a void
            for NI=1:20        %goes through the void cell array
                for PI=1:2
                    if sum(size(mid1{NI,PI})) ~= 0  %enters if actually exists
                        Ivoid=Ivoid+1;              %stores the number of voids
                        Imagvoid{HI,Ivoid}=[mid1{NI,PI};flipud(mid2{NI,PI})];   %enters hole polygon in new cell array
                    end
                end
            end
        end
        Imaginary{HI}=middle;   %stores the imaginary particle in cell array
    end
else
    for TI=1:num
        Imaginary{TI}=particles{Ipart2,2};      %generates imaginary particles identical to bottom one if no ref point was found
    end
end
%Prints out the results same as below except the z values and
%thicknesses have changed
for UI=1:num
    Iindex=Iindex+1;
    if void_val == 0
        fprintf(file,['package ''Imaginary',Name,'particle',num2str(Iindex),''' \n']);
        fprintf(file,['   material ',num2str(particles{Ipart2,3}+moffset),' \n']);
        fprintf(file,['   insert prism',' \n']);
    else
        fprintf(file,['   delete prism',' \n']);
    end
    fprintf(file,['       origin = 0, 0, ',num2str(UI*(Z(QI,1)-Z(QI-1,1))/(num+1)+Z(QI-1,1)),' \n']);
    fprintf(file,['       u1 = 1, 0, ',num2str(UI*(Z(QI,1)-Z(QI-1,1))/(num+1)+Z(QI-1,1)),' \n']);
    fprintf(file,['       v1 = 0, 1, ',num2str(UI*(Z(QI,1)-Z(QI-1,1))/(num+1)+Z(QI-1,1)),' \n']);
    fprintf(file,['       thickness = ',num2str((Z(QI,1)-Z(QI-1,1))/(num+1)),' \n']);
    for VI=1:length(Imaginary{UI})
        fprintf(file,['       point',num2str(VI),' = ',num2str(Imaginary{UI}(VI,1)),', ',num2str(Imaginary{UI}(VI,2)),' \n']);
    end
    if void_val == 0
        fprintf(file,['   endi',' \n']);
    else
        fprintf(file,['   endd',' \n']);
    end
    if stereo_val == 1
        volfrac=volfrac+polyarea(Imaginary{UI}(:,1),Imaginary{UI}(:,2))*(Z(QI,1)-Z(QI-1,1))/(num+1);
    end
    for WI=1:Ivoid
        if length(Imagvoid{UI,WI}) > 3      %only prints out voids that exist
            if polyarea(Imagvoid{UI,WI}(:,1),Imagvoid{UI,WI}(:,2)) > (4*10^-12)
                if void_val == 0
```

```
                                    fprintf(file,['   delete prism',' \n']);
                                    fprintf(file,['       origin = 0, 0, ',num2str(UI*(Z(QI,1)-Z(QI-1,1))/(num+1)+Z(QI-1,1)),' \n']);
                                    fprintf(file,['       u1 = 1, 0, ',num2str(UI*(Z(QI,1)-Z(QI-1,1))/(num+1)+Z(QI-1,1)),' \n']);
                                    fprintf(file,['       v1 = 0, 1, ',num2str(UI*(Z(QI,1)-Z(QI-1,1))/(num+1)+Z(QI-1,1)),' \n']);
                                    fprintf(file,['       thickness = ',...
                                        num2str((Z(QI,1)-Z(QI-1,1))/(num+1)),' \n']);
                                    for YI=1:length(Imagvoid{UI,WI})
                                        fprintf(file,['       point',num2str(YI),' = ',num2str(Imagvoid{UI,WI}(YI,1)),', ',num2str(Imagvoid{UI,WI}(YI,2)),' \n']);
                                    end
                                    fprintf(file,['   endd',' \n']);
                                else
                                    if matrix_val == 1
                                        fprintf(file,['   insert prism',' \n']);
                                        fprintf(file,['       origin = 0, 0, ',num2str(UI*(Z(QI,1)-Z(QI-1,1))/(num+1)+Z(QI-1,1)),' \n']);
                                        fprintf(file,['       u1 = 1, 0, ',num2str(UI*(Z(QI,1)-Z(QI-1,1))/(num+1)+Z(QI-1,1)),' \n']);
                                        fprintf(file,['       v1 = 0, 1, ',num2str(UI*(Z(QI,1)-Z(QI-1,1))/(num+1)+Z(QI-1,1)),' \n']);
                                        fprintf(file,['       thickness = ',...
                                            num2str((Z(QI,1)-Z(QI-1,1))/(num+1)),' \n']);
                                        for YI=1:length(Imagvoid{UI,WI})
                                            fprintf(file,['       point',num2str(YI),' = ',num2str(Imagvoid{UI,WI}(YI,1)),', ',num2str(Imagvoid{UI,WI}(YI,2)),' \n']);
                                        end
                                        fprintf(file,['   endi',' \n']);
                                    end
                                end
                                if stereo_val == 1
                                    volfrac=volfrac-polyarea(Imagvoid{UI,WI}(:,1),Imagvoid{UI,WI}(:,2))*(Z(QI,1)-Z(QI-1,1))/(num+1);
                                end
                            end
                        end
                    end
                    if void_val == 0
                        fprintf(file,['endp',' \n']);
                    end
                    fprintf(file,'* \n');
                end
            end
        end
    end
end
clear Imagvoid
clear Imaginary
clear middle
%$$$$$$$$$$$$$$$$$$$$$$$$$$$$$$$$$$$$$$$$$$$$$$$$$$$$$$$$$$$$$$$$$$$$$$$$$$$
%print out results
if slices == 1
    area=(dim(1)*dim(2)*scale^2);
    for r=(PART(1)+1):PART(2)
        perimeter = 0;
        if void_val == 0
            fprintf(file,['package ''',Name,' particle3.',num2str(r),''' \n']);
            fprintf(file,['   material ',num2str(particles{r,3}+moffset),' \n']);
            fprintf(file,['   insert UDS',' \n']);
        else
            fprintf(file,['   delete UDS',' \n']);
        end
        for s=1:length(particles{r,2})
            fprintf(file,['       point',num2str(s),' = ',num2str(particles{r,2}(s,1)),', ',num2str(particles{r,2}(s,2)),' \n']);
            if stereo_val == 1
                if s > 1
                    perimeter=perimeter+sqrt(((particles{r,2}(s,1)-particles{r,2}(s-1,1))^2)+((particles{r,2}(s,2)-particles{r,2}(s-1,2))^2));
```

```
        end
        if s == length(particles{r,2})
            perimeter=perimeter+sqrt(((particles{r,2}(s,1)-particles{r,2}(1,1))^2)+((particles{r,2}(s,2)-particles{r,2}(1,2))^2));
        end
    end
end
if void_val == 0
    fprintf(file,['   endi',' \n']);
else
    fprintf(file,['   endd',' \n']);
end
if stereo_val == 1
    volfrac=volfrac+polyarea(particles{r,2}(:,1),particles{r,2}(:,2));
end
for t=1:length(V)
    if V(t) == r
        if void_val == 0
            fprintf(file,['*',' \n']);
            fprintf(file,['   delete UDS',' \n']);
            for u=1:length(voids{t,2})
                fprintf(file,['       point',num2str(u),' = ',num2str(voids{t,2}(u,1)),', ',num2str(voids{t,2}(u,2)),' \n']);
                if stereo_val == 1
                    if u > 1
                        perimeter=perimeter+sqrt(((voids{t,2}(u,1)-voids{t,2}(u-1,1))^2)+((voids{t,2}(u,2)-voids{t,2}(u-1,2))^2));
                    end
                    if u == length(voids{t,2})
                        perimeter=perimeter+sqrt(((voids{t,2}(u,1)-voids{t,2}(1,1))^2)+((voids{t,2}(u,2)-voids{t,2}(1,2))^2));
                    end
                end
            end
            fprintf(file,['   endd',' \n']);
            if stereo_val == 1
                volfrac=volfrac-polyarea(voids{t,2}(:,1),voids{t,2}(:,2));
            end
        else
            if matrix_val == 1
                fprintf(file,['*',' \n']);
                fprintf(file,['   insert UDS',' \n']);
                for u=1:length(voids{t,2})
                    fprintf(file,['       point',num2str(u),' = ',num2str(voids{t,2}(u,1)),', ',num2str(voids{t,2}(u,2)),' \n']);
                    if stereo_val == 1
                        if u > 1
                            perimeter=perimeter+sqrt(((voids{t,2}(u,1)-voids{t,2}(u-1,1))^2)+((voids{t,2}(u,2)-voids{t,2}(u-1,2))^2));
                        end
                        if u == length(voids{t,2})
                            perimeter=perimeter+sqrt(((voids{t,2}(u,1)-voids{t,2}(1,1))^2)+((voids{t,2}(u,2)-voids{t,2}(1,2))^2));
                        end
                    end
                end
                fprintf(file,['   endi',' \n']);
                if stereo_val == 1
                    volfrac=volfrac-polyarea(voids{t,2}(:,1),voids{t,2}(:,2));
                end
            end
        end
    end
end
if void_val == 0
    fprintf(file,['endp',' \n']);
end
fprintf(file,'* \n');
```

```
    if stereo_val == 1
        surfacearea=surfacearea+perimeter;
    end
end
%output 2D image
if plot_val == 1
    cla
    axis([0 dim(2)*scale -dim(1)*scale 0]);
    for xx=1:PART(2)
        hold on;
        if particles{xx,3} == 1
            fill(particles{xx,2}(:,1),particles{xx,2}(:,2),'b');
        elseif particles{xx,3} == 2
            fill(particles{xx,2}(:,1),particles{xx,2}(:,2),'g');
        elseif particles{xx,3} == 3
            fill(particles{xx,2}(:,1),particles{xx,2}(:,2),'y');
        elseif particles{xx,3} == 4
            fill(particles{xx,2}(:,1),particles{xx,2}(:,2),'m');
        elseif particles{xx,3} == 5
            fill(particles{xx,2}(:,1),particles{xx,2}(:,2),'c');
        elseif particles{xx,3} == 6
            fill(particles{xx,2}(:,1),particles{xx,2}(:,2),'r');
        elseif particles{xx,3} == 7
            fill(particles{xx,2}(:,1),particles{xx,2}(:,2),'k');
        elseif particles{xx,3} == 8
            fill(particles{xx,2}(:,1),particles{xx,2}(:,2),[0.8 0.8 0.8]);
        elseif particles{xx,3} == 9
            fill(particles{xx,2}(:,1),particles{xx,2}(:,2),[1 0.4 0.6]);
        elseif particles{xx,3} == 10
            fill(particles{xx,2}(:,1),particles{xx,2}(:,2),[0 1 0.5]);
        elseif particles{xx,3} == 11
            fill(particles{xx,2}(:,1),particles{xx,2}(:,2),[0 0.7 1]);
        elseif particles{xx,3} == 12
            fill(particles{xx,2}(:,1),particles{xx,2}(:,2),[0.7 1 0]);
        elseif particles{xx,3} == 13
            fill(particles{xx,2}(:,1),particles{xx,2}(:,2),[1 0.5 0]);
        elseif particles{xx,3} == 14
            fill(particles{xx,2}(:,1),particles{xx,2}(:,2),[1 1 0.5]);
        elseif particles{xx,3} == 15
            fill(particles{xx,2}(:,1),particles{xx,2}(:,2),[0.7 0.3 0.3]);
        elseif particles{xx,3} == 16
            fill(particles{xx,2}(:,1),particles{xx,2}(:,2),[0.2 0.5 0.3]);
        elseif particles{xx,3} == 17
            fill(particles{xx,2}(:,1),particles{xx,2}(:,2),[0.5 0.1 1]);
        elseif particles{xx,3} == 18
            fill(particles{xx,2}(:,1),particles{xx,2}(:,2),[0.2 0.4 0.6]);
        elseif particles{xx,3} == 19
            fill(particles{xx,2}(:,1),particles{xx,2}(:,2),[0.5 0.5 0.5]);
        elseif particles{xx,3} == 20
            fill(particles{xx,2}(:,1),particles{xx,2}(:,2),[1 0.7 0.3]);
        end
    end
    for yy=1:VOID(2)
        hold on;
        fill(voids{yy,2}(:,1),voids{yy,2}(:,2),'w');
    end
end
if stereo_val == 1
    volfrac=(volfrac/area)*100;
    stereo=[volfrac surfacearea/area];
else
```

```
        stereo=0;
    end
else
    cla
    volume=(dim(1)*dim(2)*scale^2)*(Z(slices+1));
    %print out results in 3D
    for K=1:slices
        for r=(PART(K)+1):PART(K+1)
            if void_val == 0
                fprintf(file,['package ''',Name,'particle',num2str(r),''' \n']);
                fprintf(file,['   material ',num2str(particles{r,3}+moffset),' \n']);
                fprintf(file,['   insert prism',' \n']);
            else
                fprintf(file,['   delete prism',' \n']);
            end
            fprintf(file,['       origin = 0, 0, ',num2str(Z(K,1)),' \n']);
            fprintf(file,['       u1 = 1, 0, ',num2str(Z(K,1)),' \n']);
            fprintf(file,['       v1 = 0, 1, ',num2str(Z(K,1)),' \n']);
            fprintf(file,['       thickness = ',num2str((Z(K+1,1)-Z(K,1))/(num+1)),' \n']);
            for s=1:length(particles{r,2})
                fprintf(file,['       point',num2str(s),' = ',num2str(particles{r,2}(s,1)),', ',num2str(particles{r,2}(s,2)),' \n']);
            end
            if void_val == 0
                fprintf(file,['   endi',' \n']);
            else
                fprintf(file,['   endd',' \n']);
            end
            if stereo_val == 1
                volfrac=volfrac+polyarea(particles{r,2}(:,1),particles{r,2}(:,2))*(Z(K+1,1)-Z(K,1))/(num+1);
            end
            for t=1:length(V)
                if V(t) == r
                    if void_Val == 0
                        fprintf(file,['   delete prism',' \n']);
                        fprintf(file,['       origin = 0, 0, ',num2str(Z(K,1)),' \n']);
                        fprintf(file,['       u1 = 1, 0, ',num2str(Z(K,1)),' \n']);
                        fprintf(file,['       v1 = 0, 1, ',num2str(Z(K,1)),' \n']);
                        fprintf(file,['       thickness = ',...
                            num2str((Z(K+1,1)-Z(K,1))/(num+1)),' \n']);
                        for u=1:length(voids{t,2})
                            fprintf(file,['       point',num2str(u),' = ',num2str(voids{t,2}(u,1)),', ',num2str(voids{t,2}(u,2)),' \n']);
                        end
                        fprintf(file,['   endd',' \n']);
                        if stereo_val == 1
                            volfrac=volfrac-polyarea(voids{t,2}(:,1),voids{t,2}(:,2))*(Z(K+1,1)-Z(K,1))/(num+1);
                        end
                    else
                        if matrix_val == 1
                            fprintf(file,['   insert prism',' \n']);
                            fprintf(file,['       origin = 0, 0, ',num2str(Z(K,1)),' \n']);
                            fprintf(file,['       u1 = 1, 0, ',num2str(Z(K,1)),' \n']);
                            fprintf(file,['       v1 = 0, 1, ',num2str(Z(K,1)),' \n']);
                            fprintf(file,['       thickness = ',...
                                num2str((Z(K+1,1)-Z(K,1))/(num+1)),' \n']);
                            for u=1:length(voids{t,2})
                                fprintf(file,['       point',num2str(u),' = ',num2str(voids{t,2}(u,1)),', ',num2str(voids{t,2}(u,2)),' \n']);
                            end
                            fprintf(file,['   endi',' \n']);
                            if stereo_val == 1
                                volfrac=volfrac-polyarea(voids{t,2}(:,1),voids{t,2}(:,2))*(Z(K+1,1)-Z(K,1))/(num+1);
                            end
```

```
                end
            end
        end
    end
    if void_val == 0
        fprintf(file,['endp',' \n']);
    end
    fprintf(file,'* \n');
end
if plot_val == 1
    axis([0 dim(2)*scale -dim(1)*scale 0 Z(1) Z(slices+1)]);
    for xx=(PART(K)+1):PART(K+1)
        hold on;
        zval=Z(K)*ones(length(particles{xx,2}(:,1)),1);
        if particles{xx,3} == 1
            fill3(particles{xx,2}(:,1),particles{xx,2}(:,2),zval,'b');
        elseif particles{xx,3} == 2
            fill3(particles{xx,2}(:,1),particles{xx,2}(:,2),zval,'g');
        elseif particles{xx,3} == 3
            fill3(particles{xx,2}(:,1),particles{xx,2}(:,2),zval,'y');
        elseif particles{xx,3} == 4
            fill3(particles{xx,2}(:,1),particles{xx,2}(:,2),zval,'m');
        elseif particles{xx,3} == 5
            fill3(particles{xx,2}(:,1),particles{xx,2}(:,2),zval,'c');
        elseif particles{xx,3} == 6
            fill3(particles{xx,2}(:,1),particles{xx,2}(:,2),zval,'r');
        elseif particles{xx,3} == 7
            fill3(particles{xx,2}(:,1),particles{xx,2}(:,2),zval,'k');
        elseif particles{xx,3} == 8
            fill3(particles{xx,2}(:,1),particles{xx,2}(:,2),zval,[0.8 0.8 0.8]);
        elseif particles{xx,3} == 9
            fill3(particles{xx,2}(:,1),particles{xx,2}(:,2),zval,[1 0.4 0.6]);
        elseif particles{xx,3} == 10
            fill3(particles{xx,2}(:,1),particles{xx,2}(:,2),zval,[0 1 0.5]);
        elseif particles{xx,3} == 11
            fill3(particles{xx,2}(:,1),particles{xx,2}(:,2),zval,[0 0.7 1]);
        elseif particles{xx,3} == 12
            fill3(particles{xx,2}(:,1),particles{xx,2}(:,2),zval,[0.7 1 0]);
        elseif particles{xx,3} == 13
            fill3(particles{xx,2}(:,1),particles{xx,2}(:,2),zval,[1 0.5 0]);
        elseif particles{xx,3} == 14
            fill3(particles{xx,2}(:,1),particles{xx,2}(:,2),zval,[1 1 0.5]);
        elseif particles{xx,3} == 15
            fill3(particles{xx,2}(:,1),particles{xx,2}(:,2),zval,[0.7 0.3 0.3]);
        elseif particles{xx,3} == 16
            fill3(particles{xx,2}(:,1),particles{xx,2}(:,2),zval,[0.2 0.5 0.3]);
        elseif particles{xx,3} == 17
            fill3(particles{xx,2}(:,1),particles{xx,2}(:,2),zval,[0.5 0.1 1]);
        elseif particles{xx,3} == 18
            fill3(particles{xx,2}(:,1),particles{xx,2}(:,2),zval,[0.2 0.4 0.6]);
        elseif particles{xx,3} == 19
            fill3(particles{xx,2}(:,1),particles{xx,2}(:,2),zval,[0.5 0.5 0.5]);
        elseif particles{xx,3} == 20
            fill3(particles{xx,2}(:,1),particles{xx,2}(:,2),zval,[1 0.7 0.3]);
        end
    end
    for yy=(VOID(K)+1):VOID(K+1)
        hold on;
        zvalv=Z(K)*ones(length(voids{yy,2}(:,1)),1);
        fill(voids{yy,2}(:,1),voids{yy,2}(:,2),zvalv,'w');
    end
```

```
        end
    end
    if stereo_Val == 1
        stereo=(volfrac/volume)*100;
    else
        stereo = 0;
    end
end

if matrix_val == 1
    if void_val == 0
        fprintf(file,['package ''',Matrix_String,''' \n']);
        fprintf(file,['   material ',num2str(Matrix_mat),' \n']);
        fprintf(file,['   insert Box',' \n']);
        if TwoD == 1
            fprintf(file,['       p1 = ',num2str(0),', ',num2str(-HH*scale*fatten),' \n']);
            fprintf(file,['       p2 = ',num2str(WW*scale*fatten),', ',num2str(0),' \n']);
        else
            fprintf(file,['       p1 = ',num2str(0),', ',num2str(-HH*scale*fatten),', ',num2str(0),' \n']);
            fprintf(file,['       p2 = ',num2str(WW*scale*fatten),', ',num2str(0),', ',num2str(Z(end)),' \n']);
        end
        fprintf(file,['   endi',' \n']);
        fprintf(file,['endp',' \n']);
    else
        fprintf(file,['endp',' \n']);
    end
end
toc
```

APPENDIX C

COMPUTATIONAL PROCESSING MATLAB CODE

The MATLAB script to determine the location of the shock front, shock peak, and steady state pressure is presented here. The code takes in an ASCII file generated by CTH containing the cell center values at each output time. The code develops a matrix with these values with the rows corresponding to the y direction and the columns corresponding to the x direction. The maximum, minimum, and average pressure values at each x (column) location are then calculated. The shock front is then determined by identifying the point in the rise of the average pressure closest to 0.1 GPa. For identification of the shock peak, all the local maximums in average pressure response are identified based on changes in the slope. These local maximums are then compared to each other to determine the shock peak. Finally, the impact face is found by determining the location at which the average volume fraction of the driver is above 60%. To determine the steady state pressure, the code takes the middle 70% of the pressure values between the impact face and shock peak. With the steady state pressure found, the points in the shock rise corresponding to 25, 50, and 75% of this value are identified. These points are then tracked and stored at each time interval to generate three measures of the shock velocity. All of this data, along with the steady state pressure and density, values are output into an Excel file for easy viewing. The basic processing of this code was also used to generate the pressure traces and profiles seen in Chapter 4.

```
%%Paul Specht
%%HSR LAB 2009
%%This code is designed to generate all the post processing data
%%manipulation from CTH. It will tabulate the shock speed

function iters=Shock
tic
%Obtain the details of the shot to be used in the calucluations
```

```
tag=input('Enter the File Tag:                          ','s');
tspan=input('Enter the Time Span Between Outputs [ns]:    ');
trange=input('Enter Time Range in ns:[Start stop]        ');
tag2=input('Enter the Output File Name:                  ','s');
%%%%%%%%%%%%%%%%%%%%%%%%%%%%%%%%%%%%%%
%determine the number of output files
Names=dir([tag,'*']);
x=trange(1)/tspan:trange(2)/tspan;
iters=length(x);
%set up variables for speed
Driverloc=zeros(1,iters);
Frontloc=zeros(1,iters);
Centerloc=zeros(1,iters);
VFront=zeros(1,iters-1);
VDriver=zeros(1,iters-1);
VCenter=zeros(1,iters-1);
VPpeak=zeros(1,iters-1);
VPSS10=zeros(1,iters-1);
VPSS50=zeros(1,iters-1);
VPSS90=zeros(1,iters-1);
PSS=zeros(1,iters-1);
PSTD=zeros(1,iters-1);
DSS=zeros(1,iters-1);
DSTD=zeros(1,iters-1);
PSS10loc=zeros(1,iters-1);
PSS50loc=zeros(1,iters-1);
PSS90loc=zeros(1,iters-1);
counter=0;
%go through each output file individually
for h=1:iters
    %open the file and read the data
    fid=fopen(Names(x(h),1).name);
    data=textscan(fid,'%f %f %f %f %f %f','headerlines',1);
    %save the data from a cell array into a matrix
    DATA(:,1)=data{1,1}*10^4;    %X in microns
    DATA(:,2)=data{1,2}*10^4;    %Y microns
    DATA(:,3)=data{1,3}*10^-10;  %Pressure GPa
    DATA(:,4)=data{1,4}*11605;   %Temperature in K
    DATA(:,5)=data{1,5};         %Density g/cc
    DATA(:,6)=data{1,6};         %Driver Volume fraction
    %sort the data by x then y
    DATA=sortrows(DATA,[2 1]);
    %find all locations of inital x value
    reset=DATA(:,1)==DATA(1,1);
    %divide the total number of x points by the number of times the
    %starting x appears to get how many points till the value repeats
    shift=length(DATA(:,1))/sum(reset);
    %Same thing in the Y
    reset2=DATA(:,2)==DATA(1,2);
    shift2=length(DATA(:,2))/sum(reset2);
    %preset variables for speed
    P=zeros(shift2,shift);
    VOLM=zeros(shift2,shift);
    DENS=zeros(shift2,shift);
    Y=DATA(1:shift,1);
    %generate a grid of pressure and driver volume fraction data
    for k=1:shift2
        P(k,:)= DATA((k-1)*shift+1:k*shift,3);
        VOLM(k,:)= DATA((k-1)*shift+1:k*shift,6);
        DENS(k,:)= DATA((k-1)*shift+1:k*shift,5);
    end
    %%%%%%%%%%%%%%%%%%%%%%%%%%%%%%%%%%%%%%
    %get the average over each y value
    Pave=mean(P);
    VOLMave=mean(VOLM);
    DENSave=mean(DENS);
    %look for the driver front in the material
    driver=0;
```

```
while driver == 0
    counter=counter+1;
    %finds point at which the cross section is mostly the driver
    if VOLMave(counter) < 0.6
        Driverloc(h)=Y(counter-1);
        driver=1;
    end
end
%find the shock front in the material only consider from driver on
Pfront=abs(Pave(counter:length(Pave))-0.1); %front is when hit 0.1 GPa
[val ind]=min(Pfront);
%reset indices to match since only searched over a section of Y
ind=ind+counter;
%save the position of the front
Frontloc(h)=Y(ind);
%obtain location of center point
Centerloc(h)=(Frontloc(h)-Driverloc(h))/2;
%%%%%%%%%%%%%%%%%%%%%%%%%%%%%%%%%%%%%%%%%%%%%%%%%%%%%%%%%%%%%%%%%%%%%%%%%%%%
%obtain the steady state pressure
%first get the difference between points
Pdiff=Pave;
for n=1:length(Pdiff)-1
    Pdiff(n)=Pdiff(n+1)-Pdiff(n);
end
%set the last value to zero so same length for plotting mainly
Pdiff(length(Pdiff))=0;
%get the sign of the difference term at front of shock
S=sign(Pdiff(ind));
%counter for peaks
index=1;
%go through range between front and driver face and get every peak and
%trough in the pressure signal by using the sign change in the difference
Ppeakloc=0;
Ppeaks=0;
for r=ind:-1:counter
    if sign(Pdiff(r)) ~= S
        %when sign change find point closest to zero and save the
        %pressure and location.  Then reset to look for oposite sign
        if abs(Pdiff(r)) > abs(Pdiff(r+1))
            Ppeakloc(index)=r+1;
            Ppeaks(index)=Pave(r+1);
            S=sign(Pdiff(r));
        else
            Ppeakloc(index)=r;
            Ppeaks(index)=Pave(r);
            S=sign(Pdiff(r));
        end
        index=index+1;
    end
    %Save the pressure at driver face.  For early times when rise might
    %not be complete
    if r == counter
        Ppeakloc(index)=r;
        Ppeaks(index)=Pave(r);
    end
end
%set up parameters for the while loop
top=0;
index2=0;
Ppeaksmax=max(Ppeaks);
if length(Ppeaks) > 2
    while top == 0
        index2=index2+1;
        %check every peak and want a peak that is greater than the previous
        %but smaller then the next, but also close to the maximum pressure
        %Makes sure it is a peak
        if Ppeaks(index2) > Ppeaks(index2+1)
            %makes sure it is significantly larger than the previous peak
```

```
                if Ppeaks(index2) > 0.9*Ppeaks(index2+2)
                    %makes sure close to max pressure so not early in rise
                     %if Ppeaks(index2) > 0.7*Ppeaksmax
                        %makes sure the max is no the next peak
                     %    if Ppeaks(index2+2) ~= Ppeaksmax
                             ploc=Ppeakloc(index2);
                             Ptop(h)=Y(ploc);
                             top=1;
                      %   end
                    % end
                end
            end
            %if have not found yet it save the point at the driver
            if index2 == length(Ppeaks)-2
                ploc=Ppeakloc(index2+2);
                Ptop(h)=Y(ploc);
                top=1;
            end
        end
    else
        ploc=Ppeakloc(1);
        Ptop=Y(ploc);
    end
    Shockregion=ploc-counter;
    PSS(h)=mean(mean(P(1:shift2,counter+round(0.15*Shockregion):counter+round(0.85*Shockregion)),2));
    DSS(h)=mean(mean(DENS(1:shift2,counter+...
           round(0.15*Shockregion):counter+round(0.85*Shockregion)),2));
    PSTD(h)=std(mean(P(1:shift2,counter+round(0.15*Shockregion):counter+round(0.85*Shockregion)),2));
    DSTD(h)=std(mean(DENS(1:shift2,counter+...
           round(0.15*Shockregion):counter+round(0.85*Shockregion)),2));
    %get point at 25% of P steady state
    PSS10=abs(Pave(ploc:ind)-0.25*PSS(h));
    [val2 ind2]=min(PSS10);
    PSS10loc(h)=Y(ind2+ploc);
    %get point at 50% of P steady state
    PSS50=abs(Pave(ploc:ind)-0.5*PSS(h));
    [val3 ind3]=min(PSS50);
    PSS50loc(h)=Y(ind3+ploc);
    %get point at 75% of P steady state
    PSS90=abs(Pave(ploc:ind)-0.75*PSS(h));
    [val4 ind4]=min(PSS90);
    PSS90loc(h)=Y(ind4+ploc);
    %%%%%%%%%%%%%%%%%%%%%%%%%%%%%%%%%%%%%%%%%%%%%%%%%%%%
    %Need to generate plots and then save them
    scrnsize=get(0,'ScreenSize');
    figure1=figure('IntegerHandle','off','color',[1 1 1],'Visible','off','Position',...
        [scrnsize(1)+0.02*scrnsize(3) scrnsize(2)+0.03*scrnsize(4) .95*scrnsize(3) 0.9*scrnsize(4)]);
    axes1 = axes('Parent',figure1,'FontSize',18);
    plot(Y,Pave,'b',Y,VOLMave,'y','LineWidth',2,'Parent',axes1);
    hold on
    plot([Ptop(h) Ptop(h)],[0 1.1*max(Pave)],'k--','LineWidth',2,'Parent',axes1);
    plot([Driverloc(h) Driverloc(h)],[0 1.1*max(Pave)],'k--','LineWidth',2,'Parent',axes1);
    plot([Frontloc(h) Frontloc(h)],[0 1.1*max(Pave)],'k--','LineWidth',2,'Parent',axes1);
    plot([0 Y(length(Y))],[PSS(h) PSS(h)],'b:','LineWidth',2,'Parent',axes1);
    axis([0 Y(length(Y)) 0 1.1*max(Pave)]);
    xlabel('Distance ({\mu}m)','FontSize',18);
    ylabel('Pressure (GPa)','FontSize',18');
    label1=['Data_',num2str(h*tspan),'.jpg'];
    set(gcf,'PaperPositionMode','auto');
    print(figure1,'-djpeg',label1);
    close
end
%%%%%%%%%%%%%%%%%%%%%%%%%%%%%%%%
%get velocities and statistical data
for m=2:iters
    VFront(m-1)=((Frontloc(m)-Frontloc(m-1))/tspan)*1000;
    VDriver(m-1)=((Driverloc(m)-Driverloc(m-1))/tspan)*1000;
    VCenter(m-1)=((Centerloc(m)-Centerloc(m-1))/tspan)*1000;
```

```
    VPpeak(m-1)=((Ptop(m)-Ptop(m-1))/tspan)*1000;
    VPSS10(m-1)=((PSS10loc(m)-PSS10loc(m-1))/tspan)*1000;
    VPSS50(m-1)=((PSS50loc(m)-PSS50loc(m-1))/tspan)*1000;
    VPSS90(m-1)=((PSS90loc(m)-PSS90loc(m-1))/tspan)*1000;
end
VFrontave=mean(VFront);
VFrontstd=std(VFront);
VDriverave=mean(VDriver);
VDriverstd=std(VDriver);
VCenterave=mean(VCenter);
VCenterstd=std(VCenter);
VPpeakave=mean(VPpeak);
VPpeakstd=std(VPpeak);
VPSS10ave=mean(VPSS10);
VPSS10std=std(VPSS10);
VPSS50ave=mean(VPSS50);
VPSS50std=std(VPSS50);
VPSS90ave=mean(VPSS90);
VPSS90std=std(VPSS90);
%%%%%%%%%%%%%%%%%%%%%%%%%%%%%%%%%%%%%%%%%%%%
%Write the data out to an excel file
Velocities=cell(19,iters+4);
Velocities(1,1:19)={'Time (s)', 'Driver Y (um)','Center Point Y (um)','Pressure Peak Y (um)',...
    '75% SS Pressure Y (um)','50% SS Pressure Y (um)','25% SS Pressure Y (um)',...
    'Shock Front Y (um)','Driver V (m/s)','Center Point V (m/s)','Pressure Peak V (m/s)',...
    '75% SS Pressure V (m/s)','50% SS Pressure V (m/s)','25% SS Pressure V (m/s)',...
    'Shock Front V (m/s)','Density SS (g/cc)','Density SS std','Pressure SS (GPA)',...
    'Pressure SS std',};
for n=1:iters
    if n == 1
        Velocities(n+1,1:19)={tspan*x(n),Driverloc(n),Centerloc(n),Ptop(n),PSS90loc(n),PSS50loc(n),...
            PSS10loc(n),Frontloc(n),'','','','','','','',DSS(n),DSTD(n),PSS(n),PSTD(n)};
    else
        Velocities(n+1,1:19)={tspan*x(n),Driverloc(n),Centerloc(n),Ptop(n),PSS90loc(n),PSS50loc(n),...
            PSS10loc(n),Frontloc(n),VDriver(n-1),VCenter(n-1),VPpeak(n-1),VPSS90(n-1),...
            VPSS50(n-1),VPSS10(n-1),VFront(n-1),DSS(n),DSTD(n),PSS(n),PSTD(n)};

    end
end
Velocities(iters+2,1:19)={'','','','','','','','','','','','','','','','','','','',''};
Velocities(iters+3,1:19)={'','','','','','','','AVERAGE',VDriverave,VCenterave,...
    VPpeakave,VPSS90ave,VPSS50ave,VPSS10ave,VFrontave,'','','',''};
Velocities(iters+4,1:19)={'','','','','','','','AVERAGE',VDriverstd,VCenterstd,...
    VPpeakstd,VPSS90std,VPSS50std,VPSS10std,VFrontstd,'','','',''};
xlswrite(tag2,Velocities, 'Velocities')
toc
```

APPENDIX D

IMPEDANCE MATCHING MATLAB CODE

The impedance matching calculations and corresponding error were found with the following routine. The code presented is nearly identical to that used by Frendenburg [54]. The only differences stem from the hard coding of the Cu EOS fit and the use of U_P as the input parameter.

```
%Paul Specht
%Georgia Tech HSR lab
%1/19/2012

% This program is designed to obtain the Us-Up fit to copper up to 1000 m/s
% bashed on the LANL data.  It will compute the best fit along with the 95%
% confidence intervals for each parameter.  It will then determine the error
% in the fit at a give particle velocity.

function UsUN=ImpedanceMatch
close all
clear
clc
%% Experiment Parameters
vi=1.0579;      %impact velocity in km/s
UpM=0.6447;     %measured Particle Velocity in km/s
rho=5.3;     %measured density of the sample in g/cc

%--Enter driver and flier properties
po=8.924;    %driver and Flier density in g/cc
go=1.99;        %Gruniesen Parameter for Driver and Flier
%---------------------------------
%% Copper Us-Up Fit
%--The Copper data in km/s---
Up=[0 0.21 0.211 0.223 0.281 0.282 0.286 0.289 0.301 0.302 ...
    0.312 0.395 0.398 0.406 0.407 0.409 0.413 0.434 0.439 ...
    0.483 0.483 0.484 0.488 0.490 0.522 0.522 0.531 0.535 ...
    0.538 0.549 0.562 0.576 0.609 0.610 0.618 0.618 0.620 ...
    0.624 0.637 0.662 0.679 0.680 0.689 0.709 0.728 0.732 ...
    0.737 0.744 0.749 0.757 0.786 0.787 0.788 0.800 0.807 ...
    0.816 0.816 0.832 0.832 0.832 0.846 0.864 0.865 0.868 ...
    0.870 0.940 0.942 0.945 0.952 0.979 0.980 0.995 1.008];

Us=[3.927 4.314 4.215 4.217 4.341 4.352 4.321 4.350 4.378 4.303...
    4.316 4.512 4.501 4.477 4.532 4.494 4.566 4.471 4.501 4.599 4.594 ...
    4.717 4.713 4.687 4.712 4.732 4.802 4.746 4.704 4.711 4.769 4.713 ...
    4.801 4.792 4.807 4.798 4.765 4.886 4.910 4.854 5.011 4.995 5.009 ...
    4.955 5.039 4.909 5.067 4.888 5.061 4.939 5.067 5.077 5.066 5.195 ...
    5.180 5.055 5.055 5.239 5.238 5.222 5.185 5.223 5.215 5.154 5.318 ...
    5.326 5.329 5.332 5.362 5.473 5.471 5.442 5.442];
%-------------------------------------------------

%---Set up the variable to determine the best fit
n=length(Up);              %number of data points
K1=sum(Up.^2);
K2=sum(Up);
```

```
%-----------------------------------------------

%---Determine the Best fit parameters from Beers
Co=(K1*sum(Us)-K2*sum(Us.*Up))/(n*K1-K2^2);
S=(n*sum(Up.*Us)-K2*sum(Us))/(n*K1-K2^2);
%-----------------------------------

%--Compute the error of the fit Parameters-------------
Usave=Co+S.*Up;                                 %Shock velocity as determined by best fit
sigUs=sqrt(sum((Us-Usave).^2)/(n-1));           %standard deviation of fit to experimental data
sigCo=sigUs*sqrt((n*K1)/((n-1)*(n*K1-K2^2)));   %standard deviation of Co
sigS=sigUs*sqrt((n^2)/((n-1)*(n*K1-K2^2)));     %standard deviation of S
%-------------------------------------------------------

%---determine the error of the fit at a give Up--------
points=1000;
up=linspace(0,1,points);
sigF=sigUs*sqrt((n*(K1-2.*up.*K2+n.*(up.^2)))./((n-1).*(n.*K1-K2^2)));
%-------------------------------------------------------

%--fit error to a polynomial----------------------------
coef=polyfit(up,2*sigF,5);
%-------------------------------------------------------

%--Print out desired results
fprintf('The Sound Speed Co is:  %f pm %f \n',[Co 2*sigCo]);
fprintf('The Material Parameter S is:  %f pm %f \n',[S 2*sigS]);
%-------------------------------
%% Driver and Flier Interface
%---Set up the error for each Hugoniot based on the Us-Up fit
EF=coef(1)*(up.^5)+coef(2)*(up.^4)+...
    coef(3)*(up.^3)+coef(4)*(up.^2)+...
    coef(5)*up+coef(6);      %Polynomial fit to Fit error
%-------------------------------------------------------

%---Determine the Driver Hugoniot and uncertainty----------------
PHD=po.*(Co+S.*up).*up;
PHDun1=po.*(Co+EF+S.*up).*up;
PHDun2=po.*(Co-EF+S.*up).*up;
%---------------------------------------

%---Determine the Flier Hugoniot and Uncertainty-------------
PHF=po.*(Co+S.*(vi-up)).*(vi-up);
PHFun1=po.*(Co+EF+S.*(vi-up)).*(vi-up);
PHFun2=po.*(Co-EF+S.*(vi-up)).*(vi-up);
%-----------------------------------------

%--Determine intersection of Hugoniots
UpDF=vi/2;
PDF=po*(Co+S*UpDF)*UpDF;
VDF=(1/po)-(UpDF^2)/PDF;
%----------------------------------

%---Determine Uncertainty in the Driver-Flier Particle Velocity
%-Upper Bound
ef=coef(1)*(UpDF^5)+coef(2)*(UpDF^4)+...
    coef(3)*(UpDF^3)+coef(4)*(UpDF^2)+...
    coef(5)*UpDF+coef(6);
UpDFUIntU=@(x) po.*(Co+ef+S.*(vi-x)).*(vi-x)-po.*(Co-ef+S.*x).*x;
UpDFU=fsolve(UpDFUIntU,vi/2);
PDFU=po*(Co+S*UpDFU)*UpDFU;
VDFU=(1/po)-(UpDFU^2)/PDFU;
%-Lower Bound
UpDFUIntL=@(x) po.*(Co-ef+S.*(vi-x)).*(vi-x)-po.*(Co+ef+S.*x).*x;
UpDFL=fsolve(UpDFUIntL,vi/2);
PDFL=po*(Co+S*UpDFL)*UpDFL;
VDFL=(1/po)-(UpDFL^2)/PDFL;
%-----------------------------------
```

```
%---print out the results
fprintf('The Driver/Flier Particle Velocity is:  %f \n',UpDF)
fprintf('The Driver/Flier Pressure is:  %f pm %f \n',[PDF mean([abs(PDFU-PDF) abs(PDFL-PDF)])]);
fprintf('The Driver/Flier Volume is:  %f pm %f \n',[VDF mean([abs(VDFU-VDF) abs(VDFL-VDF)])]);
fprintf('The fit to the error is \n');
fprintf('A5:  %f \n',coef(1));
fprintf('A4:  %f \n',coef(2));
fprintf('A3:  %f \n',coef(3));
fprintf('A2:  %f \n',coef(4));
fprintf('A1:  %f \n',coef(5));
fprintf('A0:  %f \n',coef(6));
%-----------------------

%--Determine reflected Hugoniot of driver
% UpRH=linspace(0,vi-UpDF,1000);
% V2=(1/po)*(Co+(S-1)*(vi-UpRH))./(Co+S*(vi-UpRH));
% V1=(1/po)*(Co+(S-1)*(vi-UpDF))./(Co+S*(vi-UpDF));
% Ph=po*(Co+S*(vi-UpRH)).*(vi-UpRH);
% PRH=(Ph-go*((Ph-PDF).*((1/po)-V2)*0.5))./(1-go*(V1-V2)*0.5);
%-------------------------------
%% Isentrope Calculation

%--Define Parameters for developing the Driver Hugoniot in P-V space
vpoints=1000;
Vo=1/po;

%---Solve for the Isentrope in P-V space
VSspan=linspace(VDF,1.1*Vo,vpoints);
[VS PS]=ode45(@(vs,ps) Isentfunct(vs,ps,Co,S,Vo,go),VSspan,PDF);
%---------------------------------------

%---Fit the P-V Isentrope to a polynomial
PScoef=polyfit(VS,PS,5);
PSfit=PScoef(1)*(VSspan.^5)+PScoef(2)*(VSspan.^4)+PScoef(3)*(VSspan.^3)+...
    PScoef(4)*(VSspan.^2)+PScoef(5)*(VSspan)+PScoef(6);
%----------------------------------------


%---Solve for the Isentrope Uncertainty
%-Upper Bound
VSspanU=linspace(VDFU,1.1*Vo,vpoints);
[VSU PSU]=ode45(@(vsu,psu) Isentfunct(vsu,psu,Co+ef,S,Vo,go),VSspanU,PDFU);
%-Lower Bound
VSspanL=linspace(VDFL,1.1*Vo,vpoints);
[VSL PSL]=ode45(@(vsl,psl) Isentfunct(vsl,psl,Co-ef,S,Vo,go),VSspanL,PDFL);
%---------------------------------------

%---Fit the P-V Isentrope Uncertainties to a polynomial
%-Upper Bound
PSUcoef=polyfit(VSU,PSU,5);
PSUfit=PSUcoef(1)*(VSspanU.^5)+PSUcoef(2)*(VSspanU.^4)+PSUcoef(3)*(VSspanU.^3)+...
    PSUcoef(4)*(VSspanU.^2)+PSUcoef(5)*(VSspanU)+PSUcoef(6);
%-Lower Bound
PSLcoef=polyfit(VSL,PSL,5);
PSLfit=PSLcoef(1)*(VSspanL.^5)+PSLcoef(2)*(VSspanL.^4)+PSLcoef(3)*(VSspanL.^3)+...
    PSLcoef(4)*(VSspanL.^2)+PSLcoef(5)*(VSspanL)+PSLcoef(6);
%----------------------------------------

%--Obtain the P-Up Isentrope
VPScoef=polyfit(PS,VS,5);            %fit the Isentrope in V-P space
dPSdVfunct=@(x) sqrt(-1*(5*VPScoef(1)*(x.^4)+4*VPScoef(2)*(x.^3)+3*VPScoef(3)*(x.^2)+...
    2*VPScoef(4)*(x)+VPScoef(5)));
PSUpint=linspace(PDF,0,1000);
UpS=zeros(1,length(PSUpint));
for m=1:length(PSUpint)
    UpS(m)=quad(dPSdVfunct,PSUpint(m),PDF)+UpDF;
end
```

```
PSUpcoef=polyfit(UpS,PSUpint,5);
PSUpfit=PSUpcoef(1)*(UpS.^5)+PSUpcoef(2)*(UpS.^4)+PSUpcoef(3)*(UpS.^3)+...
    PSUpcoef(4)*(UpS.^2)+PSUpcoef(5)*(UpS)+PSUpcoef(6);
%----------------------------------------

%---Obtain the Undertanty in P-Up Isentrope
%-Upper Bound
VPSUcoef=polyfit(PSU,VSU,5);            %fit the Isentrope in V-P space
dPSUdVfunct=@(x) sqrt(-1*(5*VPSUcoef(1)*(x.^4)+4*VPSUcoef(2)*(x.^3)+3*VPSUcoef(3)*(x.^2)+...
    2*VPSUcoef(4)*(x)+VPSUcoef(5)));
PSUpUint=linspace(PDFU,0,1000);
UpSU=zeros(1,length(PSUpUint));
for m=1:length(PSUpUint)
    UpSU(m)=quad(dPSUdVfunct,PSUpUint(m),PDFU)+UpDFU;
end
PSUpUcoef=polyfit(UpSU,PSUpUint,5);
PSUpUfit=PSUpUcoef(1)*(UpSU.^5)+PSUpUcoef(2)*(UpSU.^4)+PSUpUcoef(3)*(UpSU.^3)+...
    PSUpUcoef(4)*(UpSU.^2)+PSUpUcoef(5)*(UpSU)+PSUpUcoef(6);
%-Lower Bound
VPSLcoef=polyfit(PSL,VSL,5);            %fit the Isentrope in V-P space
dPSLdVfunct=@(x) sqrt(-1*(5*VPSLcoef(1)*(x.^4)+4*VPSLcoef(2)*(x.^3)+3*VPSLcoef(3)*(x.^2)+...
    2*VPSLcoef(4)*(x)+VPSLcoef(5)));
PSUpLint=linspace(PDFL,0,1000);
UpSL=zeros(1,length(PSUpLint));
for m=1:length(PSUpLint)
    UpSL(m)=quad(dPSLdVfunct,PSUpLint(m),PDFL)+UpDFL;
end
PSUpLcoef=polyfit(UpSL,PSUpLint,5);
PSUpLfit=PSUpLcoef(1)*(UpSL.^5)+PSUpLcoef(2)*(UpSL.^4)+PSUpLcoef(3)*(UpSL.^3)+...
    PSUpLcoef(4)*(UpSL.^2)+PSUpLcoef(5)*(UpSL)+PSUpLcoef(6);
%----------------------------------------

%% Finding Uncertainty in Us Value
PM=PSUpcoef(1)*(UpM.^5)+PSUpcoef(2)*(UpM.^4)+PSUpcoef(3)*(UpM.^3)+...
    PSUpcoef(4)*(UpM.^2)+PSUpcoef(5)*(UpM)+PSUpcoef(6);
PMU=PSUpUcoef(1)*(UpM.^5)+PSUpUcoef(2)*(UpM.^4)+PSUpUcoef(3)*(UpM.^3)+...
    PSUpUcoef(4)*(UpM.^2)+PSUpUcoef(5)*(UpM)+PSUpUcoef(6);
PML=PSUpLcoef(1)*(UpM.^5)+PSUpLcoef(2)*(UpM.^4)+PSUpLcoef(3)*(UpM.^3)+...
    PSUpLcoef(4)*(UpM.^2)+PSUpLcoef(5)*(UpM)+PSUpLcoef(6);
UsM=PM/(rho*UpM);
UsMU=PMU/(rho*UpM);
UsML=PML/(rho*UpM);
UsUN=mean([abs(UsMU-UsM) abs(UsM-UsML)]);
VM=(1/rho)*((UsM-UpM)/UsM);
VMU=(1/rho)*((UsMU-UpM)/UsMU);
VML=(1/rho)*((UsML-UpM)/UsML);
RVM=((UsM-UpM)/UsM);
RVMU=((UsMU-UpM)/UsMU);
RVML=((UsML-UpM)/UsML);
%---Print out the Results
fprintf('The Specific Volume is: %f pm %f \n',[VM,mean([abs(VMU-VM) abs(VML-VM)])]);
fprintf('The Relative Volume is: %f pm %f \n',[RVM,mean([abs(RVMU-RVM) abs(RVML-RVM)])]);
fprintf('The Pressure is: %f pm %f \n',[PM mean([abs(PMU-PM) abs(PML-PM)])]);
fprintf('The Shock Velocity is: %f pm %f \n',[UsM UsUN])
%-------------------------

%% ODE Functions
%--Define Isentrope
function dPSdV = Isentfunct(VS,PS,Co,S,Vo,Go)
    PH=((Co.^2).*(Vo-VS))./((Vo-S.*(Vo-VS)).^2);
    dPHdV=-((Co.^2)*(Vo+S.*(Vo-VS)))./((Vo-S.*(Vo-VS)).^3);
    G=Go/Vo;
    dPSdV=0.5*G*PH+dPHdV*(1-0.5*G*(Vo-VS))-G*PS;
end
end
```

REFERENCES

[1] D. Eakins and N. Thadhani, "Shock-induced reaction in a flake nickel + spherical aluminum powder mixture," *Journal of Applied Physics*, vol. 100, no. 113521, 2006.

[2] E. Dunbar, N. Thadhani, and R. Graham, "High-pressure shock activation and mixing of nickel-aluminium powder mixtures," *Journal of Materials Science*, vol. 28, pp. 2903–2914, 1993.

[3] K. Vandersall and N. Thadhani, "Time-resolved measurements of the shock-compression response of Mo+2Si elemental powder mixtures," *Journal of Applied Physics*, vol. 94, no. 3, pp. 1575–1583, 2003.

[4] X. Xu and N. Thadhani, "Investigation of shock-induced reaction behavior of as-blended and ball-milled Ni+Ti powder mixtures using time-resolved stress measurements," *Journal of Applied Physics*, vol. 92, no. 4, pp. 2000–2009, 2004.

[5] A. Advani and N. Thadhani, "Shock-induced reaction synthesis of isomorphous (Cu-Ni) and immiscible (Cu-Nb) compounds," *Metallurgical and Materials Transactions A*, vol. 30, no. 5, pp. 1367 – 1379, 1999.

[6] K. Vecchio, L. Yu, and M. Meyers, "Shock synthesis of silicides - I. Experimentation and microstructural evolution," *Acta Metallurgica et Materialia*, vol. 42, no. 3, pp. 701–714, 1994.

[7] R. Austin, D. McDowell, and D. Benson, "Numerical simulation of shock wave propagation in spatially-resolved particle systems," *Modeling and Simulation in Materials Science and Engineering*, vol. 14, pp. 537–561, 2006.

[8] R. Ames, "Energy release characteristics of impact-initiated energetic materials," in *Multifunctional Energetic Materials* (N. Thadhani, R. Armstrong, A. Gash, and W. Wilson, eds.), pp. 123–132, Materials Research Society, 2006.

[9] I. Song and N. Thadhani, "Shock-induced chemical reactions and synthesis of nickel aluminides," *Metallurgical Transactions A*, vol. 23, pp. 41 – 48, 1992.

[10] D. Eakins and N. Thadhani, "Discrete particle simulation of shock wave propagation in a binary Ni+Al powder mixture," *Journal of Applied Physics*, vol. 101, no. 043508, 2007.

[11] D. Eakins and N. Thadhani, "Mesoscale simulation of the configuration-dependent shock-compression response of Ni+Al powder mixtures," *Acta Materialia*, vol. 56, pp. 1496–1510, 2008.

[12] S. Batsanov, G. Doronin, S. Klochkov, and A. Teut, "Synthesis reactions behind shock fronts," *Fizika Goreniya i Vzryva (Combustion, Explosion, and Shock Waves)*, vol. 22, no. 6, pp. 134–137, 1986.

[13] S. Batsanov, "Synthesis and modification of materials by shock waves: real-time measurements and mechanisms of reaction," *Materials Science and Engineering A*, vol. 210, pp. 57–63, 1996.

[14] N. Thadhani, R. Graham, T. Royal, E. Dunbar, M. Anderson, and G. Holman, "Shock-induced chemical reactions in titianium-silicon powder mixtures of different morphologies: time-resolved pressure measurements and materials analysis," *Journal of Applied Physics*, vol. 82, no. 3, pp. 1113–1128, 1997.

[15] H. Chen, J. LaSalvia, V. Nesterenko, and M. Meyers, "Shear localization and chemical reaction in high-strain, high-strain-rate deformation of Ti-Si powder mixtures," *Acta Materialia*, vol. 46, no. 9, pp. 3033–3046, 1998.

[16] H. Chen, V. Nesterenko, and M. Meyers, "Shear localization and chemical reaction in Ti-Si and Nb-Si powder mixtures: thermochemical analysis," *Journal of Applied Physics*, vol. 84, no. 6, pp. 3098–3106, 1998.

[17] M. Meyers, S. Batsanov, S. Gavrilkin, H. Chen, J. LaSalvia, and F. Marquis, "Effect of shock pressure and plastic strain on chemical reactions in Nb-Si and Mo-Si systems," *Materials Science and Engineering A*, vol. 201, pp. 150–158, 1995.

[18] T. Aizawa, "Shock-induced reaction of molybdenum silicide from pretreated powders by mechanical alloying," *Journal of Materials Processing Technology*, vol. 85, pp. 87–90, 1999.

[19] A. Merzhanov and F. Dubovitsky, "Quasi-stationary thermal regime of explosive reaction processes," *Doklady Akademii Nauk SSSR*, vol. 120, pp. 1068–1071, 1958.

[20] K. Blobaum, D. Van Heerden, A. Gavens, and T. Weihs, "Al/Ni formation reactions: characterization of the metastable Al_9Ni_2 phase and analysis of its formation," *Acta Materialia*, vol. 51, pp. 3871–3884, 2003.

[21] T. Aizawa, S. Kamenosono, J. Kihara, T. Kato, K. Tanaka, and Y. Nakayama, "Shock reactive synthesis of TiAl," *Intermetallics*, vol. 3, pp. 369–379, 1995.

[22] Z. Munir and U. Anselmi-Tamburini, "Self-propagating exothermic reactions: the synthesis of high-temperature materials by combustion," *Material Science Reports*, vol. 3, pp. 277–365, 1989.

[23] T. Barbee, W. Troy, and T. Weihs, "Ignitable heterogeneous stratified structure for the propagation of an internal exothermic chemical reaction along an expanding wavefront and method of making same," *U.S. Patent No. 5538795*, 1996.

[24] P. Kelly, S. Tinston, and R. Arnell, "The deposition and analysis of pyrotechnic devices deposited by magnetron sputtering," *Surface and Coating Technology*, vol. 60, pp. 597–602, 1993.

[25] A. Gavens, D. Van Heerden, A. Mann, M. Reiss, and T. Weihs, "Effect of intermixing on self-propagating exothermic reactions in Al/Ni nanolaminate foils," *Journal of Applied Physics*, vol. 87, no. 3, pp. 1255–1263, 2000.

[26] L. Battezzati, P. Pappalepore, F. Durbiano, and I. Gallino, "Solid state reactions in Al/Ni alternate foils induced by cold rolling and annealing," *Acta Materialia*, vol. 47, no. 6, pp. 1901–1914, 1999.

[27] D. Eakins, *Role of Heterogeneity in the Chemical and Mechanical Shock-Response of Nickel and Aluminum Powder Mixtures*. PhD thesis, Georgia Institute of Technology, 2007.

[28] G. Fowles, "Shock wave physics," in *Metallurgical Effects at High Strain Rates* (R. Rohde, B. Butcher, J. Holland, and C. Karnes, eds.), pp. 15–31, New York: Plenum Press, 1973.

[29] D. Hayes, "Introduction to stress wave phenomena." Course Notes, 1973. SLA-73-0801.

[30] W. Rankine, "On the thermodynamic theory of waves of finite longitudinal disturbance," *Philosophical Transactions of the Royal Society of London*, vol. 160, pp. 277–288, 1870.

[31] P. Hugoniot, "Sur la propagation du mouvement dans les corps et specialement dans les gaz parfaits," *Journal de L'Ecole Polytechnique*, pp. 1–125, 1889.

[32] W. Gourdin, "Dynamic consolidation of metal powders," *Progress in Materials Science*, vol. 30, pp. 39–80, 1986.

[33] M. Rice, M. McQueen, and J. Walsh, "Compression of solids by strong shock waves," *Solid State Physics IV*, vol. 6, no. 1, pp. 1–63, 1958.

[34] L. Chhabildas and R. Graham, "Developments in measurement techniques for shock-loaded solids," in *Techniques and Theory of Stress Measurements for Shock Wave Applications* (R. Stout, F. Norwood, and M. Fourney, eds.), pp. 1–18, The American Society of Mechanical Engineers, 1987.

[35] O. Jones, "Shock wave physics," in *Metallurgical Effects at High Strain Rates* (R. Rohde, B. Butcher, J. Holland, and C. Karnes, eds.), pp. 33–55, New York: Plenum Press, 1973.

[36] L. Davison, "Material response II: inviscid compressible fluids," in *Fundamentals of Shock Wave Propagation in Solids*, (Berlin), pp. 81–120, Springer, 2008.

[37] J. Walsh and R. Christian, "Equation of state of metals from shock wave measurements," *Physical Review*, vol. 97, no. 6, pp. 1544–1556, 1955.

[38] M. Meyers, *Dynamic Behavior of Materials*. New York: John Wiley and Sons, 1994.

[39] E. Grüneisen, "Relation between compressibility, thermal expansion, atom volume and atomic heat of metals," *Annalen der Physik*, vol. 26, pp. 394–402, 1908.

[40] J. Johnson, "Single-particle model of a solid: the Mie-Grüneisen equation," *American Journal of Physics*, vol. 36, no. 10, pp. 917–919, 1968.

[41] R. Menikoff, "Emperical equations of state for solids," in *Shock Wave Science and Technology Reference Library* (Y. Horie, ed.), vol. 2, pp. 143–188, Springer, 2007.

[42] V. Zharkov and V. Kalinin, "Compression of solids by strong shock waves," in *Equation of state for solids at high pressures and temperatures*, (New York), pp. 106–177, Consultants Bureau, 1971.

[43] J. Slater, *Introduction to Chemical Physics*. New York: McGraw-Hill, 1939.

[44] J. Dugdale and D. MacDonald, "The thermal expansion of solids," *Physical Review*, vol. 89, no. 4, pp. 832–834, 1953.

[45] R. McQueen, S. Marsh, J. Taylor, J. Fritz, and W. Carter, "The equation of state of solids from shock wave studies," in *High Velocity Impact Phenomena*, pp. 293–471, New York: Academic Press, 1970.

[46] M. Baer, C. Hall, R. Gustavsen, D. Hooks, and S. Sheffield, "Isentropic loading experiments of a plastic bonded explosive and constituents," *Journal of Applied Physics*, vol. 101, no. 034906, 2007.

[47] J. Jordan, D. Dattelbaum, L. Ferranti, G. Sutherland, M. Baer, W. Richards, S. Sheffield, R. Dick, and N. N. Thadhani, "Shock equation of state of single constituent and multi-constituent epoxy-based particulate composites," in *Shock Compression of Condensed Matter - 2009* (M. Elert, W. Buttler, M. Furnish, W. Anderson, and W. Proud, eds.), pp. 1253–1256, 2009.

[48] W. Hermann, "Constitutive equation for the dynamic compaction of ductile porous materials," *Journal of Applied Physics*, vol. 40, no. 6, pp. 2490–2499, 1969.

[49] D. Grady, N. Winfree, G. Kerley, L. Wilson, and L. Kuhns, "Computational modeling and wave propagation in media with inelastic deforming microstructure," *Journal de Physique IV*, vol. 10, no. Pr9, 2000.

[50] B. Butcher and C. Karnes, "Dynamic compaction of porous iron," *Journal of Applied Physics*, vol. 40, no. 7, pp. 2967–2976, 1969.

[51] M. Carroll and A. Holt, "Suggested modification of the P-α model for porous materials," *Journal of Applied Physics*, vol. 43, no. 2, pp. 759–761, 1972.

[52] G. Simons and H. Legner, "An analytic model for the shock Hugoniot in porous materials," *Journal of Applied Physics*, vol. 53, no. 2, pp. 943–947, 1982.

[53] Q. Wu and F. Jing, "Thermodynamic equation of state and application to Hugoniot predictions for porous materials," *Journal of Applied Physics*, vol. 80, no. 8, pp. 4343–4349, 1996.

[54] D. A. Fredenburg, *Shock Compaction and Impact Response of Thermite Powder Mixtures*. PhD thesis, Georgia Institute of Technology, 2010.

[55] Y. Horie and A. Sawaoka, "Thermomechanics of powder compaction and mass mixing," in *Shock Compression Chemistry of Materials*, p. 128, Tokyo: KTK Scientific, 1993.

[56] S. P. Marsh, ed., *Los Alamos Series on Dynamic Material Properties*. University of California Press, 1980.

[57] Y. B. Zel'dovich and Y. Raizer, *Physics of Shock Waves and High-Temperature Hydrodynamic Phenomena*, vol. 2. New York: Academic Press, 1967.

[58] M. Petrie and N. Page, "An equation of state for shock loaded powders," *Journal of Applied Physics*, vol. 69, no. 6, pp. 3517–3524, 1991.

[59] K. Kawakita and K. Lüdde, "Some considerations on powder compression equations," *Powder Technology*, vol. 4, pp. 61–68, 1970.

[60] K. Oh and P. Persson, "Equation of state for extrapolation of high-pressure shock Hugoniot data," *Journal of Applied Physics*, vol. 65, no. 10, pp. 3852–3856, 1989.

[61] M. Carroll and A. Holt, "Static and dynamic pore-collapse relations for ductile porous materials," *Journal of Applied Physics*, vol. 43, no. 4, pp. 1626–1636, 1972.

[62] P. DeCarli and J. Jamieson, "Formation of diamond by explosive shock," *Science*, vol. 133, pp. 1821–1822, 1961.

[63] D. Eakins and N. Thadhani, "The shock-compression of reactive powder mixtures," *International Materials Review*, vol. 54, no. 4, pp. 181–213, 2009.

[64] N. Thadhani, "Shock-induced and shock-assisted solid state chemical reactions in powder mixtures," *Journal of Applied Physics*, vol. 76, no. 4, pp. 2129–2138, 1994.

[65] Y. Horie, R. Graham, and I. Simonsen, "Synthesis of nickel aluminides under high-pressure shock loading," *Materials Letters*, vol. 3, pp. 354–359, 1985.

[66] R. Graham and D. Webb, "Fixtures for controlled explosive loading and preservation of powder samples," in *Shock Waves in Condensed Matter-1983* (J. Asay, R. Graham, and G. Straub, eds.), pp. 211–214, North-Holland, 1984.

[67] Y. Horie, R. Graham, and I. Simonsen, "Observations on the shock-synthesis of intermetallic compounds," in *Metallurgical Applications of Shock-Wave and High-Strain-Rate Phenomena* (L. E. Murr, K. P. Staudhammer, and M. Meyers, eds.), pp. 1023–1035, New York: Marcel Dekker, 1986.

[68] T. Akashi and A. Sawaoka, "High density compacts," *U.S. Patent No. 4655830*, 1987.

[69] W. Hammetter, R. Graham, B. Morosin, and Y. Horie, "Effects of shock modification on the self-propagating high temperature synthesis of nickel aluminides," in *Shock Waves in Condensed Matter-1987* (S. Schmidt and N. Holmes, eds.), pp. 431–434, Elsevier, 1988.

[70] N. Thadhani, "Shock-induced chemical synthesis of intermetallic compounds," in *Shock Compression of Condensed Matter-1989* (S. Schmidt, J. Johnson, and L. Davison, eds.), pp. 503–510, Elsevier, 1990.

[71] I. Song and N. Thadhani, "Effects of shock processing parameters on synthesis of nickel aluminides," in *Shock Compression of Condensed Matter-1989* (S. Schmidt, J. Johnson, and L. Davison, eds.), pp. 499–502, Elsevier, 1990.

[72] L. Bennett, F. Sorrell, I. Simonsen, Y. Horie, and K. Iyer, "Ultrafast chemical reactions between nickel and aluminum powders during shock loading," *Applied Physics Letters*, vol. 61, no. 5, pp. 520–521, 1992.

[73] B. Krueger and T. Vreeland, "Shock-initiated chemical reactions in 1:1 atomic percent nickel-silicon powder mixtures," in *Shock-Wave and High-Strain-Rate Phenomena in Materials* (M. Meyers, L. Murr, and K. Staudhammer, eds.), pp. 245–252, New York: Marcel Dekker, 1992.

[74] Y. Yang, R. Gould, Y. Horie, and K. Iyer, "Shock-induced chemical reactions in a Ni/Al powder mixture," *Applied Physics Letters*, vol. 70, no. 25, pp. 3365–3367, 1997.

[75] R. Graham, M. Anderson, Y. Horie, S. You, and G. Holman, "Pressure measurements in chemically reacting powder mixtures with bauer piezoelectric polymer gauge," *Shock Waves*, vol. 3, pp. 79–82, 1993.

[76] L. Bennett and Y. Horie, "Shock-induced inorganic reactions and condensed phase detonations," *Shock Waves*, vol. 4, pp. 127–136, 1994.

[77] A. Dremin and O. Breusov, "Processes occurring in solids under the action of powerful shock waves," *Russian Chemical Reviews*, vol. 37, pp. 392–402, 1968.

[78] S. Tamura and Y. Horie, "Discrete meso-dynamic simulation of thermal explosion in shear bands," *Journal of Applied Physics*, vol. 84, no. 7, pp. 3574–3580, 1998.

[79] V. Nesterenko, M. Meyers, H. Chen, and J. LaSalvia, "Controlled high-rate localized shear in porous reactive media," *Applied Physics Letters*, vol. 65, no. 24, pp. 3069–3071, 1994.

[80] R. Graham, "Issues in shock-induced solid state chemistry," in *3rd International Symposium on High Dynamic Pressures* (R. Charet, ed.), (La Grande-Motte, France), pp. 175–180, CEA, 1989.

[81] S. Lee, A. Gokhale, and A. Sreeranganathan, "Reconstruction and visualization of complex 3D pore morphologies in a high-pressure die-cast magnesium alloy," *Materials Science and Engineering A*, vol. 427, pp. 92–98, 2006.

[82] D. Benson, "Computational methods in Lagrangian and Eulerian hyrdocodes," *Computer Methods in Applied Mechanics and Engineering*, vol. 99, pp. 235–394, 1992.

[83] J. Zukas, *Introduction to Hydrocodes*. Amsterdam: Elsevier, 2004.

[84] R. Williamson, "Parametric studies of dynamic powder consolidation using a particle-level numerical model," *Journal of Applied Physics*, vol. 68, no. 3, pp. 1287–1296, 1990.

[85] D. Benson, "An analysis by direct numerical simulation of the effects of particle morphology on the shock compaction of copper powder," *Modelling and Simulation in Materials Science and Engineering*, vol. 2, pp. 535–550, 1994.

[86] D. Benson, "The calculation of the shock velocity-particle velocity relationship for a copper powder by direct numerical simulation," *Wave Motion*, vol. 21, pp. 85–99, 1995.

[87] D. Benson, "A multi-material Eulerian formulation for the efficient solution of impact and penetration problems," *Computational Mechanics*, vol. 15, no. 6, pp. 558–571, 1995.

[88] Sandia National Laboratories, *CTH v8.1, v9.1, and v10.2*, 2007-2011.

[89] M. Baer, "Modeling heterogeneous energetic materials at the mesoscale," *Thermochimica Acta*, vol. 384, pp. 351–367, 2002.

[90] M. Baer and J. Nunziato, "A two-phase mixture theory for the deflagration-to-detonation transition (DDT) in reactive granular materials," *International Journal of Multiphase Flow*, vol. 12, no. 6, pp. 861–889, 1986.

[91] I. Do and D. Benson, "Modeling shock-induced chemical reactions," *International Journal of Computational Engineering Science*, vol. 1, no. 1, pp. 61–79, 2000.

[92] D. Reding and S. Hanagud, "Chemical reactions in reactive powder metal mixtures during shock compression," *Journal of Applied Physics*, vol. 105, no. 024912, 2009.

[93] M. Baer, D. Gartling, and P. DesJardin, "Probabilistic models for reactive behavior in heterogeneous condensed phase media," *Combustion Theory and Modeling*, vol. 16, pp. 75–106, 2012.

[94] G. Johnson and W. Cook, "A constitutive model and data for metals subjected to large strains, high strain rates and high temperatures," in *Proceedings of the Seventh International Symposium on Ballistics*, (The Hague, The Netherlands), pp. 541–547, 1983.

[95] D. Steinberg, S. Cochran, and M. Guinan, "A constitutive model for metals applicable at high-strain rate," *Journal of Applied Physics*, vol. 51, no. 3, pp. 1498–1504, 1980.

[96] D. Steinberg and C. Lund, "A constitutive model for strain rates from 10^{-4} to 10^{6} s^{-1}," *Journal of Applied Physics*, vol. 65, no. 4, pp. 1528–1533, 1989.

[97] F. Zerilli and R. Armstrong, "Dislocation-mechanics-based constitutive relations for material dynamics calculations," *Journal of Applied Physics*, vol. 61, no. 5, pp. 1816–1825, 1987.

[98] R. Austin and D. McDowell, "A dislocation-based constitutive model for viscoplastic deformation of fcc metals at very high strain rates," *International Journal of Plasticity*, vol. 27, pp. 1–24, 2011.

[99] R. Austin and D. McDowell, "Parameterization of a rate-dependent model of shock-induced plasticity for copper, nickel, and aluminum," *International Journal of Plasticity*, vol. 32-33, pp. 134–154, 2012.

[100] M. Guinan and D. Steinberg, "A simple approach to extrapolating measured polycrystalline shear moduli to very high pressure," *Journal of Physics and Chemistry of Solids*, vol. 36, p. 829, 1975.

[101] R. Austin, *Modeling Shock Wave Propagation in Discrete Ni/Al Powder Mixtures*. PhD thesis, Georgia Institute of Technology, 2010.

[102] R. Austin, D. McDowell, and D. Benson, "Mesoscale simulation of shock wave propagation in discrete Ni/Al powder mixtures," *Journal of Applied Physics*, vol. 111, no. 123511, 2012.

[103] M. Reiss, C. Esber, D. Van Heerden, A. Gavens, M. Williams, and T. Weihs, "Self-propagating formation reactions in Nb/Si multilayers," *Materials Science and Engineering A*, vol. 261, pp. 217–222, 1999.

[104] X. Qiu, R. Liu, S. Guo, J. Graeter, L. Kecskes, and J. Wang, "Combustion synthesis reactions in cold-rolled Ni/Al and Ti/Al multilayers," *Metallurgical and Materials Transactions A*, vol. 40A, pp. 1541–1546, 2009.

[105] K. Coffey, L. Clevenger, K. Barmak, D. Rudman, and C. Thompson, "Experimental evidence for nucleation during thin-film reactions," *Applied Physics Letters*, vol. 55, no. 9, pp. 852–854, 1989.

[106] F. Bordeaux and A. Yavari, "Amorphization by solid-state reaction of crystalline aluminum and platinum multilayers prepared by cold rolling," *Journal of Applied Physics*, vol. 67, no. 5, pp. 2385–2389, 1990.

[107] R. Knepper, M. Snyder, G. Fritz, K. Fisher, O. Knio, and T. Weihs, "Effect of varying bilayer spacing distribution on reaction heat and velocity in reactive Al/Ni multilayer," *Journal of Applied Physics*, vol. 105, p. 083504, 2009.

[108] G. Fritz, H. Joress, and T. Weihs, "Enabling and controlling slow reaction velocities in low-density compacts of multilayer reactive particles," *Combustion and Flame*, vol. 158, pp. 1084–1088, 2011.

[109] A. Mann, A. Gavens, M. Reiss, D. Van Heerden, G. Bao, and T. Weihs, "Modeling and characterizing the propagation velocity of exothermic reactions in multilayer foils," *Journal of Applied Physics*, vol. 82, no. 3, pp. 1178–1188, 1997.

[110] T. Jeske and G. Schmitz, "Nanoscale analysis of the early interreaction stages in Al/Ni," *Scripta Materialia*, vol. 45, pp. 555–560, 2001.

[111] D. Aurongzeb, M.Holtz, M. Daugherty, J. Berg, A. Chandolu, J. Yun, and H. Temkin, "Influence of nanocrystal growth kinetics on interface roughness in nickel-aluminum multilayers," *Applied Physics Letters*, vol. 83, no. 26, pp. 5437–5439, 2003.

[112] X. Qiu, J. Graeter, L. Kecskes, and J. Wang, "Exothermic reactions in cold-rolled Ni/Al reactive multilayer foils," *Journal of Materials Research*, vol. 23, no. 2, pp. 367–375, 2008.

[113] X. Sauvage, G. Dinda, and G. Wilde, "Non-equilibrium intermixing and phase transformation in severely deformed Al/Ni multilayers," *Scripta Materialia*, vol. 56, pp. 181–184, 2007.

[114] H. Sieber, J. Park, J. Weissmüller, and J. Perepezko, "Structural evolution and phase formation in cold-rolled aluminum-nickel multilayers," *Acta Materialia*, vol. 49, pp. 1139–1151, 2001.

[115] X. Qiu and J.Wang, "Experimental evidence of two-stage formation of Al_3Ni in reactive Ni/Al multilayer foils," *Scripta Materialia*, vol. 56, pp. 1055–1058, 2007.

[116] U. Anselmi-Tamburini and Z. Munir, "The propagation of a solid-state combustion wave in Ni-Al foils," *Journal of applied Physics*, vol. 66, no. 10, pp. 5039–5045, 1989.

[117] H. Kim, D. Chung, and S. Hong, "Intermixing criteria for reaction synthesis of Ni/Al multilayered microfoils," *Scripta Materialia*, vol. 54, pp. 1715–1719, 2006.

[118] P. Zhu, J. Li, and C. Liu, "Reaction mechanism of combustion synthesis of NiAl," *Materials Science and Engineering A*, vol. 329-331, pp. 57–68, 2002.

[119] M. Atzmon, "*In Situ* thermal observation of explosive compound-formation reaction during mechanical alloying," *Physical Review Letters*, vol. 64, no. 4, pp. 487–490, 1990.

[120] F. Cardellini, G. Mazzone, and M. Vittori Antisari, "Solid state reactions and microstructural evolution of Al-Ni powders during high-energy ball milling," *Acta Materialia*, vol. 44, no. 4, pp. 1511–1517, 1996.

[121] A. Budiman, S. Han, N. Li, Q. Wei, P. Dickerson, N. Tamura, M. Kunz, and A. Misra, "Plasticity in the nanoscale Cu/Nb single-crystal multilayers as revealed by synchrotron laue x-ray microdiffraction," *Journal of Materials Research*, vol. 27, no. 3, pp. 599–611, 2012.

[122] Y. Kim, A. Budiman, J. Baldwin, N. Mara, M. A, and S. Han, "Microcompression study of Al-Nb nanoscale multilayers," *Journal of Materials Research*, vol. 27, no. 3, pp. 592–598, 2012.

[123] C. Lundergan and D. Drumheller, "Propagation of stress waves in a laminated plate composite," *Journal of Applied Physics*, vol. 42, no. 2, pp. 669–675, 1971.

[124] Y. Oved, G. Luttwak, and Z. Rosenberg, "Shock wave propagation in layered composites," *Journal of Composite Materials*, vol. 12, pp. 84–96, 1978.

[125] S. Zhuang, G. Ravichandran, and D. Grady, "An experimental investigation of shock wave propagation in periodically layered composites," *Journal of the Mechanics and Physics of Solids*, vol. 51, pp. 245–265, 2003.

[126] E. Vitali, C. Wei, D. Benson, and M. Meyers, "Effects of geometry and intermetallic bonding on the mechanical response, spalling and fragmentation of Ni-Al laminates," *Acta Materialia*, vol. 59, pp. 5869–5880, 2011.

[127] L. Barker, "A model for stress wave propagation in composite materials," *Journal of Composite Materials*, vol. 5, pp. 140–162, 1971.

[128] L. Barker, C. Lundergan, P. Chen, and M. Gurtin, "Nonlinear viscoelasticity and the evolution of stress waves in laminated composites: a comparison of theory and experiment," *Journal of Applied Mechanics*, vol. 41, pp. 1025–1030, December 1974.

[129] D. Curran, L. Seaman, and M. Austin, "The use of artificial viscosity to compute one-dimensional wave propagation in composite materials," *Journal of Composite Materials*, vol. 8, pp. 142– 159, April 1974.

[130] D. Drumheller and H. Sutherland, "A lattice model for stress wave propagation in composite materials," *Journal of Applied Mechanics*, vol. 40, pp. 149–154, March 1973.

[131] C. Sun, J. Achenbach, and G. Herrmann, "Time-harmonic waves in a stratified medium propagating in the direction of the layering," *Journal of Applied Mechanics*, vol. 35, pp. 408–411, June 1968.

[132] C. Sun, J. Achenbach, and G. Herrmann, "Continuum theory for a laminated medium," *Journal of Applied Mechanics*, vol. 35, pp. 467–475, September 1968.

[133] J. Achenbach and G. Hermann, "Dispersion of free harmonic waves in fiber-reinforced composites," *AIAA Journal*, vol. 6, no. 10, pp. 1832–1836, 1968.

[134] J. Peck and G. Gurtman, "Dispersive pulse propagation parallel to the interfaces of a laminated composite," *Journal of Applied Mechanics*, vol. 36, pp. 479–484, September 1969.

[135] F. Tsou and P. Chou, "Analytical study of Hugoniot in unidirectional fiber reinforced composites," *Journal of Composite Materials*, vol. 3, pp. 500–514, July 1969.

[136] F. Tsou and P. Chou, "The control-volume approach to Hugoniot of macroscopically homogeneous composites," *Journal of Composite Materials*, vol. 4, pp. 526–537, October 1970.

[137] P. Torvik, "Shock propagation in a composite material," *Journal of Composite Materials*, vol. 4, pp. 296–309, July 1970.

[138] D. Munson and K. Schuler, "Steady wave analysis of wave propagation in laminates and mechanical mixtures," *Journal of Composite Materials*, vol. 5, pp. 286–304, July 1971.

[139] X. Chen, N. Chandra, and A. Rajendran, "Analytical solution to the plate impact problem of layered heterogeneous material systems," *International Journal of Solids and Structures*, vol. 41, pp. 4635–4659, 2004.

[140] G. Floquet, "Sur les équations différentielles linéaires á coefficients périodiques," *C.R. Acad. Sci. Paris*, vol. 91, pp. 880–882, 1880.

[141] X. Chen and N. Chandra, "The effect of heterogeneity on plane wave propagation through layered composites," *Composites Science and Technology*, vol. 64, pp. 1477–1493, 2004.

[142] S. Spey, *Ignition properties of multilayer nanoscale reactive foils and the properties of metal-ceramic joints made with the same.* PhD thesis, Johns Hopkins University, 2005.

[143] C. Wei, B. Maddox, A. Stover, T. Weihs, V. Nesterenko, and M. Meyers, "Reaction in Ni-Al laminates by laser-shock compression and spalling," *Acta Materialia*, vol. 59, pp. 5276–5287, 2011.

[144] S. Zhao, T. Germann, and A. Strachan, "Molecular dynamics characterization of the response of Ni/Al nanolaminates under dynamic loading," *Journal of Propulsion and Power*, vol. 23, no. 4, pp. 693–697, 2007.

[145] S. Zhao, T. Germann, and A. Strachan, "Melting and alloying of Ni/Al nanolaminates induced by shock loading: a molecular dynamics simulation study," *Physical Review B*, vol. 76, no. 104105, 2007.

[146] W. Cubberly, H. Baker, D. Benjamin, P. Unterweiser, C. Kirkpatrick, V. Knoll, and K. Nieman, eds., *Metals Handbook Ninth Edition: Volume 2 Properties and Selection: Nonferrous Alloys and Pure Metals*, vol. 2. Metals Park, Ohio: American Society for Metals, 9 ed., 1979.

[147] B. Predel, *Phase Equilibria, Crystallographic and Thermodynamic Data of Binary Alloys*, vol. 5 of *Physical Chemistry: Light Metal Structural Alloys*. Berlin: Springer, 1998.

[148] ICDD, Powder Diffraction Files. # 00-040-1157, 01-074-7054, 01-073-2594, 00-046-1037, 00-002-0416, 01-072-9667.

[149] P. Desai, "Thermodynamic properties of selected binary aluminum alloy systems," *Journal of Physical and Chemical Reference Data*, vol. 16, no. 1, pp. 109–124, 1987.

[150] K. Tsai, V. Kuznetsov, P. Kaminskii, and T. Turkebaev, "Calculation of the thermodynamic properties of the phases and analysis of their stability for the Ni-Al system in the model functional electron density method," *Russian Physics Journal*, vol. 39, no. 4, pp. 375–383, 1996.

[151] Y. Xun, D. Lunking, E. Besnoin, D. Van Heerden, T. Weihs, and O. Knio, "Methods of making reactive composite materials and resulting products," *U.S. Patent Application 20110027547*, 2011.

[152] L. Alawieh, O. Knio, and T. Weihs, "Effect of thermal properties on self-propagating fronts in reactive nanolaminates," *Journal of Applied Physics*, vol. 110, no. 013509, 2011.

[153] R. DeHoff and F. Rhines, eds., *Quantitative Microscopy*. New York: McGraw-Hill, 1968.

[154] A. Gokhale and W. Drury, "Efficient measurement of microstructural surface area using trisector," *Metallurgical and Materials Transactions A*, vol. 25, pp. 919–928, 1994.

[155] J. Russ, *Practical Stereology*. New York: Plenum Press, 1986.

[156] J. White and F. Angona, "Elastic wave velocities in laminated media," *The Journal of the Acoustical Society of America*, vol. 27, no. 2, pp. 310–317, 1955.

[157] G. Postma, "Wave propagation in a stratified medium," *Geophysics*, vol. 20, no. 4, pp. 780–806, 1955.

[158] A. Tewari, A. Gokhale, J. Spowart, and D. Miracle, "Quantitative characterization of spatial clustering in three-dimensional microstructures using two-point correlation functions," *Acta Materialia*, vol. 52, pp. 307–319, 2004.

[159] H. Singh, A. Gokhale, S. Lieberman, and S. Tamirisakandala, "Image based computations of lineal path probability distributions for microstructure representation," *Materials Science and Engineering A*, vol. 474, pp. 104–111, 2008.

[160] B. White, *Microstructure and Strain Rate Effects on the Mechanical Behavior of Particle Reinforced Epoxy-Based Reactive Materials*. PhD thesis, Georgia Institute of Technology, 2011.

[161] J. Spowart, B. Maruyama, and D. Miracle, "Multi-scale characterization of spatially heterogeneous systems: implications for discontinuously reinforced metal-matrix composite microstructures," *Materials Science and Engineering A*, vol. 307, pp. 51–66, 2001.

[162] M. Tschopp, G. Wilks, and J. Spowart, "Multi-scale characterization of orthotropic microstructures," *Modelling and Simulation in Materials Science and Engineering*, vol. 16, no. 065009, 2008.

[163] M. A. Meyers and S. Wang, "An improved method for shock consolidation of powders," *Acta Metallurgica*, vol. 36, no. 4, pp. 925–936, 1988.

[164] A. Ferreira, M. Meyers, N. Thadhani, S. Chang, and J. R. Kough, "Dynamic compaction of titanium aluminides by explosively generated shock waves: experimental and materials systems," *Metallurgical Transactions A*, vol. 22, pp. 685–695, 1991.

[165] S. Du, B. Aydelotte, D. Fondse, C. Wei, F. Jiang, E. Herbold, K. Vecchio, M. Meyers, and N. Thadhani, "Explosive compations[*sic*] of intermetallic-forming powder mixtures for fabricating structural energetic materials," in *Shock Compression of Condensed Matter - 2009* (M. Elert, W. Buttler, M. Furnish, W. Anderson, and W. Proud, eds.), pp. 498–501, 2009.

[166] ASM, ed., *Atlas of Stress-Strain Curves*. Materials Park, OH: ASM International, 2 ed., 2002.

[167] F. Bauer, "Method and device for polarizing ferroelectric materials," *U.S. Patent No. 4611260*, 1986.

[168] F. Bauer, "Device for polarizing ferroelectric materials," *U.S. Patent No. 4684337*, 1987.

[169] P. Urtiew and L. Erickson, "Measurement of dynamic pressure in inert and reactive solids by PVF_2 and manganin gauges," in *Techniques and Theory of Stress Measurements for Shock Wave Applications* (R. Stout, F. Norwood, and M. Fourney, eds.), pp. 29–35, The American Society of Mechanical Engineers, 1987.

[170] D. Wackerbarth, M. Anderson, and R. Graham, "PVDFSTRESS: a PC-based computer program to reduce Bauer PVDF stress-rate gauge data," *Sandia Report*, no. SAND92-0046, 1992.

[171] R. Graham, M. Anderson, F. Bauer, and R. Setchell, "Piezoelectric polarization of the ferroelectric polymer PVDF from 10 MPa to 10 GPa: studies of loading-path dependence," in *Shock Compression of Condensed Matter 1991* (S. Schmidt, R. Dick, J. Forbes, and D. Tasker, eds.), pp. 883–886, Elsevier, 1992.

[172] F. Bauer, R. Graham, M. Anderson, H. Lefebvre, L. Lee, and R. Reed, "Response of the piezoelectric polymer PVDF to shock compression greater than 10 GPa," in *Shock Compression of Condensed Matter 1991* (S. Schmidt, R. Dick, J. Forbes, and D. Tasker, eds.), pp. 887–890, Elsevier, 1992.

[173] C. Neel, *Shock Compression of a Heterogeneous, Porous Polymer Composite*. PhD thesis, Georgia Institute of Technology, 2010.

[174] Sandia National Laboratories, *Plotdata v2.3*, 2005.

[175] L. Barker and R. Hollenbach, "Laser interferometer for measuring high velocities of any reflecting surface," *Journal of Applied Physics*, vol. 43, no. 11, pp. 4669–4675, 1972.

[176] L. Barker, "Multi-beam VISARs for simultaneous velocity vs. time measurements," in *Shock Compression of Condensed Matter-1999* (M. Furnish, L. Chhabildas, and R. Hixson, eds.), pp. 999–1002, American Institute of Physics, 2000.

[177] D. Dolan, "Foundations of VISAR analysis," *Sandia Report*, vol. SAND2006-1950, 2006.

[178] L. Barker, "The accuracy of VISAR instrumentation," in *Shock Compression of Condensed Matter-1997* (S. Schmidt, D. Dandekar, and J. Forbes, eds.), pp. 833–836, American Institute of Physics, 1998.

[179] W. Hemsing, "Velocity sensign interferomter (VISAR) modification," *Review of Scientific Instruments*, vol. 50, no. 1, pp. 73–78, 1979.

[180] L. Barker, "The development of the VISAR, and its use in shock compression science," in *Shock Compression of Condensed Matter-1999* (M. Furnish, L. Chhabildas, and R. Hixson, eds.), pp. 11–17, American Institute of Physics, 2000.

[181] D. Dolan, "Accuracy and precision in photonic Doppler velocimetry," *Review of Scientific Instruments*, vol. 81, no. 053905, 2010.

[182] O. Strand, L. Berzins, D. Goosman, W. Kuhlow, P. Sargis, and T. Whitworth, "Velocimetry using heterodyne techniques," in *26th International Congress on High-Speed Photography and Photonics* (D. Paisley, S. Kleinfelder, D. Snyder, and B. Thompson, eds.), vol. 5580, pp. 593–599, Alexandria, VA: SPIE, 2004.

[183] D. Dolan and S. Jones, "Push-pull analysis of photonic Doppler velocimetry measurements," *Review of Scientific Instruments*, vol. 78, no. 076102, 2007.

[184] B. Jensen, D. Holtkamp, P. Rigg, and D. Dolan, "Accuracy limits and window corrections for photon Doppler velocimetry," *Journal of Applied Physics*, vol. 101, no. 013523, 2007.

[185] *pTool v2.3*, 2008.

[186] A. Mitchell and W. Nellis, "Shock compression of aluminum, copper, and tantalum," *Journal of Applied Physics*, vol. 52, no. 5, pp. 3363–3374, 1981.

[187] Y. Beers, *Introduction to the Theory of Error*. Cambridge Mass.: Addison-Wesley, 1953.

[188] R. Warfield, "The Grüneisen constant of polymers," *Die Makromolekulare Chemie*, vol. 175, pp. 3285–3297, 1974.

[189] M. Broadhurst, G. Davis, J. McKinney, and R. Collins, "Piezoelectricity and pyroelectricity in polyvinylidene flouride - a model," *Journal of Applied Physics*, vol. 49, no. 10, pp. 4992–4997, 1978.

[190] R. Graham and W. Brooks, "Shock-wave compression of sapphire from 15 to 420 kbar. The effect of large anisotropic compressions," *Journal of Physical Chemistry of Solids*, vol. 32, pp. 2311–2330, 1971.

[191] S. Burghartz and B. Schulz, "Thermophysical properties of sapphire, AlN, and $MgAl_2O_4$ down to 70K," *Journal of Nuclear Materials*, vol. 212-215, pp. 1065–1068, 1994.

[192] G. Taylor, "The use of flat-ended projectiles for determining dynamic yield stress. I. Theoretical considerations," *Proceedings of the Royal Society of London. Series A, Mathematical and Physical Sciences*, vol. 194, no. 1038, pp. 289–299, 1948.

[193] A. Whiffin, "The use of flat-ended projectiles for determining dynamic yield stress. II. Tests on various metallic materials," *Proceedings of the Royal Society of London. Series A, Mathematical and Physical Sciences*, vol. 194, no. 1038, pp. 300–322, 1948.

[194] W. Carrington and M. Gayler, "The use of flat-ended projectiles for determining dynamic yield stress. III. Changes on microstructure caused by deformation under impact at high-striking velocities," *Proceedings of the Royal Society of London. Series A, Mathematical and Physical Sciences*, vol. 194, no. 1038, pp. 323–331, 1948.

[195] S. Du and N. Thadhani, "Impact initiation of pressed Al-based intermetallic-forming powder mixture compacts," in *Shock Compression of Condensed Matter - 2009* (M. Elert, W. Buttler, M. Furnish, W. Anderson, and W. Proud, eds.), pp. 470–473, 2009.

[196] B. Cour-Palais, "Hypervelocity impact in metals, glass, and composites," *International Journal of Impact Engineering*, vol. 5, pp. 221–237, 1987.

[197] X. Xu and A. Needleman, "Numerical simulations of dynamic interfacial crack growth allowing for crack growth away from the bond line," *International Journal of Fracture*, vol. 74, pp. 253–275, 1995.